INTEGRATED EVALUATION OF STRUCTURAL UNCERTAINTY

USING HISTORY MATCHING

FROM SEISMIC IMAGING UNCERTAINTY MODEL

A DISSERTATION

SUBMITTED TO THE DEPARTMENT OF ENERGY RESOURCES ENGINEERING

AND THE COMMITTEE ON GRADUATE STUDIES

OF STANFORD UNIVERSITY

IN PARTIAL FULFILLMENT OF THE REQUIREMENTS FOR THE DEGREE OF

DOCTOR OF PHILOSOPHY

Satomi Suzuki

June 2007

I certify that I have read this dissertation and that, in my opinion, it is fully adequate in scope and quality as dissertation for the degree of Doctor of Philosophy.

_____

(Jef Caers) Principal Advisor

I certify that I have read this dissertation and that, in my opinion, it is fully adequate in scope and quality as dissertation for the degree of Doctor of Philosophy.

_____

(Robert Clapp)

I certify that I have read this dissertation and that, in my opinion, it is fully adequate in scope and quality as dissertation for the degree of Doctor of Philosophy.

_____

(Andre Journel)

Approved for the University Committee on Graduate Studies.

Abstract

Structural uncertainty is the first-order uncertainty in reservoir modeling both in terms of 1) the difficulty of structural interpretation due to limited data acquisition/quality and 2) the magnitude of its impact on uncertainty in hydrocarbon in-place and fluid flow performance. Though it is a common practice to consider structural uncertainty in the evaluation of hydrocarbon in-place in the appraisal phase of field developments, structural uncertainty is rarely considered when evaluating future production performance in the production phase. The reason is mainly the difficulty in integrating dynamic data into structural uncertainty modeling. This research aims at developing a method/workflow for structural uncertainty modeling which integrates geophysical and geological data during the process of history matching.

This dissertation first proposes a semiautomatic seismic interpretation method using geostatistical pattern simulation. From the resulting multiple structural interpretations, a prior stochastic structural model is built and used as a geological/geophysical constraint for the subsequent history matching. Next, a new history matching method is proposed: numerical models are inverted from dynamic fluid flow response while honoring the previous structural model. The method consists of searching for numerical models that match production history from a large set of prior structural model realizations. To make such a search effective, a parameter space defined with a “similarity distance” is introduced. The inverse solutions are found in this space using a stochastic search method. Synthetic but realistic reservoir examples are presented to demonstrate the proposed workflow/methods.

Acknowledgments

First of all, I would like to thank Jef Caers, my adviser, for his great advice and guidance. This work would not be completed without him for sure. His advice was always accurate and from broad point of view, which significantly contributed to this dissertation. I also would like to thank my collaborators of this work, Biond Biondi and Robert Clapp from Department of Geophysics and Guillaume Caumon from Nancy School of Geology. It was Biond Biondi who practically set the research direction of this work, by pointing out that real structural uncertainty is not the perturbation of fault/horizon positions around the best estimate, but the appearance and disappearance of faults depending on the velocity model used for migration. Robert Clapp has pioneered seismic imaging uncertainty modeling for resent years, and Chapter 2 of this dissertation is mostly his work. Also, I completed the work of Chapter 5 by working very closely with Guillaume Caumon. His advice about uncertainty modeling and geological modeling greatly contributed to this chapter.

Also, I obtained great help from students and postdocs. Burc Arpat is my senior student who proposed and developed the geostatistical pattern simulation algorithm (SIMPAT), which I used in Chapter 3. The GOCAD plug-in of fault network perturbation tool, which is used in Chapter 5, was developed by Lin Zhang from Nancy School of Geology. The illustrative example discussed in Chapter 4 was done in collaboration with Kent Johansen from Technical University of Denmark. Also, I learned about the neighborhood algorithm (NA), used in Chapters 4&5, from Vasily Demyanov from Heriot Watt University. I would like to thank them for their help and useful discussions.

I had honor to have Andre Journel and Roland Horne as committee members of my dissertation defense. Andre Journel has been directing SCRF (Stanford Center of Reservoir Forecasting), the research group I belonged, together with Jef Caers. I would like to thank him for his care and encouragement during my years in SCRF. Roland Horne was Department Chair of my department until last year and took great care of each and every student in the department. I was also greatly helped by him to get adjusted to the life in Stanford. I really appreciate his care.

Finally, I would like to thank all of SCRF students and SCRF postdocs who constantly helped and encouraged me, and thank my parents in Japan who constantly worried me.

Table of Contents

List of Tables

List of Figures

Chapter 1

Introduction

History matching of structurally complex reservoirs is one of the most challenging tasks in reservoir characterization, where the difficulty arises from large uncertainty in reservoir geometry itself, resulting from limited quality and resolution of seismic data. In addition to the uncertainty in the fault/horizon positions due to the low resolution of seismic images, the process of structural interpretation and migration is not unique and often rely on subjective decisions made by experts. The traditional history matching approach starts by fixing the reservoir geometry to a single interpretation. This may results in a failure to match past production, and it may lead to future development planning based on a "wrong" structural interpretation. Indeed in many cases the reservoir geometry has a stronger impact on production behavior than the petrophysical properties distribution.

This problem is already recognized in the domains of geophysics and geoscience, and several attempts were made to quantify the structural uncertainty. Thore et al. (2002) proposed a geostatistical approach for generating equiprobable multiple structural models accounting for multiple sources of uncertainties; more precisely, the uncertainties in migration, horizon picking, and time-to-depth conversion. The method calls for perturbing the position of horizons and faults starting from a "best" structural model obtained by expert's interpretation, and accounting for uncertainties from different sources. Later, Lecour et al. (2001) applied this method to a more complex fault network modeling focusing only on the uncertainty resulting from interpretation. Similar applications are also found in Samson et al. (1996), Corre et al. (2000), and Charles et al (2001). Methods for addressing structural uncertainty resulting from seismic processing (migration) have been also proposed. Clapp (2001, 2003) proposed a stochastic methodology for assessing the uncertainty in seismic imaging resulting from velocity modeling, where multiple

seismic velocity fields are stochastically generated accounting for the uncertainty associated with the error in velocity analysis from seismic gathers. By inputting these multiple velocity models into the migration of seismic data, multiple seismic data/image sets are obtained. Grubb et al. (2001) also proposed a multiple migration method for addressing the velocity uncertainty attributed to the ill-posedness of seismic inversion, where multiple migrations are achieved by inverting multiple velocity models using a global optimization technique.

All of these approaches have the potential to open the way for "considering structural uncertainty as a parameter for history matching (Thore et al., 2002)", providing reservoir engineers access to prior information on uncertainty related to structural interpretation/seismic processing. However, a method for inverting reservoir structure from production data under the constraints of prior geological information has been lacking. An attempt of dynamic data integration into stochastic structural uncertainty modeling is found in Rivenæs et al. (2005). Their approach utilizes stochastic tools for perturbing horizons from a deterministic structural model and for simulating fault patterns. The realizations that match historical pressure data are chosen by screening realizations using a streamline flow simulator. Their practice (Rivenæs et al., 2005) showed that experts often give significantly different structural interpretations although based on the same seismic image, thus the structural models should be built based on such several geological scenarios.

The major difficulty in history matching of structural geometry is attributed to the lack of efficient optimization methods for solving an inverse problem where the (discrete) choice of the structural interpretation is one of the parameters. Gradient-based methods do not apply in such inherently discrete parameter space. Also, reservoir geometry is often too complex to be parameterized in a Cartesian parameter space or to be addressed in the context of stochastic optimization methods such as the genetic algorithm.

This dissertation proposes a new method/workflow for modeling reservoir structural uncertainty integrating dynamic production data with geophysical/geological data. The proposed methodology does not history match a reservoir structure by a mere perturbation made from a single structural interpretation: it considers the multiple alternatives of seismic processing/interpretation which constitute the major source of structural uncertainty. Figure 1.1 illustrates the proposed workflow. It consists of two stages; prior and posterior structural uncertainty modeling. The modeling of prior structural uncertainty considers the geological/geophysical sources of uncertainty such as non-

uniqueness in the migration results due to uncertainty in velocity modeling, multiple alternative structural interpretations due to different decisions made on fault/horizon identification, and the error in horizon/fault positioning due to the low resolution of seismic images or time-to-depth conversion error. Uncertainty modeling at this stage aims at providing the parameter space for history matching; i.e. a large set of structural models which consists of hundreds of structural realizations and covers a large range of prior structural uncertainty. Such a large set of structural models is built by stochastically perturbing horizon and fault positions from several alternative structural interpretations (Fig. 1.1). Note that the computational cost for generating a new realization is extremely inexpensive compared to the cost required to flow-simulate this realization in the next stage. The second stage, the modeling of posterior structural uncertainty, is implemented by searching for a set of model realizations that match past production behavior in this parameter space (history matching, Figure 1.1). The goal of this stage is to reduce the structural uncertainty through the incorporation of dynamic production data. History matching requires several flow simulations on the model realizations which can be expensive: thus at this stage it is essential to search for model realizations with a reasonable number of flow simulations using an efficient optimization technique.

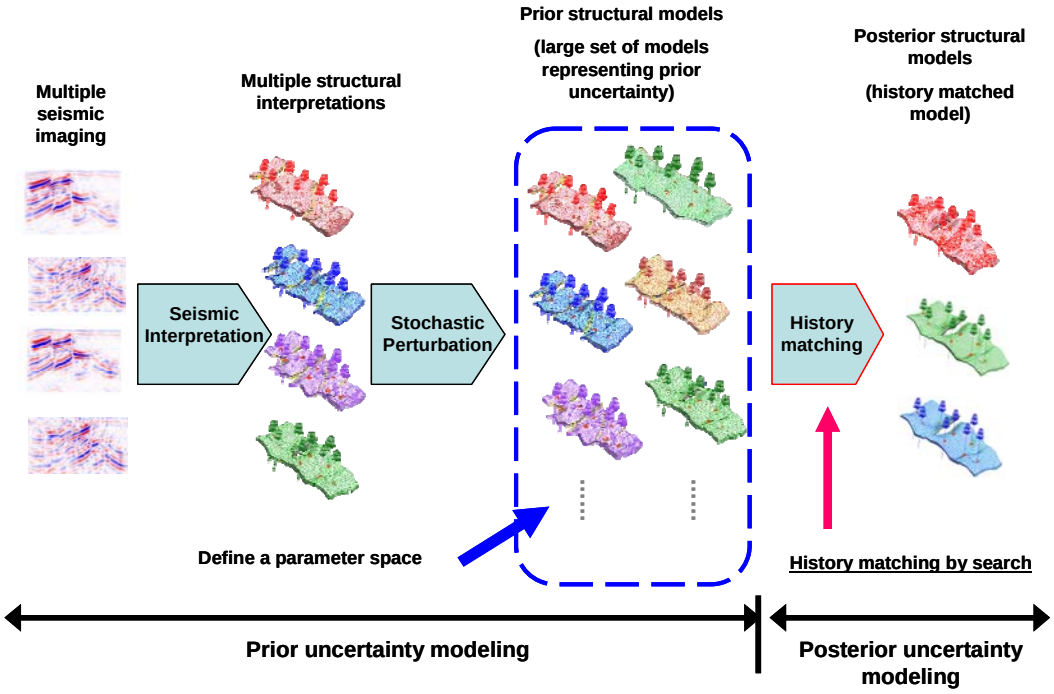

Figure 1.1: Proposed workflow for structural uncertainty modeling

This thesis consists of two parts (Parts I & II) that describe the new methodologies to implement the proposed workflow. Part I first reviews the multiple migration method of Clapp (2001, 2003) in Chapter 2. His method starts from the generation of multiple alternatives of seismic images depicting the uncertainty in the seismic velocity model used for migrating raw seismic data; this provides the multiple migration results needed to start the workflow illustrated in Figure 1.1. The next step of the workflow is to build several structural models from the previously obtained alternative seismic images. However, the manual interpretation of seismic sections is often time consuming especially when the volume of data is large. In practice, this manual labor cost may be a major obstacle to utilizing multiple alternative seismic interpretations for structural uncertainty modeling. Commercially available automatic interpretation tools are hardly applicable for structurally complex reservoirs since most algorithms rely on a simple autotracking of amplitude peaks. Therefore, a new semiautomatic seismic interpretation method is proposed in Chapter 3. This method is designed to assist in the seismic interpretation based on multiple migration results. This is done by autopicking faults and horizons on the seismic sections. A geostatistical pattern simulation method (Arpat, 2005) is used instead of the traditional autotracking technique. Once those multiple structural interpretations are obtained, a large set of structural models, which define a parameter space where history matching take places, are generated. Part II discusses how to implement the history matching in this discrete parameter space. In Chapter 4, a new method for inverting geological architecture from production data is proposed. The key idea of the method is to parameterize the geological architectures towards a spatial inverse problem. This parameter space is then provided with a distance function that measures the “similarity” between any two different geological architectures. Chapter 4 illustrates the proposed methodology through an example taken from a facies modeling problem. The method is then applied to structural modeling problems in Chapter 5. Chapter 6 summarizes and discusses the conclusions and future directions of this work.

Part I

Modeling Seismic Imaging Uncertainty

Chapter 2

Multiple Seismic Imaging Assessing Velocity Uncertainty

Clapp (2004, 2003, 2001) proposed a methodology for assessing the seismic imaging uncertainty related to the seismic velocity model used for migrating raw seismic data. By accounting for the uncertainty in seismic velocity estimation (Clapp, 2003) or moveout measurements (Clapp, 2004) and by inputting multiple velocity models into the migration, multiple seismic data/image sets are obtained. Structural models interpreted on the resulting multiple seismic images can be used as a set of prior reservoir models which starts the structural uncertainty modeling workflow proposed in this dissertation (Fig. 1.1). This chapter first reviews two methods of Clapp. The velocity uncertainty is modeled accounting for error in velocity estimation from seismic gathers in the first method (1-D super Dix, Clapp, 2003), while it is modeled in the second method (Clapp, 2004) in the context of tomography. Then, based on an actual reservoir data from the North Sea, a synthetic seismic imaging uncertainty model is constructed in collaboration with Clapp[1] and Biondi[2] to illustrate the methodology.

[1, 2] Department of Geophysics, Stanford University

2.1 Methods: Review

2.1.1 Uncertainty in Velocity Estimation Using Dix Formula

The methodology of Clapp (1-D super Dix, 2003) focuses on the uncertainty in seismic velocity estimated from common mid-point (CMP) gathers. A typical example of velocity estimation is given in Figure 2.1.

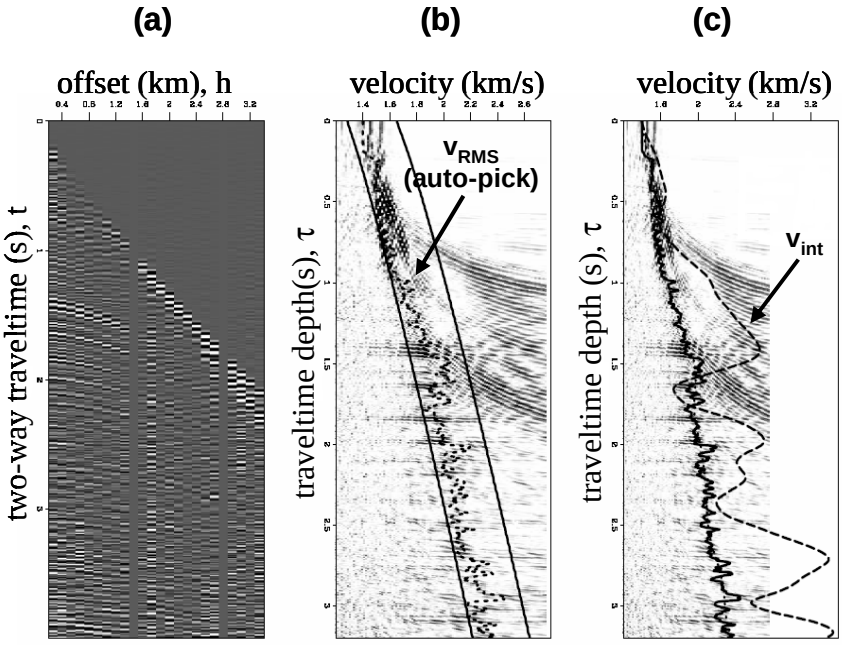

Figure 2.1: Example of velocity estimation from CMP gather, (a) CMP gather, (b) RMS velocity estimation on velocity scan, (c) interval velocity from RMS velocity

(Source: Robert G. Clapp, Multiple realizations and data variance: Successes and failures, Stanford Exploration Project, Report 113, 2003)

Figure 2.1a shows an example of a CMP gather (traveltime vs. offset) obtained at a particular common midpoint. Assuming waves as expanding circles, the relation between traveltime and offset is described as:

$$t^2 = \tau^2 + \frac{4h^2}{v_{RMS}^2} \tag{2.1}$$

t: two-way traveltime (i.e. traveltime from source to receiver)

τ: zero-offset two-way traveltime (called “traveltime depth”)

h: half-offset

v_{RMS}: root-mean-square (RMS) velocity

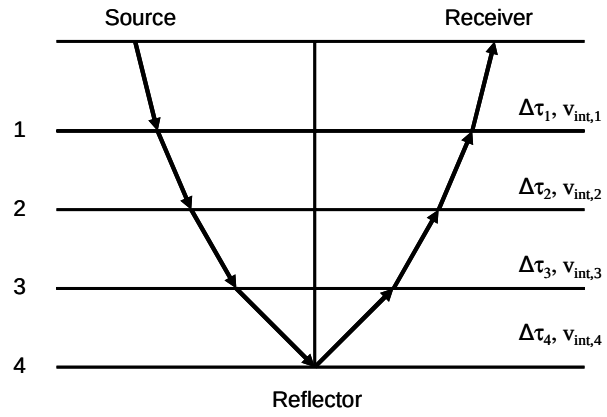

Figure 2.2: Horizontal layer assumption for a velocity field

Assuming a horizontally layered velocity field (Fig. 2.2) where the velocity of each layer is defined as interval velocity (v_{int}), RMS velocity (v_{RMS}) in Eq. 2.1 is defined from Dix Formula as below:

$$v_{RMS,i}^2 = \frac{\sum_{j=1}^{i} v_{int,j}^2 \Delta\tau_j}{\sum_{j=1}^{i} \Delta\tau_j} \quad (i = 1,2,\ldots\ldots,N) \tag{2.2}$$

$\Delta\tau$ in Eq. 2.2 is the layer thickness in traveltime depth, which is related to the physical layer thickness Δz as:

$$\Delta\tau = \frac{2\Delta z}{v_{int}} \tag{2.3}$$

According to Eq. 2.1, the amplitude shown in the CMP gather is regarded as a collection of hyperbola curves which are characterized by traveltime depth and corresponding RMS velocity at individual reflection points. The actual relation between traveltime and offset is not exactly hyperbolic since wave propagation is not precisely circular in laterally heterogeneous velocity field. However, it is an usual practice to estimate RMS velocity using this hyperbolic approximation. The velocity scan (Fig. 2.1b) for estimating RMS velocity is generated from the CMP gather by taking the summation of amplitude along each hyperbola curve, then plotting that sum in a traveltime depth vs. RMS velocity plane. On the velocity scan, we observe a peak of strong amplitude responses which indicates the RMS velocity corresponding to reflection point at traveltime depth τ. The RMS velocity is estimated as a function of τ by autopicking the maximum amplitude response on the velocity scan (dashed line in Figure 2.1b). The interval velocity (v_{int}, dashed line in Figure 2.1c) is calculated from the autopicked RMS velocity using the relationship expressed in Eq. 2.2.

However, the amplitude response peak usually shows considerable spread on the velocity scan, which indicates that the autopicked RMS velocity is uncertain. This uncertainty is attributed to the noise in the seismic data and the limited applicability of the hyperbolic approximation. Clapp (2001, 2003) proposed to generate multiple equiprobable realizations of the velocity as a function of depth, instead of obtaining a single best-estimate velocity model. The multiple velocity models are then used to produce equiprobable migrations of the seismic data. The methodology takes the following procedure.

1) Autopicking of RMS velocity and evaluation of error variance

The first step is to obtain the RMS velocity from the velocity scan by autopicking, and to evaluate the error variance of the RMS velocity from the velocity scan. The error variance $\sigma_v^2(\tau)$ at traveltime depth τ is evaluated as,

$$\sigma_v^2(\tau) = \frac{\int \left\{ v_{RMS}(\tau) - v_{RMS,auto\_pick}(\tau) \right\}^2 s(v_{RMS}, \tau)^4 \, dv_{RMS}}{\int s(v_{RMS}, \tau)^4 \, dv_{RMS}} \qquad (2.4)$$

where $v_{RMS,auto\_pick}(\tau)$ is the autopicked RMS velocity at traveltime depth τ, $s(\tau)$ is the semblance (= amplitude stacked along each hyperbola) plotted on the velocity scan. In actual application, $\sigma_v^2(\tau)$ is calculated in a discretized form of Eq. 2.4. The example of the evaluated autopicked RMS velocity and the square-root of error variance is depicted in Figure 2.3.

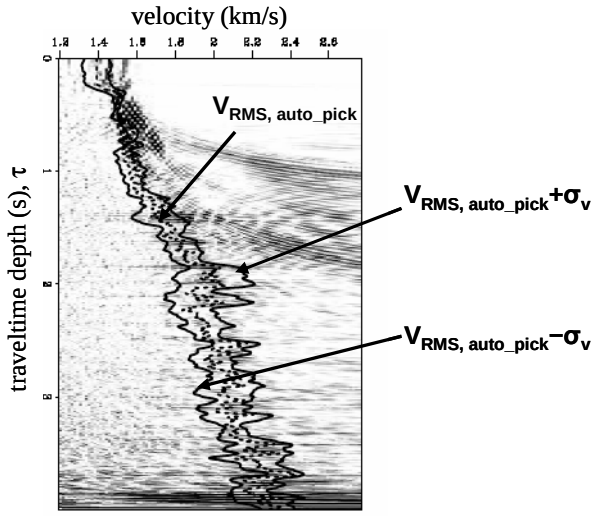

Figure 2.3: Example of autopicked RMS velocity and it's square-root error variance

Source: Robert G. Clapp, Multiple realizations and data variance: Successes and failures, Stanford Exploration Project, Report 113, 2003

2) Construction of the inversion problem

The interval velocity v_{int} is obtained from the autopicked RMS velocity v_{RMS} using the relation in Eq. 2.2. In principle, it is possible to directly solve for v_{int} by inverting the linear system in Eq. 2.2. However, in practice, the autopicked RMS velocity curve shows considerable small scale fluctuation, often due to noise in the data. Since the interval velocity is a function of the derivative of the RMS velocity, the direct calculation of v_{int} from noisy v_{RMS} by simply relying on the solution of a linear system would produce an erroneous interval velocity model.

One of the solutions to avoid a solution of Eq. 2.2, which is noisy, is to add a regularization constraint to Eq. 2.2 to smooth the modeled interval velocity. In other words, one tries to obtain an interval velocity model which has a given desired smoothness and also best fits to the autopicked RMS velocity. This is achieved by solving an inversion problem, where as input data the

autopicked RMS velocity v_{RMS} is used and a target model is the interval velocity v_{int}. This inversion problem is constructed based on Eq. 2.2 and also uses the error variance σ_v^2 of Eq. 2.4 in order to account for the uncertainty in autopicked v_{RMS}. This is done as follows:

Eq. 2.2 is rewritten as follows by specifying $\Delta\tau_j = \Delta\tau$ (constant):

$$v_{RMS,i}^2 = \frac{1}{i}\sum_{j=1}^{i} v_{int,j}^2 \qquad (i = 1,2,\ldots\ldots,N) \tag{2.5}$$

Using Eq. 2.5 as a forward model, the misfit of $v_{RMS,i}^2$ between that obtained from the autopicked RMS velocity (data), $v_{RMS,auto\_pick,i}$, and that derived from the interval velocity to be inverted (model), $v_{int,i}$, is evaluated as:

$$r_i = v_{RMS,auto\_pick,i}^2 - \frac{1}{i}\sum_{j=1}^{i} v_{int,j}^2 = \frac{1}{i}\left(i\, v_{RMS,auto\_pick,i}^2 - \sum_{j=1}^{i} v_{int,j}^2 \right) \qquad (i = 1,2,\ldots\ldots,N) \tag{2.6}$$

For simplicity, the autopicked RMS velocity $v_{RMS,auto\_pick,i}$ will be denoted as $v_{RMS,i}$ hereafter. The residual $r_{n,i}$ to be minimized in the inversion problem is defined from the misfit r_i (Eq. 2.6) and the error variance $\sigma_{v,i}^2$ (Eq. 2.4) as follows:

$$r_{n,i} = \frac{r_i}{\sigma_{v,i}^2} = \frac{1}{\sigma_{v,i}^2 i}\left(i\, v_{RMS,i}^2 - \sum_{j=1}^{i} v_{int,j}^2 \right) \quad (i = 1,2,\ldots\ldots,N) \tag{2.7}$$

The minimization of the residual $r_{n,i}$ accounts for the data uncertainty in $v_{RMS,i}$ in obtaining the best-fit model, i.e., since $r_i = \sigma_{v,i}^2 r_{n,i}$ from Eq. 2.7, a large misfit r_i is allowed for a large error variance $\sigma_{v,i}^2$ and vice versa.

Eq. 2.7 is written in matrix form as,

$$\mathbf{r_n} = \Sigma D_1 \left(\mathbf{T v_{RMS}^2} - C \mathbf{v_{int}^2} \right) \tag{2.8}$$

where:

$$\mathbf{r_n^T} = \left[r_{n,1}, r_{n,2}, \ldots\ldots, r_{n,i}, \ldots\ldots, r_{n,N}\right]$$

$$\mathbf{v_{RSM}^2}^{\mathbf{T}} = \left[v_{RSM,1}^2, v_{RSM,2}^2, \ldots\ldots, v_{RSM,i}^2, \ldots\ldots, v_{RSM,N}^2\right]$$

$$\mathbf{v_{int}^2}^{\mathbf{T}} = \left[v_{int,1}^2, v_{int,2}^2, \ldots\ldots, v_{int,i}^2, \ldots\ldots, v_{int,N}^2\right]$$

$$\mathbf{T^T} = \left[1, 2, \ldots\ldots, i, \ldots\ldots, N\right]$$

Σ: diagonal matrix whose diagonal element is $1/\sigma_{v,i}^2$

D_1: diagonal matrix whose diagonal element is $1/T_i$

C: lower triangular matrix with the elements of 1 (causal integration)

A regularization term, whose purpose is to generate smooth inverted $\mathbf{v_{int}}$, is added to the problem as:

$$\mathbf{r_m} = D\mathbf{v_{int}^2} \tag{2.9}$$

By minimizing $\mathbf{r_n}$ and $\mathbf{r_m}$ jointly using the least square optimization, the maximum likelihood solution of the interval velocity $\mathbf{v_{int}}$ is obtained. This is done through the minimization of,

$$0 \approx \left\|\mathbf{r_n}\right\|^2 + \varepsilon^2 \left\|\mathbf{r_m}\right\|^2 \tag{2.10}$$

where ε is a scaling weight.

3) Generation of multiple realizations of interval velocity

The next step is to generate multiple realizations of interval velocity $\mathbf{v_{int}}^{(l)}$ based on the maximum likelihood model $\mathbf{v_{int}}^{(0)}$ obtained from Eq. 2.10. This is achieved through generating multiple residual vectors $\mathbf{r_n}^{(l)}$ which have the same covariance structure as that of the initial residual vector

$\mathbf{r_n}^{(0)}$ obtained from $\mathbf{r_n}^{(0)} = \Sigma D_1\left(\mathbf{T}\mathbf{v}_{\mathbf{RMS}}^2 - C\mathbf{v}_{\mathbf{int}}^{(0)^2}\right)$. For this purpose, a filter matrix H is constructed a method based on prediction error filter (PEF, see Claerbout and Fomel, 2004, for details).

The important property of the filter matrix H is: if we apply the filter matrix H to the initial residual vector $\mathbf{r_n}^{(0)}$, we obtain white noise vector $\mathbf{y}^{(0)}$ as output (Fig. 2.4, see Claerbout and Fomel for proof and method for obtaining H). Inversely, if we apply the inverse of the matrix H, i.e. H^{-1}, to an arbitrary chosen white noise vector $\mathbf{y}^{(l)}$, we obtain a new residual vector $\mathbf{r_n}^{(l)}$, which exhibits the same covariance structure as the initial residual vector $\mathbf{r_n}^{(0)}$.

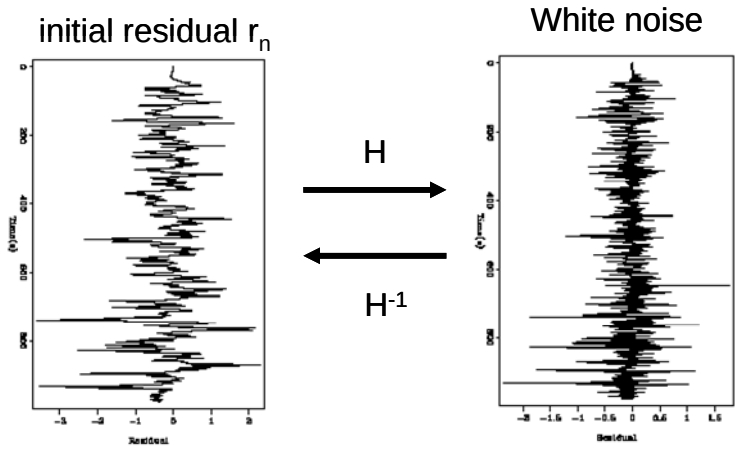

Figure 2.4: Property of filter matrix H

Source: Robert G. Clapp, Multiple realizations and data variance: Successes and failures, Stanford Exploration Project, Report 113, 2003

Therefore, introducing the filter matrix H, Eq. 2.8 is rewritten as:

$$\mathbf{y} = H\mathbf{r_n} = H\Sigma D_1\left(\mathbf{T}\mathbf{v}_{\mathbf{RMS}}^2 - C\mathbf{v}_{\mathbf{int}}^2\right) \qquad (2.11)$$

The vector **y** in Eq. 2.11 is white noise. The multiple realizations of interval velocity $\mathbf{v_{int}}^{(l)}$ are generated by substituting **y** by a series of randomly chosen white noise vectors $\mathbf{y}^{(l)}$, and solving Eq. 2.11 for $\mathbf{v_{int}}$. The use of prediction error filter results in the preservation of the covariance vector. The corresponding multiple RMS velocity models $\mathbf{v_{RMS}}^{(l)}$ are calculated from $\mathbf{v_{int}}^{(l)}$ using Eq. 2.5.

Using the multiple velocity models $\mathbf{v}_{\mathbf{RMS}}^{(l)}$, multiple seismic data sets are obtained by migrating raw seismic data, and then depth-converted using $\mathbf{v}_{\mathbf{int}}^{(l)}$.

The migration takes considerable CPU time (much larger than any other reservoir modeling process such as geostatistical or flow simulation). This is because, while geostatistical simulation operates only on the physical model space (i.e. three-dimensions at most), migration operates both on data and model space increasing the dimensionality of the problem. For example, a three-dimensional poststack migration calls for 5-dimensional nested loops and could take several days of CPU time (for each migration). Adding the uncertainty in velocity to the problem adds one more loop. Furthermore, the volume of a seismic data/image is generally much larger than the volume covered by a reservoir model grid.

2.1.2 Velocity Uncertainty in Tomography

Clapp (2004) extended the methodology described above (Section 2.1.1) to a more complex problem, namely, tomography or tomographic migration velocity analysis (MVA).

Migration Velocity Analysis (MVA)

Suppose that raw seismic data is already migrated using a given velocity model, and we are interested in whether this velocity model is reasonable. One way to investigate this is to plot the amplitude of the migrated data on depth vs. half-offset plot or depth vs. reflection angle (i.e. reflection angle between source and receiver) plot, which method depends on the migration method used. As conceptually illustrated in Figure 2.5, an amplitude peak (reflector) appearing on this plot should be flat if the velocity used for the migration is correct. If the velocity is too high or too low, the reflector deviates from the flatness as depicted in Figure 2.5. With the correct velocity model the reflector will migrate to the same position, deviation from flat (i.e. moveout) indicates an error in the velocity model. The moveout is often parameterized as a function of offset (or reflection angle) and a parameter γ. This function is called moveout function and the parameter γ is the ratio of slowness (inverse of velocity) to "true" slowness. Thus the value of parameter γ indicates the desired change of velocity to obtain a better migration result. The standard approach for estimating the γ field is to take the summation of amplitude values along the moveout function over the range of offset (or reflection angle) and generate a parameter γ vs. depth plot, and then pick γ value at the highest amplitude peak. Notice the similarity of this approach to the velocity

estimation by autopicking from a velocity scan (Section 2.1.1). Similarly to the velocity estimation in Section 2.1.1, one desires the estimated γ field to be smooth by avoiding noise.

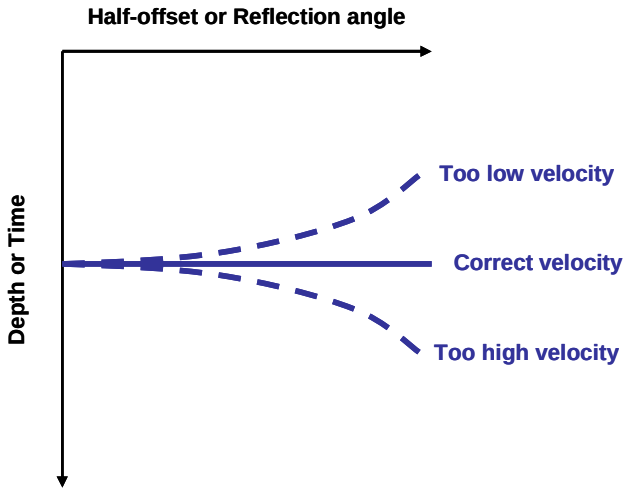

Figure 2.5: Conceptual illustration of moveout

Tomography

Once the initial guess of γ field is estimated, the slowness (inverse of velocity) is solved using tomography. Tomography is a nonlinear problem. The standard solution is to linearize around the slowness model used for migration. The residuals to minimize in this tomography problem are:

$$\mathbf{r}_{\mathbf{data}} = \mathbf{D}\gamma - \mathbf{T}_{\mathbf{0}}\Delta\mathbf{s} \tag{2.12}$$

$$\mathbf{r}_{\mathbf{model}} = \mathbf{A}(\mathbf{s}_{\mathbf{0}} + \Delta\mathbf{s}) \tag{2.13}$$

D is an operator to convert parameter γ (i.e. the parameter that informs desired change in slowness to reduce moveout) into corresponding change in travel-time Δt. $\mathbf{T_0}$ is constructed based on the slowness model used for migration and tells how a change in slowness Δs corresponds to a change in travel-time Δt. Therefore, minimizing $\mathbf{r_{data}}$ by fitting $\mathbf{T_0}\Delta$s to **D**γ serves as the minimization of moveout. The residual $\mathbf{r_{mode}}$ is a regularization term to smooth slowness **s**. $\mathbf{s_0}$ is an initial slowness. The slowness **s** is iteratively updated by minimizing

$$\mathbf{0} \approx \left\|\mathbf{r}_{\mathbf{data}}\right\|^2 + \varepsilon^2 \left\|\mathbf{r}_{\mathbf{model}}\right\|^2 \tag{2.14}$$

where ε is a scaling weight. The γ field is also updated after every iteration step and converges toward to γ = 1.0.

Multiple realizations of γ field

Clapp (2004) proposed to perform multiple tomography starting from multiple realizations of initial guess of γ field, instead of using a single "best" estimation of γ. The methodology takes two hierarchical procedures.

First, some number of realizations of smooth γ field that reasonably fits to the highest amplitude peak on the parameter γ vs. depth plot is generated by minimizing

$$\mathbf{0} \approx \left\|\mathbf{r}'_{\mathbf{data}}\right\|^2 + \varepsilon^2 \left\|\mathbf{r}'_{\mathbf{model}}\right\|^2 \tag{2.15}$$

where:

$$\mathbf{r}'_{\mathbf{data}} = \mathbf{W}_{\mathbf{g}}(\mathbf{g}_{\mathbf{max}} - \mathbf{g}_{\mathbf{smooth}}) \tag{2.16}$$

$$\mathbf{r}'_{\mathbf{model}} = \mathbf{A}\mathbf{g}_{\mathbf{smooth}} \tag{2.17}$$

$\mathbf{g}_{\mathbf{max}}$ is the value of parameter γ at the highest amplitude peak on the plot. This $\mathbf{g}_{\mathbf{max}}$ is updated after each iteration step by selecting new $\mathbf{g}_{\mathbf{max}}$ from the vicinity of current $\mathbf{g}_{\mathbf{smooth}}$ within a given range. Weight $\mathbf{W}_{\mathbf{g}}$ is to consider the amplitude value for fitting. The residual $\mathbf{r'}_{\mathbf{mode}}$ is a regularization term to smooth $\mathbf{g}_{\mathbf{smooth}}$. Multiple realizations are obtained by adding random noise to $\mathbf{r'}_{\mathbf{data}}$ in Eq. 2.16.

Then, starting from each of multiple initial guess of γ fields, multiple slowness fields are solved through tomography. Again, multiple realizations of slowness are generated for each initial guess of γ by adding random noise to $\mathbf{r}_{\mathbf{data}}$ in Eq. 2.14.

2.2 Synthetic Reservoir Example

2.2.1 Model Description

The synthetic reservoir model is constructed based on an actual reservoir data from the North Sea. The model is a two dimensional cross-section consisting of 680*340 grid blocks, 3400m in horizontal direction and 850m in vertical direction. The grid block size is 5m in horizontal and 2.5m in vertical. The depth of reservoir is 2270 ~ 3120 m-TVDSS. Figures 2.6 and 2.7 show the facies distribution and net-to-gross ratio, i.e. (net sand thickness in gridblock)/(gross gridblock thickness), distribution of the reservoir model. The reservoir is a faulted sand stone reservoir with thin shale layers and tiny calcite bodies (Fig. 2.6). The upper and lower part of the reservoir is shaly sand while the middle part of the reservoir is clean sand embedded by discontinuous thin calcite bodies. Porosity and permeability were geostatistically simulated constrained by the facies and net-to-gross ratios and are depicted in Figures 2.8 and 2.9. Average porosity and permeability are 0.24 and 537 mD, respectively. Water saturation distribution (Fig. 2.10) was modeled with OWC at 2688.5 m-TVDSS and capillary transition using J-function from the porosity and permeability realization (Table 2.1). The fluid densities are obtained from the field data. The reservoir is modeled as undersaturated reservoir without gas cap. The water saturation of shale and calcite bodies is specified as 1.0.

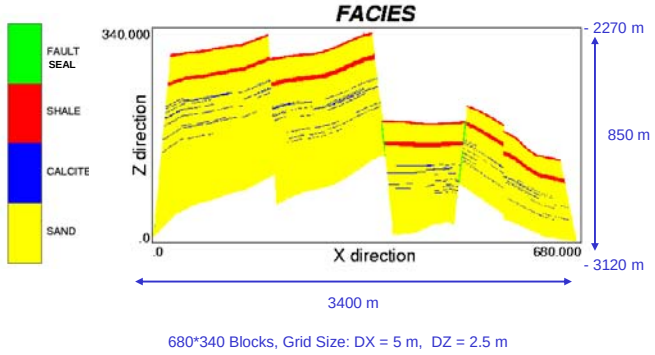

Figure 2.6: Facies model

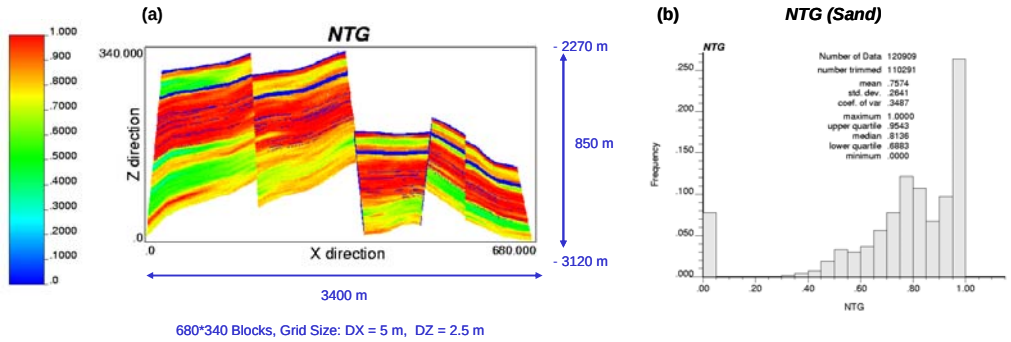

Figure 2.7: Net-to-gross ratio model (a) and histogram of net-to-gross ratio in Sand (b). Net-to-gross ratio in Shale and Calcite is set to 0.0

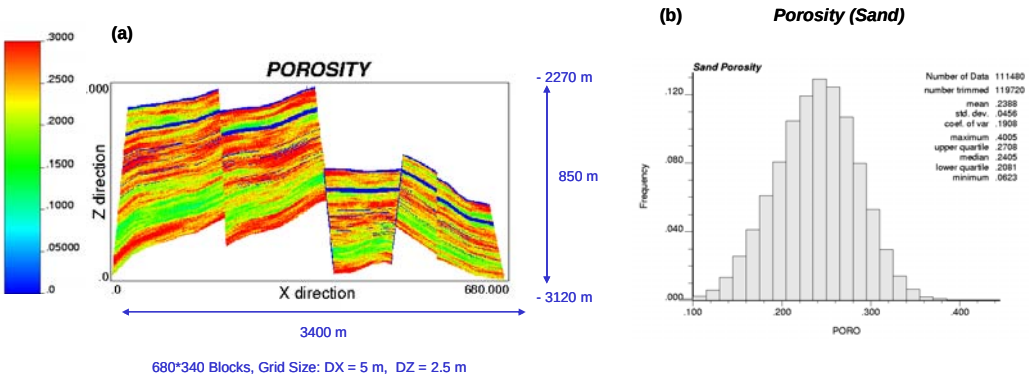

Figure 2.8: Porosity model (a) and histogram of porosity in Sand (b).Porosity in Shale and Calcite is set to 0.001

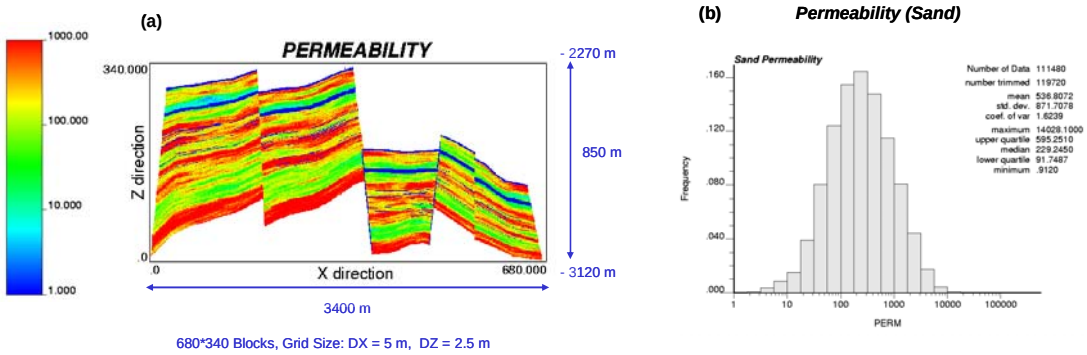

Figure 2.9: Permeability model (a) and histogram of permeability in Sand (b).Permeability in Shale and Calcite is set to 0.001 mD

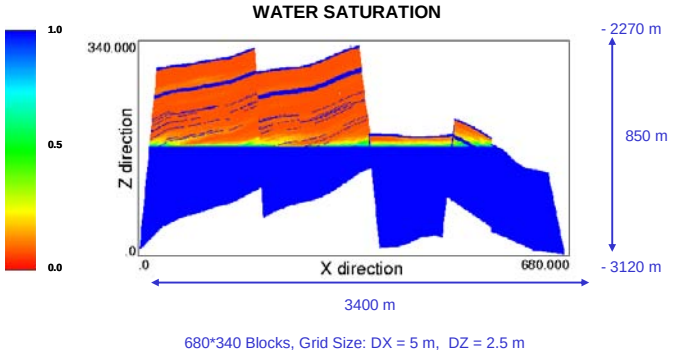

Figure 2.10: Water saturation model

Table 2.1: Parameters for modeling capillary transition of water saturation

Sand	$J(S_w)=0.12*(S_w - S_{wir})^{-0.5} - 0.12504071$ (φ=0.25, K=500 mD) $H = 31831.6*J(S_w)*TS*(\varphi/K)^{0.5} / (\rho_w - \rho_o)$ OWC = 2688.5 m TS = 22 dynes/cm ρ_w = 995 kg/m^3 ρ_o = 730 kg/m^3
Shale/Calcite	S_w = 1.00

The rock physics properties are simulated based on the petrophysical properties model. Figure 2.11 depicts the bulk density section calculated from the simulated porosity and net-to-gross ratio realizations. The fluid densities are obtained from actual field data (Table 2.2). Mineral density and composition for sand and shale are given in Table 2.2. The density of calcite is taken from the literature (Table 2.2; see Mavko et. al, 1998). Figure 2.12 shows a P-wave velocity section generated from the porosity, net-to-gross ratio, and water saturation realizations. The P-wave velocity of water saturated sand is calculated using the empirical correlation given in Table 2.3 (Han, 1986; see Mavko et. al, 1998). Gassmann's relation (1951; see Mavko et. al, 1998) was applied for fluid substitution using bulk modulus obtained from field data and literature value (Table 2.3). The P-wave velocity of shale is calculated using empirical correlation (Table 2.3, Gardner, 1974; see Mavko et. al, 1998). P-wave velocity of calcite is obtained from the literature (Table 2.3; see Mavko et. al, 1998). The P-wave impedance model (Fig. 2.13) is computed from bulk density and P-wave velocity. As depicted in Figure 2.13, shale layers and calcite bodies are highlighted by high impedance.

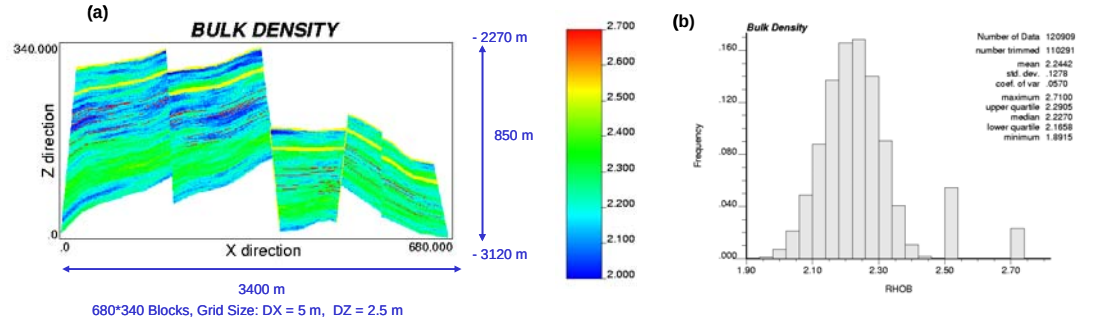

Figure 2.11: Bulk-density model (a) and histogram of bulk-density (b)

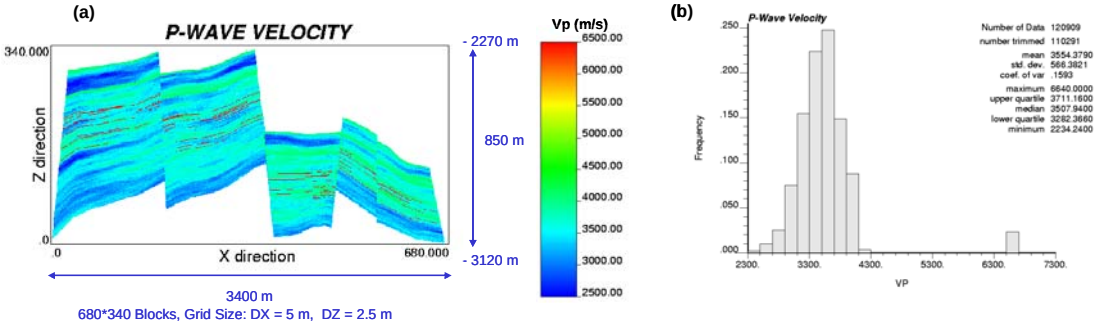

Figure 2.12: P-wave velocity (a) and histogram of P-wave velocity (b)

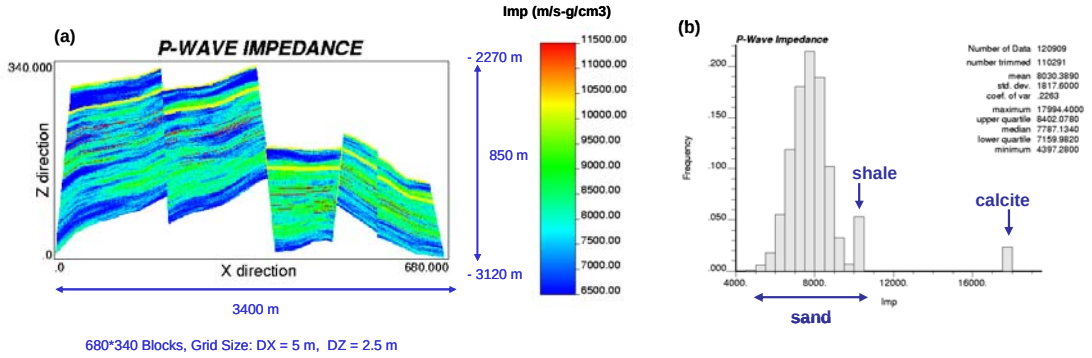

Figure 2.13: P-wave impedance model (a) and histogram of P-wave impedance (b)

Table 2.2: Parameters for bulk-density calculation

Bulk density	$\rho_b = \varphi * \rho_{fl} + (1-\varphi) * \rho_m$		
Fluid density	$\rho_{fl} = \rho_w * S_w + \rho_o * (1-S_w)$		
Matrix density	Sand/Shale: $\rho_m = \rho_{sand} * NTG + \rho_{sh} * (1-NTG)$ Calcite: $\rho_m = 2.71$		
Mineral composition for ρsand & ρsh			
	Mineral	**Density**	**Composition**
Clean Sand	Quarts	2.654	0.6
	Feldspar	2.630	0.3
	Rock frg.	2.710	0.1
Shale	Quarts+Rock frg.	2.642	0.2
	Clay minerals	2.500	0.8

Table 2.3: Parameters for P-wave velocity calculation

Sand	Vp = (5.55 - 6.96*φ-2.18C)*1000. (30 MPa, Han 1986, Water saturated rock) Vs = (3.47 - 4.84*φ-1.87C)*1000. (30 MPa, Han 1986, Water saturated rock) C = 1 – NTG
	Fluid Substitution (Gassmann 1951) $K_{fl1} = K_{wat}$, K_{fl2} = Russ average of K_{wat} & K_{oil} K_{min} = Russ average of K_{sand} & K_{clay} K_{wat} = 2.14 GPa, Koil = 0.5 GPa K_{sand} = 39 GPa, Kclay = 25 GPa (from Han 1986)
Shale	$\rho_b = 1.75*(Vp/1000.)^{0.265}$ (Gardner 1974)
Calcite	Vp = 6640 m/s

2.2.2 Result and Discussions

A synthetic seismograph is generated from the rock physics property model and utilized for seismic imaging. Figure 2.14 depicts the result of multiple seismic imaging (courtesy of Robert Clapp) obtained by the method of Clapp (2004).

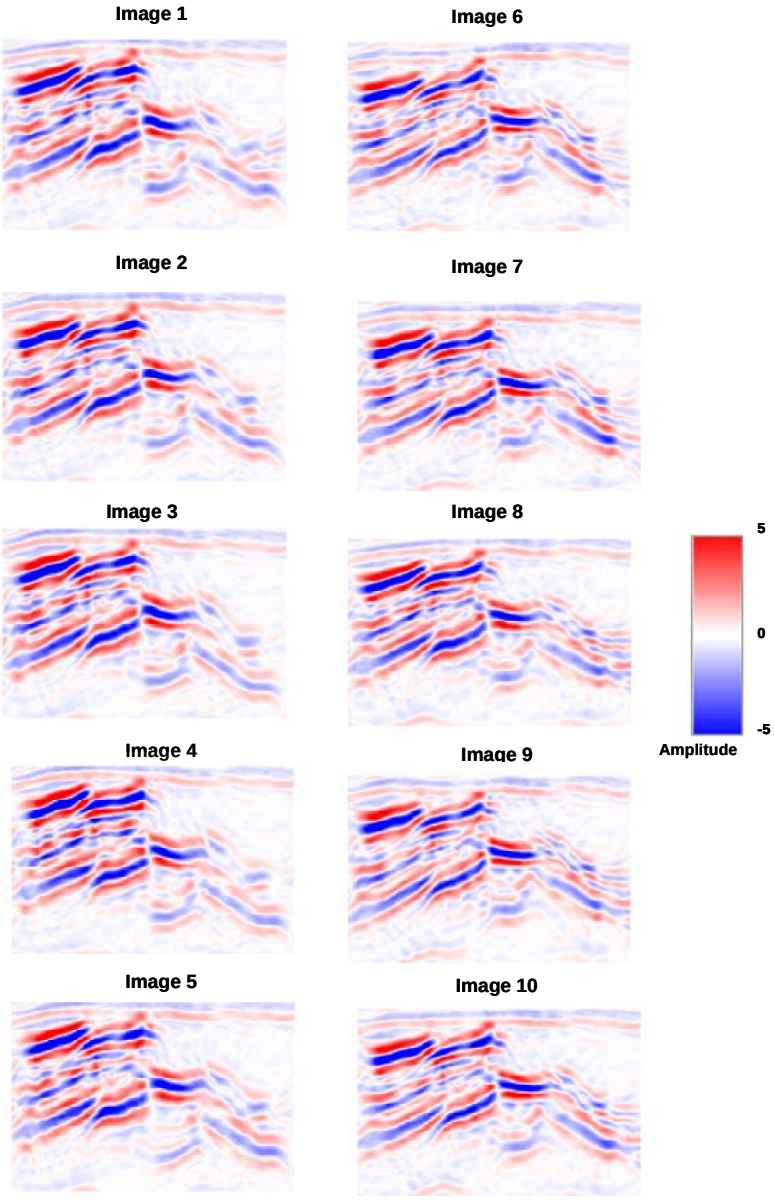

Figure 2.14: Multiple seismic images stochastically modeled accounting for velocity uncertainty (Courtesy of Robert Clapp)

These seismic images are generated using the multiple tomography method (Clapp, 2004). As depicted in Figure 2.14, the seismic imaging uncertainty model results in a nonuniqueness in horizon reflector positions due to the stochastic perturbation of seismic velocity, accounting for the error variance associated with the estimate of RMS velocity. The continuity of reflectors also changes at the location of the fault with small throw. These variations are subtle visually. However, such subtle difference in a structure can cause a significant change in fluid flow behavior depending on the type of a reservoir. For example, in a layer-cake-type reservoir comprising alternating clean sand and shale layer, a change in the juxtaposition of layers across faults due to a slight perturbation of horizon reflector positions results in a significant difference in flow pattern and flow communication between fault blocks. On the other hand, the position of the faults with large throw and their throw do not exhibit significant uncertainty in this uncertainty model. Images 1~5 in Figure 2.14 are created from the same initial guess of γ filed, where as images 6~10 are from another initial guess of γ filed. Note that difference between the group of images 1~5 and the group of images 6~10 are larger than the difference between the images in the same group.

The seismic imaging uncertainty modeled in Figure 2.14 considers two hierarchical sources of uncertainty; 1) uncertainty associated with different initial guess for the tomography problem, which is modeled accounting for the error associated with the moveout measurement, and 2) uncertainty due to the error in fitting goal of the tomography problem. The magnitude of uncertainty is larger in the former than the latter. However, the difficulty in this approach is, even using different initial guesses, the final solutions of the velocity model can fall into the same local minimum due to the nonlinearity of the tomography problem. In such cases, it is a practical idea to increase the number of realizations of the initial guess, and also to increase the variability among the multiple initial guesses. Then, the resulting uncertainty in seismic imaging would be much larger. Figure 2.15 shows such an example (courtesy of Robert Clapp). In this figure, “image B” is obtained by migrating the same seismic data as used for “image A”, but using a velocity model related to a different subsurface structure above the reservoir (Fig. 2.16). These two velocity models are obtained by the tomography using significantly different initial guesses of γ field. Both γ fields are from Eqs. 2.15~2.17 but using different tuning parameters. As depicted in Figure 2.15, the resulting seismic images are also significantly different exhibiting different fault positions and fault throws in addition to the different horizon positions.

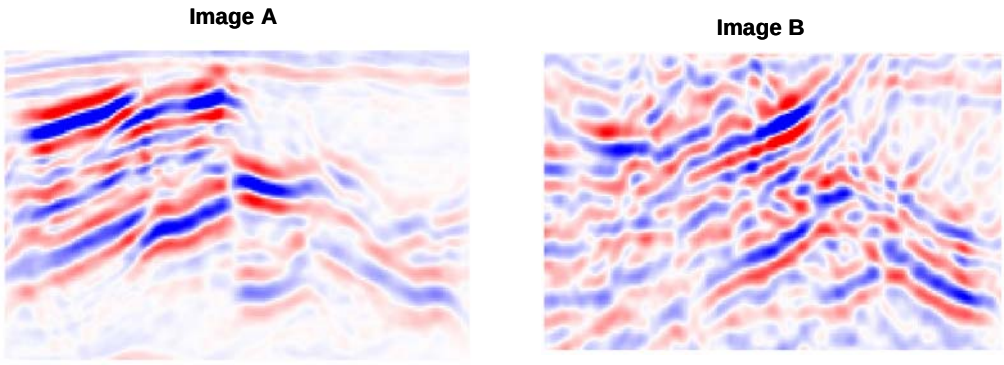

Figure 2.15: Multiple seismic images modeled accounting for the uncertainty in prior knowledge in velocity uncertainty (Courtesy of Robert Clapp)

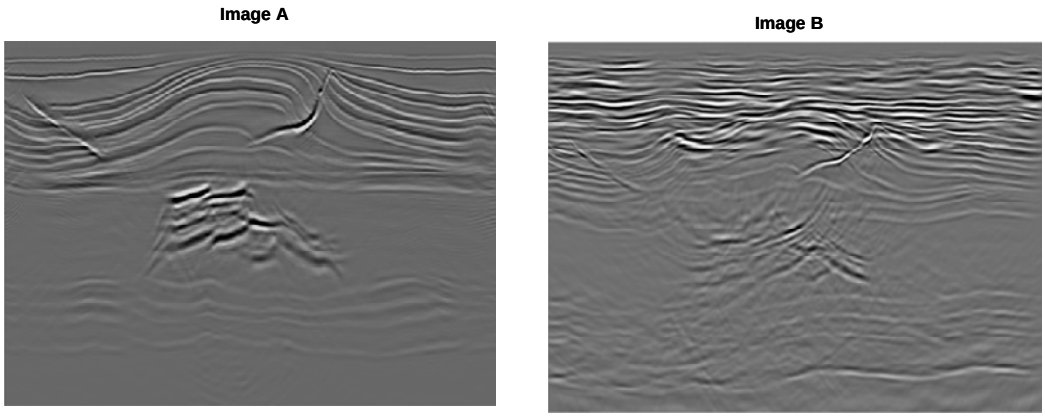

Figure 2.16: The subsurface structures corresponding to Image A and Image B in Figure 2.15. Notice the difference in the structure above the reservoir (Courtesy of Robert Clapp)

Chapter 3

Semiautomatic Seismic Interpretation Using Pattern Simulation

Aside from the CPU cost of migration, the manual labor cost of seismic interpretation is a primary factor preventing the consideration of multiple alternative seismic data sets. Since manual interpretation is time consuming especially when the volume of data is large, it is critical to automate some part of that interpretation process in order to build large numbers of structural models from various seismic images. Unfortunately, commercially available automatic interpretation tools are hardly applicable for structurally complex reservoirs since most algorithms rely on a simple autotracking of amplitude peaks. For that reason, the need for a new method that reduces manual interpretation for seismic interpretation arises.

Recently, a pattern-based geostatistical sequential simulation (SIMPAT) algorithm was proposed by Arpat (2005). The algorithm is designed to simulate facies or petrophysical property models using a training image as prior model for the spatial patterns being simulated. Although the SIMPAT algorithm is originally developed for characterizing geological objects such as fluvial channels, it also has the potential to be applied to seismic interpretation problems for the following reasons.

1) The SIMPAT algorithm is built on a pattern recognition process. This process is similar to horizon/fault picking in manual seismic interpretation process, since manual horizon picking is done based on visual inspection of reflections “patterns” rather than on a mere tracking of amplitude peaks.

2) The pattern similarity evaluation method used in SIMPAT algorithm works better for filtered (training) images (Arpat, 2005). Considering that a seismic amplitude image represents the earth's filter of naturally occurring horizons, the problem is relevant to SIMPAT.

This chapter proposes a semiautomatic seismic interpretation method by adapting the SIMPAT algorithm. The idea is to use the SIMPAT algorithm to automate a part of the interpretation task as an aid to identify and extract faults and horizons on seismic sections. In order to improve the pattern simulation accuracy of the SIMPAT algorithm, a dual-scale pattern recognition method is proposed. This method is particularly effective to jointly simulate geological objects characterized by different representative scales, such as faults and horizons. This chapter briefly reviews the SIMPAT algorithm first and shows how we can implement a seismic interpretation using SIMPAT. Then, a dual-scale pattern recognition approach is proposed. Finally, the complete workflow of a SIMPAT-aided semiautomatic seismic interpretation is presented. The methodology is demonstrated using seismic images generated in Chapter 2.

3.1 SIMPAT Algorithm: Review

The semiautomatic seismic interpretation problem is categorized as a "soft data conditioning" problem amongst the algorithms covered by SIMPAT (Arpat, 2005). Numerous implementation details are discussed in Arpat (2005). This section first reviews unconditional simulation by SIMPAT to illustrate the basic concept of the SIMPAT algorithm. Then, a mutigrid approach (Tran, 1994; Strebelle, 2002), which is an essential algorithm adapted by SIMPAT, is discussed. Finally, the review focuses on how soft data conditioning is performed by the SIMPAT algorithm.

3.1.1 Unconditional Simulation

The SIMPAT algorithm belongs to the family of multiple-point geostatistics, i.e. a multiple-point statistic (MPS) simulation (Srivastava, 1992; Guardano and Srivastava, 1993; Strebelle, 2002), which has become increasingly popular because of its ability to reproduce complex geological patterns (e.g. sinuous channels) that cannot be modeled by two-point statistics moments (i.e. variograms). The MPS simulation advocates the use of a "training image", a reservoir analog of sorts, which depicts a set of geological patterns or heterogeneities to be reproduced on a realization being simulated. The role of the training image is to provide information about spatial continuity

and patterns of geological features. Thus it can be a purely conceptual image inferred through geological interpretation without the need of being constrained to any specific reservoir data. Unlike kriging-based simulation techniques such as sequential Gaussian simulation, the information on spatial continuity is directly borrowed from the training image without requiring an analytical formulation. Due to this flexibility of the algorithm, the multiple-point geostatistical methods can reproduce complex geological features (e.g. meandering channel) which can not be simulated by traditional variogram-based techniques, since the conditional spatial continuity does not need to be simple enough to be expressed by an analytical formula (e.g. variogram).

The major difference between the MPS simulation and the SIMPAT algorithm is that, while the MPS simulation simulates geological facies at a single grid node based on a conditional probability inferred from a training image, the SIMPAT algorithm simulates geological objects as a “pattern”. The “pattern” for the simulation is retrieved from a pattern database (Fig. 3.1) constructed from a training image using a template, thus the algorithm does not require any probability model.

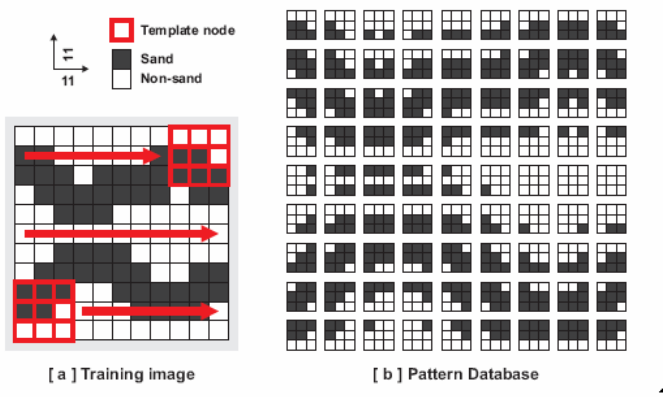

Figure 3.1: Pattern database construction of SIMPAT algorithm, Unconditional simulation

Source: Guven Burc Arpat, Sequential simulation with patterns, Ph.D. Dissertation, 2005

Figure 3.1 illustrates an example of the pattern database construction from a training image. As depicted, the training image is scanned by a template to extract the geological patterns. The extracted patterns are stored in the pattern database, i.e. a set of the patterns in the size of the template that appear on the given training image. The next step of the SIMPAT algorithm is the pattern simulation on a simulation grid, utilizing a sequential simulation algorithm; i.e., visiting nodes on a simulation grid along a random path. The procedure takes the following steps:

1. Visit an empty grid node at location **u** and place the template there. Extract any data from any previously simulated nodes covered by the template. The SIMPAT notation denotes this pattern as a "hard" pattern **hd**(**u**), in order to distinguish this pattern from a "soft" pattern which is discussed later.

2. Search the pattern database (Fig. 3.1) and find a pattern **hpat** which is most "similar" to the pattern **hd**(**u**) extracted in step 1. To evaluate the similarity between the patterns, the SIMPAT algorithm uses the Manhattan distance as a similarity measure. The Manhattan distance between the patterns **a** and **b**, where **a** and **b** are expressed as vectors whose elements a_i and b_i are grid values filled in the template, is given as below:

$$d\langle \mathbf{a}, \mathbf{b} \rangle = \sum_i |a_i - b_i| \tag{3.1}$$

   A smaller distance $\mathrm{d}\langle \mathbf{a}, \mathbf{b} \rangle$ indicates a greater similarity between **a** and **b**. Therefore, in order to find the most similar pattern **hpat** to the pattern **hd**(**u**) from the training database, the SIMPAT algorithm simply calculates the Manhattan distance between **hd**(**u**) and each of the patterns included in the training database, and selects a pattern **hpat** that achieves the minimum Manhattan distance.

4. Paste the selected best-matching pattern **hpat** on the template location at grid node **u**.

5. Go to another empty grid node by following a random path, and repeat steps 1~4 until the entire grid is simulated.

Note that, at each simulation on empty grid node **u**, a pattern **hd**(**u**) (which includes some empty grid nodes in the template) is overwritten by the whole pattern of **hpat**. In other words, the SIMPAT algorithm copies patterns from the training image on the simulation grid randomly, by matching the patterns to the previously copied patterns. The reproduction of the geological pattern depicted in the training image is achieved by this direct copying. However, since the algorithm uses a random path for sequential simulation, a different realization is obtained by changing the random path.

3.1.2 Multiple-Grid Approach

Since the SIMPAT algorithm consists of copying patterns using a template, naturally, using a larger template captures the pattern of geological variability better. However, the large template size requires considerable CPU time (= increased time for looking up most similar pattern), and also requires a larger hard and soft training images in order to extract a large enough numbers of pattern pairs to construct a meaningful pattern database. In order to avoid this problem, the SIMPAT algorithm adopts a multiple-grid approach (Tran, 1994; Strebelle, 2002).

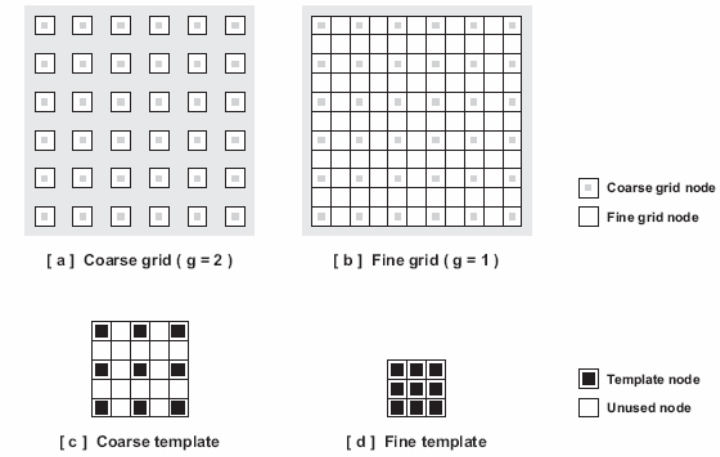

Figure 3.2: Illustration of the multiple-grid concept in SIMPAT algorithm

Source: Guven Burc Arpat, Sequential simulation with patterns, Ph.D. Dissertation, 2005

Figure 3.2 illustrates the concept of the multiple-grid simulation. As shown in the figure, the algorithm first simulates geological patterns by visiting every *g*-th grid node (Fig. 3.2a) using a coarse template (Fig. 3.2c). The coarse template consists of the same number of template nodes as the fine template (Fig. 3.2d), but its template nodes are placed with the spacing of *g* pixels. This coarse template is used for evaluating the Manhattan distance (Eq. 3.1) between **hpat** and **hd**(**u**). However, once the best-matching pattern is found, the full pattern of **hpat** (i.e. a pattern extracted from the training image at the same location as the "sparse" pattern of **hpat** is extracted) is pasted on the simulation grid. Then, the simulation proceeds to a refined grid (Fig. 3.2b) using a refined template (Fig. 3.2d). This refining is repeated until $g = 1$.

3.1.3 Soft Data Conditioning

Consider the problem of simulating fluvial channels using seismic data as soft conditioning data. This problem is called a "soft data conditioning" problem since the simulated geological object will be conditioned to soft (secondary) information from seismic images rather than to the direct (hard) information such as from well observations. The soft data conditioning technique in SIMPAT requires supplying two training images, i.e. a "hard training image" and a "soft training image". In Figure 3.3, the example of the hard training image contains fluvial channels reflecting the desired pattern of channel objects to be simulated. The soft training image is a seismic image obtained by forward-modeling the seismic data on the hard training image. It can be as simple as a moving average of the hard training image or as complex as the result of full seismic wave modeling.

The hard variable patterns (e.g. channel object) and soft variable (e.g. seismic amplitude) patterns are related to each other and stored in a pattern database. An example of pattern database construction is as shown in Figure 3.3:

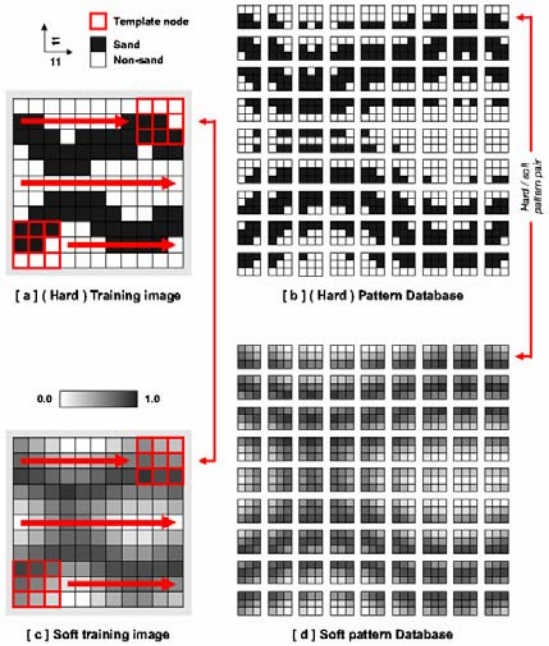

Figure 3.3: Pattern database construction of SIMPAT algorithm, Soft data conditioning

Source: Guven Burc Arpat, Sequential simulation with patterns, Ph.D. Dissertation, 2005

As depicted in the figure, both training images are scanned by a template to extract the patterns. The hard image patterns and the soft image patterns extracted at the collocated grid node are coupled and stored in the pattern database as a pair of hard and soft patterns. Thus the constructed pattern database can be considered as a training database which stores the information about pattern-to-pattern correlation observed between hard and soft training images.

Using the constructed pattern database, channel objects are simulated while being conditioned to actual seismic data. The actual seismic data is denoted as "soft data" in SIMPAT. The procedure takes the following steps:

1. Visit an empty grid node at location **u** and place the template there. Extract any data from any previously simulated nodes covered by the template. Denote this (hard) pattern as **hd**(**u**).

2. Extract the pattern of the soft data at node **u** by placing the template on the collocated soft data grid. Denote this (soft) pattern as **sft**(**u**).

3. Search the pattern database and find a joint pair of hard and soft patterns (**hpat**, **spat**) 1) whose hard pattern (**hpat**) is most similar to **hd**(**u**) and 2) whose soft pattern (**spat**) is also most similar to **sft**(**u**). The individual similarity between the patterns (i.e. hard-to-hard and soft-to-soft) is evaluated using the Manhattan distance (Eq. 3.1). Therefore, the pair of patterns (**hpat**, **spat**) which best matches **hd**(**u**) and **sft**(**u**) jointly is found by searching the pattern database for the pair of (**hpat**, **spat**) which shows a minimum for $w_1 d\langle \mathbf{hpat}, \mathbf{hd}(\mathbf{u}) \rangle + w_2 d\langle \mathbf{spat}, \mathbf{sft}(\mathbf{u}) \rangle$, for some user-specified weights w_1 and w_2.

4. Paste the best-matched pattern **hpat** on the template location at grid node **u**.

5. Go to another empty grid node and repeat steps 1~4 until the entire grid is simulated.

The SIMPAT simulation with soft data conditioning is also implemented using the multiple-grid approach (Section 3.1.2). Notice that, at the early stage in the multiple-grid simulation with the coarsest grid, a pattern is determined mostly based on matching soft data patterns, i.e. **spat** and **sft**(**u**), since at this stage there are few previously simulated patterns. Thus the algorithm first draws a rough framework of channels mostly by conditioning to soft data, then, fills the gaps with patterns consistent with the hard training image.

3.2 Application of SIMPAT Algorithm to Seismic Interpretation Problems

The semiautomatic seismic interpretation proposed in this dissertation is designed to assist in interpreting multiple seismic images, obtained in Chapter 2. As illustrated in Figure 3.4, an interpreter first selects one seismic image from the set of multiple seismic images, and manually interprets its geological structure. Then, using this pair of 1) one seismic image and 2) corresponding structural interpretation as a "training pattern database", a new structural interpretation on another seismic image is geostatistically simulated using SIMPAT. As shown in Figure 3.4, the selected seismic image and the corresponding (manual) structural interpretation are input as "soft training image" and "hard training image", respectively, in SIMPAT. Then, the soft image patterns extracted from the seismic image and the hard image patterns from the structural interpretation are paired at the collocated grid nodes and stored in the training pattern database as in Figure 3.4. This training pattern database serves as a "teacher" in the subsequent simulation process by providing information about how an interpreter correlated the pattern of amplitude to the pattern of horizons or faults during manual structural interpretation. The new seismic image is then input as "soft data" to SIMPAT. The sequential simulation is implemented as described in the previous section: i.e., at grid node **u**, SIMPAT algorithm extracts the pattern of previously simulated faults and horizons **hd**(**u**) by placing a template window. The pattern of seismic image **sft**(**u**) is also extracted at the collocated grid node **u** using the same template. Then, a pair of hard image pattern and soft image pattern (**hpat**, **spat**) that yields a minimum in Eq. 3.2, is selected from the training pattern database and **hpat** is pasted at the template location at **u**:

$$\text{Weighted sum} = w_1 d\langle \mathbf{hpat}, \mathbf{hd}(\mathbf{u}) \rangle + w_2 d\langle \mathbf{spat}, \mathbf{sft}(\mathbf{u}) \rangle \qquad (3.2)$$

d = Manhattan distance

The term d<**spat**, **sft**(**u**)> in Eq. 3.2 is used to find the pattern pair (**hpat**, **spat**) whose **spat** (= amplitude pattern) is as similar as possible to the amplitude pattern **sft**(**u**) observed on the currently interpreted seismic image at location **u**. Thus the minimization of this term can be seen as an attempt to find **hpat** (= pattern of fault and horizon) which is best correlated to the amplitude pattern **sft**(**u**) observed at **u**. The criterion for choosing the "best correlated **hpat** to **sft**(**u**)" is given by the training pattern database which relates **hpat** and **spat** based on the manual structural interpretation by an expert. On the other hand, the minimization of the term d<**hpat**, **hd**(**u**)> in Eq. 3.2 is to find **hpat** that yields the smoothest transition from the previously simulated faults and

horizons **hd**(**u**). The pattern pair (**hpat**, **spat**) that minimizes d<**spat**, **sft**(**u**)> and the one that minimizes d<**hpat**, **hd**(**u**)> often conflict. Thus by minimizing the weighted sum of these terms, SIMPAT algorithm seeks the pattern pair (**hpat**, **spat**) that provides the best compromise between reproduction of pattern-to-pattern correlation and smoothness of the simulated realization.

The seismic image input to SIMPAT can be a two-dimensional seismic data or a two-dimensional section of three-dimensional seismic data. The "simulated" seismic interpretation is produced as a pixelized "image" of faults and horizons, and will be converted into the final structural interpretation result with some interactive manual editing by the interpreter as described later. The faults and horizons are simulated at this stage as fault picks and horizon picks extracted from a seismic image, without conditioning to well markers. Although a geostatistical method is used for seismic interpretation, the additional stochasticity brought by the pattern simulation is of minor importance at this stage in terms of the uncertainty modeling: the major source of uncertainty is attributed to the seismic imaging uncertainty discussed in Chapter 2.

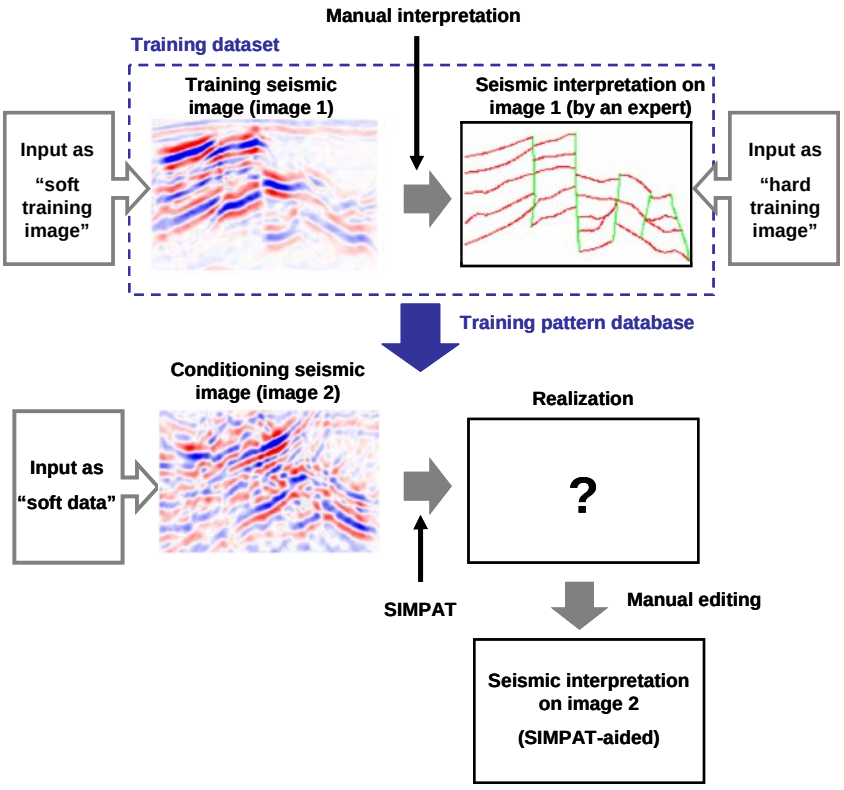

Figure 3.4: Schematics of semiautomatic seismic interpretation using SIMPAT algorithm

In actual applications, the SIMPAT algorithm can not be used to directly simulate edge images due to the limitation of the Manhattan distance, Eq. 3.1, in capturing the difference between complex edge-type patterns. When applied to "sparse" images, the "most similar" patterns evaluated by Manhattan distance are prone to be biased toward "sparser" patterns, resulting in the underestimation of the continuity of edge image (see Arpat, 2005, for an example on fractures). Arpat suggested applying a distance transformation to this categorical edge image in order to avoid this problem (2005). The basic idea is to convert edge images into more blurred images such as proximity maps (Fig. 3.5) and simulate proximity maps instead of simulating "sparse" edge patterns. The example of proximity maps generated from the structural interpretation (i.e. faults and horizons) is depicted in Figure 3.5.

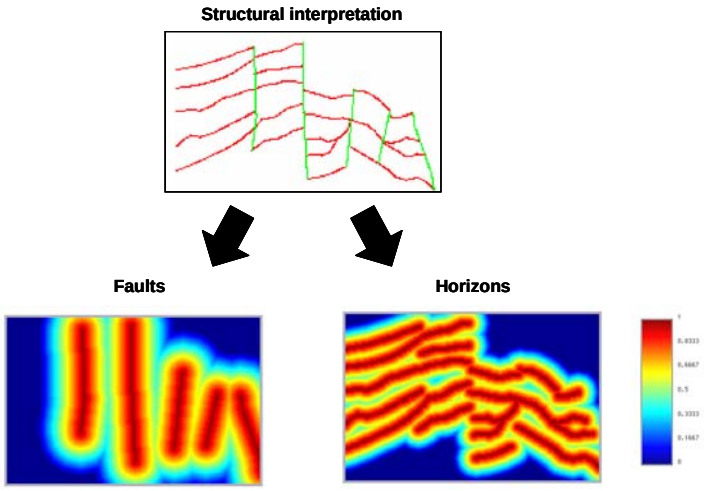

Figure 3.5: Distance transformation of structural interpretation into proximity maps for faults and horizons

The proximity map is practically the opposite of a distance map, thus it is created by calculating the distance to the closest fault or horizon and reversing the normalized distance to a proximity measure. To jointly simulate proximity maps of faults and horizons using the SIMPAT algorithm, Eq. 3.2 is rewritten as;

$$\text{Weighted sum} = w_1 d\left\langle \mathbf{hpat}_1, \mathbf{hd}_1(\mathbf{u}) \right\rangle + w_1 d\left\langle \mathbf{hpat}_2, \mathbf{hd}_2(\mathbf{u}) \right\rangle + w_2 d\left\langle \mathbf{spat}, \mathbf{sft}(\mathbf{u}) \right\rangle \quad (3.3)$$

where subscripts 1 and 2 denote the proximity maps of faults and horizons, respectively. The pattern triplet (**hpat**$_1$, **hpat**$_2$, **spat**) is used in constructing the training database instead of the pattern pair (**hpat**, **spat**). The simulated structural model (= faults and horizons) is obtained by

back-transforming the simulated proximity maps. This back-transformation can be a simple thresholding of the proximity map (i.e., convert the pixels with the value of proximity exceeding a given threshold to edge pixels and rest of the pixels to background pixels), or can be a more sophisticated method described in a later section.

The SIMPAT simulation is implemented on the multiple seismic images obtained in Chapter 2 (Fig. 2.14). To create a training structural interpretation result, the horizon and faults are manually picked on an arbitrary selected seismic image (image 1 in Figure 2.14) as shown in Figure 3.6. In this particular example, the boundary between shaly sand/clean sand and that between calcite/clean sand are relatively clear on the seismic image. We decided to pick positive amplitude peaks to create a training structural interpretation result (Fig. 3.7).

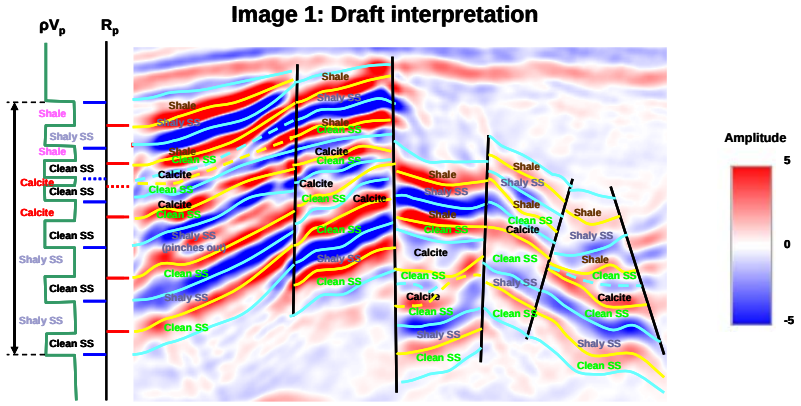

Figure 3.6: Preliminary manual seismic interpretation

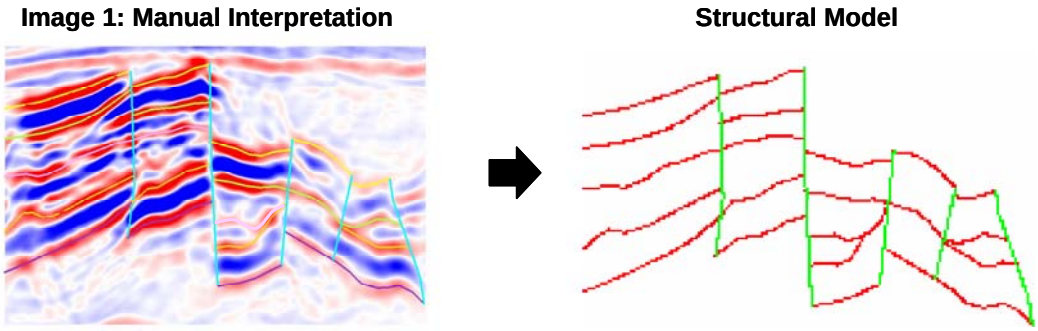

Figure 3.7: Final structural interpretation and structural model

Figure 3.8 shows the result of seismic interpretation with SIMPAT using the manually interpreted structural model (Fig. 3.7) and also using the seismic image utilized for manual interpretation (image 1). The training interpretation results and the seismic images are showing in the top row in the figure. The rest of the rows are the results of SIMPAT-aided seismic interpretation. The left column shows the seismic images on which the algorithm is applied. The center column depicts the simulated horizons and faults. The right column shows the seismic image overlaid by the simulated horizons and faults. As shown in the figure, the results are quite encouraging, at least for this simple application.

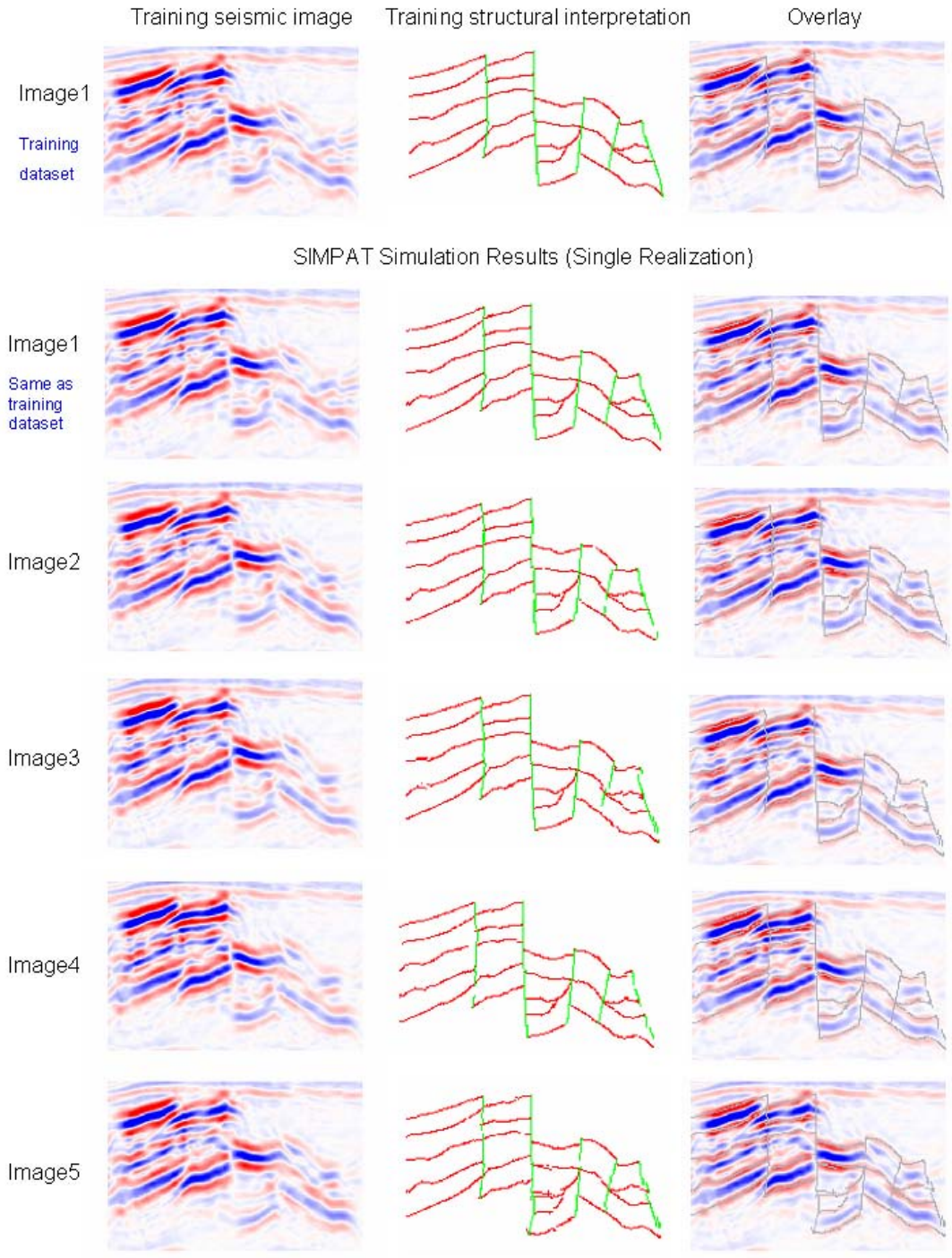

Figure 3.8: Simulated structural models from seismic images in Figure 2.14

Part of the reason for the successful results in Figure 3.8 is due to the relatively small variability between the seismic images. As depicted in Figure 2.14, most of the structural uncertainty is observed in horizon positions, whereas the overall structural configuration does not show much variability between the images. In such a case, SIMPAT executes a relatively simple task since the seismic image stored in the training database and that used for the pattern conditioning are similar to each other. However, as discussed in Chapter 2, a much larger structural uncertainty can be expected if the seismic velocity uncertainty is modeled by using completely different initial guesses for the tomography (Fig. 2.15), instead of modeling multiple initial guesses by a stochastic perturbation around the "best" guess. In such cases, the application of SIMPAT becomes challenging. Figure 3.9 depicts the result of the SIMPAT-aided seismic interpretation implemented on the seismic images in Figure 2.15. The training seismic image and the corresponding training structural interpretation are obtained from "image A" depicted in Figure 2.15. Using this training dataset, faults and horizons are simulated using a seismic image "image B". As shown in the figure, the result of SIMPAT simulation lacks geological reality in this "difficult" case. The next section discusses an enhancement of SIMPAT algorithm to solve this problem.

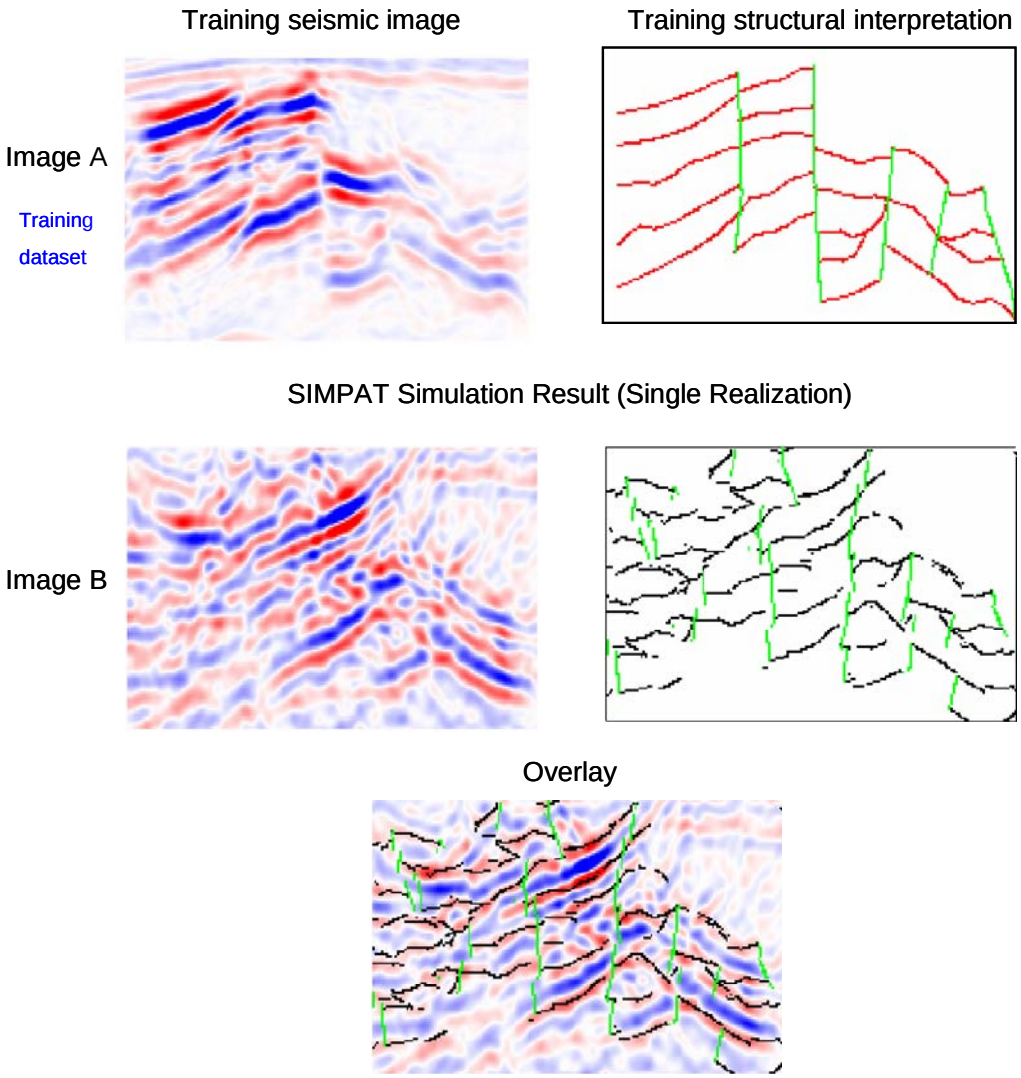

Figure 3.9: Simulated structural models from seismic images in Figure 2.15

3.3 Improvement of Pattern Simulation Accuracy Using Dual-Scale Pattern Recognition

The difficulty in jointly simulating faults and horizons is mainly due to the difference in "optimal scales" for recognizing fault patterns and horizon patterns. The scale for the pattern recognition is determined in the SIMPAT algorithm by the size of the template. When the multiple-grid approach (Tran, 1994; Strebelle, 2002) is applied, the coarseness of template is determined by the coarseness of grid nodes being simulated (see Figure 3.2). Thus the scale for evaluating the "best" pattern using Eq. 3.2 or Eq. 3.3 changes as the multiple-grid simulation proceeds. Figure 3.10 illustrates how the faults and horizons are simulated at each stage of the multiple-grid simulations for the case presented in Figure 3.8. As mentioned, the actual simulation is implemented as a joint simulation of proximity maps of faults and horizons (Fig. 3.10). The realizations depicted in Figure 3.10 are the back-transformed images from the simulated proximity maps in Figure 3.11, overlaid on the seismic image used for conditioning. As shown, SIMPAT first establishes the overall configuration of the reservoir structure at the first stage (= coarsest) of the multiple-grid simulation (multiple grid = 4*4; i.e. simulation on every 4^{th} grid node). At this stage, the realization shows an almost identical structure as the training structural interpretation, except that the number of fault blocks is increased in the simulated realization compared to the training interpretation. The faults are successfully positioned at this stage, accurately identifying significant discontinuities in seismic amplitude reflectors. However, the horizons positioned on the image do not accurately follow the reflectors due to a too large template size. As the multiple-grid simulation proceeds, the fitness of horizons to the reflectors improves with the reduction in the size of the template, whereas the fault segments tend to be broken apart because the template size has become too small.

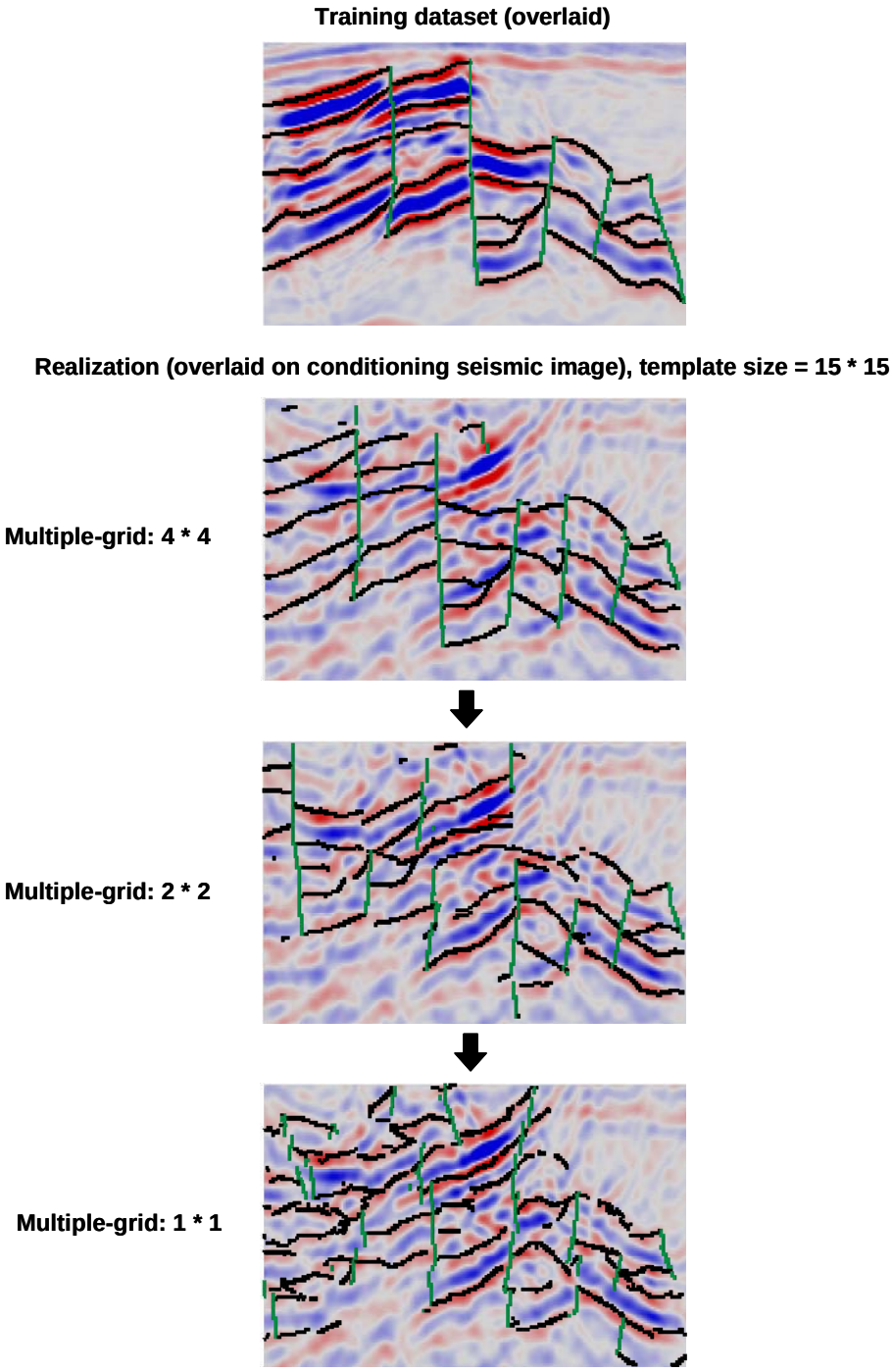

Figure 3.10: Realization of horizons and faults at each stage of multiple-grid simulation

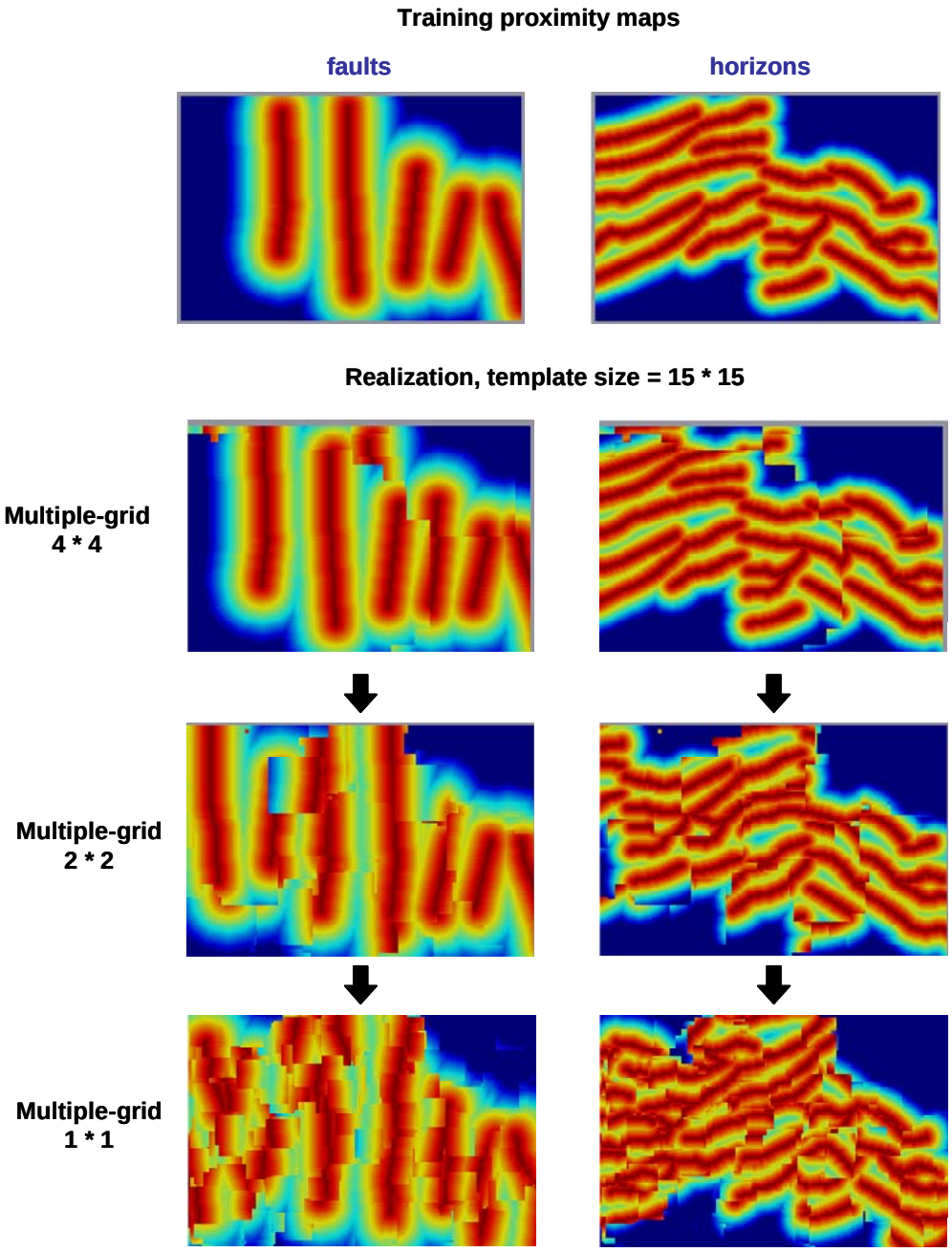

Figure 3.11: Realization of horizon and fault proximity maps at each stage of multiple-grid simulation

Figure 3.10 illustrates that the "best" pattern triplet (**hpat$_1$**, **hpat$_2$**, **spat**) chosen by Eq. 3.3 depends on the size of the template, and in addition, the optimal template size for identifying faults is larger than that for picking horizons. In fact, this observation is analogous to the general experiences in manual seismic interpretations: an interpreter might pay more attention to large scale structure than details when picking faults, while one might focus on details when picking horizons by tracing reflectors. Based on this observation, a dual-scale pattern recognition approach is designed as shown in Figure 3.12.

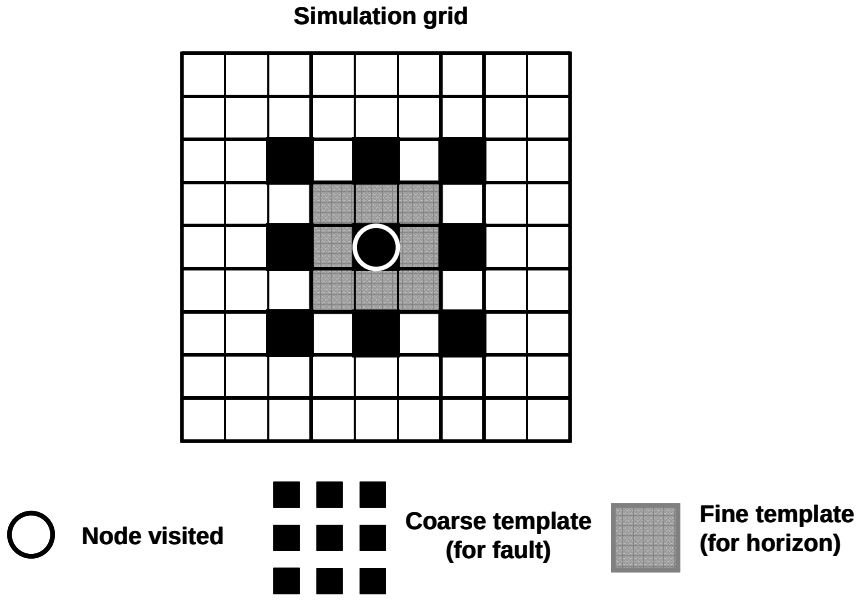

*Figure 3.12: Illustration of dual-scale pattern recognition approach, multiple-grid: 1*1, scale difference: 4, i.e., coarse template: 4*4, fine template: 1*1*

In this approach, Eq. 3.3 for choosing the "best" (**hpat$_1$**, **hpat$_2$**, **spat**) is rewritten as:

$$\text{Weighted sum}= w_1 d\left\langle \mathbf{hpat}_1^1, \mathbf{hd}_1^1(\mathbf{u}) \right\rangle + 0.5 * w_2 d\left\langle \mathbf{spat}^1, \mathbf{sft}^1(\mathbf{u}) \right\rangle + w_1 d\left\langle \mathbf{hpat}_2^2, \mathbf{hd}_2^2(\mathbf{u}) \right\rangle + 0.5 * w_2 d\left\langle \mathbf{spat}^2, \mathbf{sft}^2(\mathbf{u}) \right\rangle \quad (3.4)$$

Subscripts 1 and 2 denote the proximity maps of fault and horizon, respectively. Superscripts 1 and 2 respectively denote the patterns extracted using the coarse template (black in Figure 3.12) and

the fine template (gray in Figure 3.12). The minimization of the terms with superscript 1 attempts to account for the large scale seismic amplitude features as well as preserving the fault segment continuity, while the minimization of the terms with superscript 2 fits the horizon segments to reflectors focusing on finer scale. Thus, by minimizing the weighted sum in Eq. 3.4, one tries to find an optimal balance between fault and horizon identification. Once the "best" pattern triplet (**hpat$_1$**, **hpat$_2$**, **spat**) is found, **hpat$_1$** (fault proximity map) and **hpat$_2$** (horizon proximity map), both extracted by the fine template, are pasted on the simulation grid. In other words, the coarse-scale template is only used for evaluating Eq. 3.4 but not used for simulating (= pasting) the pattern. The latter is done to maintain consistency between the simulated fault and horizon proximity maps. The example of Figure 3.12 considers the final stage of multiple-grid simulation (i.e. multiple grid = 1*1), applying a scale difference (between the template for faults and horizons) of 2 (i.e. coarse template = 2*2, fine template = 1*1). Dual-scale templates are used during every stage of the multiple-grid simulation. The scale difference can be made larger if suitable.

The dual-scale pattern recognition approach is applied to the seismic interpretation case in Figure 3.9 and compared to the results using the original SIMPAT algorithm. Figure 3.13 compares the simulated structural models between the original SIMPAT and the dual-scale pattern recognition approach. The same results are shown in Fig. 3.14 overlaid on the conditioning seismic image. The scale of template windows at each stage of multiple-grid simulation is designed as tabulated in Table 3.1.

Table 3.1: Scale of template in multiple-grid simulation

	Coarse template (fault)	Fine template (horizon)
Multiple-grid 1	4*4	4*4
Multiple-grid 2	4*4	2*2
Multiple-grid 3	4*4	1*1

As shown in the figures, the quality of the simulated structural images has improved considerably, although the realizations still exhibit some noise. This noise will be further removed by postprocessing and some interactive manual editing by the interpreter as discussed in the next section.

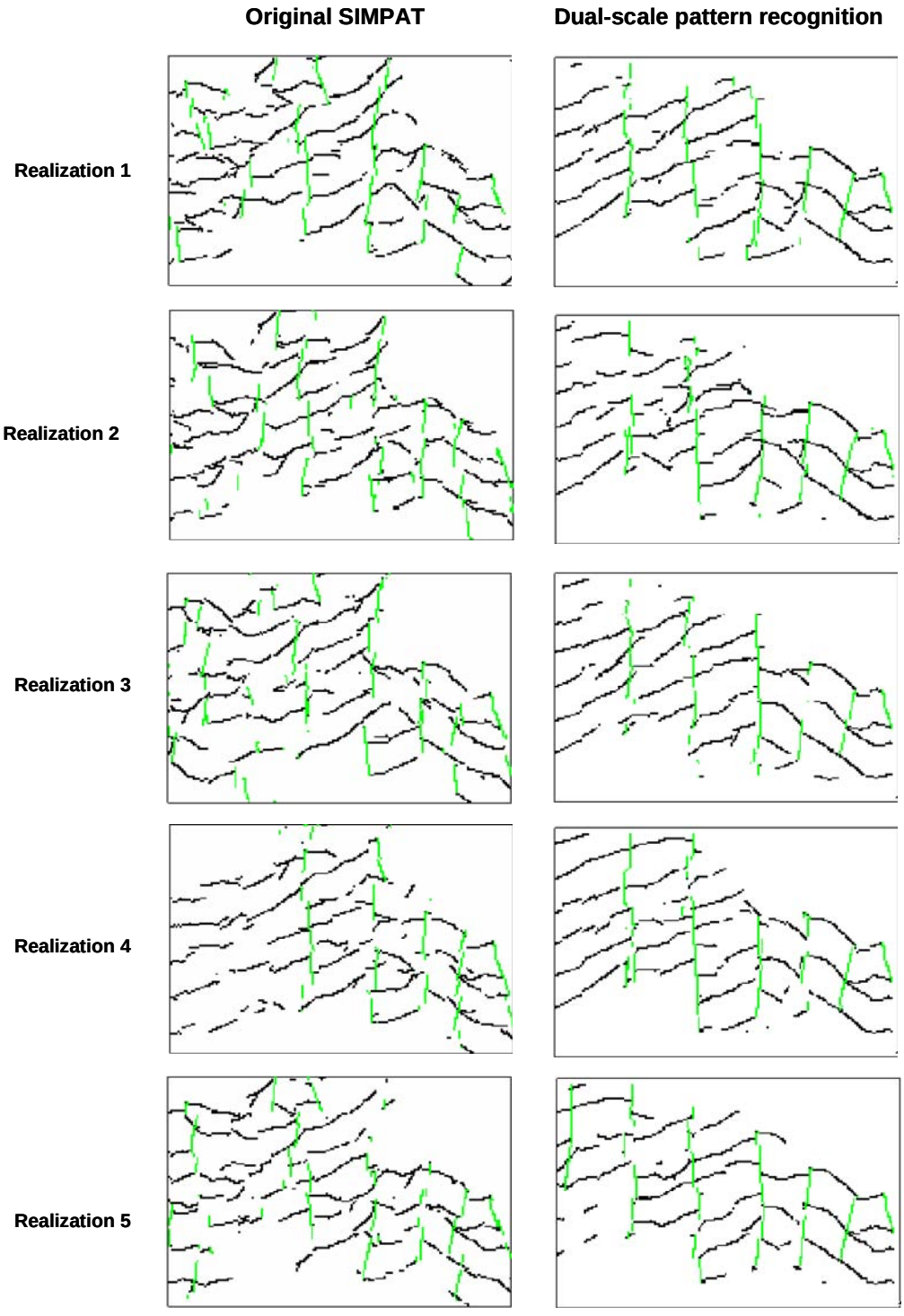

Figure 3.13: Simulated structural models, original SIMPAT vs. dual-scale pattern recognition

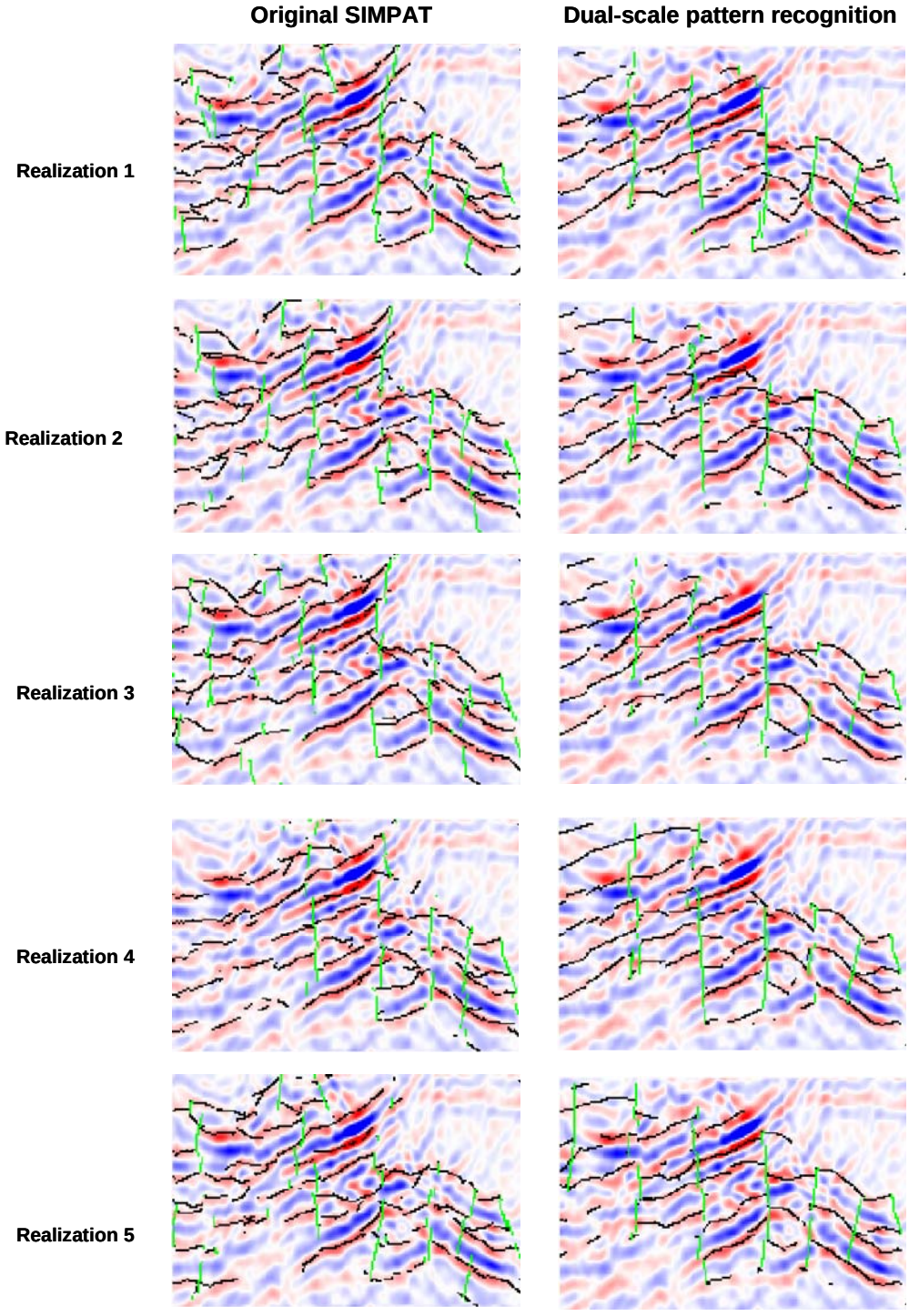

Figure 3.14: Simulated structural models overlaid on conditioning seismic image, original SIMPAT vs. dual-scale pattern recognition

Average CPU time for simulating one realization is compared as Table 3.2.

Table 3.2: Comparison of average CPU time

	Original SIMPAT	Dual-scale pattern recognition
Average CPU time per 1 realization	45.8 min	19.4 min

The reduction of CPU time is due to the decrease in the number of nodes visited during the sequential simulation. SIMPAT algorithm arranges the random path for the simulation such that the template does not exceed the boundary of the simulation grid. Thus, if a coarse template is used in conjunction with a fine template, less simulation grid nodes are visited compared to the simulation using only a single-size template (Fig. 3.15).

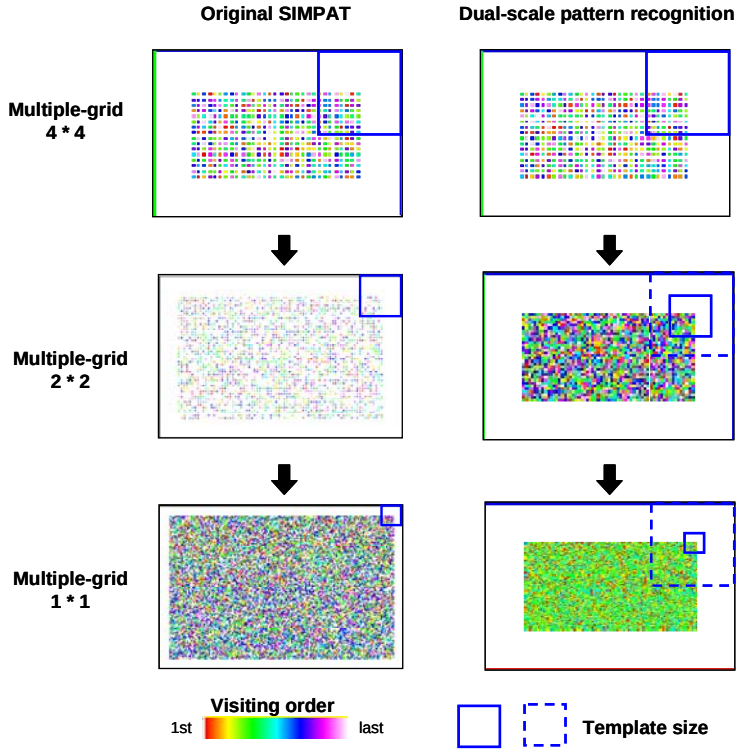

Figure 3.15: Random path arrangements for sequential simulation, original SIMPAT vs. dual-scale pattern recognition

3.4 Workflow: SIMPAT-Aided Semiautomatic Seismic Interpretation

The complete workflow of SIMPAT-aided semiautomatic seismic interpretation is summarized in Figure 3.16.

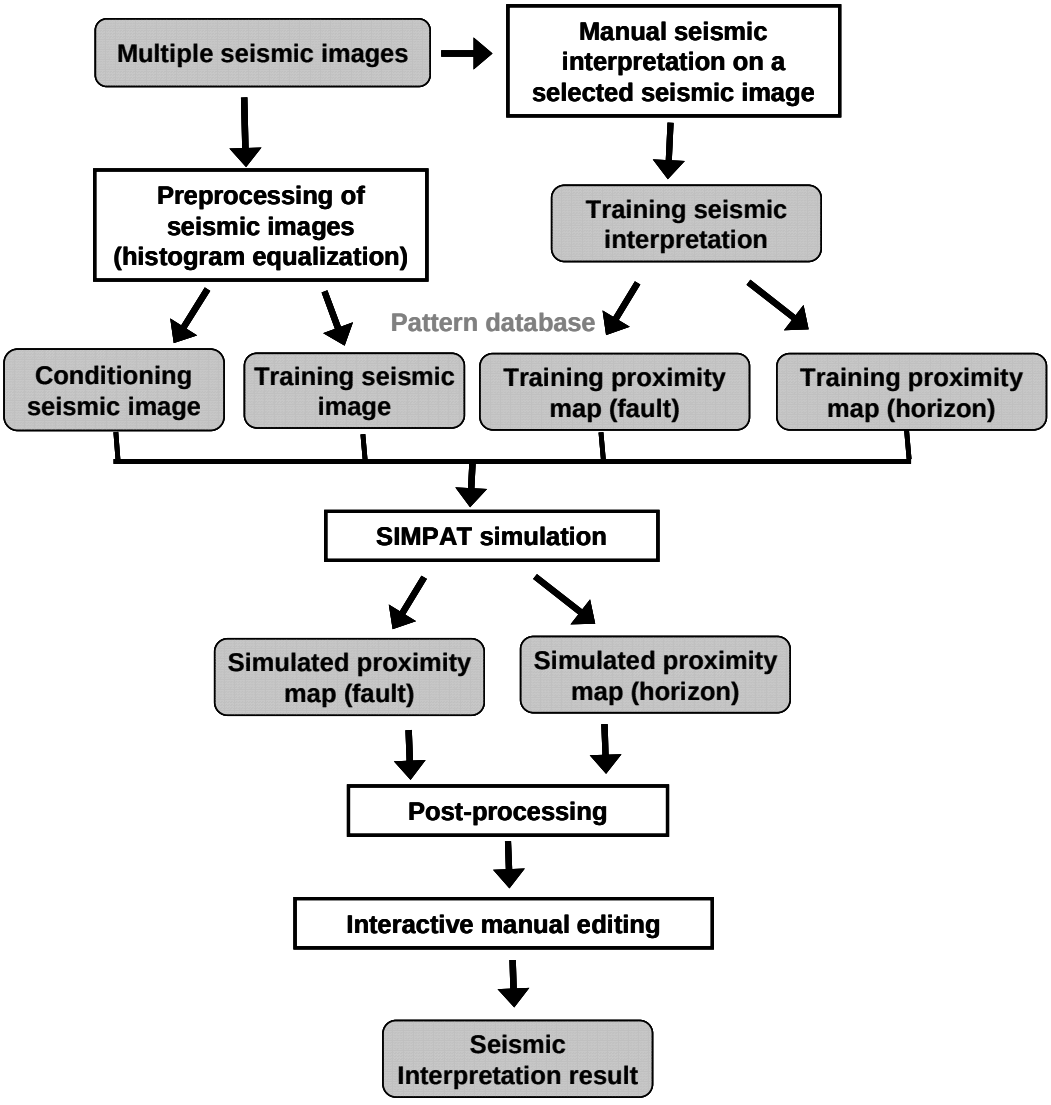

Figure 3.16: Workflow of SIMPAT-aided semiautomatic seismic interpretation

Preprocessing of Seismic Images

As shown in the figure, the seismic training image and the conditioning seismic images are preprocessed through histogram equalization (Fig. 3.17) before inputting into the SIMPAT simulation. As illustrated in Figure 3.17, the histogram equalization transforms images such that the histogram of amplitudes becomes uniformly distributed. This preprocessing enhances the contrast in the seismic image and reduces the unevenness in the amplitude. The latter is particularly important for the SIMPAT simulation as a semiautomatic seismic interpretation. The similarity evaluation based on the Manhattan distance is particularly sensitive to a dissimilarity between amplitude values of reflectors regardless of their similarity in shape. As a consequence, if the same reflector appears in the seismic training image and the conditioning seismic image but with different amplitude values, then SIMPAT may not recognize that reflector as a horizon. The histogram equalization avoids the problem by reducing the regional variation in amplitude values in seismic images, yet preserving the shape of reflectors.

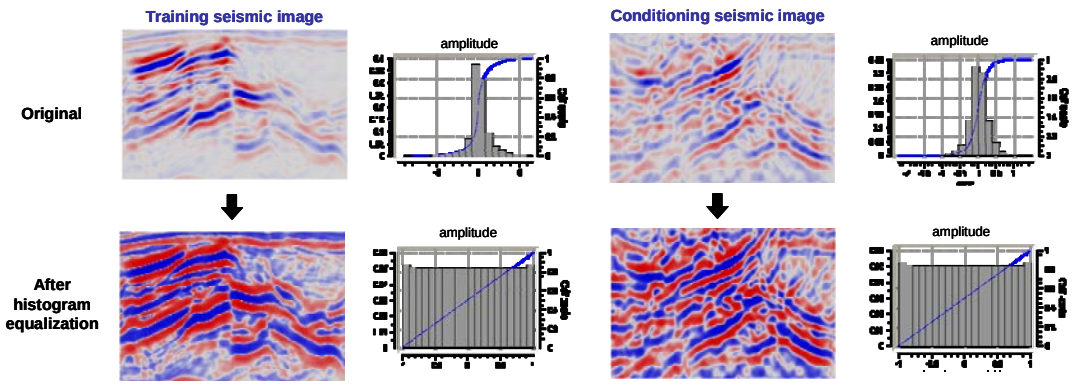

Figure 3.17: Histogram equalization of seismic images

Postprocessing of Proximity Maps

Proximity maps for faults and horizons are simulated by SIMPAT conditioned to a preprocessed seismic image, using the pattern database trained on a manual interpretation result. In order to obtain the image of structure with a minimum of noise, the simulated proximity maps are

postprocessed by the following procedure (Fig. 3.18) instead of the conventional back-transformation (= simple thresholding):

1) Smooth the proximity maps through a moving average followed by histogram equalization. A small window (e.g. 3*3) is used for the moving average to avoid losing the structure of the image. The histogram equalization is applied to recover the contrast of the image lost by the moving average. Repeat this operation 2 or 3 times.

2) Convert the smooth proximity maps into binary images using a certain threshold. This threshold is set lower than that used for the conventional back-transformation. As a result, the binary images exhibit “blobs” rather than lines (Fig. 3.18).

3) Extract the fault and horizon segments from the binary images through skeletonization. Hilditch’s algorithm (Rutovitz, 1971; Stefaneli, 1986) is used to extract skeletons in this example.

4) Overlay the resulting skeletons of faults and horizons.

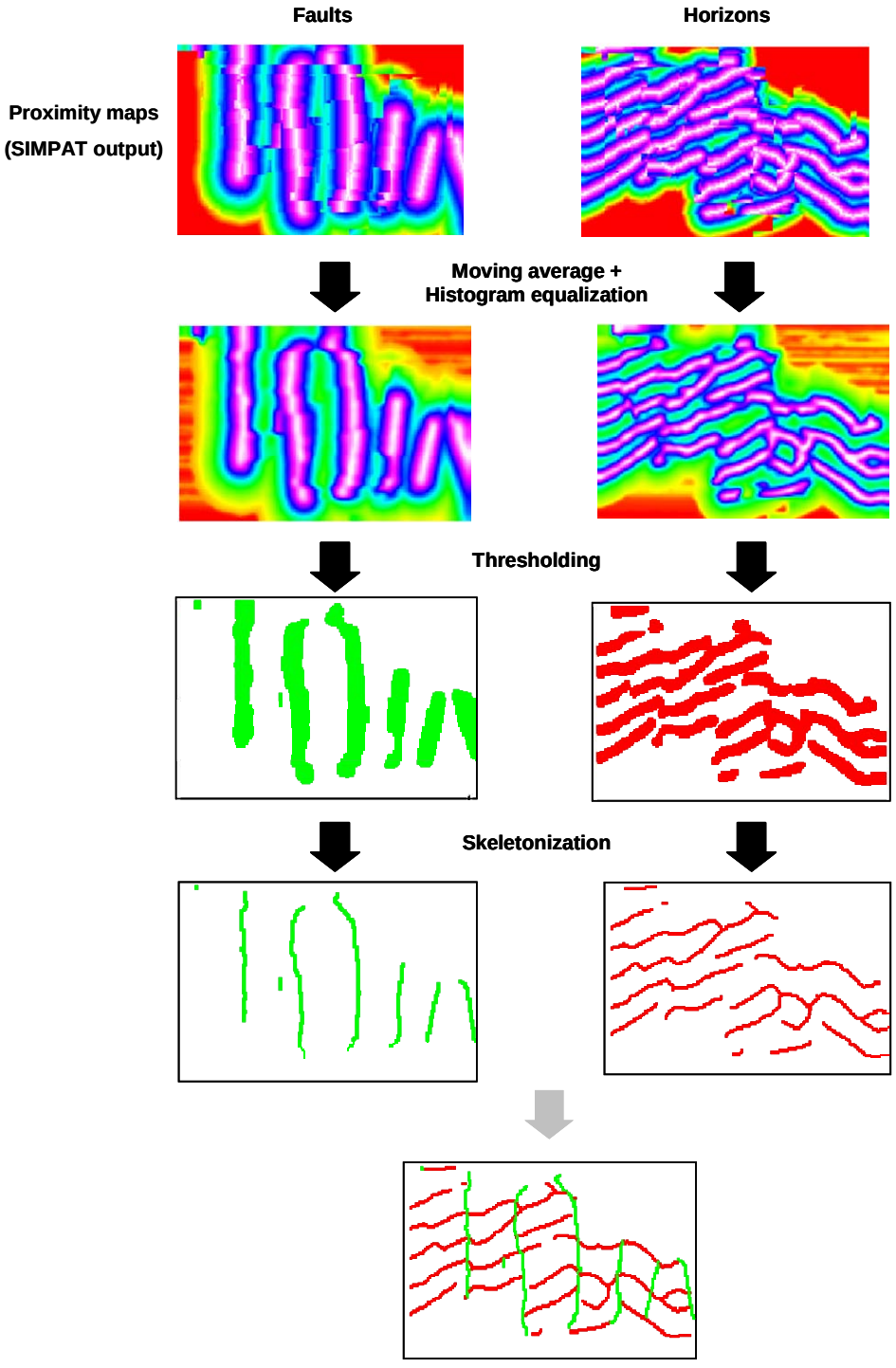

Figure 3.18: Schematics of the postprocessing of simulated proximity maps

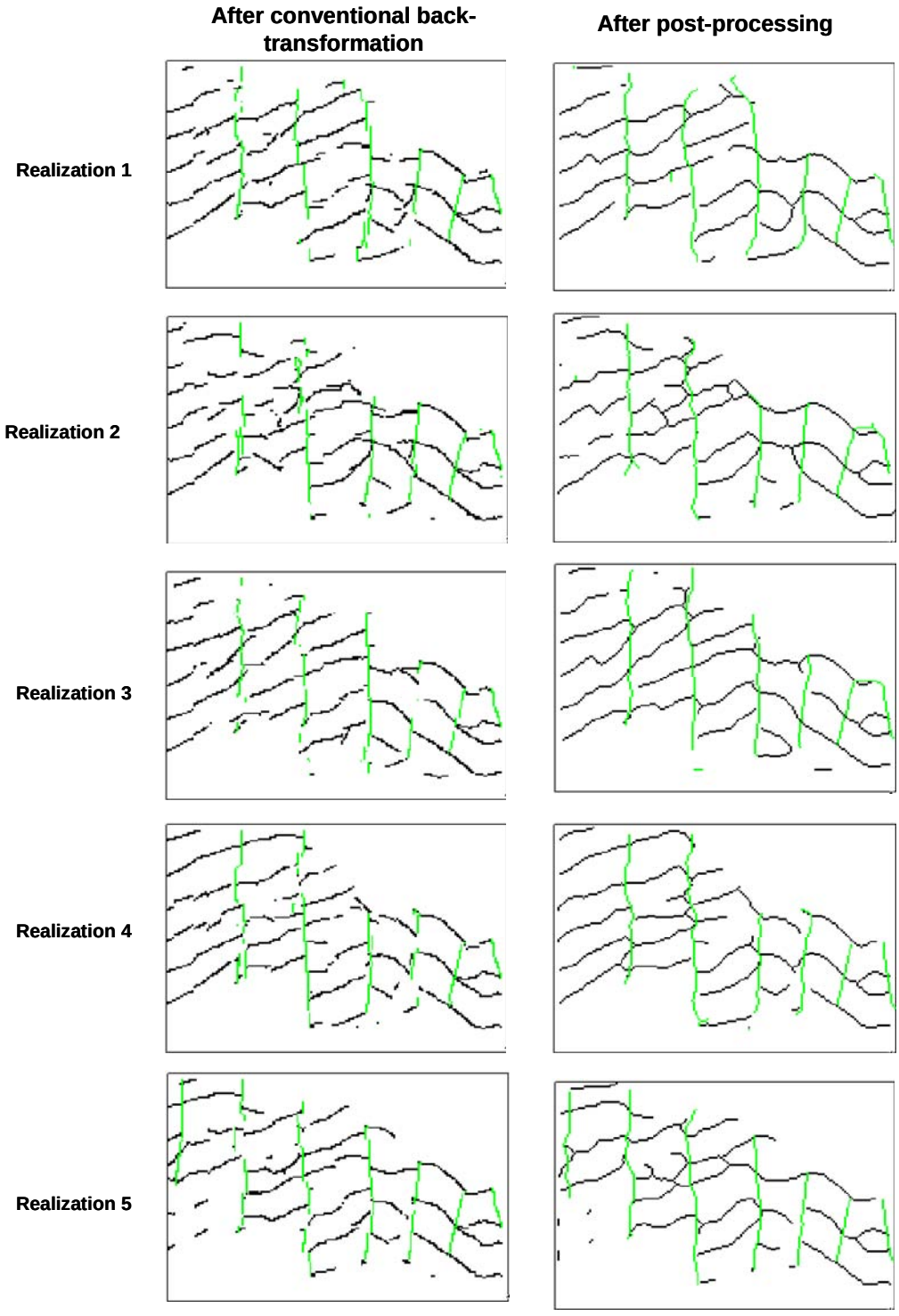

Figure 3.19: Simulated structural models, conventional back-transformation vs. postprocessing

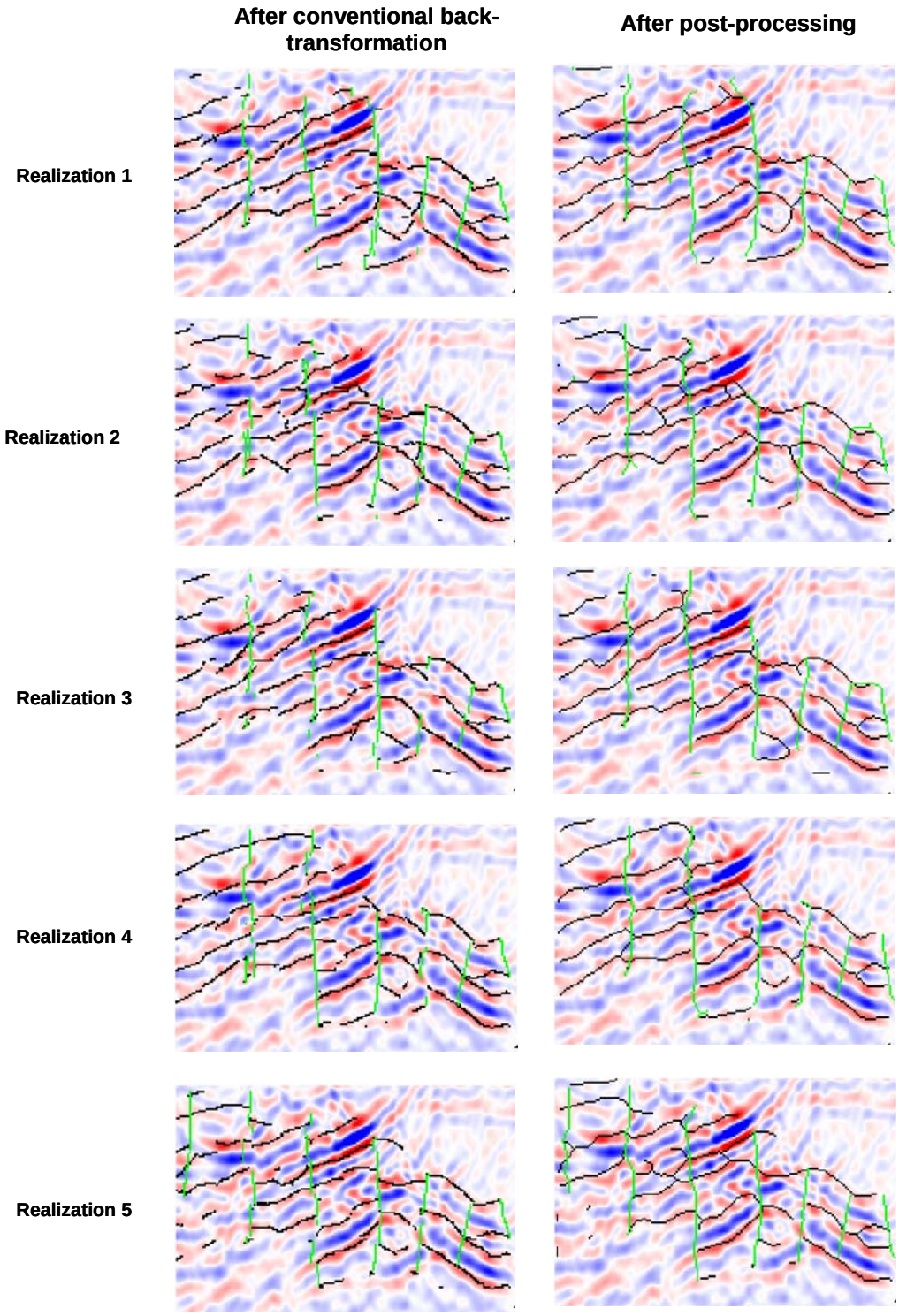

Figure 3.20: Simulated structural models overlaid on a conditioning seismic mage, conventional back-transformation vs. postprocessing

Figure 3.19 compares the structural models obtained by postprocessing the simulated proximity maps against those obtained by the conventional back-transformation. The same realizations are depicted in Figure 3.20 overlaid on the conditioning seismic image. Considerable improvement has been obtained.

Interactive Manual Editing

The skeletonization by the Hilditch's algorithm results in a binary skeleton image where the width of all skeletons is one pixel. This characteristic of skeletons allows the automatic editing of line segments such as endpoint detection, autoconnection, removal, and pruning (Fig. 3.21). Assisted by the autoediting of line segments, an interpreter can interactively edit faults and horizons by simple manual operations.

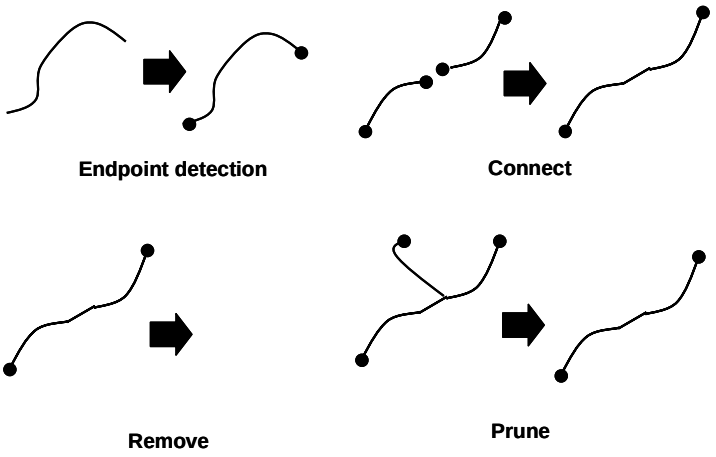

Figure 3.21: Automatic editing of line segments

Figures 3.22 and 3.23 show examples of interactive manual editing of horizons and faults on realizations 1 and 2 in Figure 3.19 (right column, after postprocessing), respectively. As depicted, the editing starts from fault segments. The endpoints of line segments are automatically detected. The interpreter decides which segments on the image to remove, connect, or prune. Then, these segments are autoedited by following the specification of the interpreter. Next, the skeletons of horizons are overlaid and cut by the edited fault segments. The endpoints of horizon segments are autodetected. The horizons are edited in the same manner as fault editing as shown in the figure. Finally, the edited horizon segments are autoconnected to faults. Figure 3.24 shows the structural models obtained after interactive manual editing.

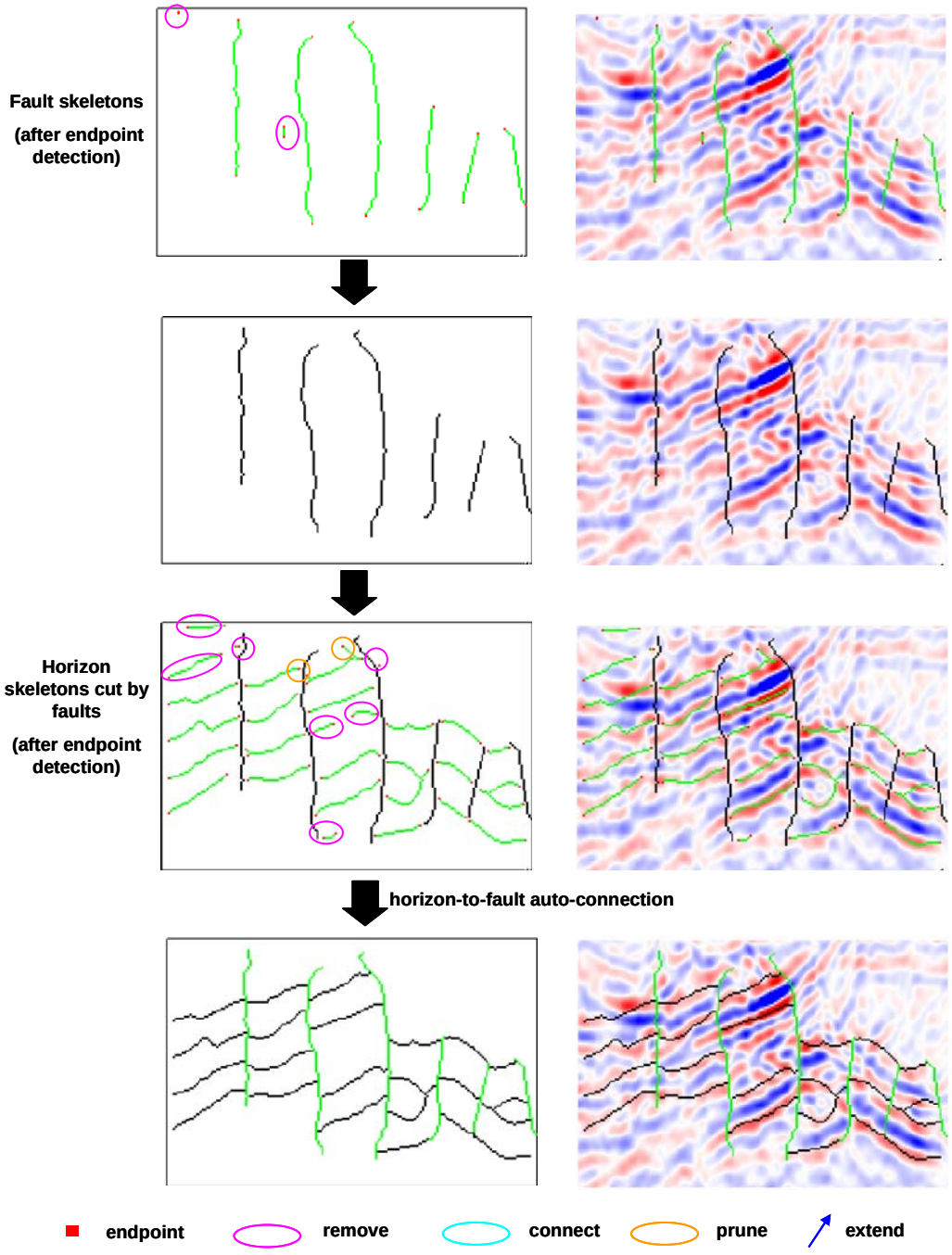

Figure 3.22: Example of interactive manual editing, Realization 1

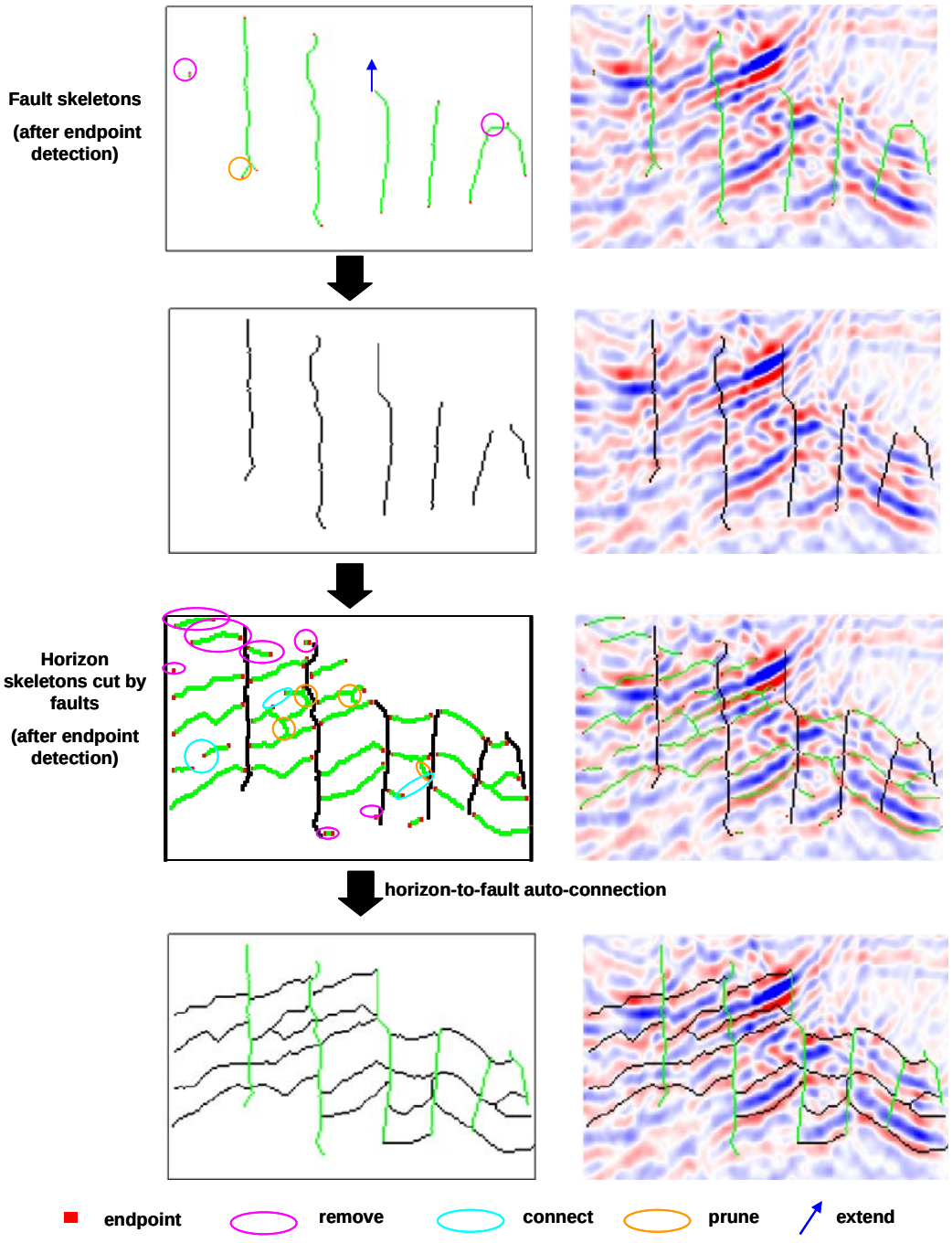

Figure 3.23: Example of interactive manual editing, Realization 2

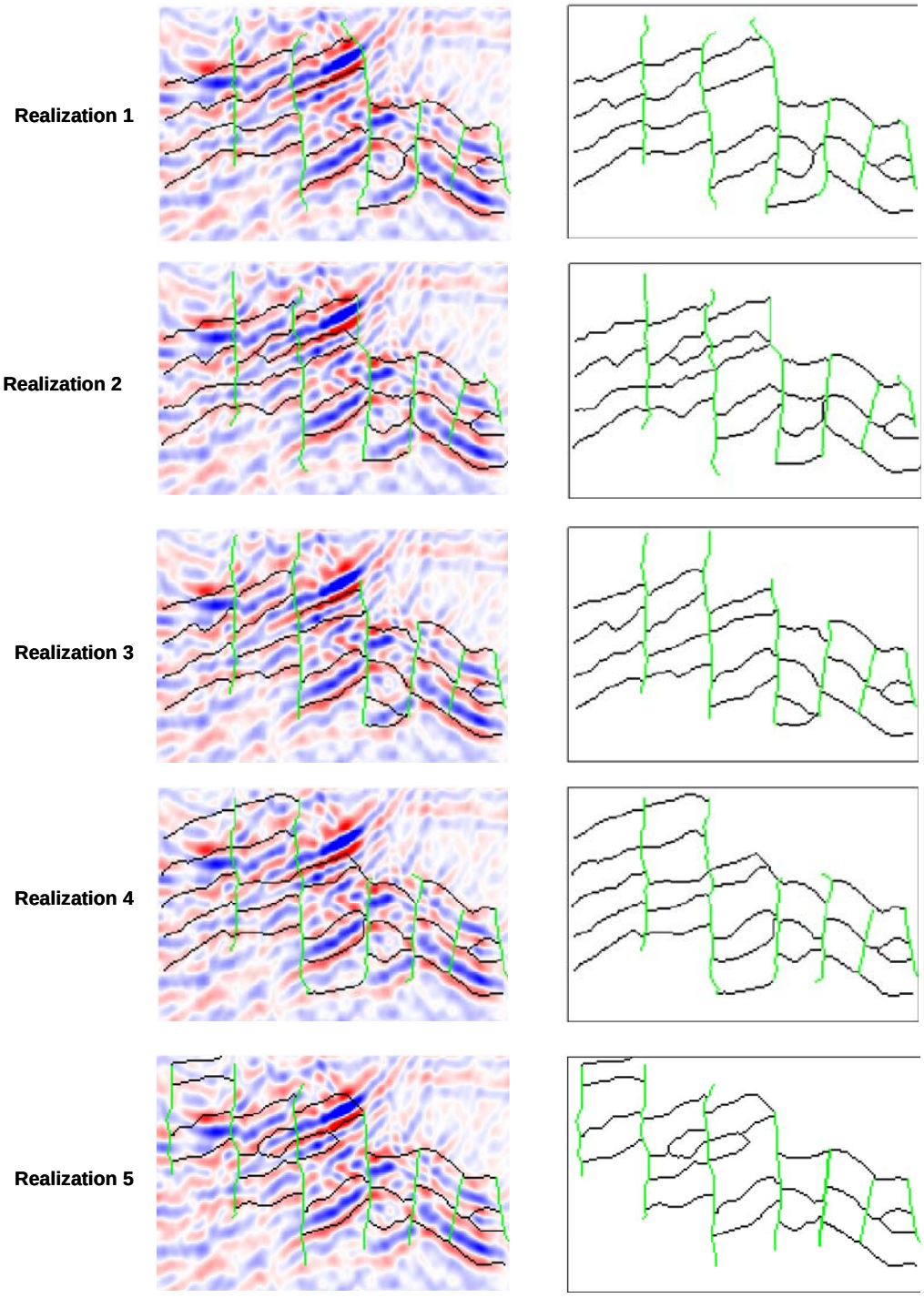

Figure 3.24: Structural models after interactive manual editing

Part II

Dynamic Data Integration

Chapter 4

Distance-based Model Parameterization for Solving Inverse Problem

The focus of the previous chapters (Part I) is on the modeling of structural uncertainty from seismic imaging based on a geophysical/geostatistical approach. Part II of this dissertation focuses on 1) the prior structural uncertainty resulting from multiple structural interpretations and 2) the dynamic data integration through history matching. This completes the workflow of Figure 1.1. A new method for inverting geological architecture from production data is proposed. This methodology is designed as a general solution for spatial inverse problems before being tailored for structural uncertainty modeling. Therefore, structural modeling problems are set aside for the next chapter. In this chapter, the general methodology is discussed and illustrated with a facies modeling problem.

4.1 Motivation

Spatial inverse problems are an important class of inverse problems in many areas of the Earth Sciences. In its general formulation, one is interested in characterizing aspects of an unknown spatial phenomenon by means of data gathered through multiple acquisition techniques, either direct and local sampling, or through what could be generally described as remote sensing techniques. The latter could consist of geophysical (e.g. seismic, gravity, EM, etc) or other

techniques that provide large scale information of the medium under investigation (e.g. pump tests, tracer tests, etc…) and these will be the focus of this chapter.

The solution to such characterization problem often starts by defining a "model" for the medium under investigation. This model is described by a set of parameters or variables **m** which could be as simple as a 1D layered model, containing for each layer one or more properties of the subsurface medium, such as electrical resistivity in an electrical sounding experiment. A more involved parameterization would be to discretize the spatial domain of interest by means of a grid with grid cells each describing one or more property values. In that case, one has as many parameters in the set **m** as there are grid cells times the number of properties considered. Depending on the model parameterization and on the type of data **d** gathered, the problem is either well-posed or ill-posed (the question of how complex a model should be is not considered in this chapter). In most spatial problems, the problem is ill-posed, hence multiple solutions are possible. In this chapter, we will consider problems that are clearly ill-posed.

The methodology proposed in this dissertation relies on a stochastic approach to solving such problems as framed by Bayes' rule (see also Tarantola, 1987; Moosegard and Tarantola, 1995; Omre and Tjelmeland, 1996). This law considers a conditional distribution (termed posterior model) of the model variables **M** given the data **d** as a model for the remaining uncertainty on **M** when **d** is known. Bayes' rule states that

$$\mathrm{f}(\mathbf{M}=\mathbf{m}\,|\,\mathbf{d}) = \frac{\mathrm{f}(\mathbf{D}=\mathbf{d}\,|\,\mathbf{m})\,\mathrm{f}(\mathbf{M}=\mathbf{m})}{\mathrm{f}(\mathbf{D}=\mathbf{d})} \tag{4.1}$$

The density f(**M**=**m**), termed prior (uncertainty) model, describes the uncertainty of the model parameters prior to obtaining or considering the data **d**. The likelihood function f(**D**=**d**|**m**) describes the relationship between the data **d** and each model **m** that could possibly be drawn from the prior uncertainty model. In ill-posed problems, the specification of the prior is critical since it determines the nature of the inverse solutions. More specifically, in a spatial and geological context the prior model can be seen as the set of possible realizations **m** that follow a certain spatial continuity model (e.g. variogram, training image) as deemed relevant for the phenomenon under study and compatible with the data at hand. Selecting an appropriate prior model is often a critical part in solving the inverse problem. If the prior model is wrong then either no solution can be found because the selected prior is incompatible with the data, or worse, solutions can be found

but they are all inconsistent with the spatial variability of the actual phenomenon. Hence, predictions made from such inverse solutions could be erroneous as well.

Current approaches to solving spatial inverse problems do not provide much flexibility in stating the prior model. In many cases one resorts to either regularization methods (e.g. Lee and Seinfeld, 1987) or to a multi-Gaussian prior (e.g. Chu, Reynolds, and Oliver, 1995; Li, Reynolds, and Oliver, 2003), because the latter (1) only requires the specification of the mean and spatial covariance and (2) is mathematically congenial, particularly if the forward model is linear. As a result, the solutions look overly smooth or consistently express homogenous spatial variability far different from the actual heterogeneity present. Boolean techniques (Viseur, 1999; Deutsch and Wang, 1996; Georgsen and More, 1992; Holden and others, 1998) or process-based model (Bridge and Leeder, 1979; Allen, 1978; Mackey and Bridge, 1995) provide alternatives to Gaussian-related models but are difficult to constrain to various different types of data and often require CPU-intensive Markov chain sampling. Markov Random Fields (MRFs, see Tjelmeland, 1998) show promise but requires a tedious parameter estimation based on training data and have not proven practicality on three-dimensional examples or large models.

The development of multiple-point geostatistics (Journel, 1992; Srivastava, 1992) jointly with the advent of fast simulation algorithms (Strebelle, 2002) provided a new avenue for defining prior models consistent with the spatial variability actually observed in nature. Multiple-point geostatistics relies on the concept of a training image, which serves as a three-dimensional analog representative for the variability of the studied phenomenon. Simulation techniques aim at reproducing some of the key lower and higher-order statistics present in the training image while at the same time constraining to local (hard and soft) data (Strebelle, 2002; Caers, Strebelle, and Payrazyan, 2003 for a case study). A practical algorithm for solving inverse problems under a training image-based prior model, termed probability perturbation method, was proposed in Caers (2003), later framed within a Bayesian context in Caers and Hoffman (2006). Several large 3D case studies including the inversion of flow, pressure and 4D seismic in turbidite and fluvial depositional systems have been published demonstrating practicality (Hoffman and others, 2005; Yamada and Okano, 2005; Caers and others, 2006; Castro and others, 2006).

These case studies have shown that the selection of an adequate training image is critical to solving the inverse problem. Solution may not be found when a wrong training image, not representative of the actual spatial variability, is chosen, and even if one can find solutions, the uncertainty

related to the training image choice is not addressed; correspondingly the uncertainty in the posterior is unrealistically small. Note that choosing a training image is no less subjective than choosing a multi-Gaussian model with given spatial covariance. Both are equally committing regarding the choice of all statistics of the prior model, hence on the nature of the inverse solutions. One solution to address uncertainty of the training image is to randomize certain aspects of it, e.g. width/thicknesses of geological features, proportions etc. Similarly, one can randomize variogram parameters in a multi-Gaussian model. However, such randomization falls short in dealing with the first order uncertainty, i.e. the existence of several very different geological scenarios. Practice (e.g. Hoffman and others, 2005; Maharaja, 2006) has shown that the choice of such training image is often discrete and limited to a small set of alternative scenarios. Within each such scenario several subcategories may exist, e.g. different turbidites in a clastic system. Geologists are able to interpret, from the available data, which categories (class or subclass of depositional systems) are likely to occur in the subsurface.

The question addressed in this chapter is: how do we solve spatial inverse problem when the discrete choice of the training image needs to be considered? This chapter does not consider the selection process that lead to this discrete set. In this chapter, it is argued that an explicit parameterization of the "training image variable" is not needed (and may be too difficult). Instead, a stochastic search method that searches for inverse solutions in a space defined by a large set of prior model realizations is proposed. These prior model realizations are generated as random outcomes from the several possible training images. To make such search effective, a static measure of difference (distance function) between any two model realizations is defined. The distance function is chosen such that the static distance between any two model realizations correlates statistically with the difference in the forward model response ("dynamic" or "response" distance). It is shown that by so doing any stochastic search for realizations that match the data **d** becomes feasible and effective. Two such search methods, termed the neighborhood algorithm (NA, Sambridge, 1999) and the tree search utilizing Geometric Near-neighbor Access Tree (GNAT, Brin, 1995), are explored. A synthetic example is used to illustrate the methodology and demonstrate the critical issue of selecting a problem-tailored distance function. The wider impact of the use of distances in such types of spatial modeling problems is discussed.

4.2 Illustrative Example

Before the methodology is described, the importance of the prior model choice in solving spatial inverse problems is illustrated. More particularly, the inversion of permeability from time-varying fluid flow and pressure response observed in wells (i.e. history matching problem) is considered. Figure 4.1 depicts a reference permeability distribution (courtesy of Kent Johansen[1]), considered as the "true" geological subsurface, in an oil reservoir where oil is recovered from three producers by injecting water from two injectors. The production data were obtained by running a flow simulation model (a finite difference implementation of porous media flow PDEs) on this reference reservoir. Our interest lies in studying the impact of the prior model and the inverse algorithm on the inverse solution(s).

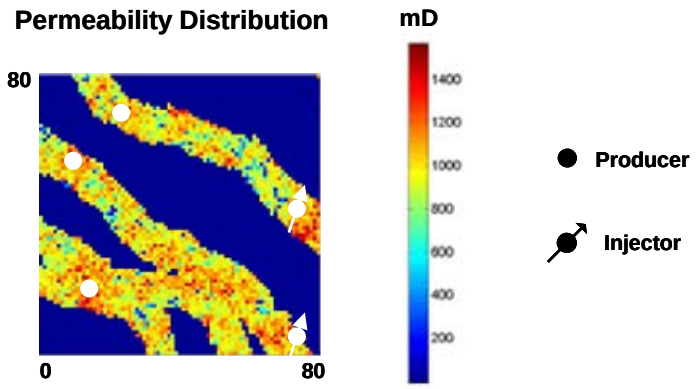

Figure 4.1: Reference model and well locations, Illustrative example (Courtesy of Kent Johansen)

Figure 4.2 shows the results obtained from applying a gradient-based optimization method (using an adjoint technique to calculate the gradient, courtesy of Kent Johansen[1]). In these methods one treats the inverse problem as one of minimizing an objective function consisting of a mismatch term and a regularization term.

[1] Department of Chemical Engineering, Technical University of Denmark

$$O(\mathbf{m}) = \frac{1}{2}\left(\frac{1}{N_{locationl} N_{time}} \sum_{l=1}^{NwellNtime} \sum_{k=1} \omega_{k,l} \left\{ g_{k,l}(\mathbf{m}) - d_{k,j} \right\}^2 + \sigma^2 \left\| \mathbf{m} - \mathbf{m}^{prior} \right\|^2 \right) \quad (4.2)$$

$g_{k,l}(\mathbf{m})$: forward model response simulated from model **m** at time *k* and location *l*

$d_{k,l}$: data observed at time *k* and location *l*

$\mathbf{m}^{prior}$: prior model (= initial model)

ω : weight for mismatch term

σ : weight for regularization term (= regularization parameter)

The vector **m** consists of the unknown permeability in each grid-block. A minimum can be obtained using nonlinear least squares optimization techniques such as Gauss-Newton or Levenberg-Marquardt, which require a gradient (or Jacobian) of the flow simulator response with respect to each grid-cell permeability. Regularization terms are chosen to enforce some smoothness on the inverse solution or, in this case, to penalize a deviation from a given initial model. The latter technique is also known as Randomized Maximum Likelihood (RML, see Li, Reynolds, and Oliver, 2003; Oliver et. al., 1996). The given initial permeability model serves as a geological constraint from which deviation is penalized. Three different constraints are considered. Case 1 (Fig. 4.2A) considers an initial guess which is very close to the reference truth. Case 2 (Fig. 4.2B) considers a wrong initial model with wrong channel geometry leading to wrong connectivity of channel sands between wells, i.e. the fluid flow path geometry between some injectors and producers is different from the truth. Case 3 (Fig. 4.2C) also starts from a wrong initial model (a simple kriged permeability map), however, it is solved without imposing any constraint (i.e. no regularization). For the case close to the truth (Case1, Fig. 4.2A), the traditional inverse solution easily reproduces the “true” geology with a perfect match to the data. However, the changes to the initial model are just a few percentages. On the other hand, if a wrong geological constraint is imposed (Case2, Fig. 4.2B), the production data cannot be matched because the inverse solution is not allowed to deviate enough from that “wrong” initial guess. The solution obtained without imposing any geological constraint (Case3, Fig. 4.2C) achieves a perfect match to the data with fairly small forward modeling cost. However, this inverse solution contains many artifacts not

representative of the geological architecture of a channel system. In other words, the inverted permeability lacks geological realism. Thus, the RML method works well if the major geometries of the spatial variable are known and only relatively small changes need to be made to obtain an inverse solution. This makes sense given that any gradient-based optimization technique can converge only to a local minimum (which need not be an acceptable inverse solution or a global minimum).

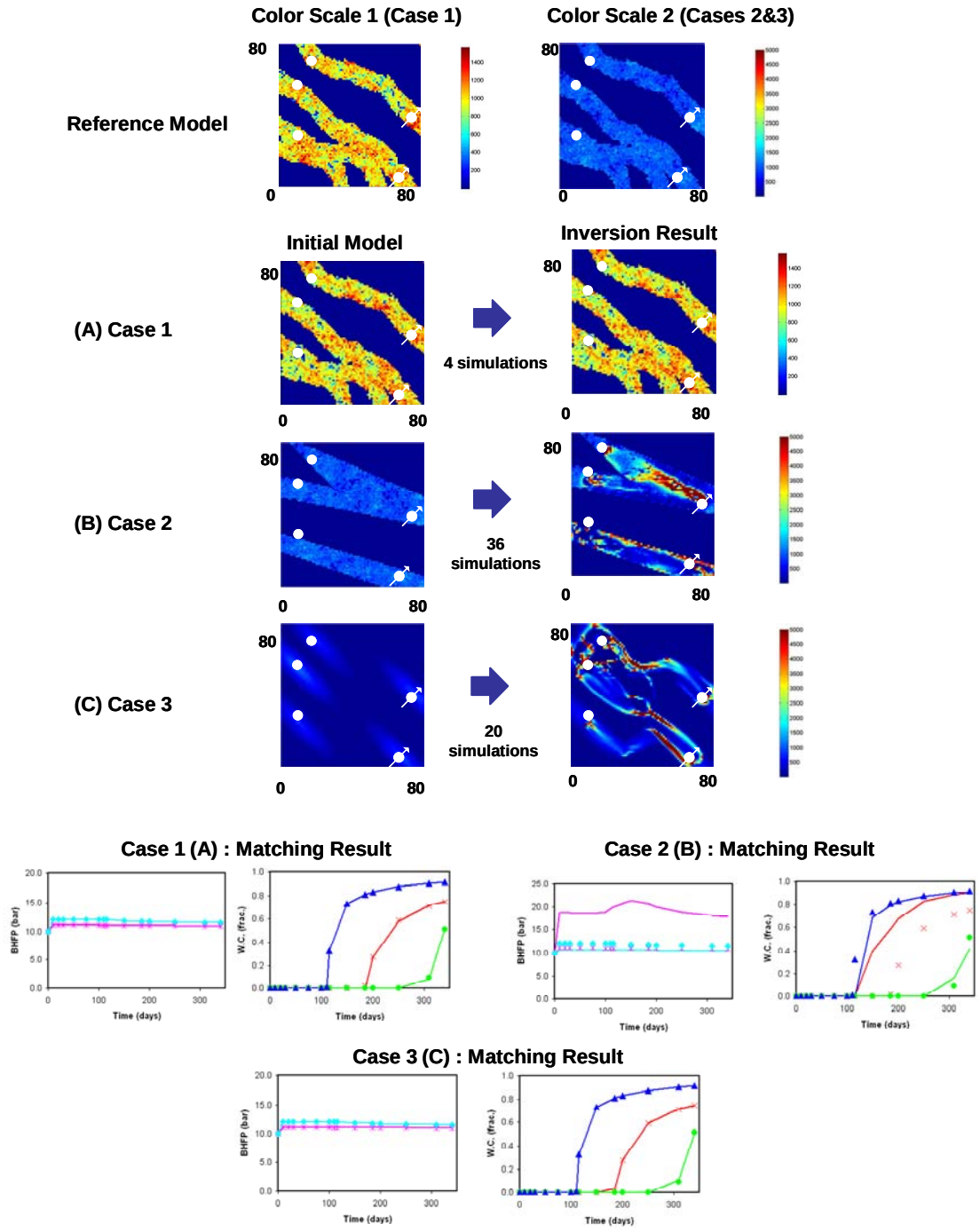

Figure 4.2: Inverse solutions by the gradient-based method vs. reference & initial models, match of forward model response to data (dot: data, line: model response), Illustrative example, Cases ~3 (Courtesy of Kent Johansen)

One effective way to impose geological realism by construction is to start with a training-image-based constraint as proposed in Caers (the probability perturbation method, PPM, 2003). The PPM method solves the inverse problem by constraining the statistics of the inverse solutions to those obtained from a given training image, instead of solving a problem with minimal deviation from an initial guess. Moreover, the PPM search for an inverse solution is stochastic as opposed to the deterministic gradient-based method; thereby, local minima can be avoided. Figure 4.3 depicts the inverse solutions using the probability perturbation method obtained with different training images. Case 4 (Fig. 4.3A) is solved using the reference training image which is used for generating the production data (true geology, Fig. 4.1). Case 5 (Fig. 4.3B) is constrained to a training image which visually resembles the “true” geological patterns. Case 6 (Fig. 4.3C) uses a training image that depicts narrower channels than the truth, yet the channel orientation is correct. Case 7 (Fig. 4.3D) is constrained to a channel orientation completely different from the “truth”. The problem is solved by inverting for sand distribution (lithology type) instead of permeability. A uniform permeability for sand and background is assumed. As illustrated in the figure, if the “true” training image is provided (Case 4, Fig. 4.3A), the inverse solution reproduces an inverse solution with the same geological patterns as the reference and with quick convergence (13 flow simulations). Unlike the gradient-based method, the methodology does not require an initial guess close to the truth; multiple alternative solutions (considered as samples of a posterior distribution) can be found by restarting with a different initial guess. The inverse solution of Case 5 (Fig. 4.3B) and Case 6 (Fig. 4.3C) also reproduces the “true” geological architecture fairly reasonably, providing the right connectivity of flow paths between producers and injectors. However, there is a significant increase in the number of flow simulations needed. If a completely wrong training image is provided (Case 7, Fig. 4.3D), the data cannot be matched.

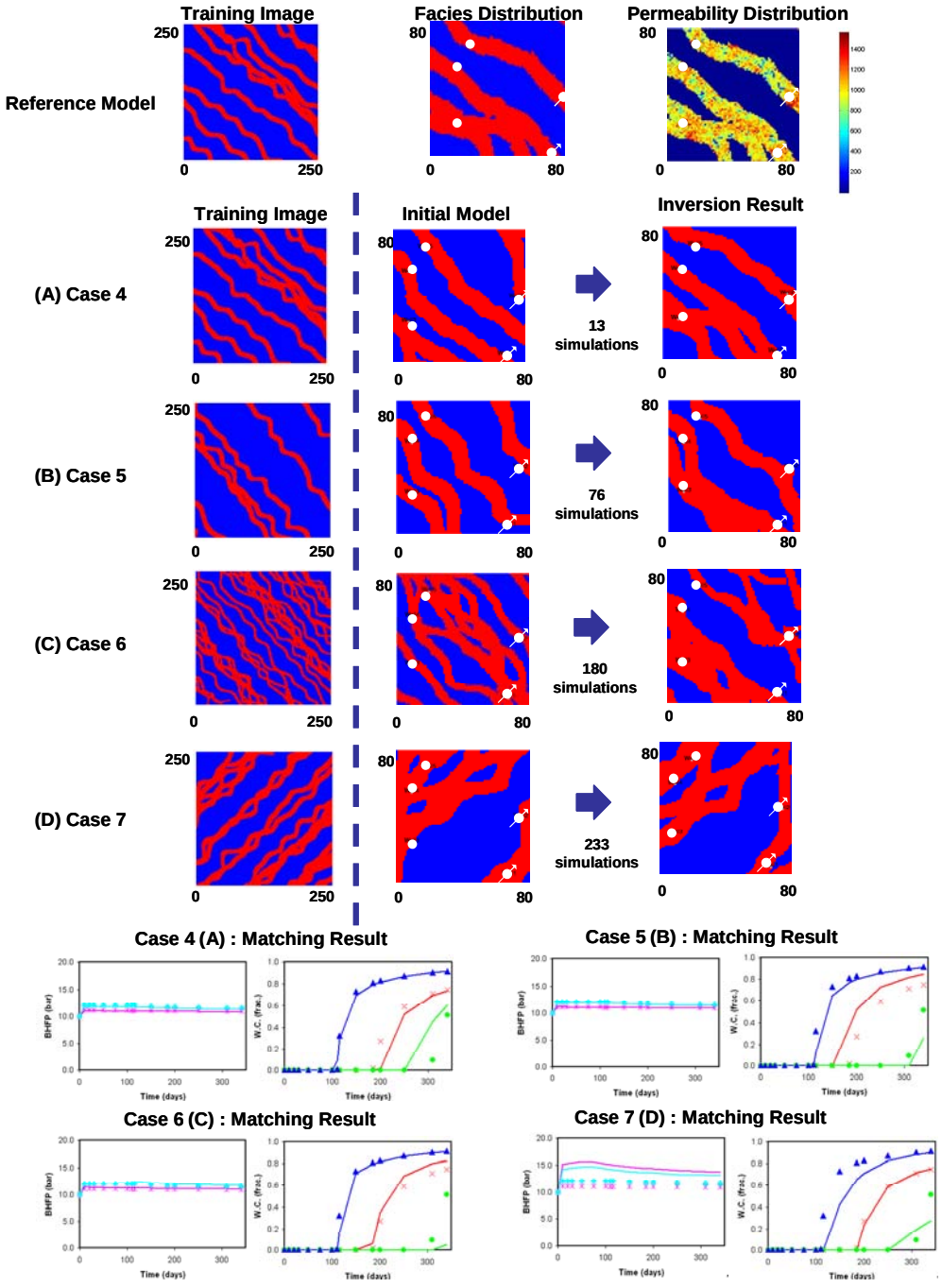

Figure 4.3: Inverse solutions by the probability perturbation method vs. reference & initial models, match of forward model response to data (dot: data, line: model response), Illustrative example, Cases 4~7

A simple fact highlighted in these examples is that, regardless of the type of inverse modeling approach, the inverse solutions strongly depend on how one chooses to impose geological constraints. In complex geological environments, an accurate determination of the geological depositional system is often difficult given limited data. In such case, the geological interpretation is not unique and relies on a subjective decision of the expert(s). Since interpretations are subjective and uncertain, one could opt for selecting multiple possible geological scenarios instead of betting on a single subjective choice (either through a particular type of regularization or one single training image) as was done in each of the above examples. Such multiple geological alternatives can be modeled through constructing several possible training images. In the context of Bayesian inversion (Eq. 4.1), this approach is regarded as an attempt to model the prior uncertainty f(**M**=**m**) by accounting for multiple geological interpretations rather than one single interpretation. A flexible methodology to achieve inverse solutions under such prior is proposed next.

4.3 Methodology

Solving spatial inverse problems by considering the discrete choice between multiple training images is a challenging task. Gradient-based optimization methods do not apply in such inherently discrete parameter space. Most stochastic search methods, including genetic algorithms, PPM, or even Markov chain Monte Carlo sampling require some form of parameterization of the problem, then finding those set of parameters that match the data. Instead of focusing solutions by means of parameterization, a methodology based on a measure of similarity between outcomes/samples of the prior model is proposed.

4.3.1 Discrete Space Parameterization

The method proposed in this dissertation does not attempt to parameterize complex geological architectures by a necessarily large set of model parameters. This set may need to be very large (example: every grid cell property could be a parameter). Instead, it is suggested to generate a large set of prior model realizations in advance, thus providing multiple training images to the geostatistical sampling algorithm.

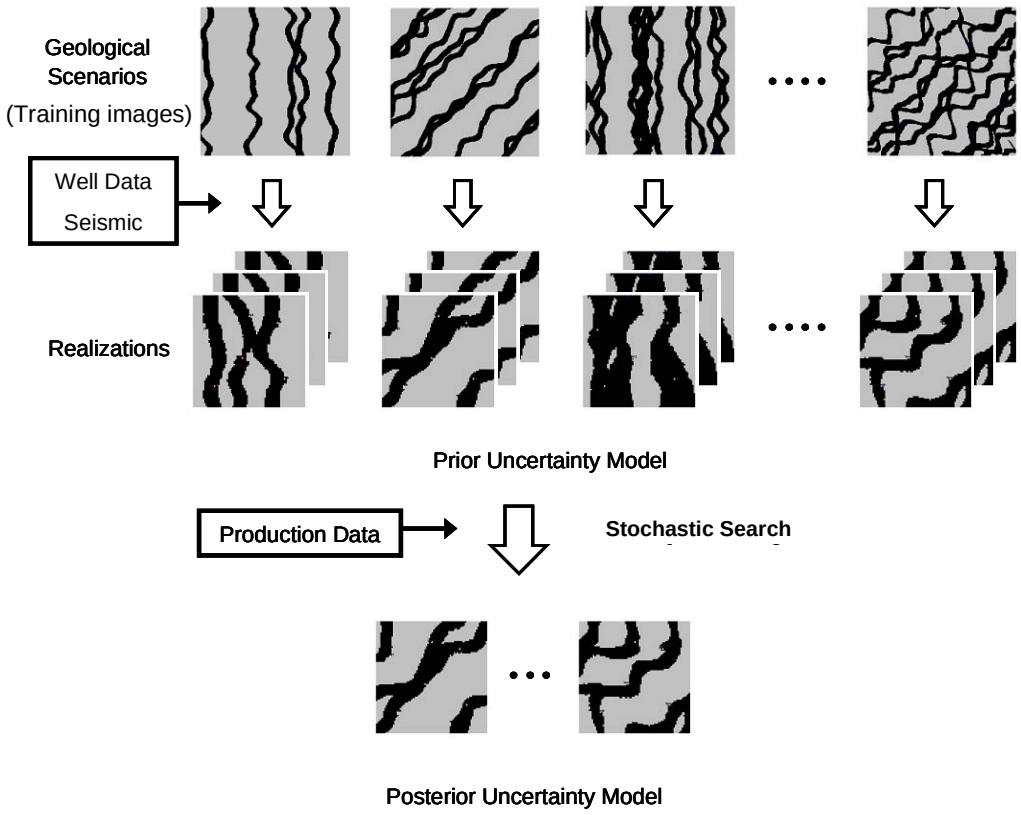

Figure 4.4: Proposed workflow for solving spatial inverse problem

Figure 4.4 illustrates this idea. The goal is to generate realizations of channel systems constrained simultaneously to dynamic fluid flow responses, facies observation at wells, and seismic data (if available) while respecting the geological concept expressed by several alternative training image(s). In order to address the uncertainty related to each geological scenario, multiple training images, each representing variations of a geological scenario, are constructed. As depicted in Figure 4.4, a large set of model realizations is geostatistically simulated from the different initial training images by conditioning only to facies observation at wells and seismic data. This potentially very large set of model realizations represents a (discrete) prior uncertainty distribution f(**M**=**m**). Any set of realizations creates a discrete space, and, if enough realizations are generated, then this space represents a rich set of prior knowledge. Inverse modeling essentially boils down to searching in that space for model realizations that match the data **d** (in case the likelihood is a

spike). The set of realizations found in this way are a discrete representation of a posterior distribution f(**M**=**m**|**d**) (Boucher, 2007). To make this search effective, the notion of similarity distance is introduced.

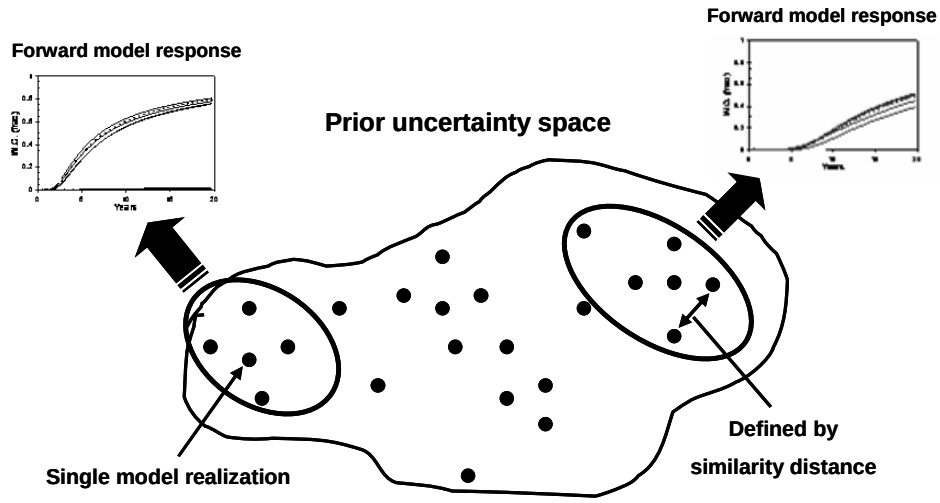

Figure 4.5: Conceptual illustration of prior uncertainty space defined by similarity distance

As shown in Figure 4.5, realizations/samples are considered as points in a space. The distance between any two model realizations is defined by a distance function called “similarity distance”. The similarity distance measures how much any two realizations look alike. Such definition is inherently a subjective decision on what is deemed “similar”. Rather than considering this as a disadvantage, we will exploit this subjectivity to tailor the distance function to the particular problem at hand, namely: 1) what are we trying to match and 2) what are the matched realizations used for? Hence, the choice of distance function is a critical element in our methodology and is discussed in extenso.

Methods for inversion that utilize a Cartesian parameter space (e.g. gradient-based methods or PPM) also consider models as points in a space. The distance between points (Euclidian distance) defined in Cartesian parameter space is essentially a similarity measure, namely, the square-root of the sum of squared differences of the model parameters. For example in gradient-based methods one relies on the smoothness of the function measuring the mismatch *O* between the data and the

model response. Two models with similar parameter sets (small Euclidean distance) would need to have a small difference in the *O* function value for gradient-techniques to apply.

The model parameterization proposed in this dissertation (Fig. 4.5) replaces the Euclidian distance by a distance function which does not require a vector form representation of the model parameters (training image, proportions, variogram parameters etc…): it works directly on the model realizations. This provides a greater flexibility to accommodate uncertainty on the prior geological scenario since 1) it does not require any explicit parameter to describe individual realizations and 2) it easily handles discrete parameters such as different choice of geological scenarios.

To search for realizations that match **d**, we will rely on the following key property: "*to make a stochastic search (using any algorithm) for realizations that match the data **d** effective, the distance between any two realizations needs to statistically correlate with the difference in their forward model response*"; the higher that statistical correlation, the more effective the search.

As will be shown by illustration, given a distance function that satisfies this key property, the function measuring the mismatch between data and forward model response becomes "structured", i.e. it is not a completely random functional of the model realizations. Unlike a Cartesian parameter space, this *metric* space is not defined by origin, dimension or direction: it is only equipped with a distance, and, as shown later, this is sufficient to apply a stochastic search effectively.

4.3.2 Distance Function

The choice of a distance function is critical to the proposed method. This choice depends on the particular type of data one is trying to match and the type of geometries present and, last, on the ultimate purpose for which the inverse solutions are used. Consider therefore the specific case of high-permeability flow paths as modeled through the channel system of Figure 4.4. The Hausdorff distance (Dubuisson and Jain, 1994, see Appendix A) is proposed here as an adequate similarity measure for capturing the similarity in channel geometry, since it is a standard similarity measure to compare the shape of two-dimensional or three-dimensional objects and is often used in object matching (shape matching) problems. Its validity for this type of flow problems is demonstrated through a numerical experiment; i.e. to show that the Hausdorff distance correlates with the difference in flow response for this particular type of application.

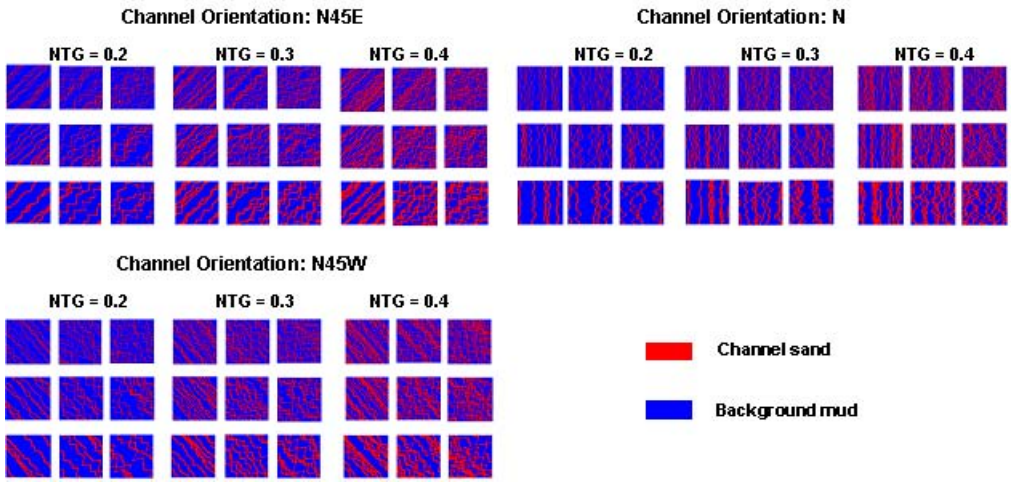

Figure 4.6: Training images representing prior uncertainty related to geological interpretation

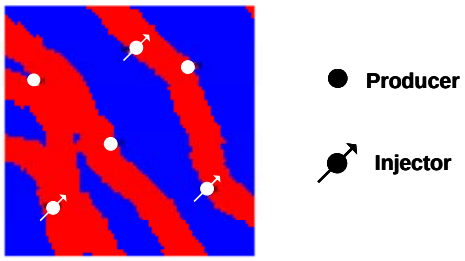

Figure 4.7: Well locations

Figure 4.6 illustrates a set of training images representing alternative geological scenarios. To construct a prior uncertainty space that accommodates a large set of model realizations, a total of 405 facies realizations (i.e. 5 from each of the 81 training images depicted in Fig. 4.6) are geostatistically simulated conditioned to facies observations at the five wells depicted in Figure 4.7, all penetrating channel sand. In this synthetic problem, background mud is understood as a sealing rock which does not have flow capacity and storage capacity. The inner channel heterogeneity in petrophysical properties is considered negligible, thus channels are modeled with constant (known) porosity/permeability. The spatial distribution of channel sands is considered the unknown in this inverse problem. The forward model response is the production performance, i.e. pressure and water cut observed at producers, under the water injection operated by 3 producers

and 3 injectors (see Fig. 4.7 for well locations). In this experiment the forward model response is computed for all 405 models which will allow one to validate the Hausdorff distance. Note that in reality, for CPU reasons, it would not be possible to flow simulate all 405 models. This exercise is only meant to check the validity of the Hausdorff distance for these kinds of problems.

The Hausdorff distance between any two realizations, $d_H(\mathbf{m}_i, \mathbf{m}_j)$, see Appendix A, is computed for every pair of 405 model realizations. Also, from the forward model response simulated on these realizations, a least-square misfit function is computed for every pair of model realizations $\mathbf{m}_i$ and $\mathbf{m}_j$ as:

$$G(\mathbf{m}_i, \mathbf{m}_j) = \frac{1}{N_{location} N_{time}} \sum_{l=1}^{Nwell} \sum_{k=1}^{Ntime} \left[g_{k,l}(\mathbf{m}_i) - g_{k,l}(\mathbf{m}_j) \right]^2 \tag{4.3}$$

$g_{k,l}(\mathbf{m}_i)$: forward model response simulated from model $\mathbf{m}_i$ at time k and location l

Note the difference between the misfit function $G(\mathbf{m}_i, \mathbf{m}_j)$ of Eq. 4.3 (= misfit of forward model response $g(\mathbf{m}_i)$ between models) and the mismatch of the forward model response $g(\mathbf{m}_i)$ to data $\mathbf{d}$ (that is the mismatch or objective function formulated when solving a inverse problem). In fact, the data $\mathbf{d}$ can be seen as a particular response $g(\mathbf{m}^{true})$, namely that of the unknown truth $\mathbf{m}^{true}$. The plot of this misfit function $G(\mathbf{m}_i, \mathbf{m}_j)$, Eq. 4.3, against the similarity distance $d_H(\mathbf{m}_i, \mathbf{m}_j)$, with some smoothing over a certain distance interval Δd_H, is similar to the omnidirectional variogram of forward model response expressed as a function of the similarity distance. If this variogram shows a structure (i.e. not a pure nugget), it indicates that the forward model response simulated on the model realizations is indeed spatially correlated in the space defined by the given similarity measure, in this case the Hausdorff distance.

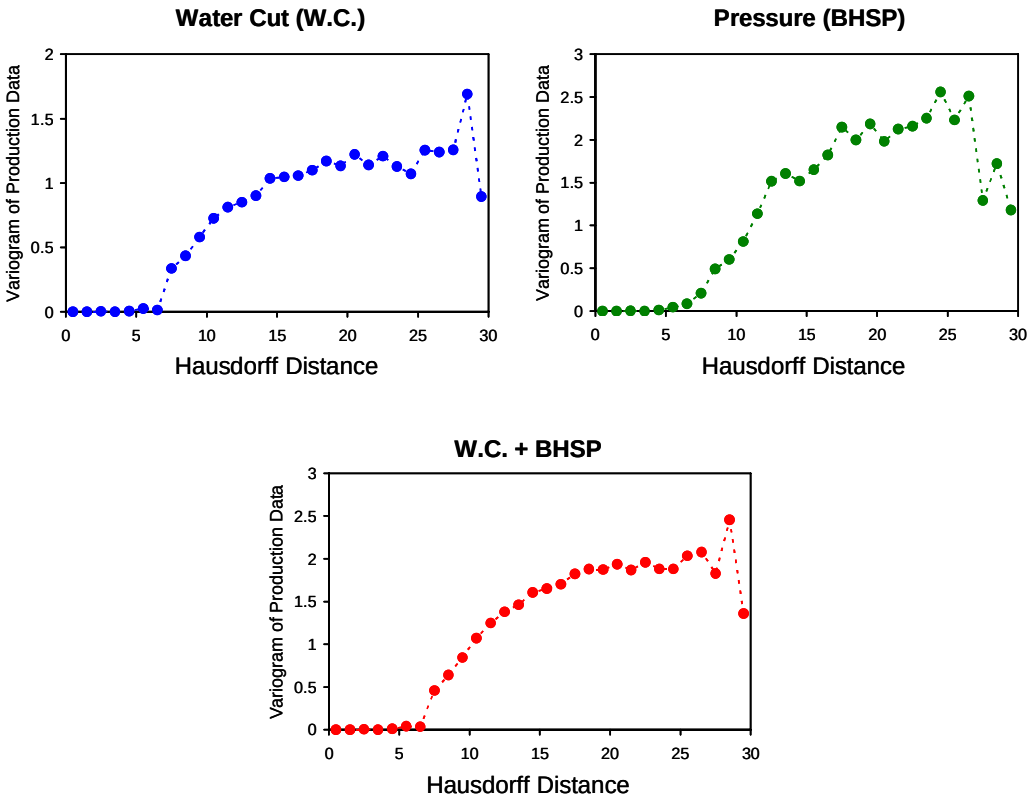

Figure 4.8: Variogram of forward model response as a function of the Hausdorff distance

Figure 4.8 depicts the pseudovariograms of the forward model response computed for pressure (BHSP), water cut (W.C.) and weighted sum of both (W.C.+BHSP). As shown in the figure, all variograms exhibit clear structure. The Gaussian structure with the lack of nugget effect observed in these particular variograms is attributed to the fact that a change in the facies distribution far away from any wells has no effect on the response function (see Fig. 4.9 for an example). The clear structure observed in the variogram should not be interpreted as a unique relation between the similarity distance and the misfit function. Like any other variograms, the variogram of forward model response only indicates at best a statistical correlation between forward model response and similarity distance, which, as shown in the next section, is satisfactory for achieving an effective stochastic search.

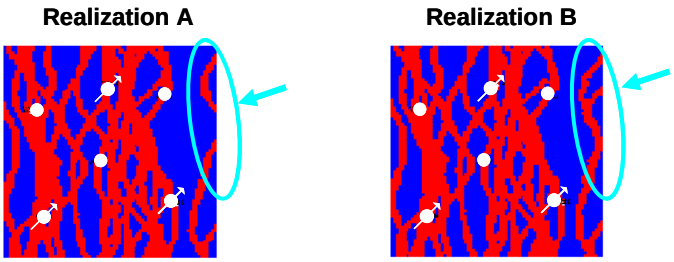

Figure 4.9: An example of realization pair that gives zero variogram at small similarity distance

4.3.4 Stochastic Search

Once a parameter space (= prior uncertain space) is defined with a distance function, the inverse problem is solved by searching in the space for model realizations that achieve minimum of objective function $O(\mathbf{m}_i)$:

$$O(\mathbf{m}_i) = \frac{1}{N_{locationl} N_{time}} \sum_{l=1}^{Nwell} \sum_{k=1}^{Ntime} \left\{ g_{k,l}(\mathbf{m}_i) - d_{k,j} \right\}^2 \tag{4.4}$$

$g_{k,l}(\mathbf{m}_i)$: forward model response simulated from model $\mathbf{m}_i$ at time k and location l

$d_{k,l}$: data observed at time k and location l

Two stochastic search methods are explored, namely, the neighborhood algorithm (NA) and tree search.

The Neighborhood Algorithm (NA)

The neighborhood algorithm (NA, Sambridge, 1999) is a stochastic optimization algorithm proposed for seismic inversion problems and also applied for history matching problems (Demyanov, Subbey, and Christie, 2004; Christie, Demyanov, and Erbas, 2006). Although the method was originally designed for multidimensional Cartesian parameter space where parameters to be inverted are expressed in the form of a vector, with some reformulation of the algorithm, it is also applicable to the proposed metric space defined using only a metric distance. The method

explores the space for multiple minima, partitioning the space into Voronoi cells as progressively more evaluations of the objective function O(**m**) are made. Note that in order to define Voronoi cells in any high-dimensional space, only knowledge of a distance is required.

Each function evaluation consists in simulating the forward model response g($\mathbf{m}_i$) and calculating the misfit function O($\mathbf{m}_i$) from Eq. 4.4. The search path is stochastically decided based on the misfit function O($\mathbf{m}_i$), which have been previously evaluated in the parameter space. A schematic of the step by step procedure of this approach is illustrated in Figure 4.10.

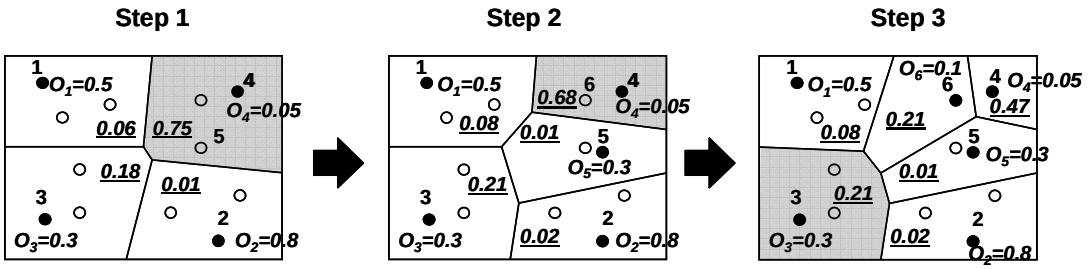

Figure 4.10: Schematic steps of the neighborhood algorithm (NA)

As depicted in the figure, the search is initiated by evaluating the objective function for some small number of initial model realizations which are separated as far as possible in terms of the similarity distance (depicted as black dots in step 1 in Fig. 4.10). Subsequently, the parameter space is compartmentalized by associating the remaining model realizations (white circles) to the nearest model (i.e. in terms of the similarity distance) whose forward model response is already simulated (black dots). Strictly speaking, one can not draw a figure as in Figure 4.10, since the space is only equipped with distance (not with direction). In the next set, one of the Voronoi cells is selected for further processing. This is decided by a Monte Carlo draw from a discrete probability distribution.

$$Prob(\text{“Selecting Voronoi cell with model initial realization } \mathbf{m}_i\text{”}) = p(\mathbf{m}_i) = \exp\left\{-\frac{1}{T}\frac{O(\mathbf{m}_i)}{N_i}\right\} \tag{4.5}$$

which is primarily a function of $O(\mathbf{m}_i)$ and of other parameters explained further on. We denote this probability value as the “selection probability” (shown as underlined in the figure). Next, in

the drawn Voronoi cell, another realization is picked at random and its mistfit function is evaluated (this is model 5 in step 1). Given this model and its misfit function value, one can further compartmentalize the space (as shown in step 2) and update the discrete selection probabilities. This procedure is repeated until one obtains the desired numbers of model realizations that achieve sufficiently low value of the objective function.

If the selected Voronoi cell does not any longer contain a model realization whose forward model response is not simulated yet (such as depicted as a white circle in Fig. 4.10), a new model realization is created by the stochastic perturbation from the model (a black dot) in the selected Voronoi cell using the probability perturbation method (PPM, Caers 2003). In other words, the initial set of 405 models is expanded by iteratively generating new models. This step is needed, since one cannot expect that, by searching on a limited (405) set, a sufficient amount of models that match the data can be found. Hence, the stochastic search can be seen as a way to create a set of initial models for more local search methods (gradient or PPM). By coupling the probability perturbation method, the prior uncertainty space turns into a potentially very large set of realizations regardless of the number of model realizations initially provided in the space.

In Eq. 4.5 N_i is the number of model realizations which are included in the Voronoi cell *i* and whose forward model response is not simulated yet. The standardization parameter T is such that the total of the selection probability $p(\mathbf{m}_i)$ over all Voronoi cells equals 1.0. As indicated in Eq. 4.5, the smaller the objective function of model $\mathbf{m}_i$ is, the greater the selection probability the Voronoi cell *i* receives, thus this Voronoi cell would be subject to intensive visits by a stochastic search path. Also, if the Voronoi cell *i* includes a larger numbers of models whose forward model response is not simulated yet, then, this Voronoi cell receives a higher chance of being visited.

The neighborhood algorithm (NA) is a global search algorithm which has the potential to find multiple minima. The search is for most problems more efficient than other stochastic search methods (such as the genetic algorithm or Markov Chain Monte Carlo method) since the selection probability, Eq. 4.5, is strongly guided by the value of misfit function: the stochastic search path visits the region with low misfit function much more intensively than the region with high objective function, resulting in a finer compartmentalization of the space in low-misfit-function regions. However, as a trade off, it does not necessarily find all of the minima in the parameter space, since the search tends to concentrate on regions with low objective function rather than to

explore the space uniformly. If uniformity of search is critical for a particular application than other search methods should be employed such as the tree search, which is discussed next.

Tree Search

Another way to search for inverse solutions in the proposed parameter space is to store a large set of model realizations in a tree data structure and implement a stochastic search by traversing the tree. The tree data structure is constructed solely based on a distance metric, thus represents the spatial structure of the parameter space without requiring any other spatial properties such as dimensions or directions. In this dissertation, tree search optimization is implemented using the Geometric Near-neighbor Access Tree (GNAT, Brin, 1995) which was originally proposed for database search problems. The GNAT is constructed by the following procedure (see Fig. 4.11 for the schematic illustration):

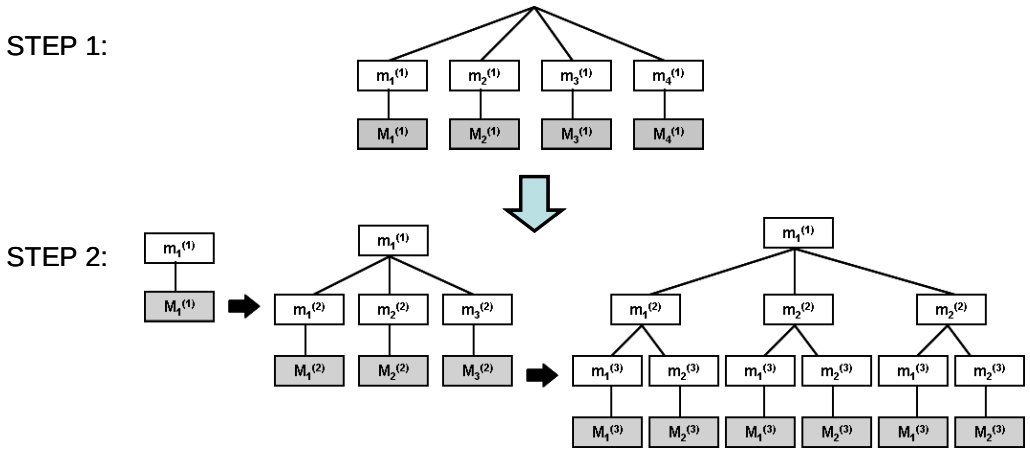

Figure 4.11: Schematic steps of GNAT construction

1. Select some model realizations $m_i^{(1)}$ from the whole set of model realizations available. These model realizations are selected based on the similarity distance such that they are separated far away enough from each other. The selected model realizations are located at the first level nodes (= root nodes) of the tree. According to the similarity distance, associate the remaining model realizations to their closest $m_i^{(1)}$ as depicted in Figure 4.11. In Figure

4.11, $m_i^{(j)}$ denotes a single model realization and $M_i^{(j)}$ denotes a set of model realizations associated to $m_i^{(j)}$.

2. Go down to the second level of nodes. Select a few model realizations $m_i^{(2)}$ from the set $M_i^{(1)}$ such that they are furthest away from each other. Locate them at the second level nodes, and then associate the remaining members of $M_i^{(1)}$ to their closest $m_i^{(2)}$ as in Figure 4.11. They are denoted as set $M_i^{(2)}$. Then go down to the third level of the nodes and do the same operation. Although Figure 4.11 only depicts the tree construction starting from $m_1^{(1)}$, actual tree branching is done for all branches.

3. Repeat this until the entire tree is completely branched (i.e., the number of model realizations included in $M_i^{(j)}$ becomes one at all branches of the tree).

The GNAT exhibits a hierarchical tree structure that resembles a family tree; i.e. children are always more similar to their parent than to the siblings of their parent. In other words, model realizations similar to each other are hierarchically clustered in the tree structure by sharing the same ancestors, while dissimilar ones are located far away from each other. The dissimilarity among the siblings is greatest at the first level node (= root node), and the siblings becomes more similar to each other as the node goes down into the deeper branches.

The optimization is implemented as a stochastic search by using the selection probability (Eq. 4.5) to decide the traversal path. The traversal is started from the top of the tree. At the currently visited node of the tree, forward response is simulated for children model realizations and selection probability (Eq. 4.5) is assigned for each child based on the evaluated objective function (Eq. 4.4). Then, the next path to go down is randomly decided based on the selection probability. In the context of the tree search optimization, N_i in Eq. 4.5 indicates the number of the model realizations which are the descendants of the realization i and also not flow-simulated yet. Thus a model realization located on top of the less explored branch receives a higher chance to be visited. Also, the selection probability is assigned in such a way that the family of realizations branching from a model that achieved the better match of forward response receives a higher chance to be explored. When the search arrives at the end of the tree, one goes back to the top of the tree, and starts the second round of tree search. This procedure is repeated until a desired number of model realizations that achieve sufficiently low objective function are found.

The GNAT structure is identical to a hierarchical Voronoi compartmentalization of the parameter space, where parents correspond to the Voronoi cells of higher hierarchy and children correspond to those of lower hierarchy. Thus, in a tree search optimization, the selection probabilities are hierarchically assigned in a prior uncertainty space, which tends to avoid a concentration of search visit to the currently found low-objective-function region which is typical for NA. The choice of the optimization algorithm between NA and the tree search optimization depends on the purpose of the inverse problem. NA is generally more efficient because of the stronger control of the objective function over the stochastic search (i.e. the selection probability is determined accounting for all objective functions previously evaluated in the entire space). On the other hand, the tree search optimization can be more global due to the hierarchical partitioning of the space. If one wishes to couple the probability perturbation method (PPM) with a stochastic search, NA is more suitable.

4.4 Application Examples

The applicability of the proposed method is investigated by considering the previous history matching problem. The synthetic data set and geological setting are the same as discussed in the numerical experiment for validating the Hausdorff distance (see Fig. 4.6 for a set of training images representing prior uncertainty in geological concept). Six different synthetic cases are retained by considering different reference models (= “true” geology) as depicted in Figure 4.12. The results of the neighborhood algorithm (NA) and the tree search are presented.

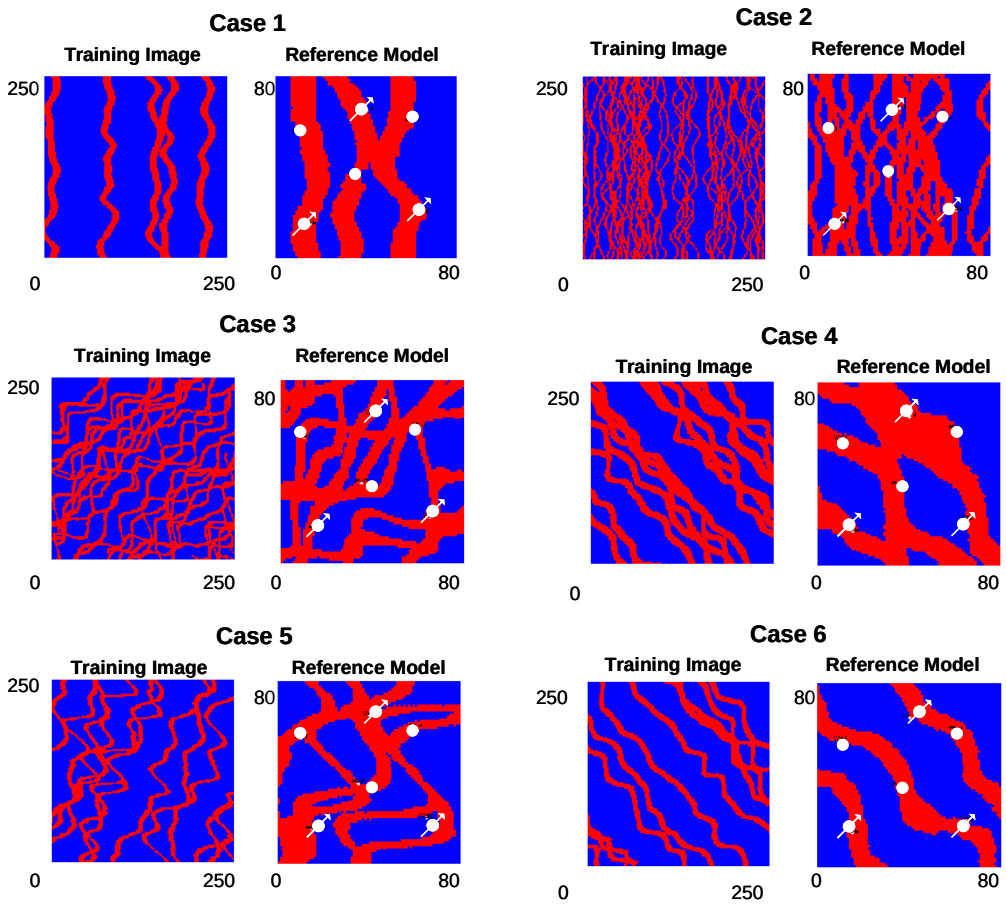

Figure 4.12: Reference models and corresponding training images

The Neighborhood Algorithm (NA)

The spatial inverse problem is solved by the neighborhood algorithm (NA) starting by generating 81 facies realizations, each realization simulated from a different training image (Fig. 4.6). The probability perturbation method is hybridized with NA. The search is terminated when four history matched models are obtained. The results of the selected 3 cases (Cases 2, 3, and 6) are presented. As shown in Figure 4.12, the "true" geology of Case 2 exhibits clear channel direction with small channel sinuosity. The channels are highly connected due to the high net-to-gross ratio, thus all producers and injectors are penetrating a single flow-communicating sand body. The "true" geology in Case 3 also exhibits high net-to-gross ratio, but consists of significantly more sinuous channel sands. Hence the channel orientation is obscured by this high sinuosity. The "true" geology in Case 6 exhibits separate channel sands, providing distinct flow path between wells. Figures 4.13, 4.15, 4.17 compare the inverse solutions obtained in these cases against the "true" model and the initial model realizations chosen to start the search. The NA search is started from 8 initial model realizations. The matched forward model responses of these cases are shown in Figures 4.14, 4.16, 4.18 together with the data and the initial forward model responses. A satisfactory match of production data is achieved in each case (see Figs. 4.14, 4.16, 4.18 for examples). Figure 4.19 compares the posterior distribution of net-to-gross ratio (= sand proportion) calculated from the model realizations sampled by the stochastic search against the prior distribution computed from the prior model realizations.

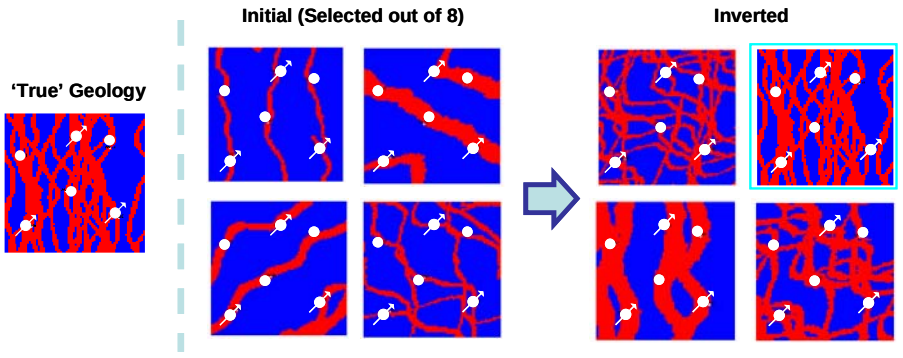

Figure 4.13: Inverted model realizations vs. reference model, initial models, NA, Case 2 (The inverted model highlighted by light blue reasonably resembles to the reference model)

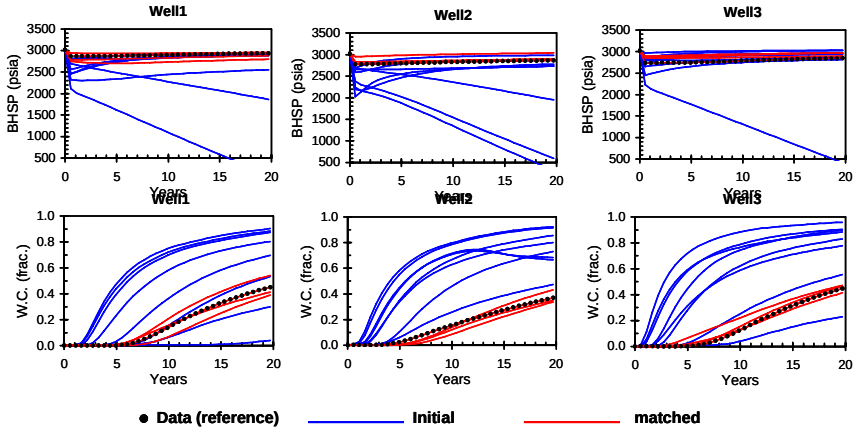

Figure 4.14: Match of forward model response to data, bottom-hole shut-in pressure (BHSP, upper row) and water cut (W.C., lower row), NA, Case 2

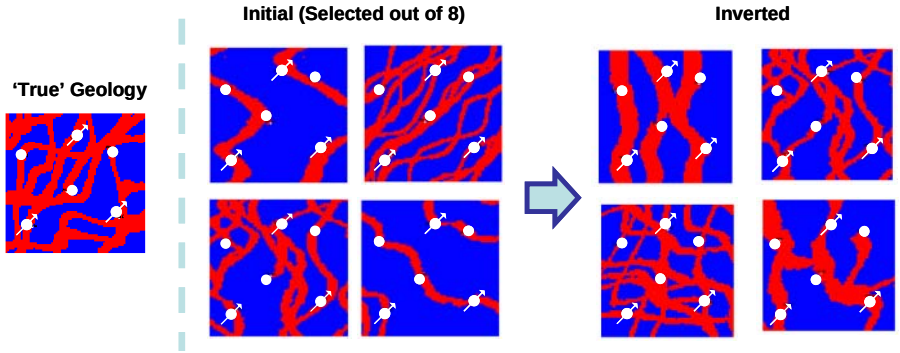

Figure 4.15: Inverted model realizations vs. reference model, initial models, NA, Case 3

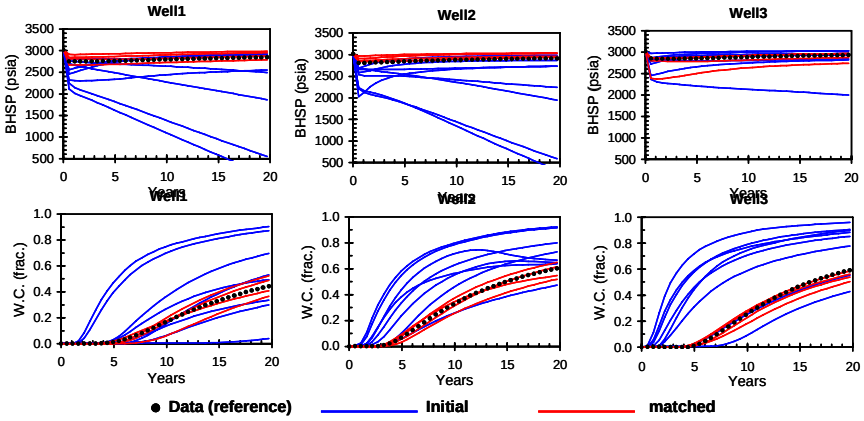

Figure 4.16: Match of forward model response to data, bottom-hole shut-in pressure (BHSP, upper row) and water cut (W.C., lower row), NA, Case 3

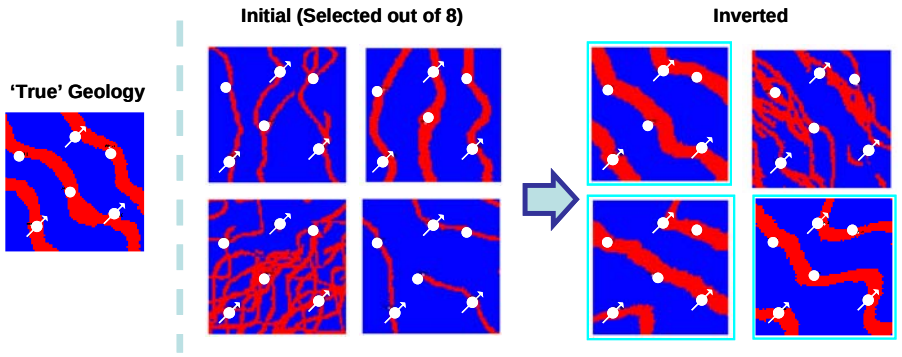

Figure 4.17: Inverted model realizations vs. reference model, initial models, NA, Case 6(The inverted models highlighted by light blue reasonably resemble to the reference model)

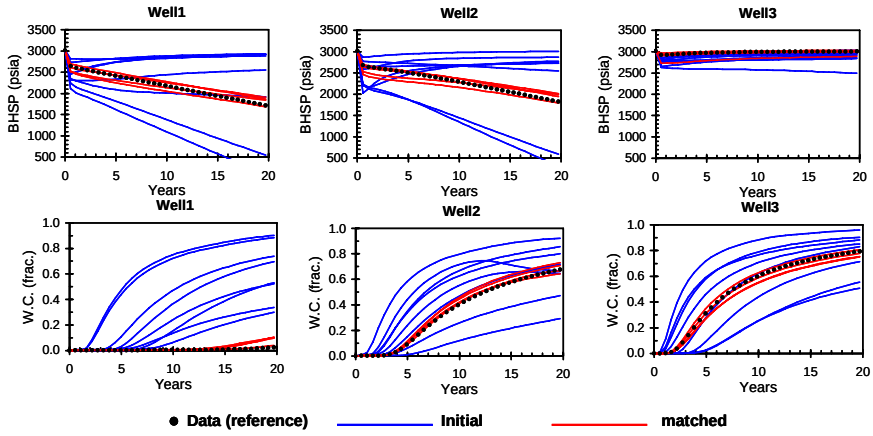

Figure 4.18: Match of forward model response to data, bottom-hole shut-in pressure (BHSP, upper row) and water cut (W.C., lower row), NA, Case 6

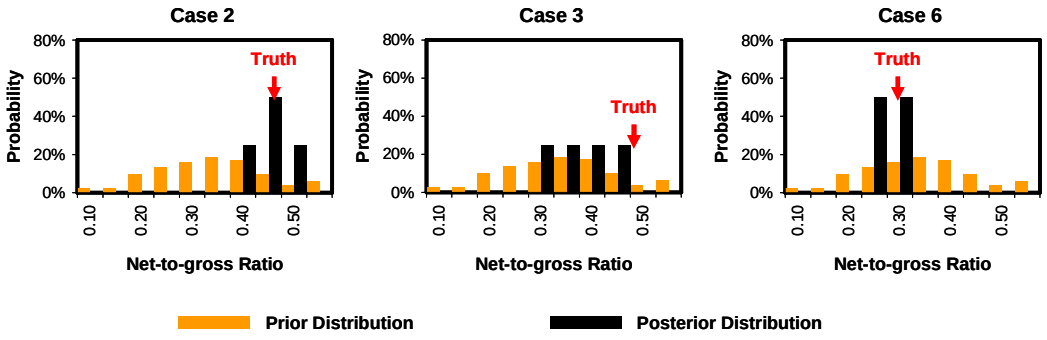

Figure 4.19: Comparison of the prior vs. posterior distribution of net-gross-ratio, NA, Cases 2, 3, and 6

As shown in Figures 4.17 and 4.19, the inverse solution reasonably identified both channel geometry and net-gross-ratio of the "true" geology in Case 6 (the case where the "true" geology provides distinct flow path between wells); i.e., 3 out of 4 model realizations sampled by the stochastic search shows similar geological feature to the "truth". Case 2 (the case with high net-to-gross ratio and clear channel direction in "true" geology) also found at least one model realization almost identical to the "truth" by the stochastic search, while the sampled model realizations still exhibit considerable uncertainty in the geological concept (Fig. 4.13). This case at least reduced the uncertainty in net-to-gross ratio (Fig. 4.19). Case 3 (the case with high net-to-gross ratio and obscured channel direction in "true" geology) failed both to reproduce the "true" geological concept (Fig. 4.15) and to reduce uncertainty in net-to-gross ratio (Fig. 4.19). These results suggest that the magnitude of the posterior uncertainty modeled by an inverse solution is strongly controlled by the characteristic of "true" geology which produces the data. If the "true" geology provides data that properly discriminates preferential flow path in subsurface, inverse solution can easily identify the geological architecture with the limited samples from posterior (e.g., Case 6, Figure 4.17). However, given that data create multiple minima in the space, the posterior distribution still exhibits large uncertainty range (e.g., Case 2, Figure 4.13), hence even stochastic search do not sample the "true" geological architecture unless plenty enough models are sampled (e.g., Case 3, Figure 4.15).

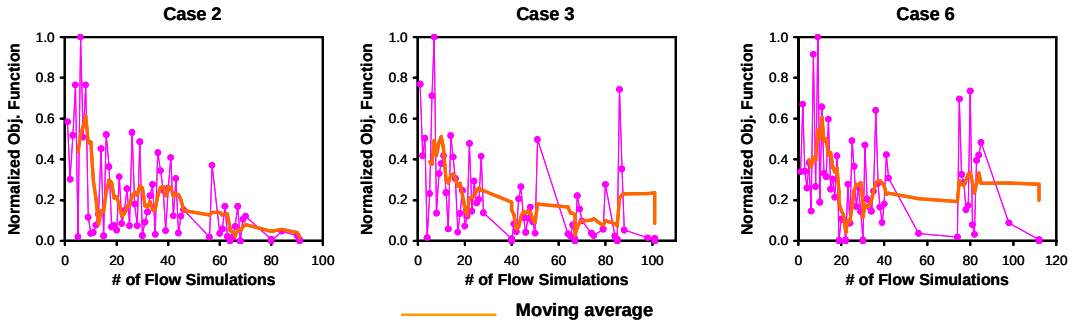

Figure 4.20: Convergence of objective function during the stochastic search, NA, Cases 2,3,6

The behavior of the misfit function (Eq. 4.4) during the iterative search is shown in Figure 4.20 for the selected cases (Cases 2, 3 and 6). As depicted, the misfit function gradually decreases during

the history matching, yet exhibiting a steep rise at some points when the search occasionally shifts to a Voronoi cell containing models with large misfit. As tabulated in Table 4.1, a history match is achieved within a reasonable number of forward model response simulations in all six cases. The term reasonable refers to the number of flow simulations that are feasible in actual real reservoir simulation involving CPU-times of several hours for a single flow simulation.

Table 4.1: Number of forward model response simulations required for stochastic search, the neighborhood algorithm (NA)

	For finding 4 history matched models	Per 1 history matched model
Case 1	69	17.25
Case 2	91	22.75
Case 3	101	25.25
Case 4	55	13.75
Case 5	53	13.25
Case 6	112	28

Tree Search

The tree search optimization is implemented by considering in the space including all of 405 facies realizations from 81 training images (Fig. 4.6); these realizations were utilized for generating the variogram in the previous section. The stochastic search is terminated after finding 4 model realizations that match historical production data. Figures 4.21, 4.23, 4.25 show the comparison of the history matched model realizations against the “true” reservoir model and the initial model realizations for the selected cases (Cases 1,4,5). The initial model realizations correspond to the realizations located on the top of the tree (in this application, the tree is branched starting from 4 models). The history matching results of these cases are presented in Figures 4.22, 4.24, 4.26. Again, the history match is achieved with sufficient accuracy in every case. In Case 1 (Fig. 4.21), where the “true geology” exhibits clear channel direction with small channel sinuosity but good connectivity, two out of four history matched realizations successfully reproduced the “true” geological scenario. Case 4 (Fig. 4.23) and Case 5 (Fig. 4.25) failed to find the “true” geological scenario due to the high sinuosity and high net-to gross ratio of channel sand. The uncertainty in net-to-gross ratio is successfully reduced in all cases (Fig. 4.27).

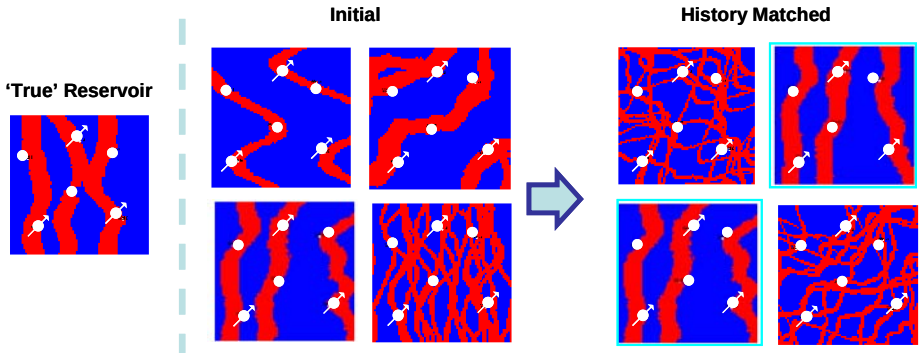

Figure 4.21: Inverted model realizations vs. reference model, initial models, Tree Search, Case 1 (The inverted models highlighted by light blue reasonably resemble to the reference model)

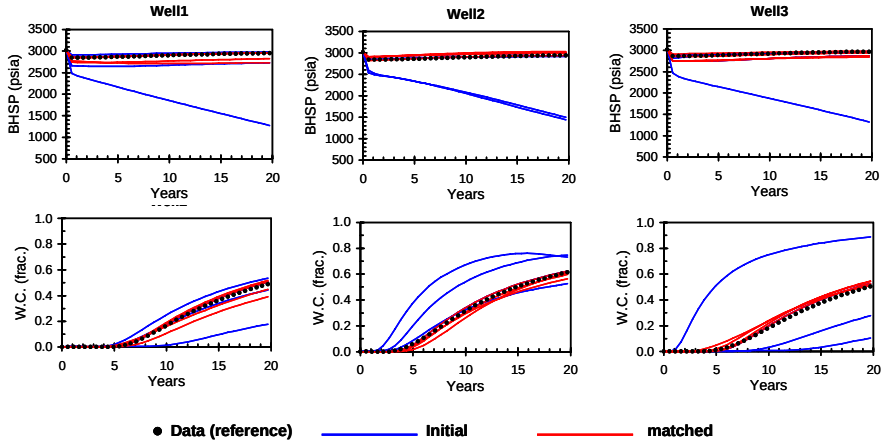

Figure 4.22: Match of forward model response to data, bottom-hole shut-in pressure (BHSP, upper row) and water cut (W.C., lower row), Tree Search, Case 1

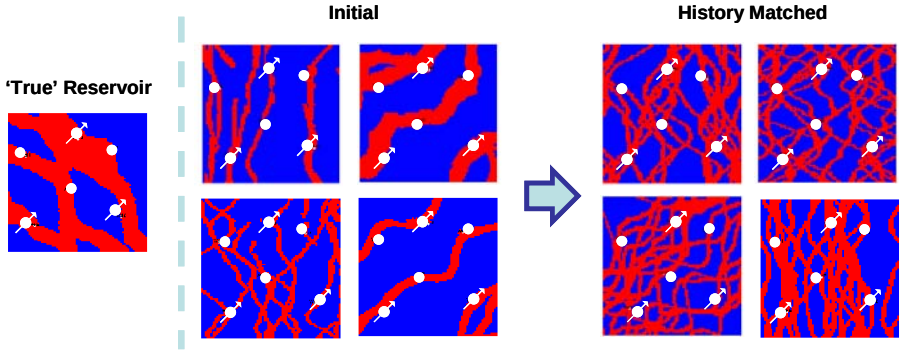

Figure 4.23: Inverted model realizations vs. reference model, initial models, Tree Search, Case 4

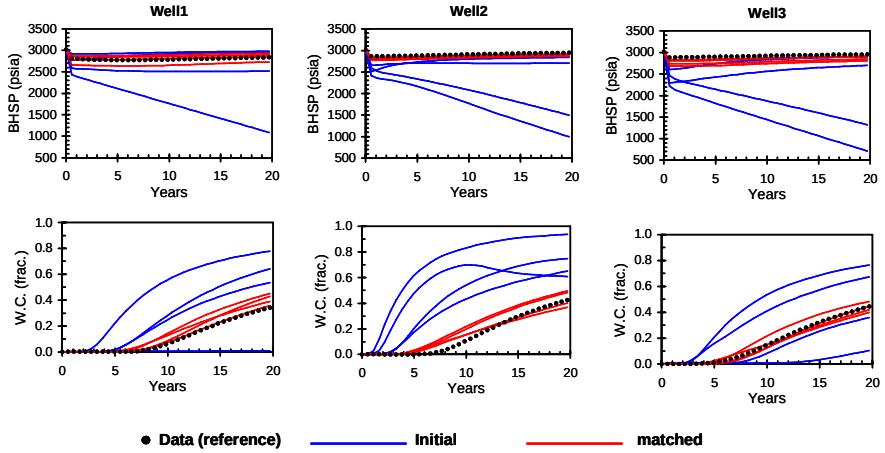

Figure 4.24: Match of forward model response to data, bottom-hole shut-in pressure (BHSP, upper row) and water cut (W.C., lower row), Tree Search, Case 4

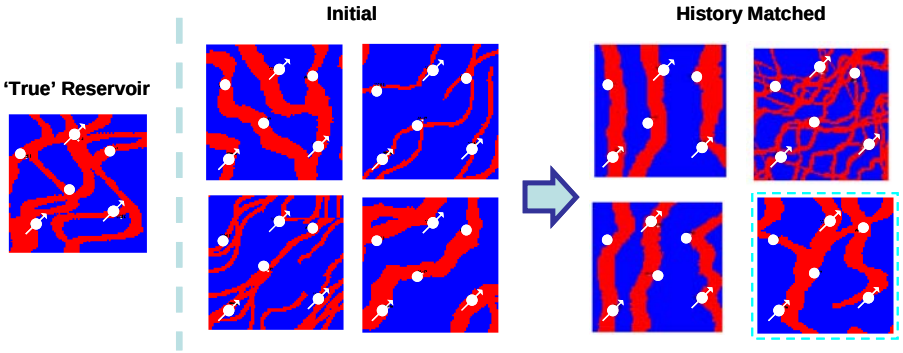

Figure 4.25: Inverted model realizations vs. reference model, initial models, Tree Search, Case 5 (The inverted model highlighted by light blue reasonably resembles to the reference model)

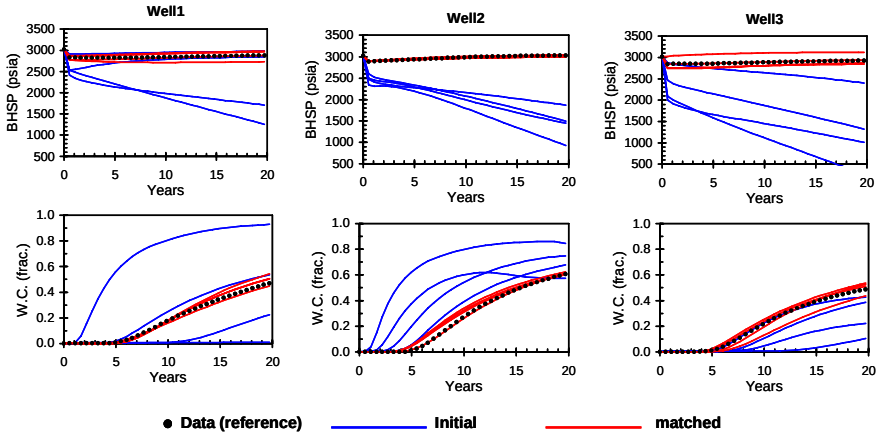

Figure 4.26: Match of forward model response to data, bottom-hole shut-in pressure (BHSP, upper row) and water cut (W.C., lower row), Tree Search, Case 5

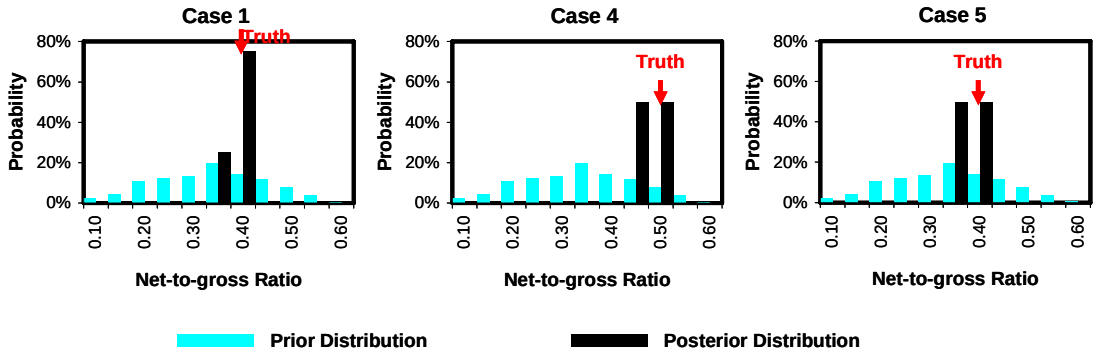

Figure 4.27: Comparison of the prior vs. posterior distribution of net-gross-ratio, Tree Search, Cases 1, 4, and 5

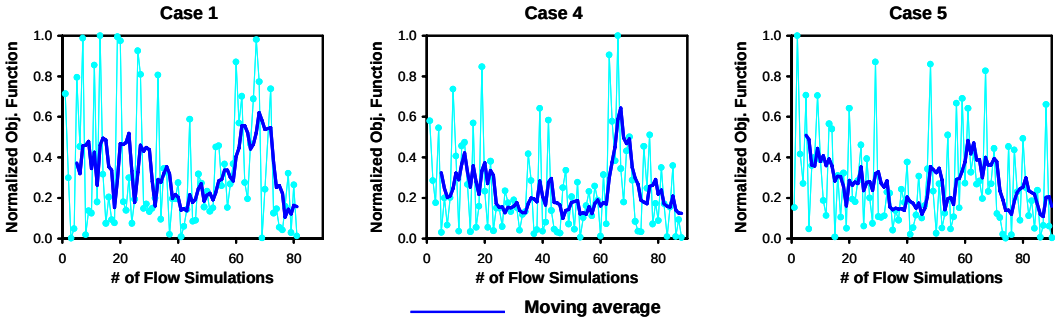

Figure 4.28: Convergence of objective function during the stochastic search, Tree Search, Cases 1,4,5

As depicted in Figure 4.28, the objective function exhibits a periodic fluctuation during the tree search optimization as the search repeatedly goes down the tree structure. In the tree search optimization, the choice of next trial for forward model response simulation is always limited to the children of the current trial, thus the search path is always restricted to the descendants of the current trial. This characteristics makes the tree search optimization less efficient compared to the Neighborhood Algorithm (NA): as shown in Table 4.2, the number of forward model response simulations required for the tree search optimization is generally larger than that of NA (Table 4.1), although they are still reasonable CPU cost. However, on the other hand, it provides a greater possibility to explore the space globally than NA.

Table 4.2: Number of forward model response simulations required for stochastic search, Tree Search

	For finding 4 history matched models	Per 1 history matched model
Case 1	81	20.25
Case 2	190	47.5
Case 3	93	23.25
Case 4	88	22
Case 5	90	22.25
Case 6	186	46.5

Chapter 5

History Matching of Reservoir Structure

In Chapter 4, a new method to parameterize geological architecture for solving an inverse problem was proposed. The significant advantage of the proposed method over the traditional parameterization is that it can accommodate any kind of geological architecture in the parameter space, hence enables the inversion of discrete parameters such as outcomes from multiple geological scenarios, allowing one to assess easily a more realistic range of prior. The application of this method is not limited to the inversion of facies models: it is also applicable for the inversion of geological structure (i.e. horizons and faults) from dynamic fluid flow response. This chapter presents the application of the proposed distance-based parameterization method to a structural uncertainty modeling problem. By utilizing the proposed methodology, the implementation of the complete workflow proposed in Chapter 1 (Figure 1.1) is demonstrated.

First, a prior structural uncertainty model depicted by multiple structural interpretations is discussed. These multiple structural interpretations can be the results from multiple migrations (Chapter 2) and the subsequent multiple seismic interpretations (Chapter 3) created as a seismic imaging uncertainty model, or they can be various structural interpretations based on a single seismic image depending on different decisions on fault/horizon identification. The aim of this prior structural uncertainty model is to provide a parameter space where a history matching exercise can take place. History matching of the reservoir structure is performed by applying the method of Chapter 4, using synthetic but real reservoir inspired examples.

5.1 Prior Structural Uncertainty Modeling

Structural uncertainty is attributed to various sources, each with a different impact on fluid flow behavior. The level of uncertainty arising from each source can be different depending on the data acquisition condition in the field (e.g. land data vs. marine data, two-dimensional or three-dimensional seismic, type of deposition environment, availability and accuracy of well correlations, availability of production data, etc.), the subsurface heterogeneity, and the complexity of the reservoir geometry. For example, land data generally provides poorer seismic data than marine data. The error in horizon positioning or time-to-depth conversion can be marginal if the wells are densely and evenly drilled over the entire field. The uncertainty in gross thickness can be affected by whether the wells are penetrating the entire reservoir interval. Also, if production data used for fault identification is available, uncertainty in fault pattern may be reduced.

Although it is difficult to set general rules, a typical example of hierarchy in structural uncertainty is suggested in Figure 5.1, assuming poor seismic data and limited availability of well markers/production data. Each component of uncertainty appearing in Figure 5.1 is explained as below:

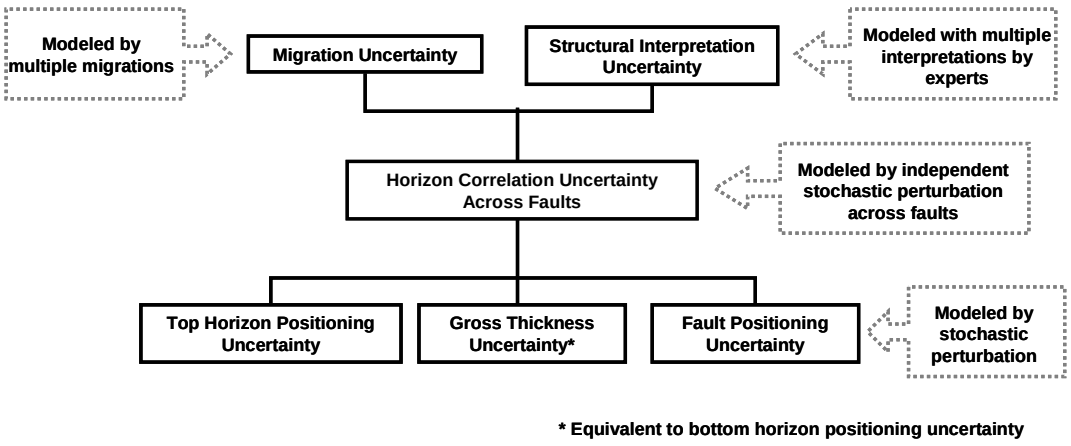

Figure 5.1: Typical example of hierarchy in structural uncertainty

Migration Uncertainty

Structural uncertainty resulting from uncertain migration can be a first order structural uncertainty especially when seismic data is of poor quality (i.e. large uncertainty in velocity analysis from seismic gathers) or when the lateral heterogeneity of subsurface velocity field is significant (i.e. multiple possible velocity fields from seismic inversion). In such situation, multiple seismic images migrated using different velocity models can produce significantly different structural interpretations that exhibit different fault patterns, appearance or disappearance of faults depending on which seismic image is considered. This uncertainty can be modeled using methods proposed by Clapp (2001, 2003; see Chapter 2 for the discussion) or Grubb et al. (2001).

Structural Interpretation Uncertainty

With poor seismic data, a single seismic image can produce considerably different structural interpretations depending on the different decisions made on horizon/fault identification (Rivenæs et al., 2005). Such an uncertainty from structural interpretation can be first order, especially when the structure is complex, since multiple interpretations can exhibit significant difference in fault intensity and fault pattern which may strongly affect fluid flow behavior. This uncertainty is modeled by providing multiple possible alternatives of structural interpretations.

Horizon Correlation Uncertainty Across Faults

Correlating horizons across a fault can be difficult unless well markers are available on both side of the fault, since a “wrong” pair of reflectors can be picked as indicating the same horizon (Rivenæs et al., 2005). An erroneous horizon identification would lead to misinterpreting the fault throw, which would result in a wrong determination of flow communication between fault compartments. Ideally, this uncertainty should be modeled by providing multiple structural interpretations which covers every possible horizon identification. However, such a modeling is too time-consuming since this process requires expert decisions and manual handling which can not be easily automated. An alternative method is to stochastically perturb a horizon discontinuously across the fault, focusing only on the modeling of the uncertainty in fault throw. This method is practical because such modeling is fast and inexpensive. Although the multiple structural models generated by stochastic perturbation of a horizon do not perfectly honor the different alternative horizon picks, this inaccuracy is of marginal importance since the impact of

the horizon position on fluid flow is usually smaller than that of the fault throw (if the fault is not completely sealing).

Top Horizon Positioning Uncertainty

The uncertainty in horizon position is attributed to 1) the error in horizon picking due to low seismic resolution, and 2) time-to-depth conversion error. The uncertainty range associated with the former can be evaluated from the thickness of reflectors (after time-to-depth conversion). The uncertainty due to the latter is evaluated by analyzing the match between seismic and well depths (Charles et al., 2001), depth maps resulting from several conversion techniques (Corre et al, 2000), or the depth of a flat spot (Corre et al, 2000; Charles et al., 2001). The magnitude of uncertainty varies locally depending on the distance from well markers. The uncertainty due to horizon positioning is considered to be of lower order importance compared to the uncertainty resulting from migration, interpretation (i.e. decision on fault/horizon identification), and horizon correlation across faults, in both terms of magnitude and impact on fluid flow. However, a typical exception is found in reservoirs with a gently dipping flank accompanied with an aquifer: in such reservoirs, a small error in top horizon positioning (often due to the time-to-depth conversion) can significantly affect the estimation of oil in-place or the prediction of water encroachment to producers coming from the aquifer. This situation arises since wells are preferentially drilled at the crest of the reservoir (unless the oil is recovered by water injection from an aquifer). Thus the reservoir structure is often uncertain near the aquifer unless sufficient delineation wells are drilled at the appraisal stage. The uncertainty in top horizon depth is stochastically modeled by perturbing a horizon position obtained from interpretation, using a spatially correlated perturbation magnitude (Samson et al., 1996).

Gross Thickness Uncertainty

The uncertainty in gross thickness is modeled by fixing the top horizon depth, and perturbing the bottom horizon from the interpretation using a spatially correlated perturbation magnitude (JACTA™/GOCAD[1]; Samson et al., 1996; Corre et al, 2000; Charles et al., 2001). Thus this uncertainty is equivalent to the uncertainty in the positioning of the bottom horizon. The magnitude of uncertainty is evaluated in the same manner as done for the top horizon. However,

[1] Geo-modeling software released by Earth Decision Science.

the range of uncertainty is upper-bounded by the reservoir thickness. This uncertainty is also considered to be of lower order. The impact of gross thickness uncertainty is mostly felt in the pressure behavior.

Fault Positioning Uncertainty

The magnitude of uncertainty related to fault positioning depends on the resolution of the seismic image, thus its magnitude is evaluated from a visual inspection of the seismic image. This uncertainty is also of lower order importance compared to the uncertainty related to the fault identification or the uncertainty in fault throw. However, in case some wells are located close to a fault, a small perturbation of the fault position can strongly affect the production behavior.

The first order uncertainties (migration uncertainty, structural interpretation uncertainty) located at the top of the hierarchy in Figure 5.1 are modeled by providing multiple structural models based on expert interpretations. The lower order uncertainties (smaller scale uncertainty) are modeled by stochastically perturbing horizons and faults from the interpretation. The stochastic perturbation of horizons can be implemented using JACTA^{TM}/GOCAD (Samson et al., 1996; Corre et al, 2000; Charles et al., 2001). Faults are stochastically perturbed using a method of Zhang and Caumon (2006).

The structural uncertainty modeling tool in JACTA^{TM} (Samson et al., 1996; Corre et al, 2000; Charles et al., 2001) is designed to perturb the depth of a horizon by directly deforming a stratigraphic grid (i.e. corner point geometry grid which can be used for flow simulation) which is built from a structural model. The magnitude of the perturbation at each grid node on the horizon surface is modeled with a spatially correlated perturbation field which is stochastically simulated using geostatistical technique. JACTA^{TM} (Samson et al., 1996; Corre et al, 2000; Charles et al., 2001) uses p-field simulation (Srivastava, 1992) for modeling the perturbation field. This perturbation field can vary spatially in accordance with the regional variation of uncertainty range; e.g. a large uncertainty range at a fault block without well markers and smaller uncertainty range at a fault block with wells. When perturbing a top horizon, the stratigraphic grid is deformed such that the displacement specified by the perturbation field is applied to all grid layers. When perturbing gross thickness, the specified displacement is applied to the bottom horizon of the stratigraphic grid, while the top horizon depth is frozen. The internal grid layers are displaced proportionally between the top and bottom horizons. The horizon depth at well markers is honored

by conditioning the perturbation field to zero at the well marker locations. If the perturbation field is simulated continuously across the faults, the horizons are perturbed continuously over the entire grid. If the perturbation field is modeled as discontinuous across the fault, the horizon is perturbed independently at the both side of the fault, allowing the modeling of uncertainty in fault throw.

The fault network geometry perturbation method of Zhang and Caumon (2006) is also designed to directly deform a stratigraphic grid. Similarly to the horizon perturbation, the magnitude of the perturbation of a fault surface is provided as a geostatistically simulated perturbation field for each fault surface. The stratigraphic grid is deformed such that the specified perturbation magnitude is honored at the fault surfaces. This deformation takes place under constraints in order for such deformation not to destroy the grid structure. The perturbation also changes the horizon shape: however, the horizon depth at well markers is honored by freezing the displacement at grid blocks penetrated by wells.

The prior structural uncertainty is modeled by creating a large set of structural models, consisting of hundreds of realizations, hierarchically by the following steps:

1. The modeling starts by providing multiple structural models either from 1) structural interpretations based on the multiple seismic images migrated using several velocity models, or 2) multiple structural interpretations from a single seismic image with different decisions on fault/horizon identification. The stratigraphic grids are built for each structural model.

2. For each of the structural models in step 1, a subset of structural models is generated by considering uncertainty on horizon correlation (fault throw uncertainty). This is implemented by perturbing the top horizon of the stratigraphic grids from step 1 using the stochastic perturbation field which is simulated discontinuously across the fault.

3. The uncertainty on the top horizon position is modeled by perturbing the top horizon of each stratigraphic grid generated in step 2. This time, a continuous perturbation field over the entire grid is used.

4. The gross thickness of each stratigraphic grid generated in step 3 is perturbed using a continuous perturbation field.

5. The fault surfaces of the stratigraphic grid generated in step 4 is perturbed.

The range of perturbation at each step is decided based on the uncertainty range inferred from data, and can be different depending on the reservoir case at hand. The resulting large set of structural models represents a parameter space in which subsequent history matching takes place.

5.2 History Matching

History matching of reservoir geometry is implemented using the method proposed in Chapter 4. As discussed in Chapter 4, the choice of the distance function is crucial for the effective stochastic search. Near-neighbor search methods such as the neighborhood algorithm (NA) or tree search rely on the similarity of production response from the model realizations in the same neighborhood. In other words, the production response should be spatially correlated in the space provided with a particular distance function. The choice of the distance function can be problem dependent. However, once a proper distance function is found for a particular problem, it can be applied to the problem of the same type. Such a distance function can be selected by testing its applicability through a numerical experiment using a synthetic data set typical to the type of the problem in question, i.e., structural modeling in our case.

The use of Hausdorff distance (Appendix A) is proposed to parameterize the space for inverting structural models. In order to calculate the Hausdorff distance between a pair of structural models, the geometry of each reservoir model is represented as a point set as depicted in Figure 5.2. This point set is generated by extracting the corner points of the stratigraphic grid belonging to the top and bottom horizon surfaces of the structure (Fig. 5.2). Figure 5.3 shows similarity distance calculations between some example structural models. As shown in the figure, the Hausdorff distance reasonably captures the similarity (or dissimilarity) of the reservoir geometry between the models. In order to reduce CPU cost for distance calculation, an efficient tree search technique (Octree) is utilized; otherwise, the computation cost can be expensive. Later in the next section, it is also shown that the Hausdorff distance correlates with the difference in production response using a synthetic set of structural models.

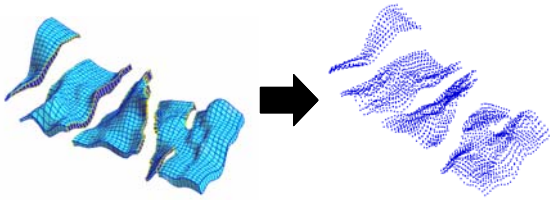

Figure 5.2: Representation of reservoir geometry as a point set

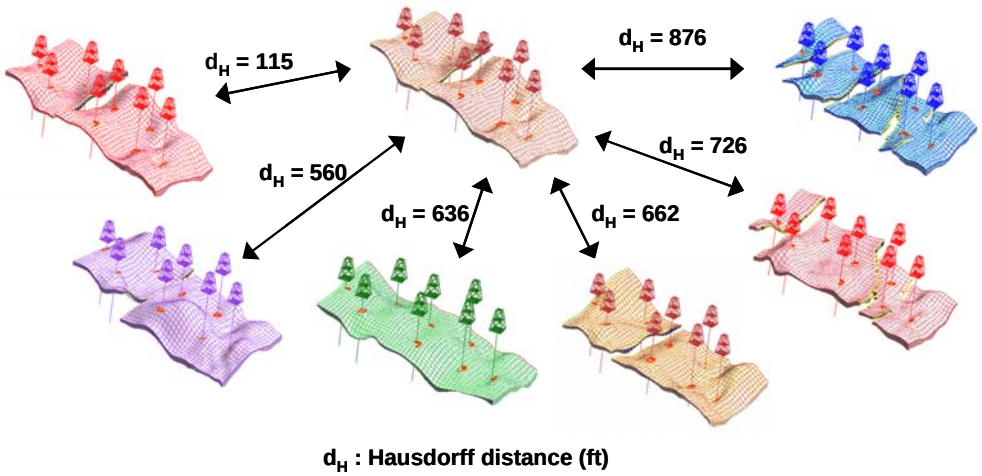

Figure 5.3: Examples of Hausdorff distance between structural models

5.3 Synthetic Reservoir Applications

Synthetic case studies are conducted to demonstrate the applicability of the proposed method. First, an application example is shown using single layer models with homogeneous petrophysical properties (Case A). The purpose in this first example is to test the robustness of the methodology, mainly in terms of convergence efficiency. Therefore, in this case, exaggerated uncertainty ranges are used. The applicability of the Hausdorff distance to structural modeling problems is also tested in this case. Then, we apply the method to a more realistic synthetic reservoir example which is built based on actual geological settings (Case B).

5.3.1 Case A

5.3.1.1 Prior Structural Uncertainty Modeling

The prior structural uncertainty is modeled considering the uncertainty in 1) geological interpretation (fault or no fault), 2) position of top horizon, 3) gross thickness and 4) the position of faults. The total of 400 prior structural models are built by:

1) 4 different interpretations: w/ 3 faults, 2 faults, 1 fault and no fault

2) 5 different perturbations of top horizons for each of the models from step 1: uncertainty range = 150 m

3) 5 different perturbations of bottom horizons for each of the models from step 2: uncertainty range = 20 m

4) 5 different perturbations of fault locations for each of the models from step 3: uncertainty range = 150 m

The models with different interpretations are depicted in Figure 5.4. As shown in the figure, the variation of the structural geometry due to the different interpretations is exaggerated: i.e. the reservoir compartmentalization would be informed by the production data to some extent in realistic situations, thus it is unlikely that interpreter provides a model where the reservoir is completely partitioned by 3 faults (M1H1G0F0 in Fig. 5.4) and a model without fault (M4H1G0F0 in Fig. 5.4). However, since the purpose of Case A is to test the proposed methodology, this exaggerated uncertainty is adopted. Models generated by a stochastic perturbation of the top horizon based on a single interpretation are shown in Figure 5.5. In this case, the top horizon depth is stochastically perturbed using a discontinuous perturbation field across the faults (if the model includes faults), thus it accounts for the uncertainty related to the horizon correlation (fault throw uncertainty). As shown in Figure 5.5, the fault blocks exhibits connection and disconnection depending on the perturbation of the top horizon. For an interpretation that does not include a fault, this perturbation models the uncertainty related to horizon positioning. Figure 5.6 shows the structural models generated by perturbing gross thickness from a single model. Since the average reservoir thickness is approx. 30 m in this reservoir, the uncertainty range in gross thickness is set to 20 m, which leads to a smaller perturbation of the bottom horizon compared to that of the top

horizon (uncertainty range = 150 m). Figure 5.7 depicts the models generated by the lateral perturbation of faults from a single model. As shown Figures 5.4 ~ 5.7, the depth of top and bottom horizons are honored at the well markers.

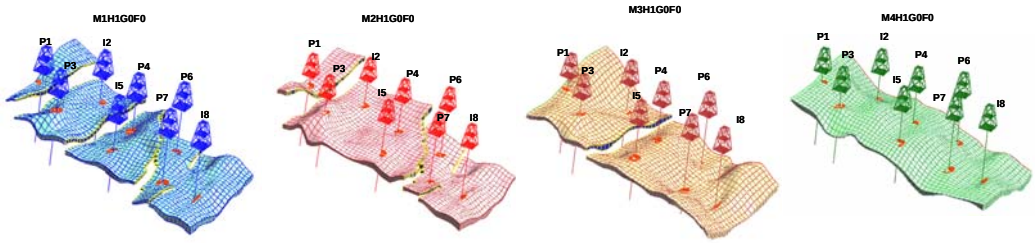

Figure 5.4: Structural models from different interpretation, Case A

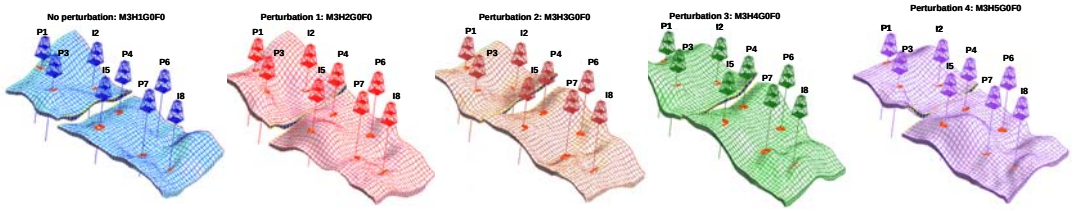

Figure 5.5: Structural models generated by the stochastic perturbation of top horizon from the same interpretation, Case A

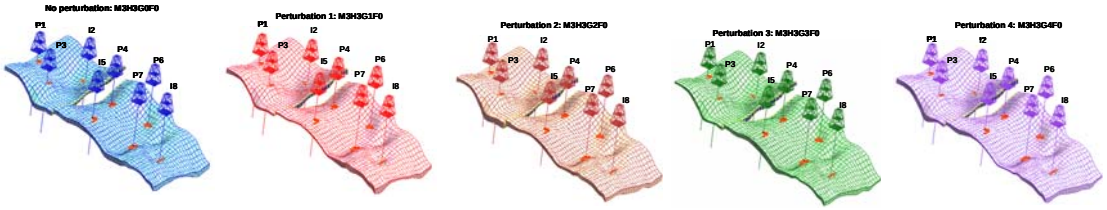

Figure 5.6: Structural models generated by the stochastic perturbation of gross thickness from the same model, Case A

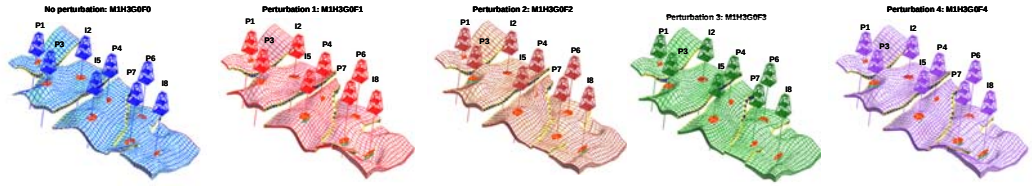

Figure 5.7: Structural models generated by the stochastic perturbation of fault position from the same model, Case A

The similarity distance (Hausdorff distance) is calculated for every pair of 400 structural models in the prior uncertainty set and the distance matrix is constructed. CPU time for calculating the distance matrix was 18.4 min. An efficient tree search technique (Octree) is utilized to reduce CPU cost for calculating the Hausdorff distance (otherwise, the matrix construction requires 3.6 hours).

In this synthetic application study, flow simulations are run for all reservoir models retained in the parameter space, in order to confirm that the pseudovariogram of the production data actually shows structure in the parameter space defined by the Hausdorff distance. The water flooding performance is simulated for 10 years with 5 producers (P1, P3, P4, P6, P7) and 3 injectors (I2, I5, I8) (see Figs. 5.4~5.7 for well locations). The constant porosity and permeability are specified. The model is an undersaturated reservoir (no gas cap) with an oil-water contact at the depth of 2540m, located between wells P7 and I8. The flow simulation is performed with fixed oil rate and water injection rate, and bottom-hole shut-in pressure (BHSP) and water cut (W.C.) are recorded. The pseudovariograms of production data are computed for the misfits of water cut, shut-in pressure, and the total misfit (i.e. BHSP + water cut) and are depicted in Figure 5.8. The total misfit is calculated by weighting each of the water cut misfit and pressure misfit using the inverse of error variance. The error variance is specified as $(2\%)^2$ for water cut, and $(100 \text{ psi})^2$ for pressure, based on the desired history matching accuracy. As shown in the figure, the pseudovariogram of production data exhibits clear structure. A Gaussian-type structure with some nugget is observed at the distance less than 300 ft. This part of the variogram is mostly attributed to the perturbation of gross thickness and the perturbation of fault location. This small scale perturbation may affect production response if the perturbation occurs near a well. However, if the structure is perturbed far from the wells, the perturbation would have almost no impact on the flow. Thus many of the misfit functions, if not all, evaluated between the models separated by this small similarity distance

are almost zero depending on the location where the stochastic perturbation took place, resulting in a low variogram at this scale of the similarity distance.

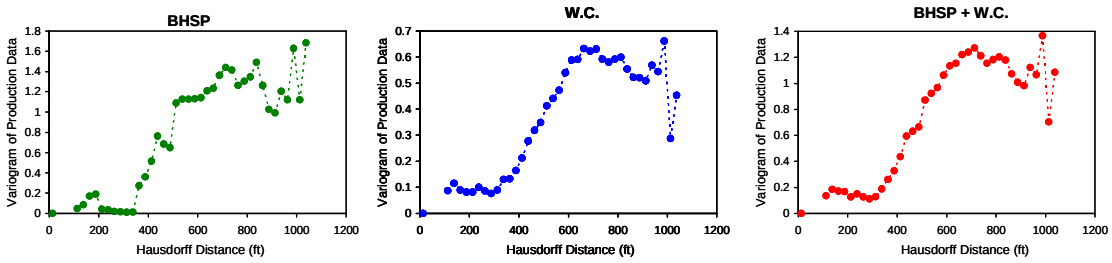

Figure 5.8: Variogram of production data (standardized), Case A

5.3.1.2 Case Setting

Stochastic search is performed in the constructed parameter space, using 1) the neighborhood algorithm (NA) and 2) tree search. 6 cases are considered by selecting a reference model (considered as a "true" reservoir) from a set of prior uncertainty models for each case. This is an ideal case where it is known that the parameter space is large enough to span the structural uncertainty and include the real reservoir. Figure 5.9 depicts the reference structural models used for Cases A1 ~ A6. History matching is performed by including a reference model in the parameter space. The petrophysical parameters are fixed for simplicity. Bottom-hole shut-in pressure (BHSP) and water cut (W.C.) are simulated for 10 years by fixing oil production rate and water injection rate, and matched to the history (i.e. reference production data).

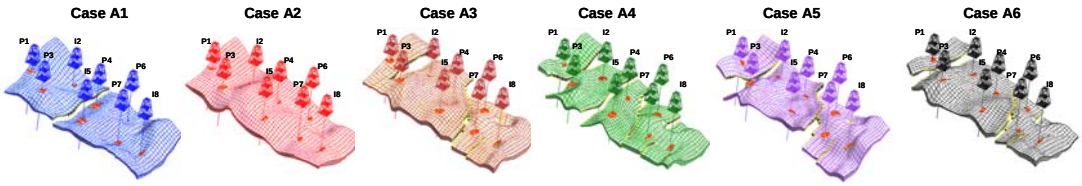

Figure 5.9: Reference structural geometries, Case A

The number of reservoir models that can achieve history match to each reference model is known in advance in this synthetic case, since all prior models are already flow simulated for generating the variogram. Therefore, the target number of history matched models to be found by the stochastic search in each case is specified as tabulated in Table 5.1:

Table 5.1: Number of reservoir models known to match production history

	# of models in parameter space that matches history	Target # of history matched models to be found by stochastic search
Case A1	14	4
Case A2	10	4
Case A3	5	4
Case A4	3	3
Case A5	2	2
Case A6	1	1

From the table, it is predicted that the history matching is easier in Cases A1~2, and more difficult in Cases A3~A6.

5.3.1.3 Results

Neighborhood Algorithm (NA)

The history matched structural models found in Cases A1~6 are compared to the reference model and the initial models chosen to start the neighborhood algorithm (NA) in Figures 5.10, 5.12, 5.14, 5.16, 5.18, 5.20. The stochastic search is started from 10 initial models in each of these cases. The history matching results are shown in Figures 5.11, 5.13, 5.15, 5.17, 5.19, 5.21 together with the simulated performance of the initial models.

As depicted in the figures, a satisfactory match of production data is achieved in every case (Figs. 5.11, 5.13, 5.15, 5.17, 5.19, 5.21). The structural models that achieved history match exhibit almost identical structural geometry to the reference model in all cases except Case A2 (Figs.5.10, 5.12, 5.14, 5.16, 5.18, 5.20). As shown in the figures, the difference between the history matched models and reference model is either in gross thickness or in fault position. In Case A2 (Fig. 5.12), where

the reference model does not include any faults, a history match is also obtained with models which have a single fault with flow communication between fault blocks.

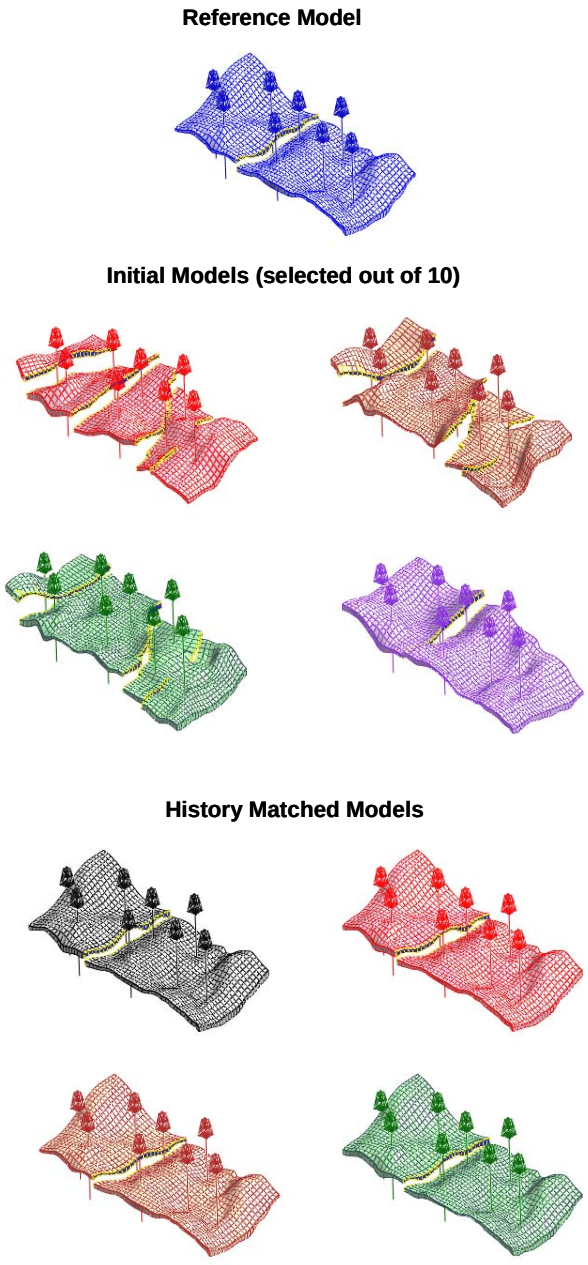

Figure 5.10: History matched structural models vs. reference model, initial models, NA, Case A1

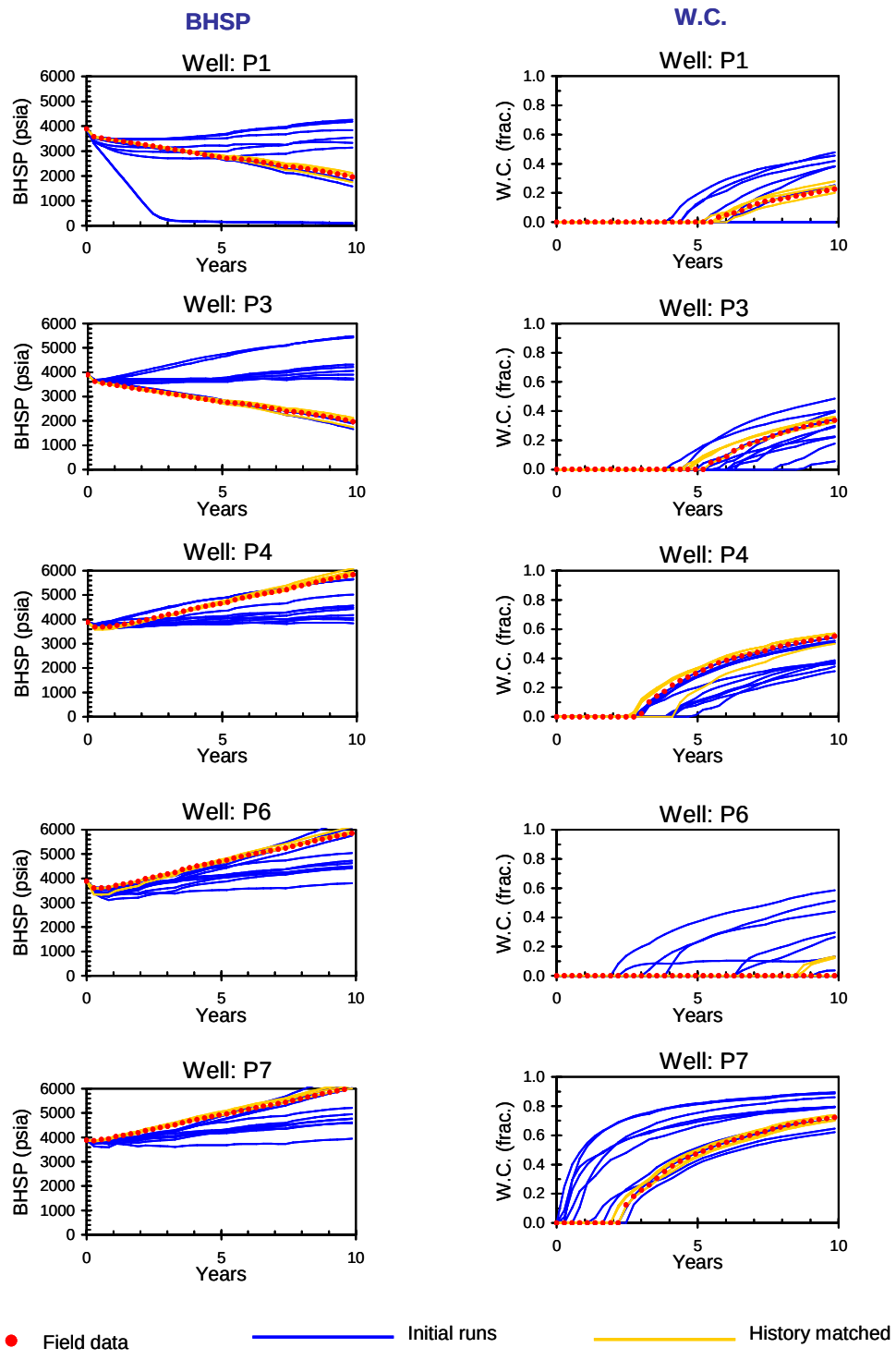

Figure 5.11: History matching result, NA, Case A1

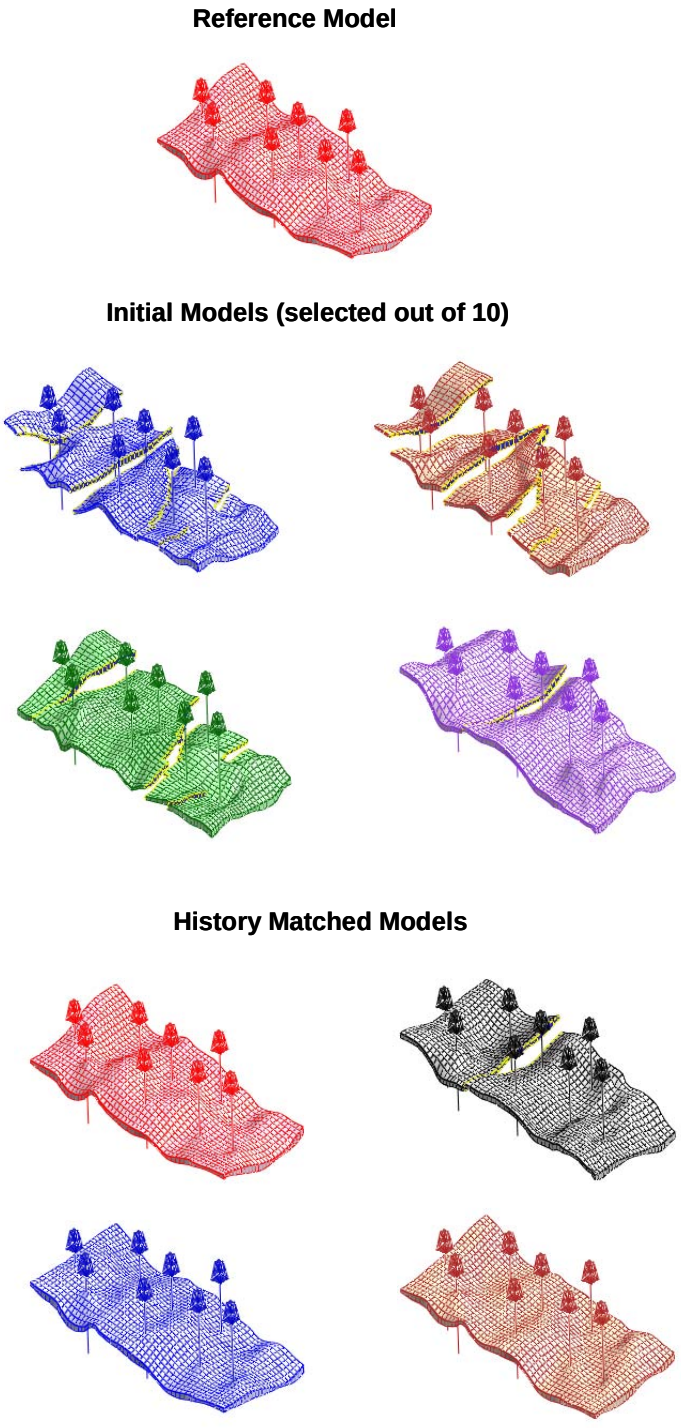

Figure 5.12: History matched structural models vs. reference model, initial models, NA, Case A2

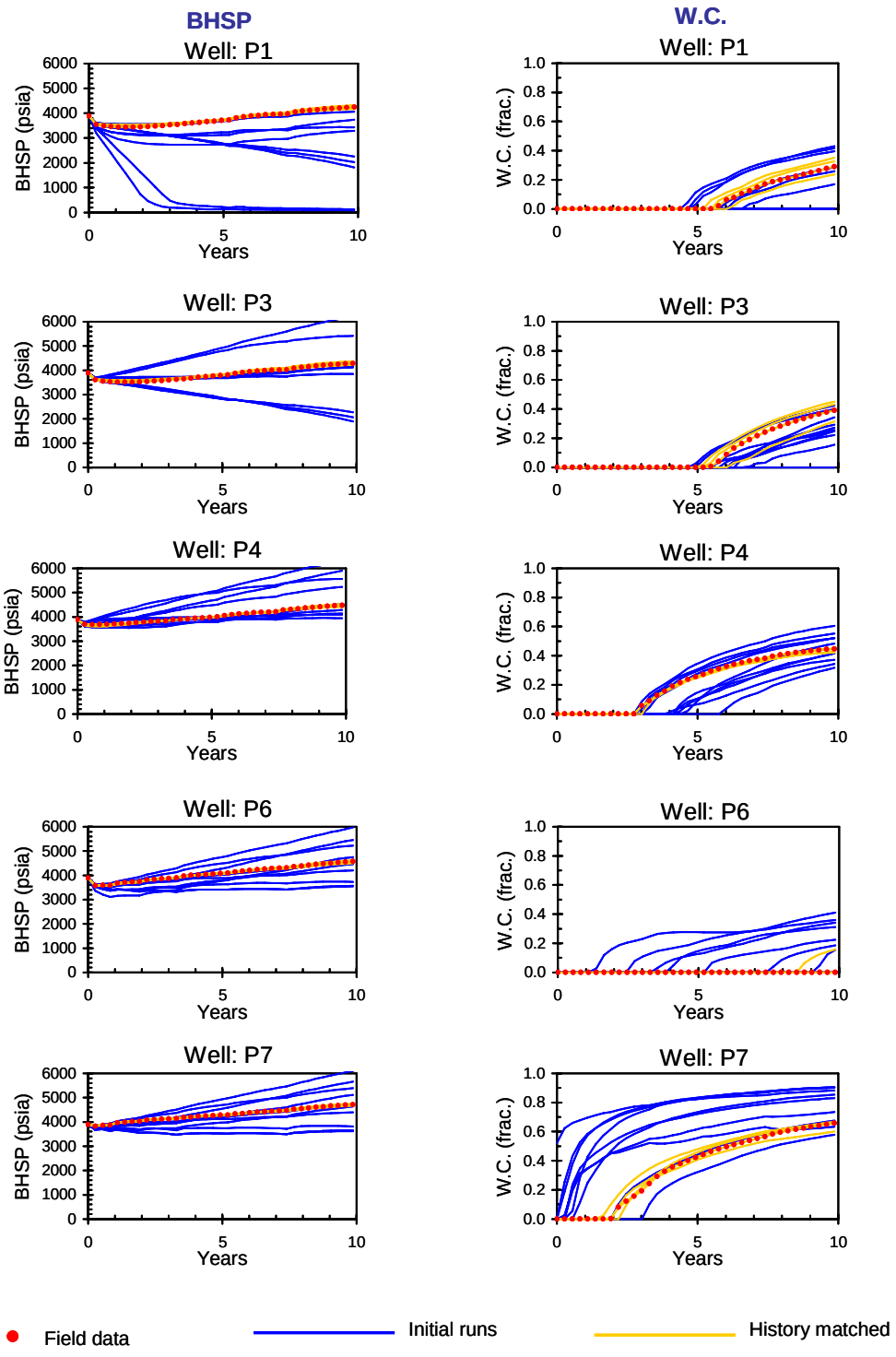

Figure 5.13: History matching result, NA, Case A2

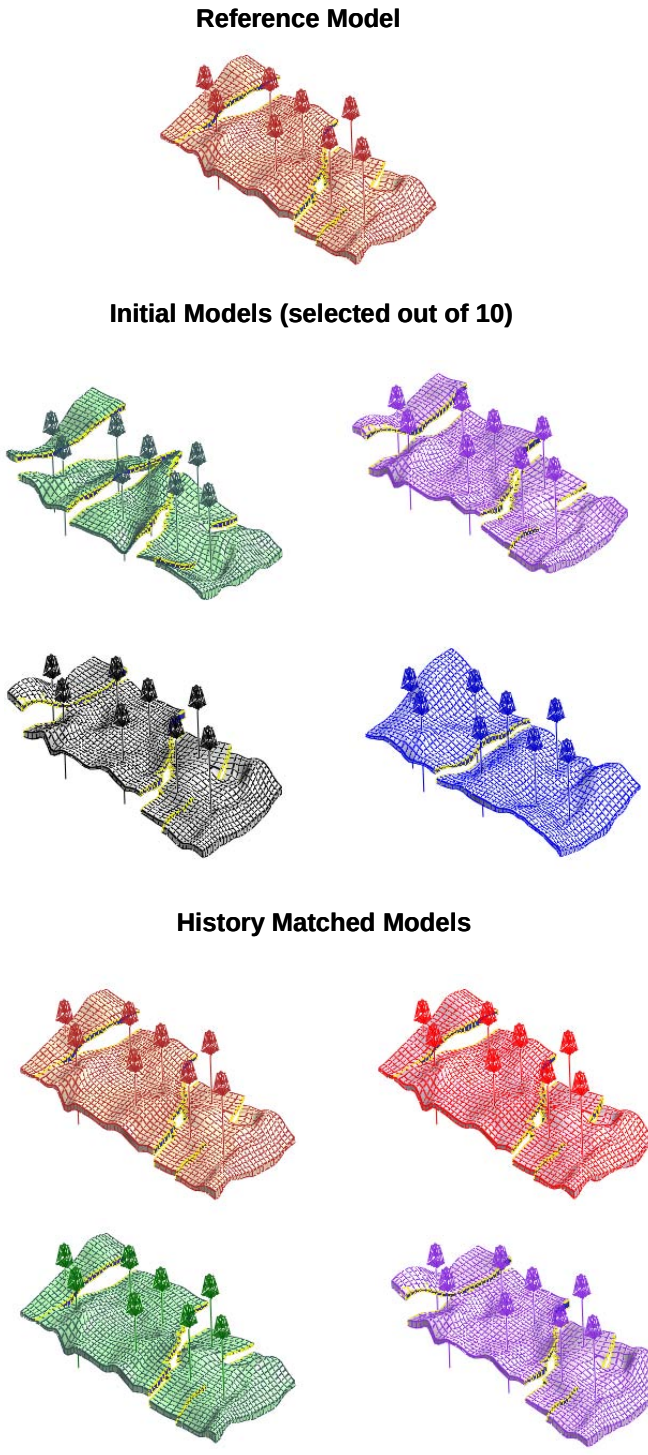

Figure 5.14: History matched structural models vs. reference model, initial models, NA, Case A3

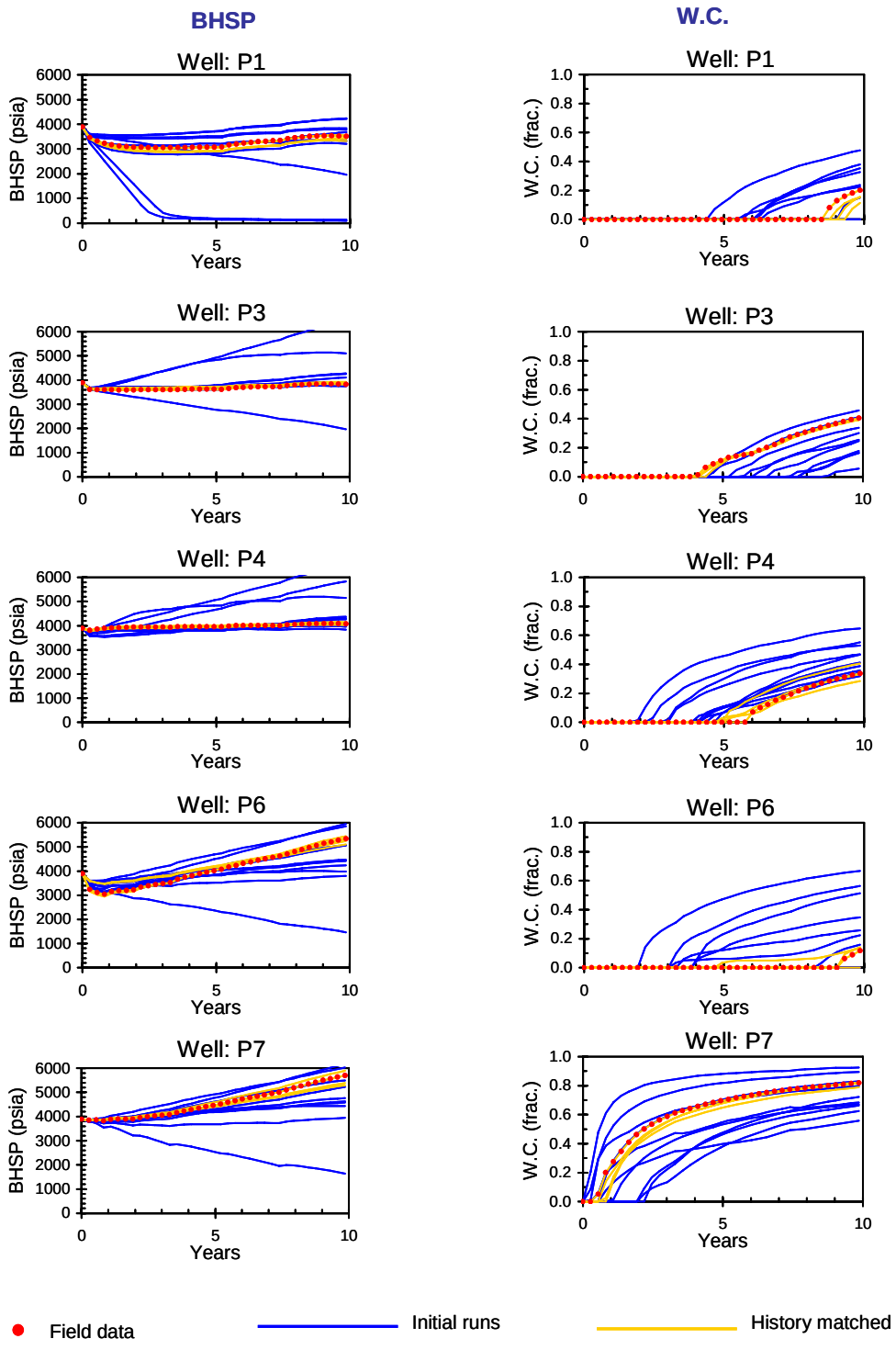

Figure 5.15: History matching result, NA, Case A3

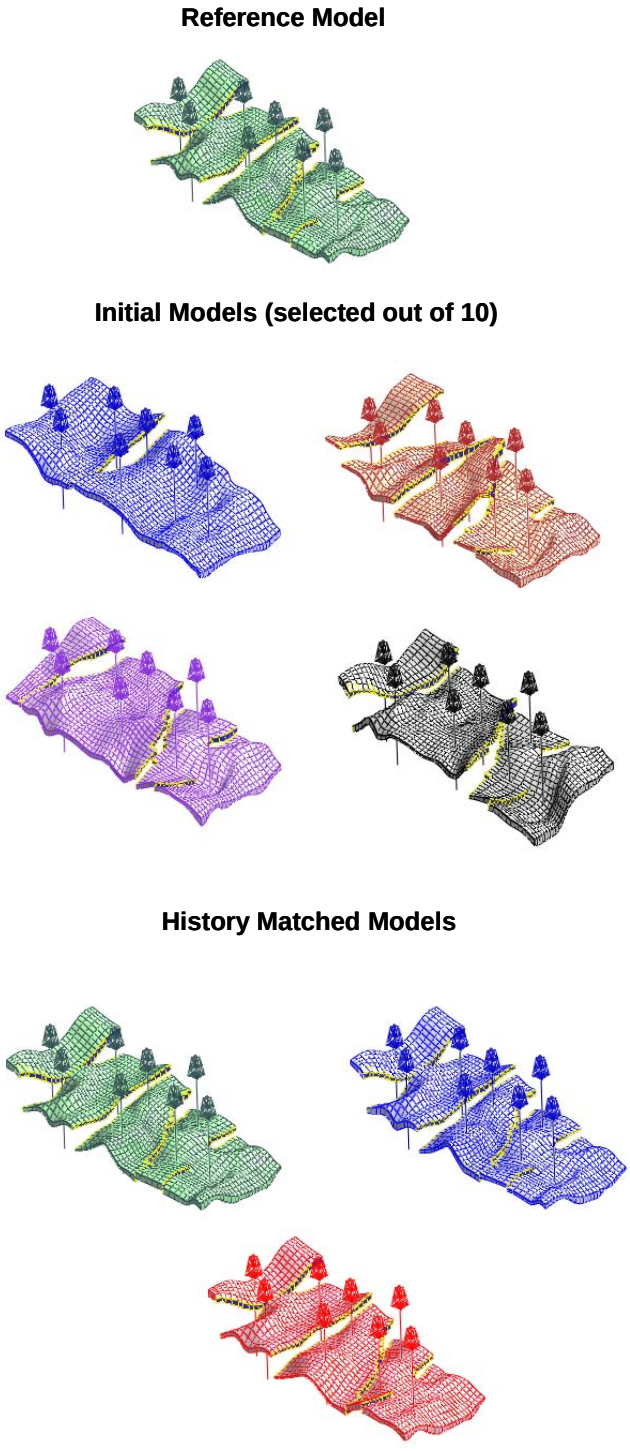

Figure 5.16: History matched structural models vs. reference model, initial models, NA, Case A4

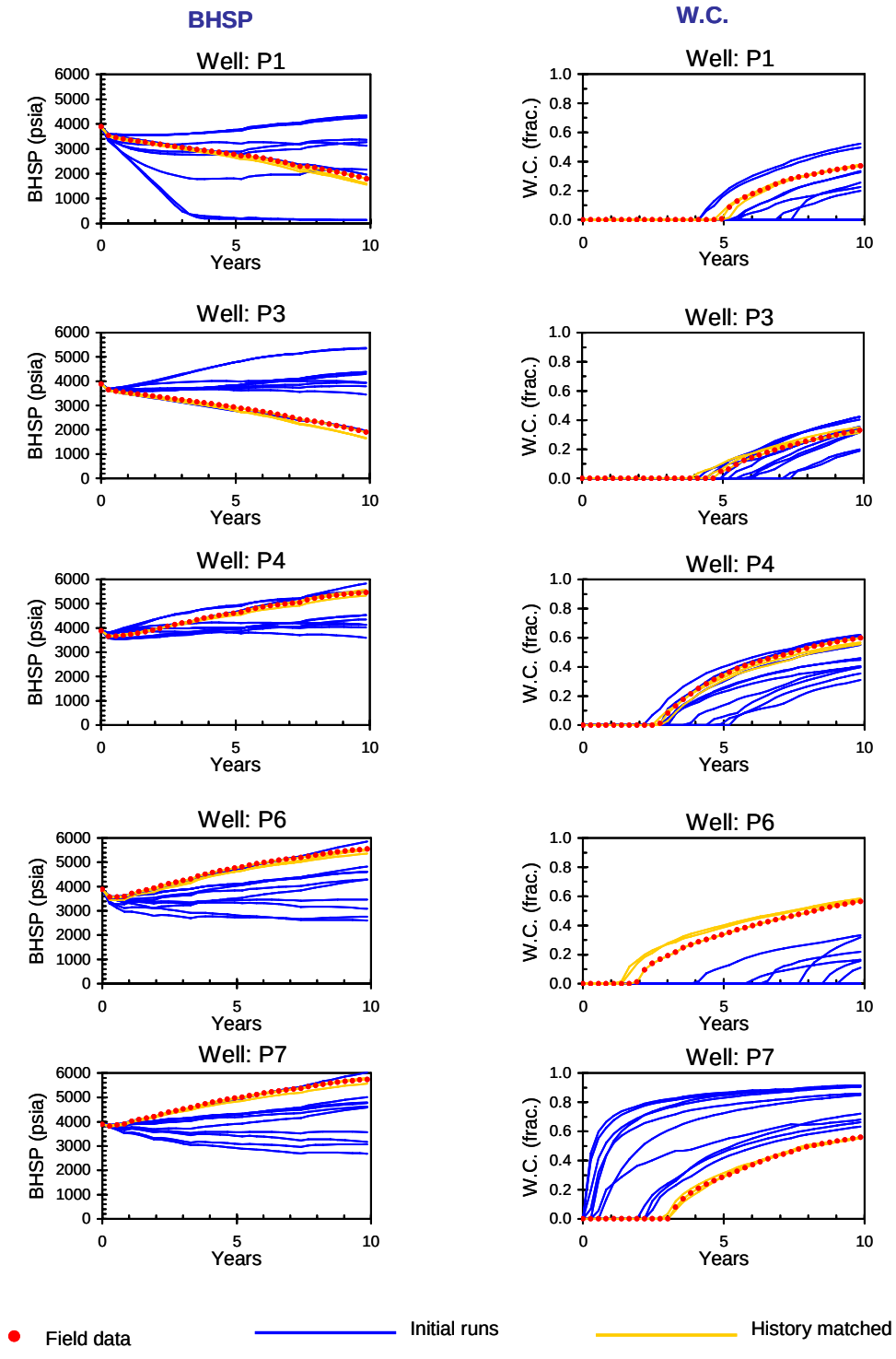

Figure 5.17: History matching result, NA, Case A4

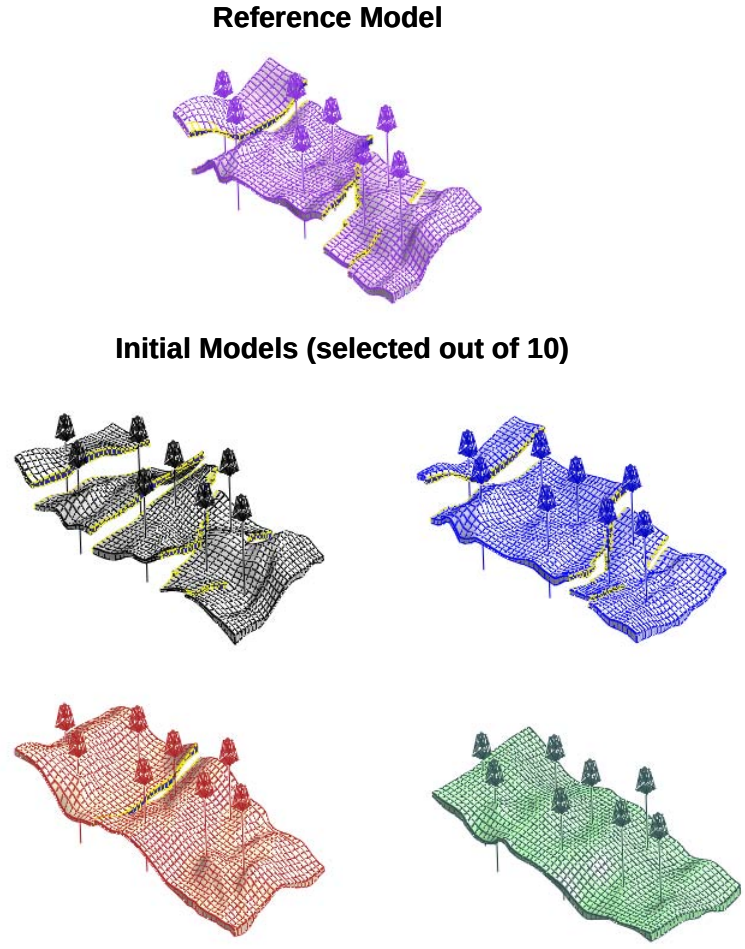

Figure 5.18: History matched structural models vs. reference model, initial models, NA, Case A5

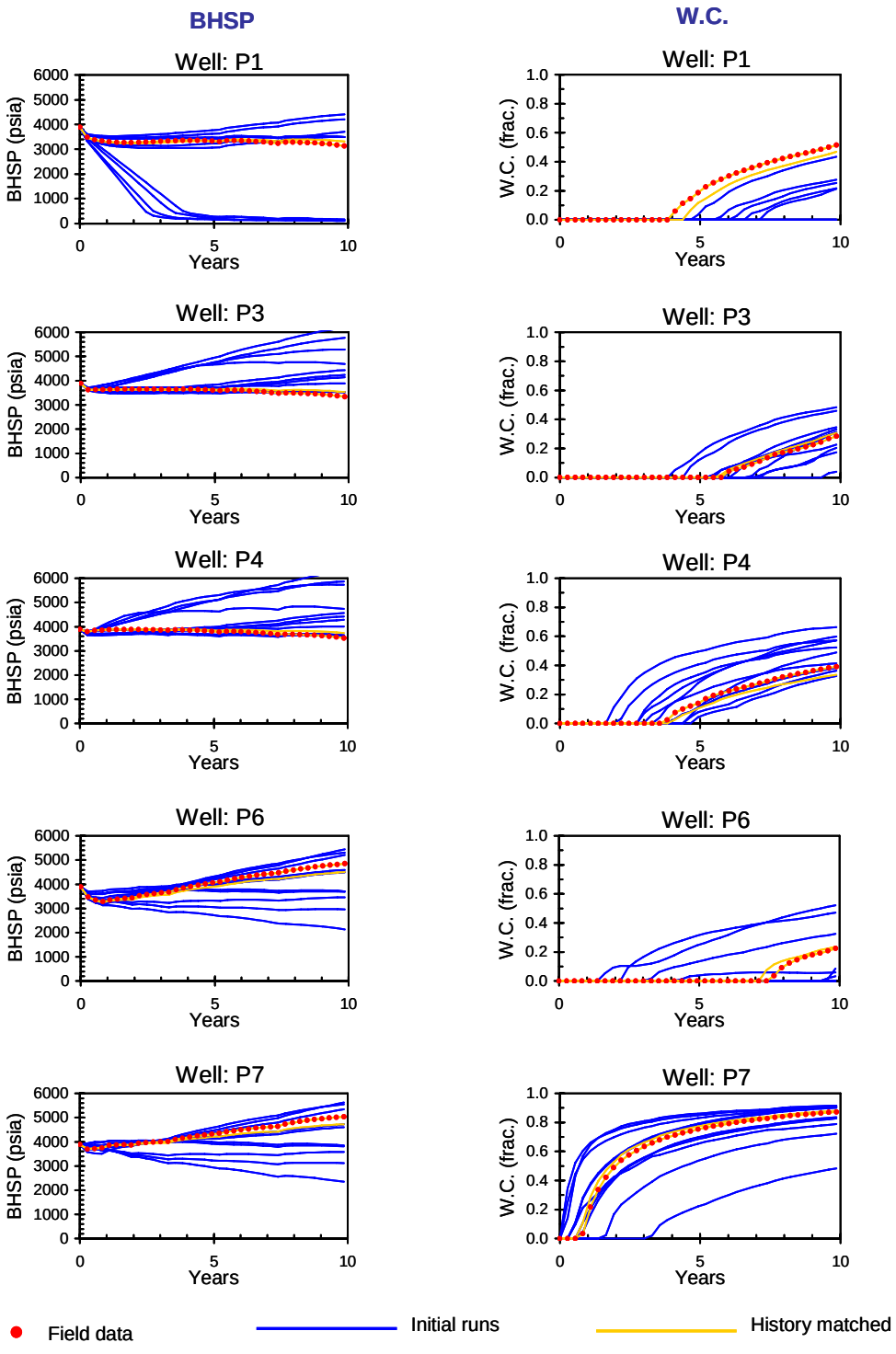

Figure 5.19: History matching result, NA, Case A5

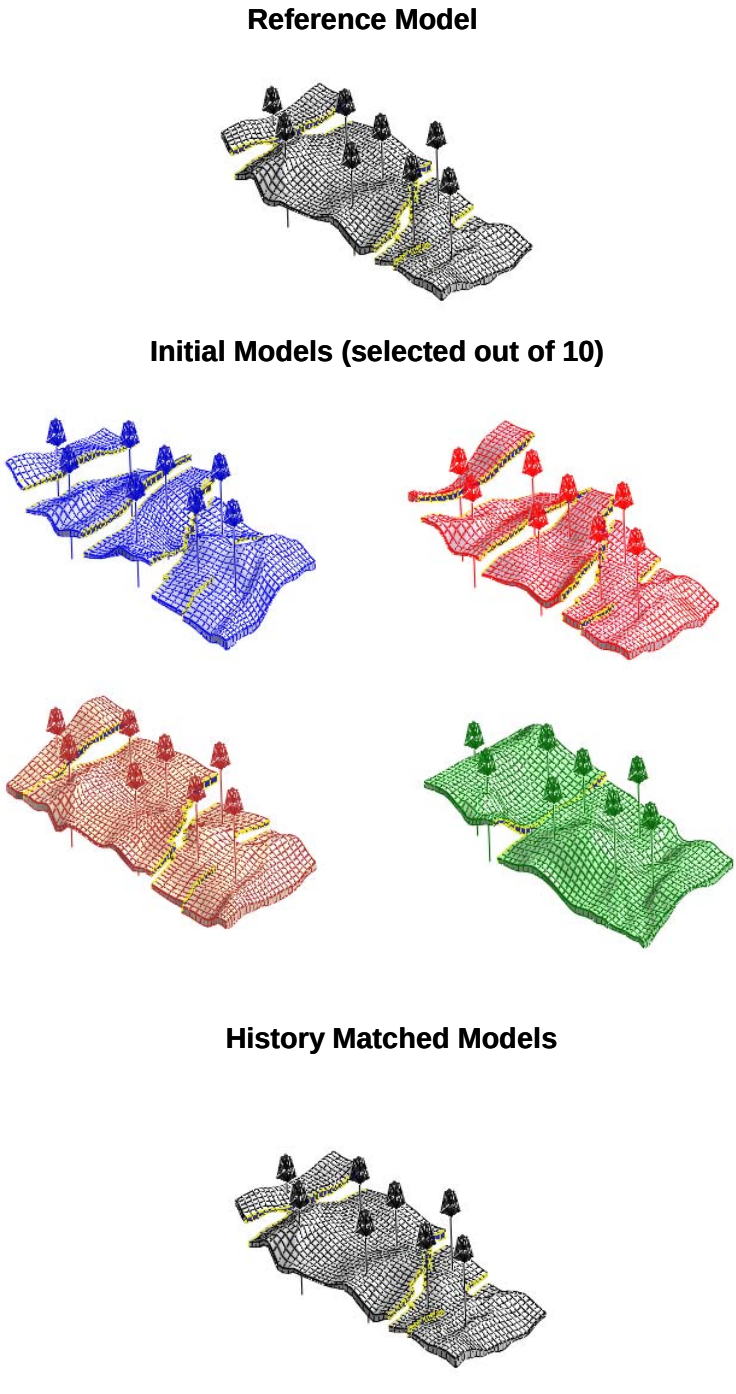

Figure 5.20: History matched structural models vs. reference model, initial models, NA, Case A6

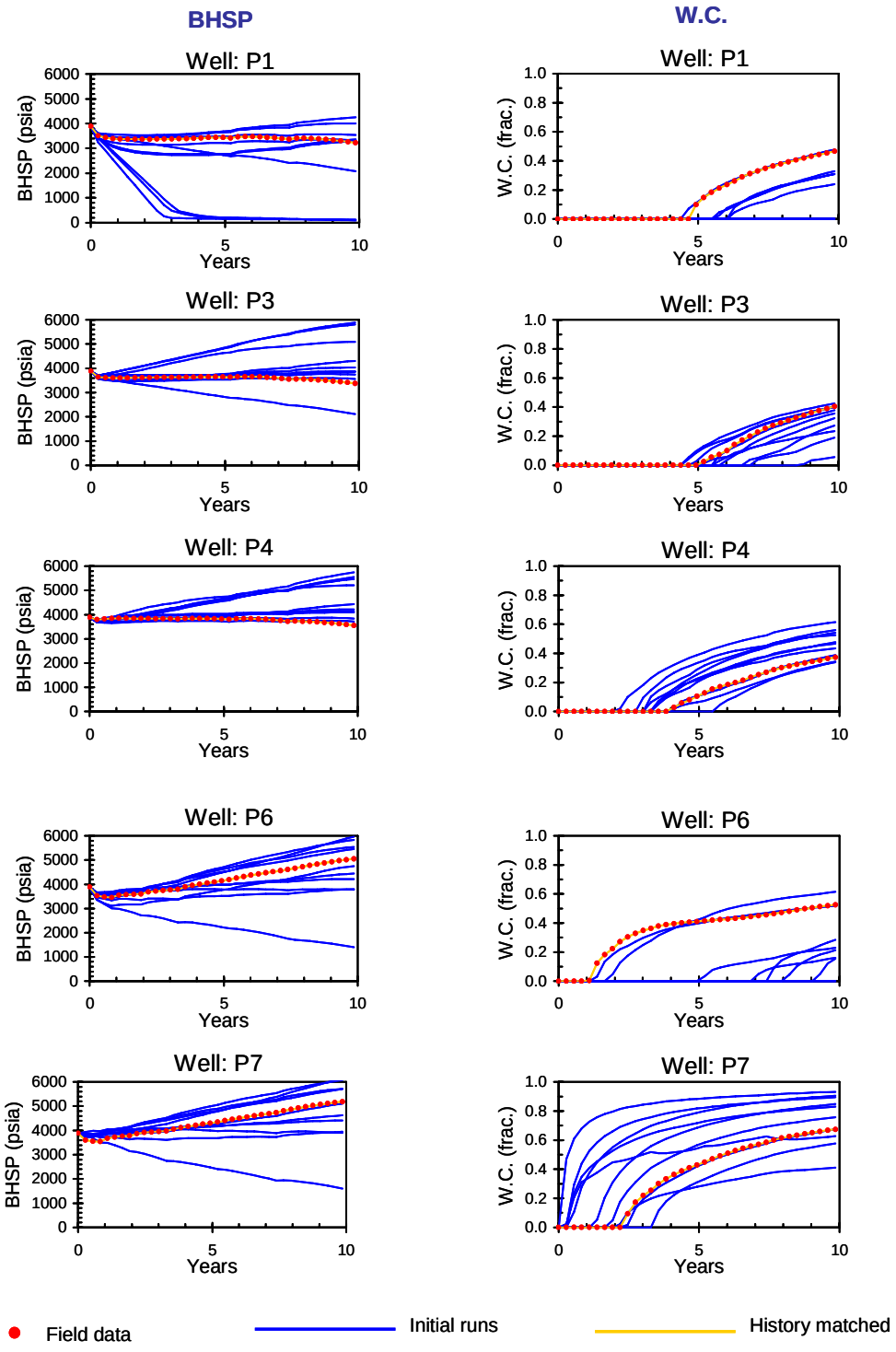

Figure 5.21: History matching result, NA, Case A6

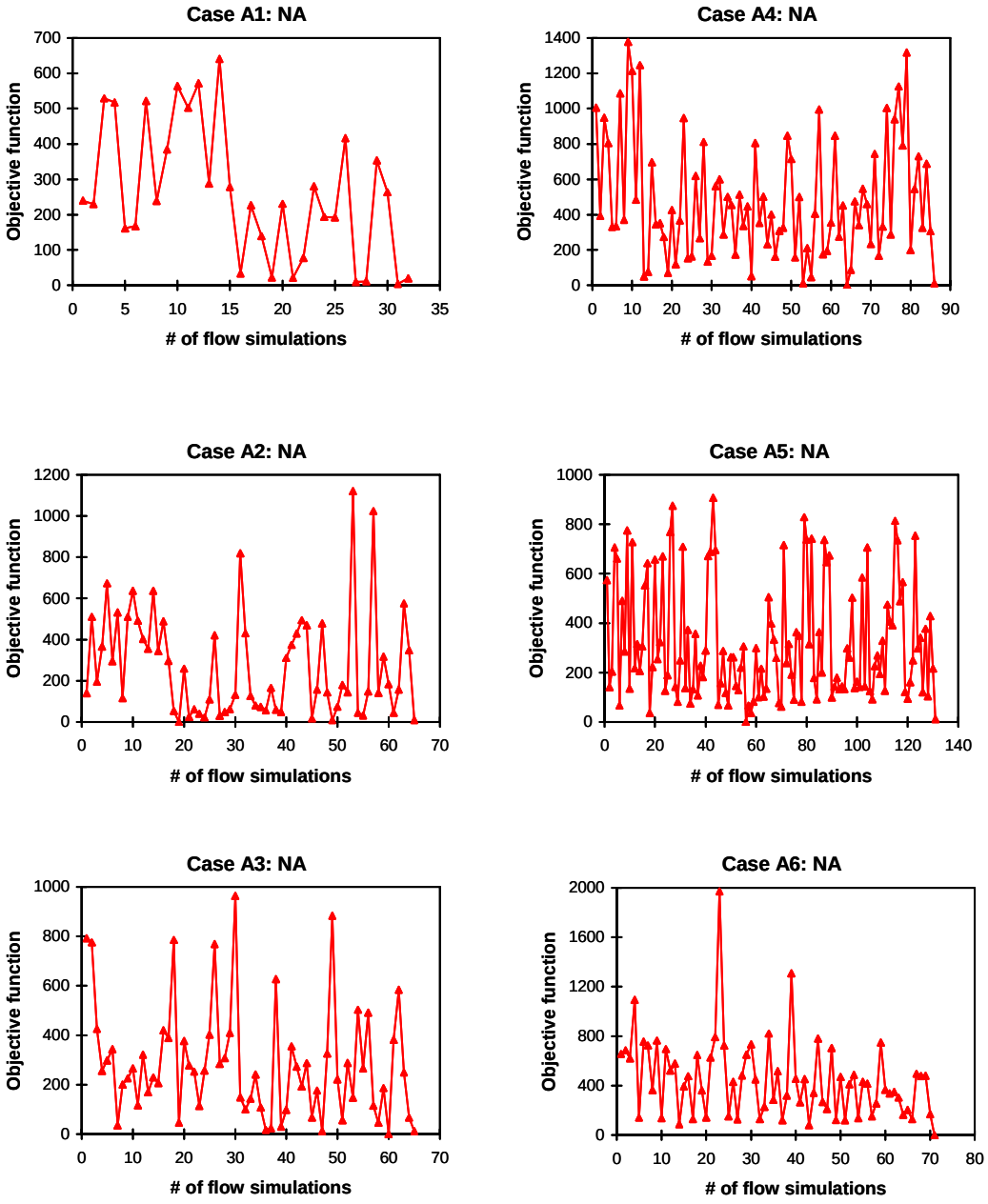

Figure 5.22: Optimization behavior, NA, Case A

The number of flow simulations required for the history matching is summarized in Table 5.2.

Table 5.2: Number of flow simulations required for history matching

	# of flow simulations required		# of history matched models targeted in stochastic search
	Total	per HM model	
Case A1	32	8	4
Case A2	65	16.25	4
Case A3	65	16.25	4
Case A4	86	28.6	3
Case A5	131	65.5	2
Case A6	71	71	1

As tabulated, the history matches are efficiently achieved with a fairly reasonable number of flow simulations in Cases A1 ~A4. The computation cost, while acceptable, is more expensive in Cases A5 and A6, where only one or two models that can reproduce the past history are included in the prior uncertainty space. Figure 5.22 depicts the behavior of the objective function during the stochastic search. As shown in the figure, convergence of objective function is not clear: i.e. the objective function shows considerable fluctuations. This is because, in this implementation of the neighborhood algorithm, the probability of selecting a Voronoi cell is set to zero as soon as the Voronoi cell runs out of unvisited prior model. In other words, a Voronoi cell already fully explored is not visited any more. Such a Voronoi cell is usually located in the region where a low objective function is achieved; otherwise, it would not have been explored so intensely. Note that a Voronoi cell fully explored but not achieving history match is not necessarily a local minimum, it could have achieved history match had a larger number of prior models been provided in the prior uncertainty space. A better convergence of the objective function could be expected if the probability perturbation method (PPM, Caers, 2003) is coupled with the neighborhood algorithm as demonstrated in Chapter 4: i.e. when the search arrives into an “empty” Voronoi cell, a new structural model is generated trough a stochastic perturbation of the currently visited model. However, obstacles that prevent implementation of the probability perturbation method in this case are: 1) stochastic perturbation of horizon/fault is done as a black box inside the GOCAD software, which we require to access for implementing PPM, and 2) the number of perturbation parameters required for structural modeling could be potentially large, since PPM requires an explicit parameterization of the perturbation.

The sensitivity of the optimization efficiency to the number of initial models in the neighborhood algorithm is tested and depicted in Figure 5.23. Although the number of flow simulations required for finding one history matched model depends on the number of initial models in each case, the optimal number of initial models is case dependent. The sensitivity itself is not extremely large except for Case 5A (Fig. 5.23) where the required number of flow simulations is significantly high when the number of initial models is set to 10.

The optimization was performed using a stochastic search method in this case study. Another way to perform the optimization is to use a “greedy” search method, where, the decision of a next trial is then deterministic (no selection probability). The Voronoi cell with the current best history matching model is selected. The advantage of the stochastic search method over the “greedy” method is that it can be implemented as a global search method that searches for multiple history matched models. In addition, in this case study, it was found that the stochastic search method is better than the “greedy” method even for finding a single history matched model. Figure 5.24 compares the number of flow simulations required for the “greedy” search against that required for the stochastic search in finding a single history matched model. The “greedy” search could be more efficient than the stochastic search in terms of the require number of flow simulation in many cases (Cases A1, A2, A3 and A5). However, as observed in Case 4A and Case 6A in Figure 5.24, it requires a significantly larger number of flow simulations. In such cases, the search first arrives at a local minimum which is not deep enough to achieve history match, then seeks for another local minimum until arriving at a “deep-enough” minimum. Such a search path, which is unfortunately dependent on a random selection of the initial models, can be extremely inefficient. The efficiency of the stochastic search is more robust compared to the “greedy” search (Fig. 5.24) since the stochastic nature of the search path selection reduces the risk of heading to “not-deep-enough” local minima.

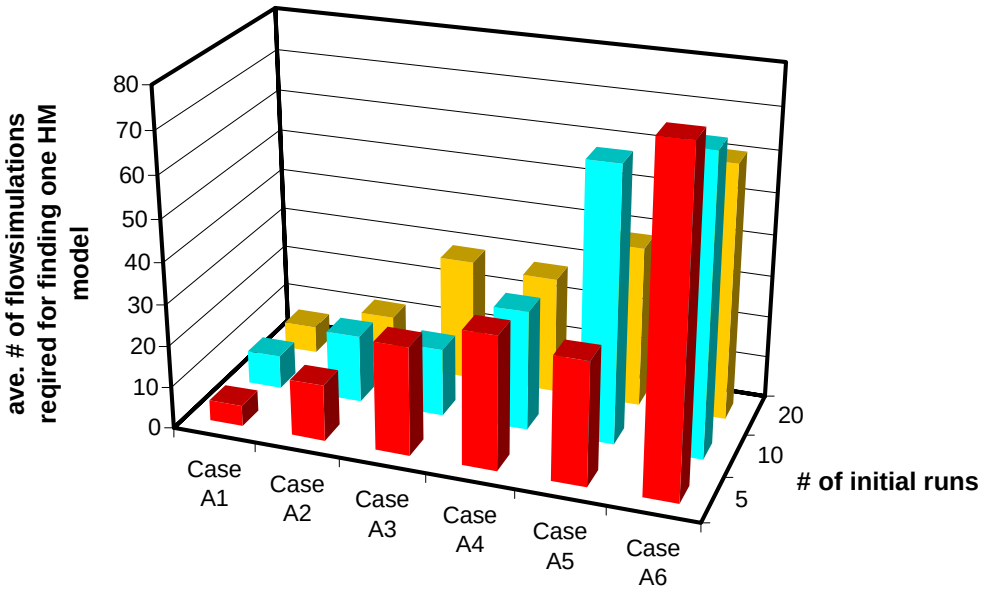

Figure 5.23: Sensitivity of optimization efficiency to the number of initial runs, NA, Case A

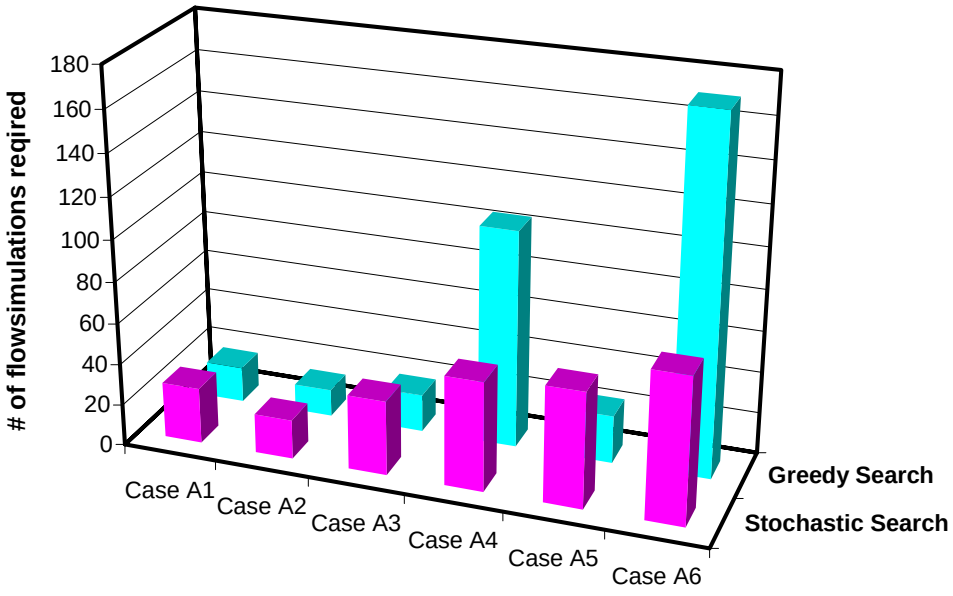

Figure 5.24: Comparison of optimization efficiency, stochastic search vs. greedy search , NA, Case A

Tree Search Optimization

The tree search is applied to the previous cases (i.e. Cases A1 ~ A6). The history matched structural models are compared to the initial models and to the reference model in Figures 5.25, 5.27, 5.29, 5.31, 5.33, 5.35. The GNAT is constructed in this case study by locating 4 models at the root of the tree. Figures 5.26, 5.28, 5.30, 5.32, 5.34, 5.36 show the results of history matching together with the simulated production on the initial models (flow simulation performed on the models located at the root of the tree).

As depicted in the figures, a satisfactory match is obtained (Figs. 5.26, 5.28, 5.30, 5.32, 5.34, 5.36). Similarly to the results of the neighborhood algorithm, the history matched structural models are almost identical to the reference model in all cases except Case A2 (Figs. 5.25, 5.27, 5.29, 5.31, 5.33, 5.35).

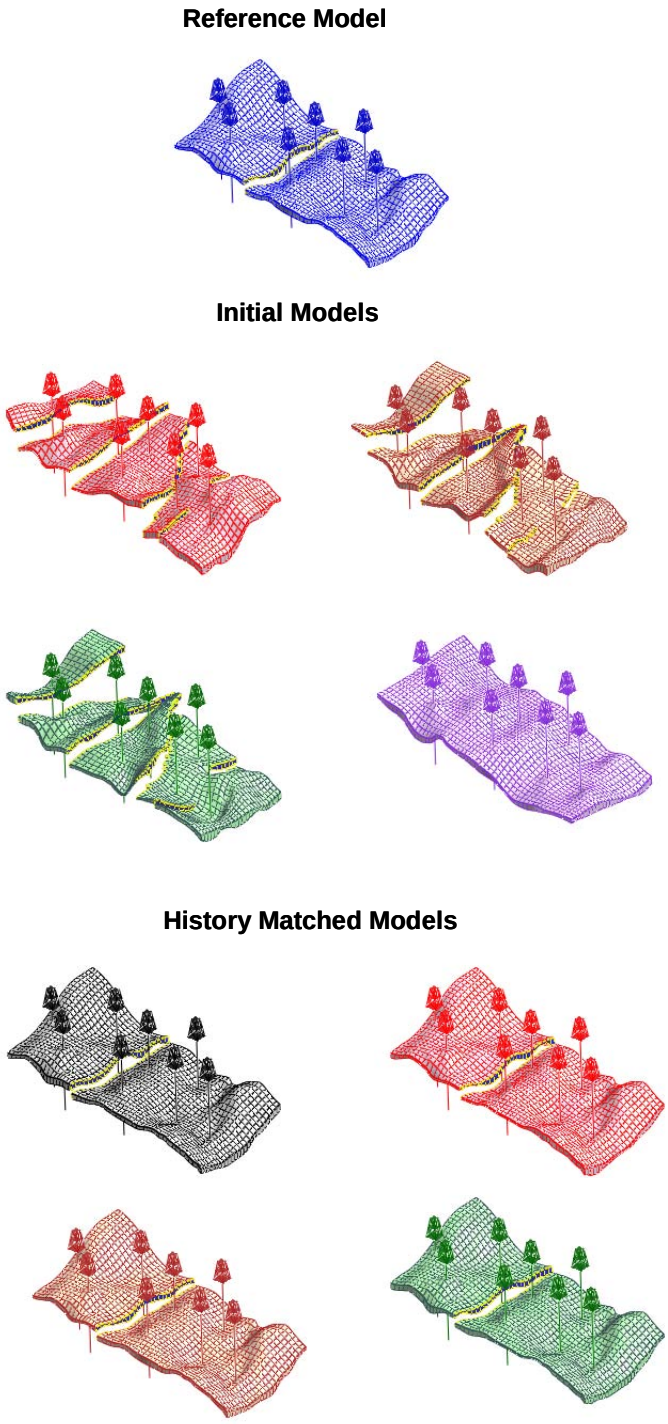

Figure 5.25: History matched structural models vs. reference model, initial models, Tree Search, Case A1

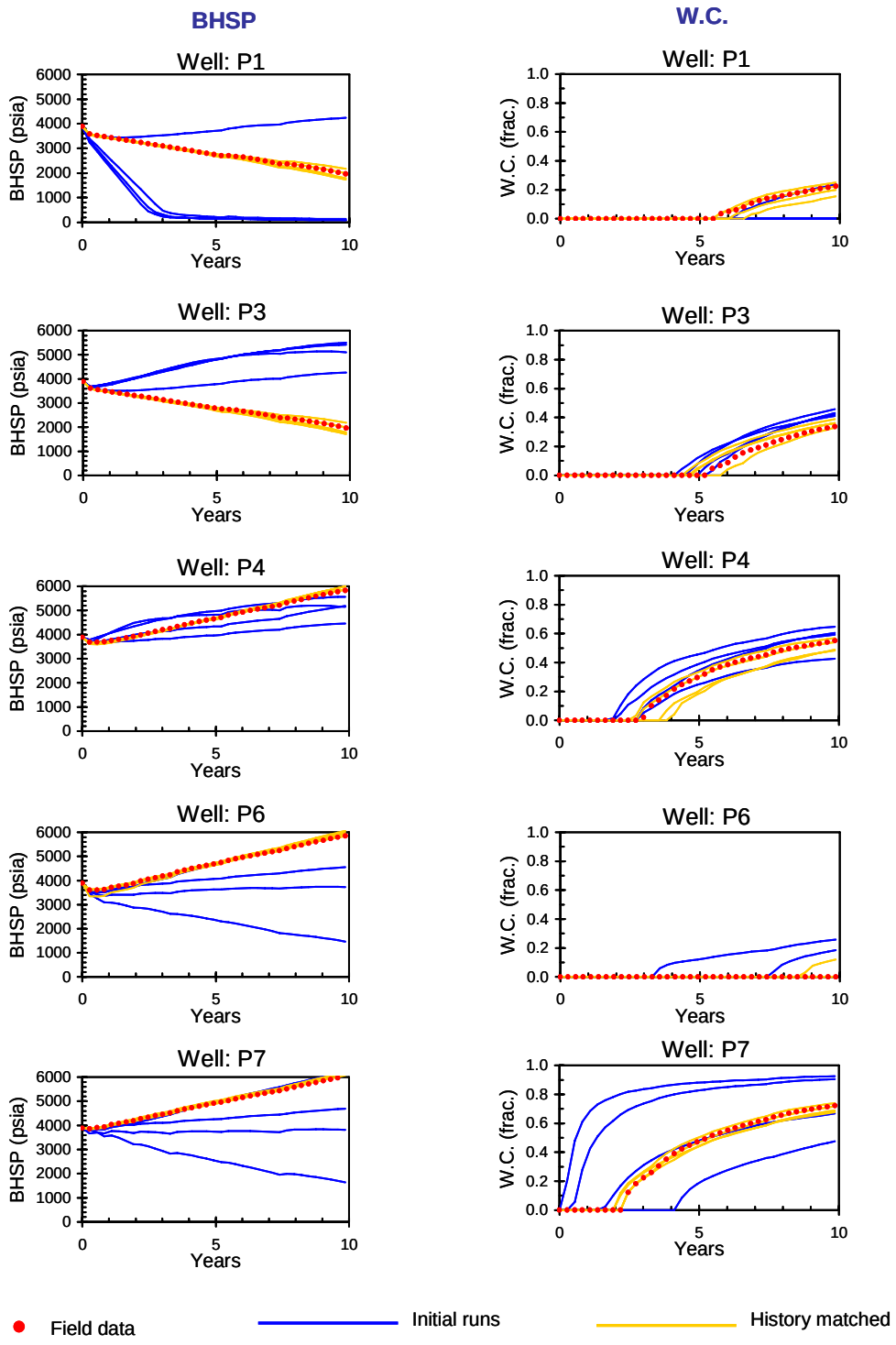

Figure 5.26: History matching result, Tree Search, Case A1

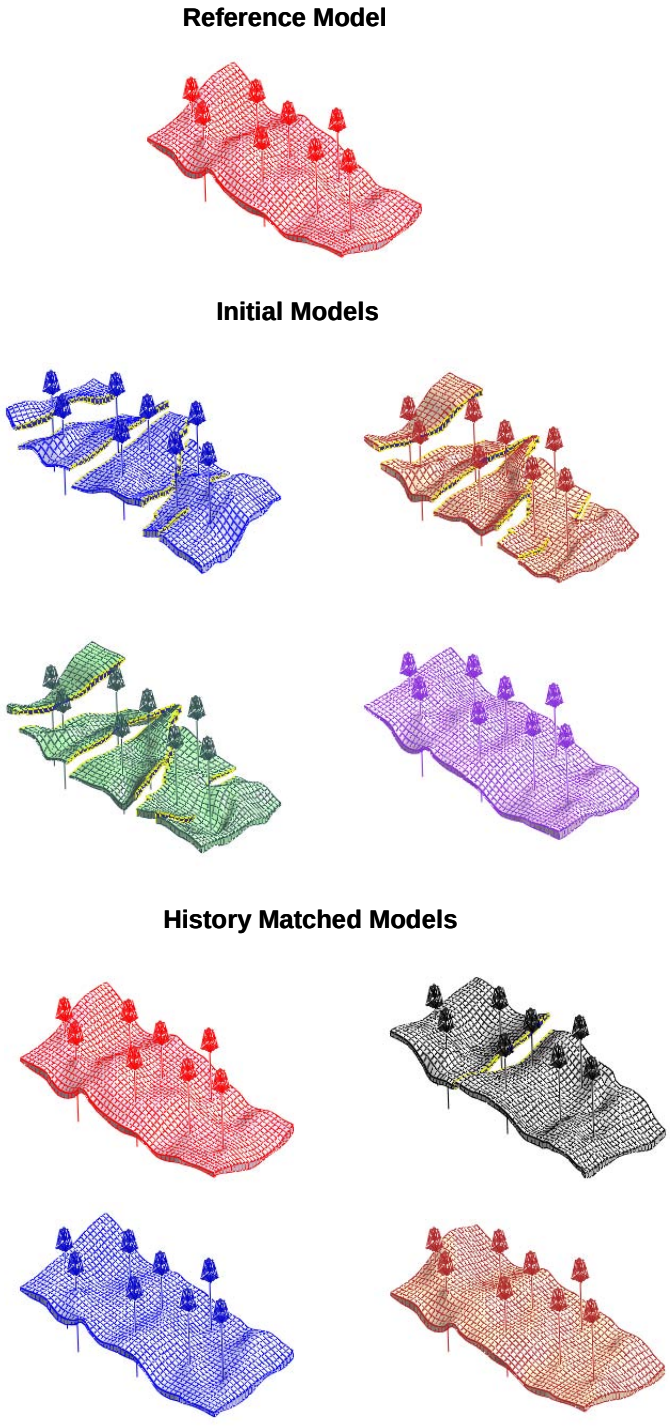

Figure 5.27: History matched structural models vs. reference model, initial models, Tree Search, Case A2

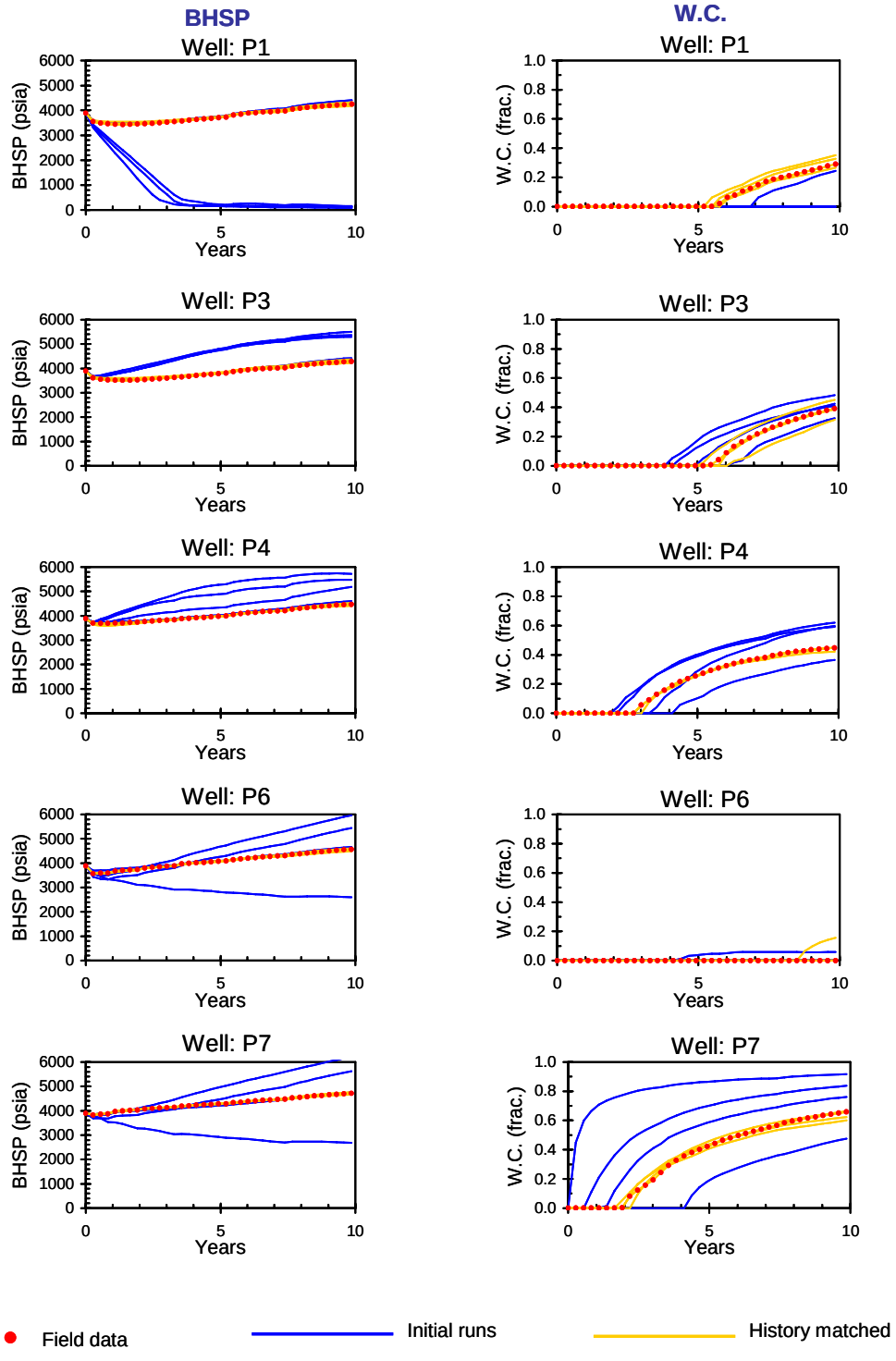

Figure 5.28: History matching result, Tree Search, Case A2

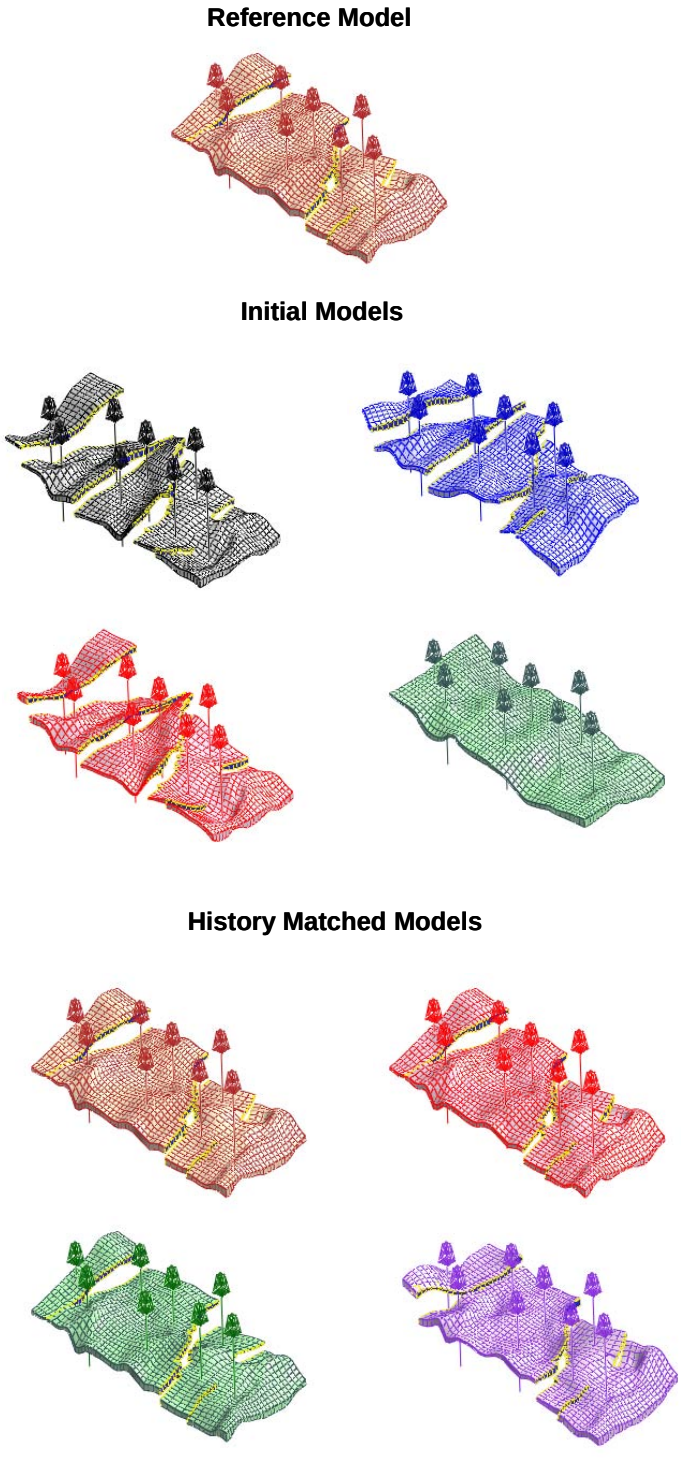

Figure 5.29: History matched structural models vs. reference model, initial models, Tree Search, Case A3

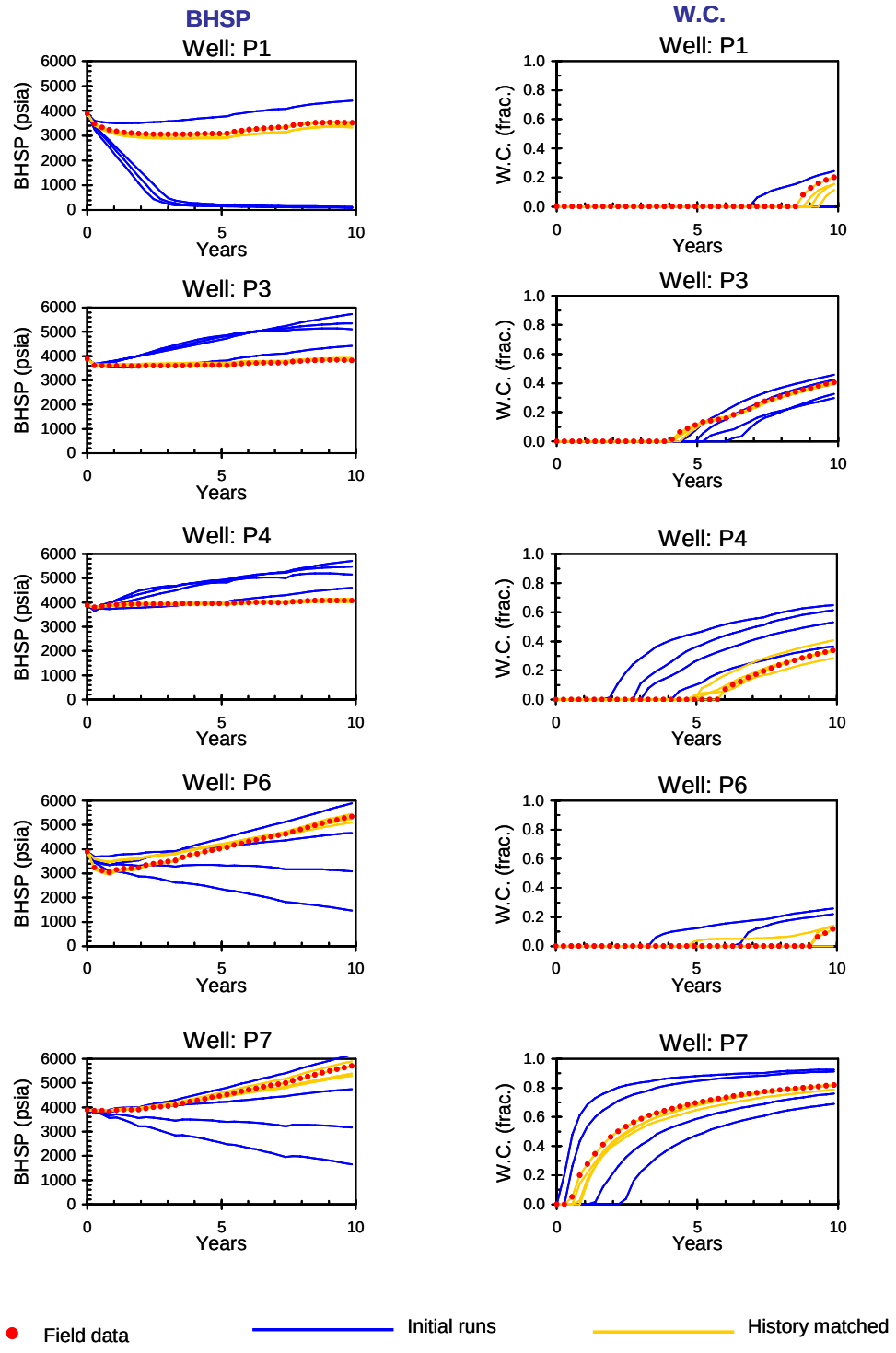

Figure 5.30: History matching result, Tree Search, Case A3

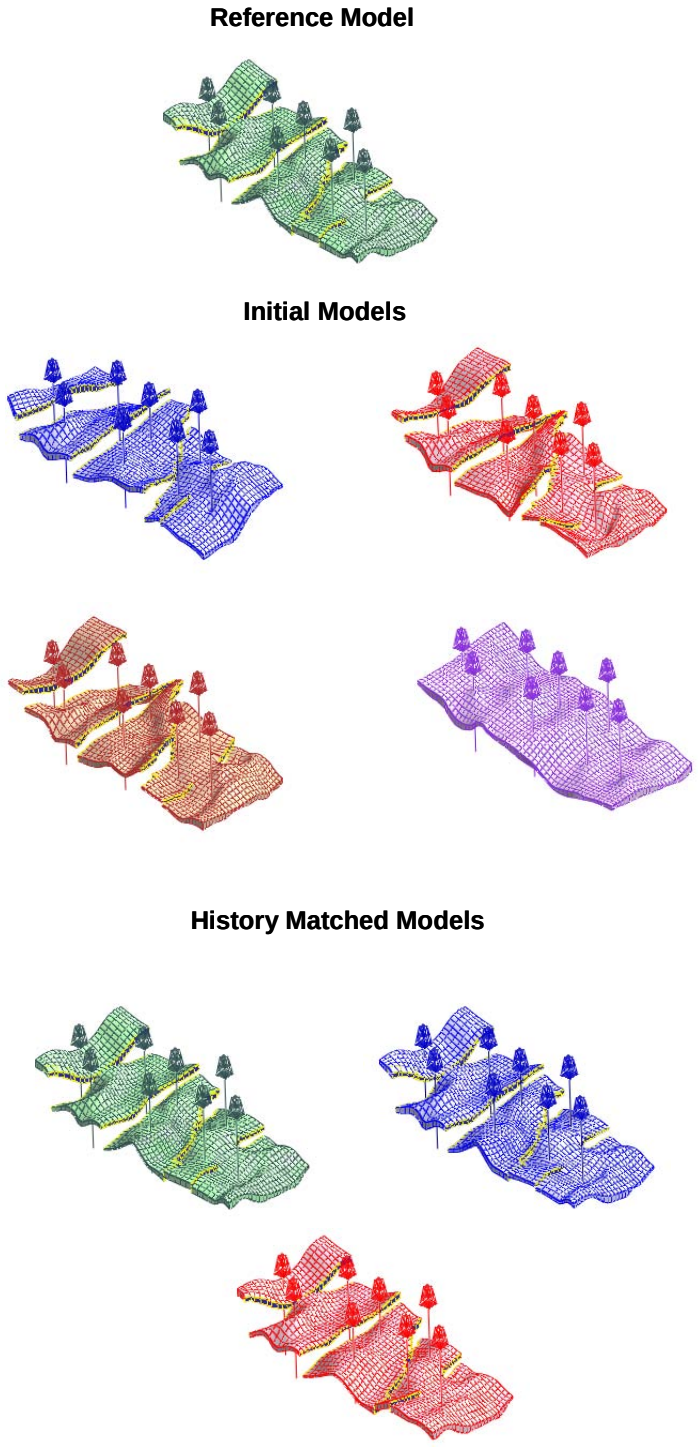

Figure 5.31: History matched structural models vs. reference model, initial models, Tree Search, Case A4

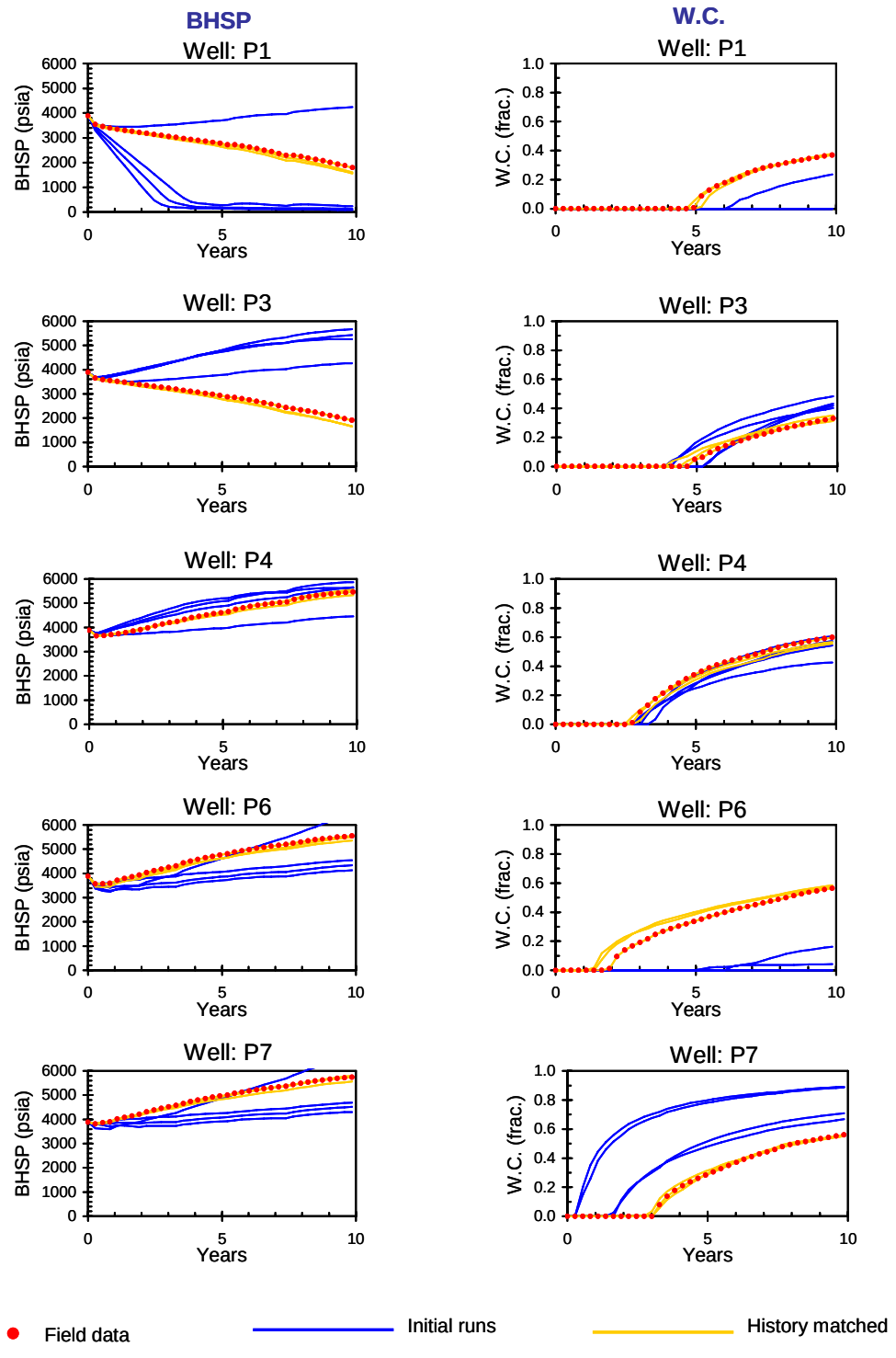

Figure 5.32: History matching result, Tree Search, Case A4

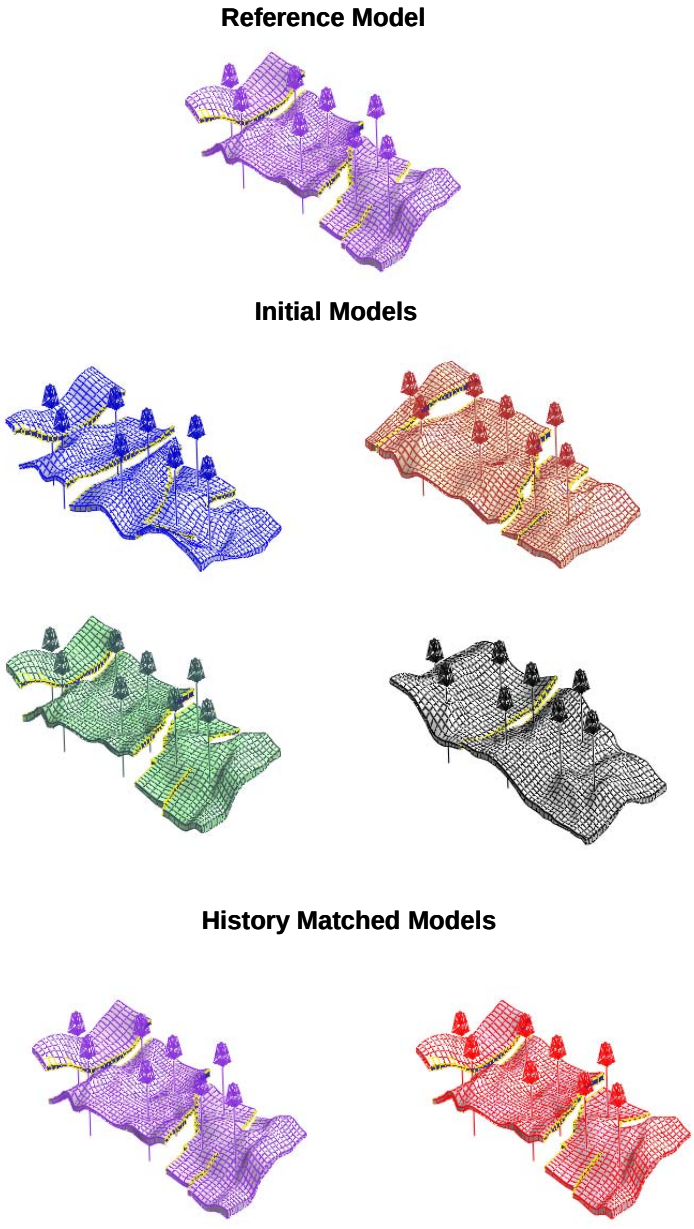

Figure 5.33: History matched structural models vs. reference model, initial models, Tree Search, Case A5

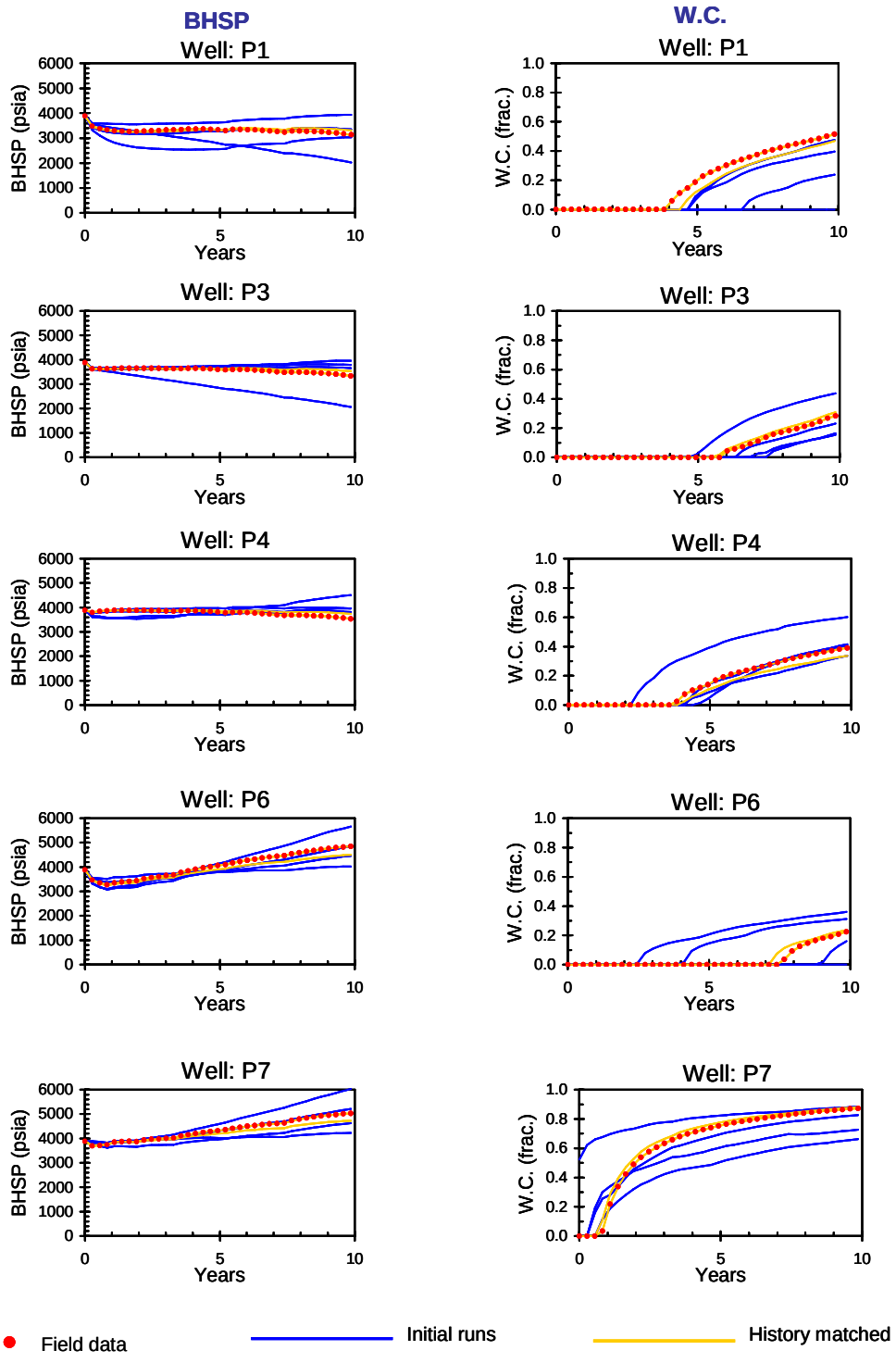

Figure 5.34: History matching result, Tree Search, Case A5

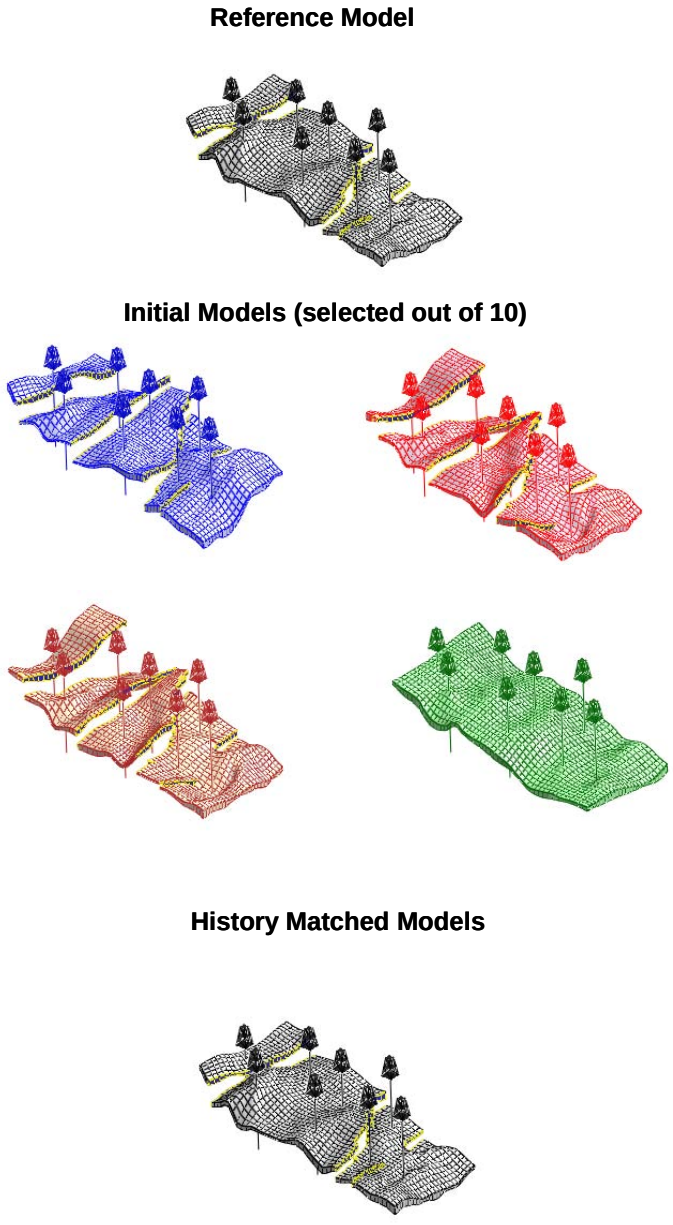

Figure 5.35: History matched structural models vs. reference model, initial models, Tree Search, Case A6

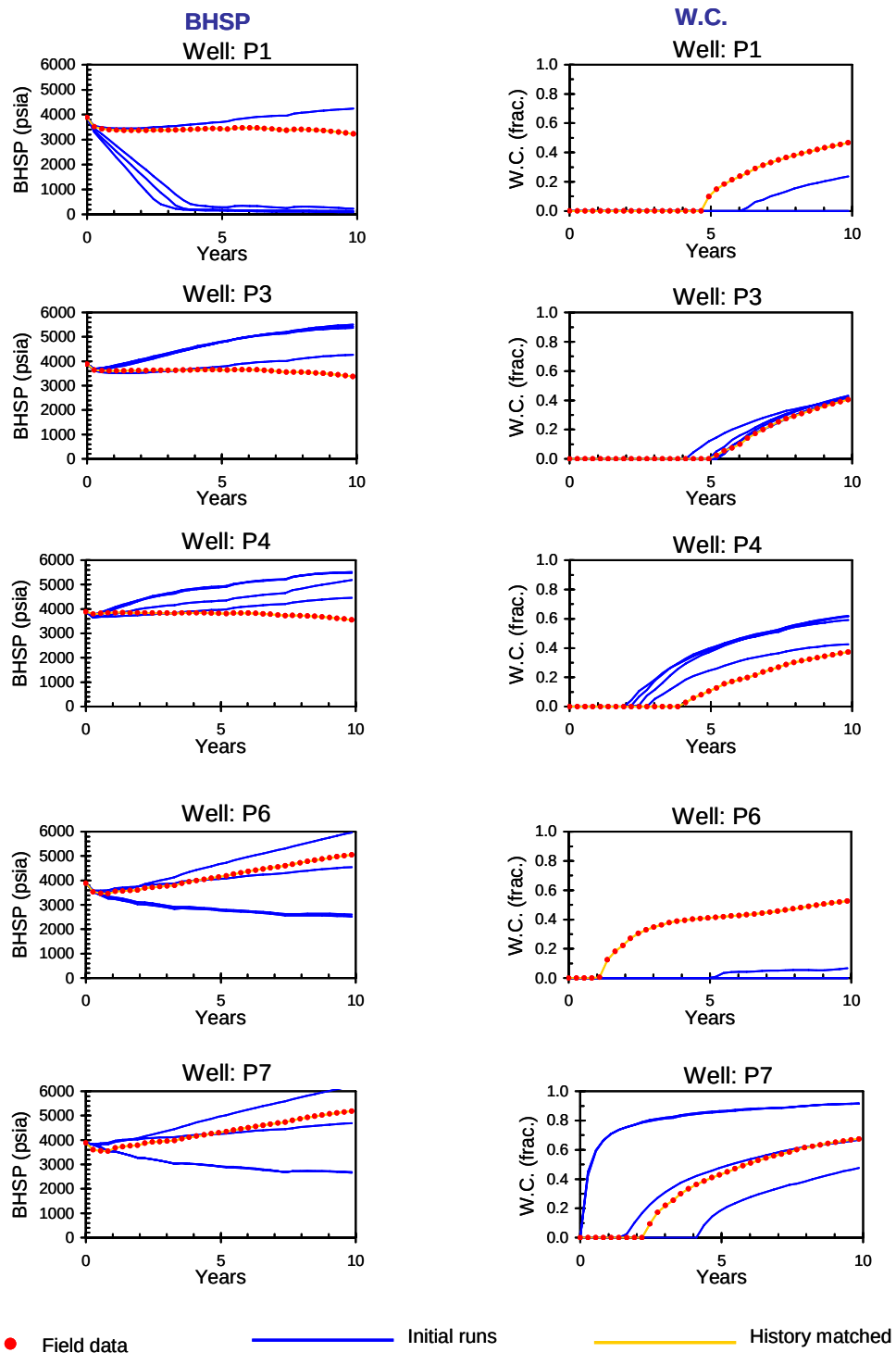

Figure 5.36: History matching result, Tree Search, Case A6

The number of flow simulations required for history matching is tabulated in Table 5.3.

Table 5.3: Number of flow simulations required for history matching

	# of flow simulations required		# of history matched models targeted in stochastic search
	Total	per HM model	
Case A1	99	24.8	4
Case A2	63	15.8	4
Case A3	206	51.5	4
Case A4	163	54.3	3
Case A5	38	19.0	2
Case A6	20	20.0	1

Again, history matches are achieved with a reasonable number of flow simulations. Figure 5.37 depicts the optimization behavior of Cases A1~A6. As shown in the figure, the objective function exhibits a periodic fluctuation during the tree search optimization as the search repeatedly goes down the tree structure. The tree search optimization can also be implemented as a “greedy” search method by always selecting the children that achieved the best history match among the siblings as a next path to go down, instead of randomly drawing a next path based on a selection probability. Figure 5.38 compares the required number of flow simulations between the “greedy” search and the stochastic search in determining a single history matched model. This time, the optimization efficiency of the stochastic search is not necessarily robust: Case A4 required more than 100 flow simulations for finding a single history matched model. However, the robustness of the optimization efficiency of the stochastic search is still better than the “greedy” search.

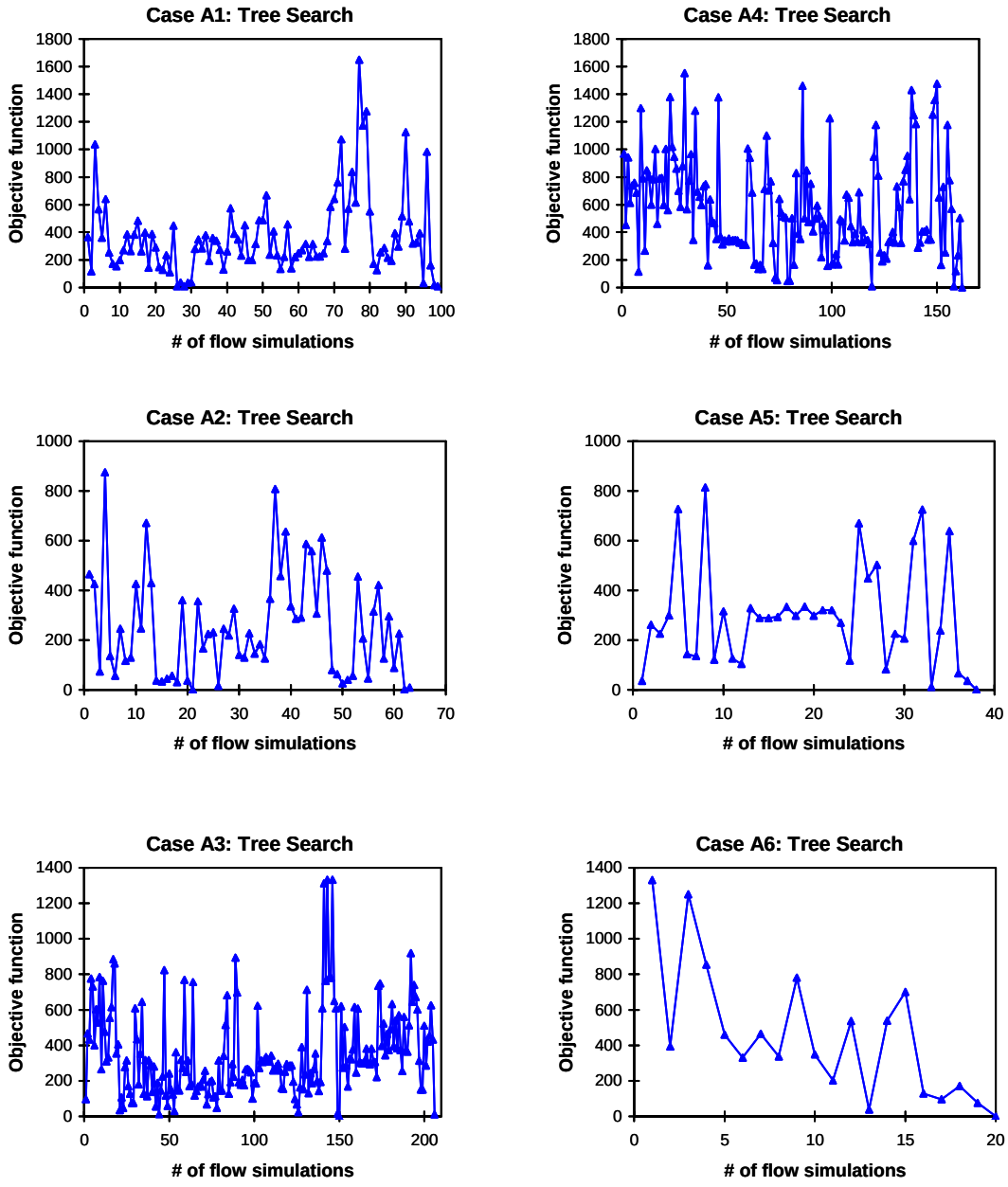

Figure 5.37: Optimization behavior, Tree Search, Case A

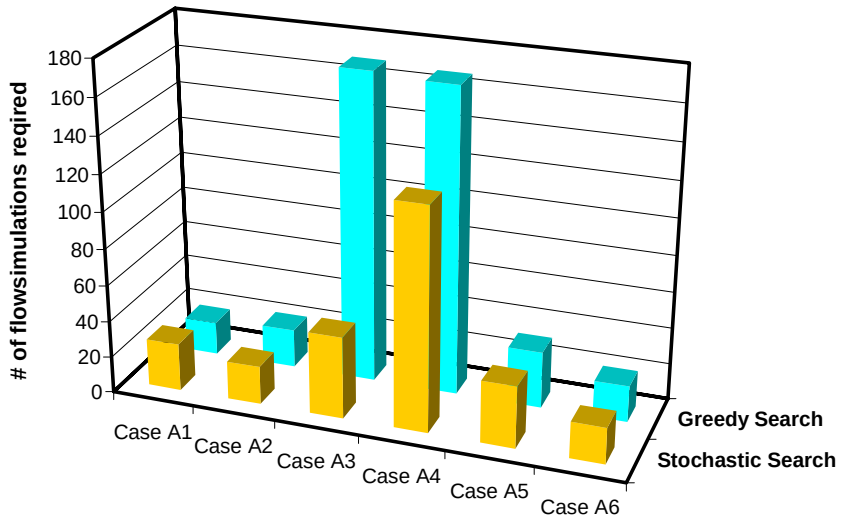

Figure 5.38: Comparison of optimization efficiency, Stochastic search vs. greedy search, Tree search, Case A

5.3.1.4 Impact of the Type of Structural Uncertainty on History Matching

In order to investigate which structural uncertainty has the most significant impact on the success of obtaining a history matching, a sensitivity study is conducted. Figure 5.39 compares the bottom-hole shut-in pressure (BHSP) and water cut (W.C.) simulated on models with different geological interpretations (see Fig. 5.3 for the structural models used for the simulation), while fixing all other uncertainties. Figure 5.40 depicts the comparison of the production behavior from models generated by perturbing the top horizon depth (using a discontinuous perturbation field across the faults), while fixing all other uncertainties. The structural models are depicted in Figure 5.4. Figures 5.41 and 5.42 show the sensitivity of the production behavior to the perturbations of gross thickness and fault position, respectively (The structural models are depicted in Figs.5.5 and 5.6). As shown in the figures, the greatest impact on production behavior is associated to uncertainty in geological interpretation, in other words, the decision on the fault identification. Also, the significance of the uncertainty modeled by the perturbation of the top horizon (in this case, the perturbation of fault throw) is almost comparable to the uncertainty in geological interpretation. This is because a change in fault throw leads to a connection or disconnection in flow communication between fault blocks, which may exert almost identical effect as a decision of

"fault or no fault". As expected, the effects of uncertainties in gross thickness and fault position on the production behavior are least significant.

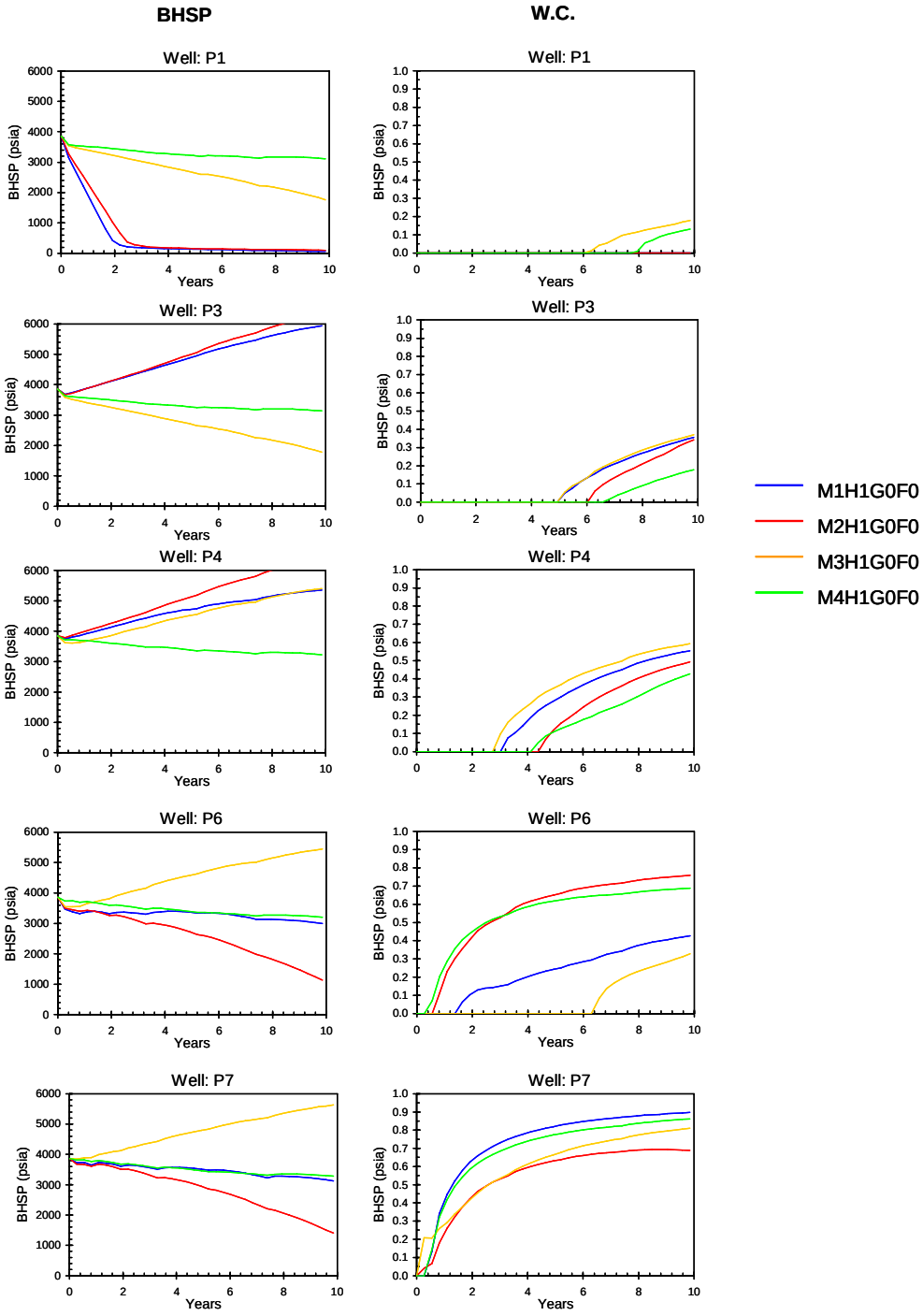

Figure 5.39: Sensitivity of the production behavior to the geological interpretation, Case A

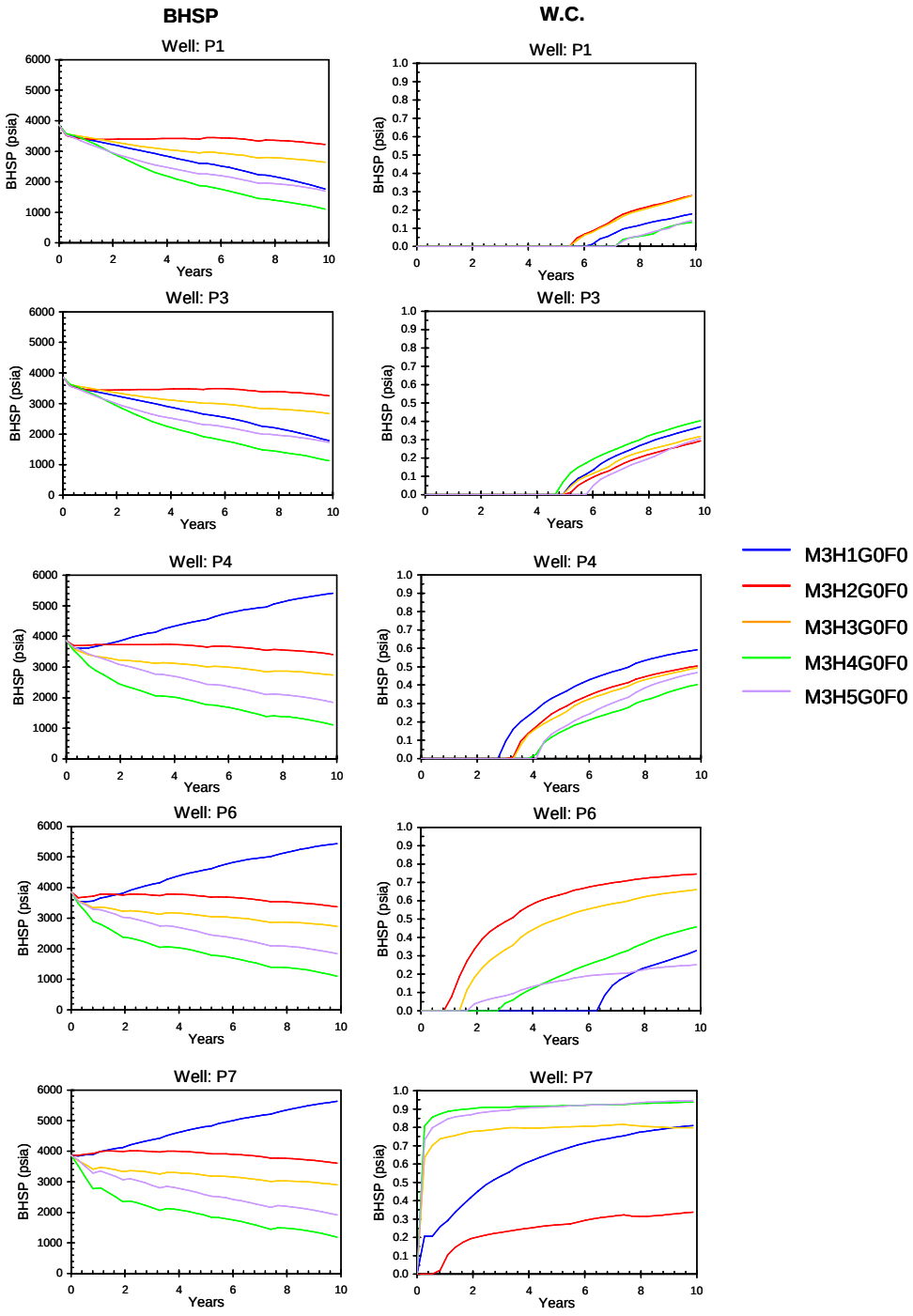

Figure 5.40: Sensitivity of the production behavior to the top horizon position (fault throw), Case A

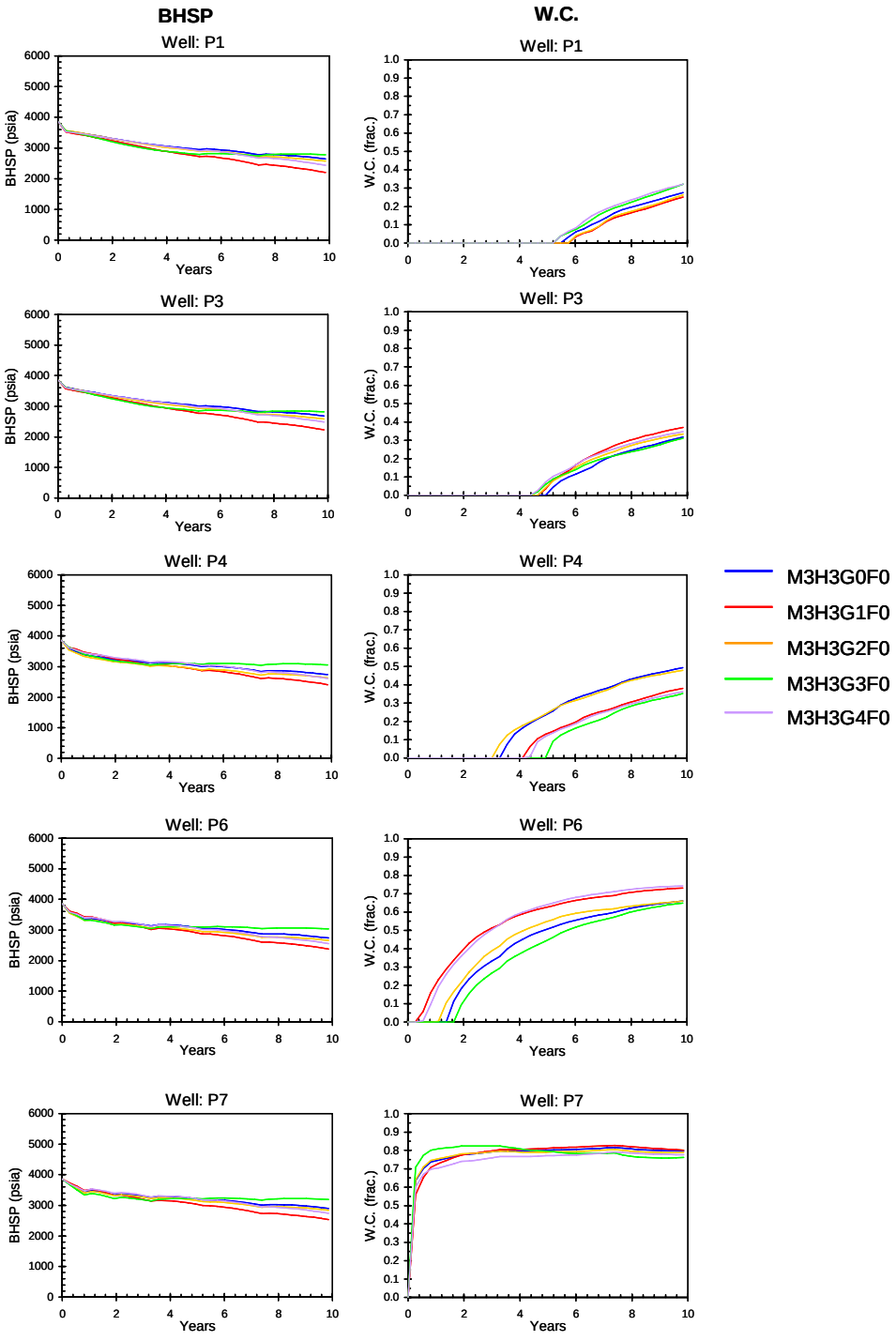

Figure 5.41: Sensitivity of the production behavior to gross thickness, Case A

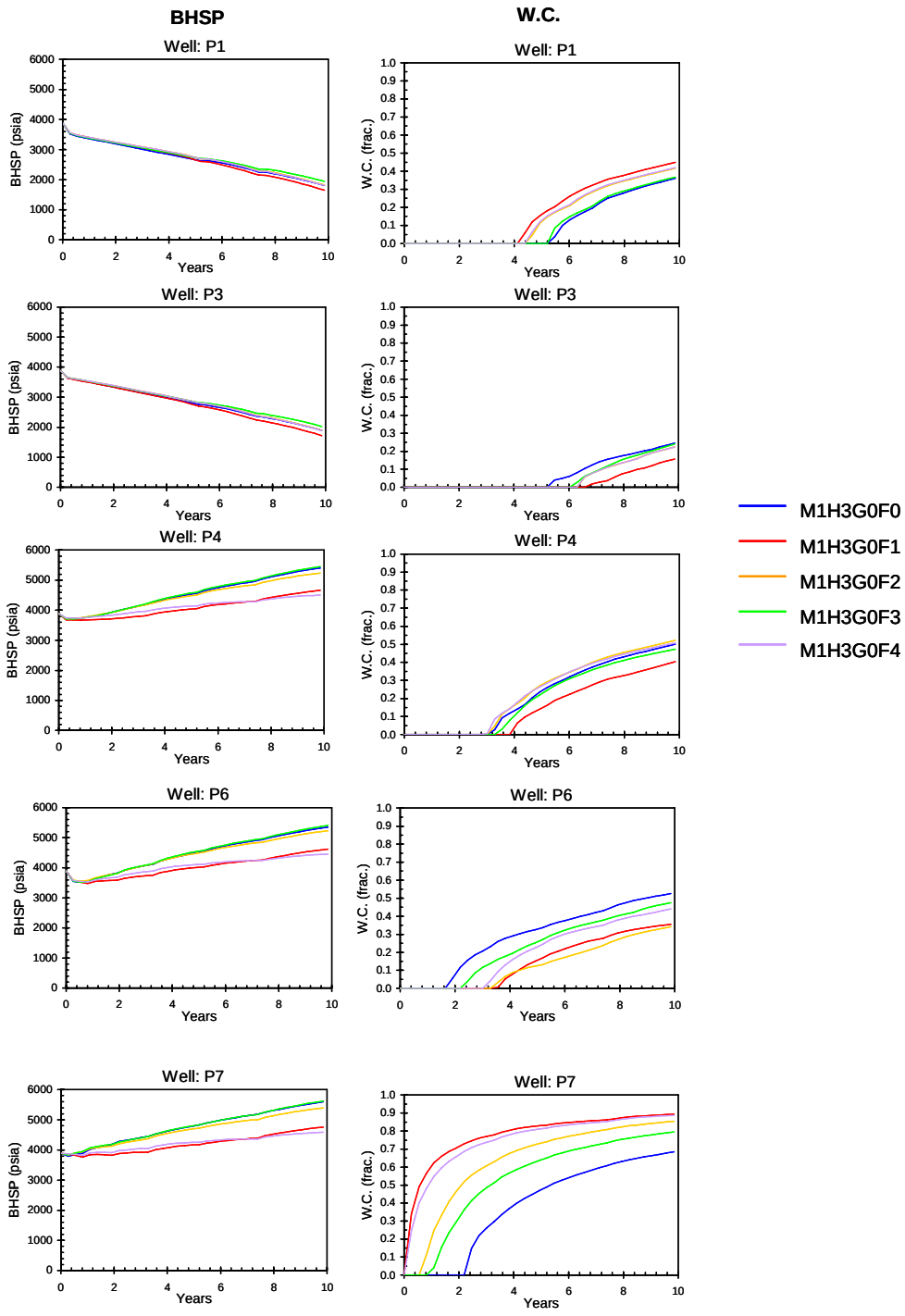

Figure 5.42: Sensitivity of the production behavior to fault position, Case A

5.3.2. Case B

5.3.2.1 Synthetic Reservoir Data

The proposed methodology is now applied to a synthetic reservoir case which considers a more realistic situation than Case A. The "true" reservoir model used in this Case B is built based on an actual geological setting. Figure 5.43 illustrates the "true" reservoir structure together with well locations. The reservoir is located at the flank of a salt dome and bounded by 2 sealing faults, a salt flank and an edge water. It is faulted by 4 parallel faults elongated along the slope of the salt flank. 12 producers and 4 injectors are drilled as shown in the figure. The petrophysical properties models for the "true" reservoir are generated using sequential Gaussian simulation (Fig. 5.44).

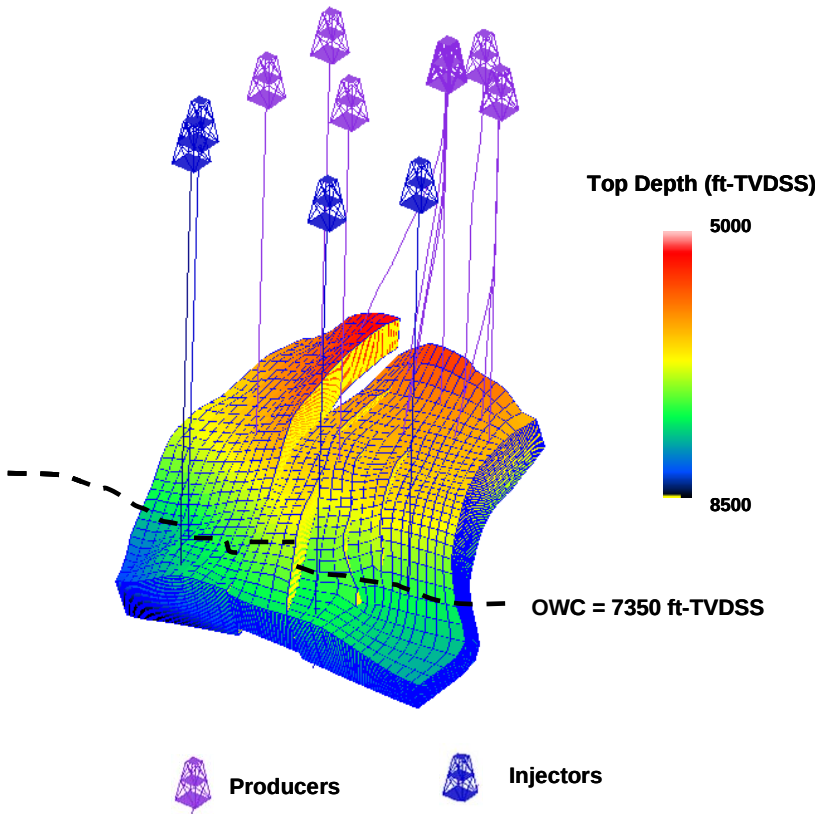

Figure 5.43: "True" reservoir structural model, Case B

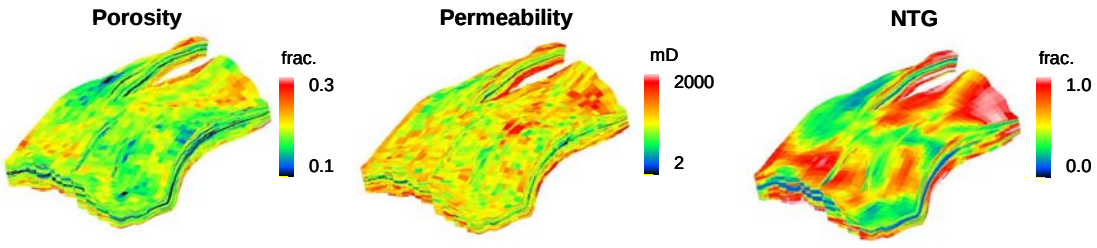

Figure 5.44: Petrophysical properties models, Case B

A synthetic historical production performance is simulated for 10 years, specifying the oil production rate and water injection rate depicted in Figure 5.45. The oil is initially recovered by natural depletion. However, due to limited pressure support from the aquifer, oil production started declining after 2 years of production. One year later, peripheral water injection is started to maintain reservoir pressure. The reservoir pressure is successfully boosted, and the field production achieved a plateau rate for approximately 3 years. Then, due to increase in the water cut, oil production starts declining with the rise of water cut. The synthetic well production data (BHSP and W.C.) is generated from the simulated production behavior by adding some Gaussian noise. An example is shown in Figure 5.46. Figure 5.47 overlays the bottom-hole shut-in pressure at the reference depth of 6000 ft-TVSDSS, measured at 12 producers. This figure indicates that the reservoir fluid flow can communicate over the entire field, since the rises and falls of the pressure observed at all producers are synchronized. No significant discrete changes in pressure behavior between the various wells are observed. This insight can be utilized for structural interpretation.

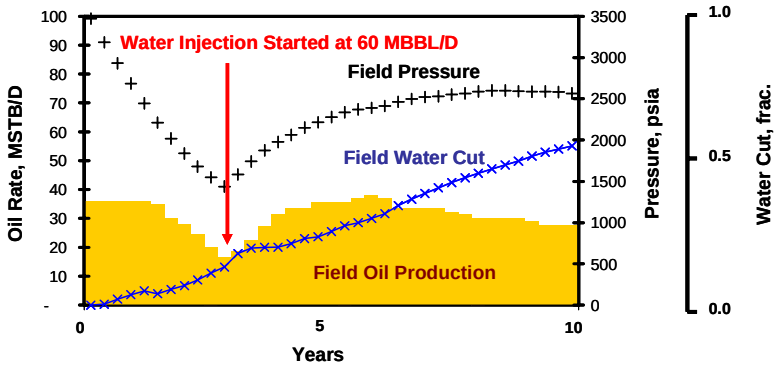

Figure 5.45: Synthetic field production performance, Case B

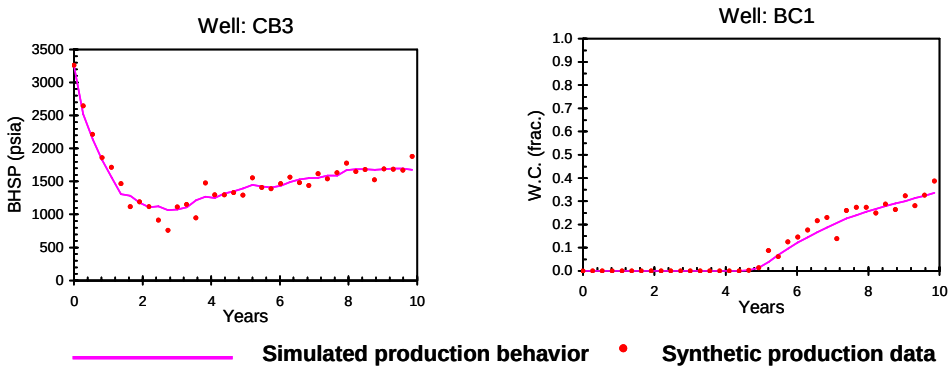

Figure 5.46: An example of synthetic well production data, Case B

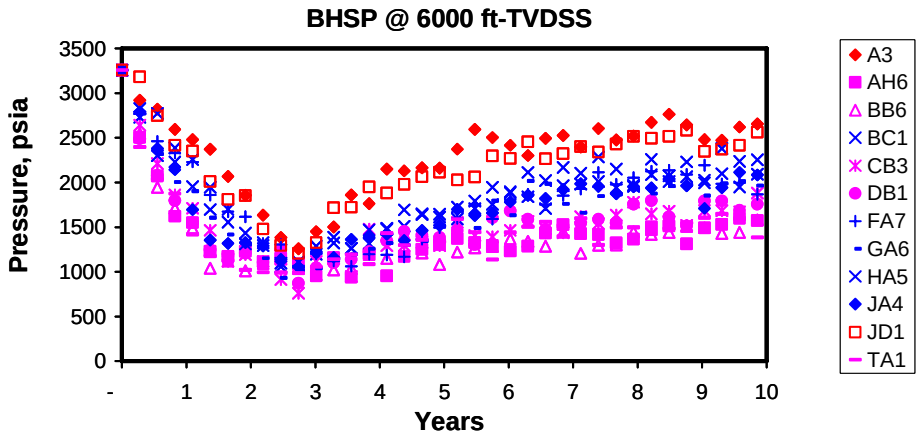

Figure 5.47: Overlaid plot of well pressure data, Case B

5.3.2.2 Prior Structural Uncertainty Modeling

The prior structural uncertainty is modeled starting from 3 structural interpretations based on different geological scenarios. In this synthetic case, it is assumed that seismic resolution is low and the quality is poor, thus it is difficult to identify faults and horizons. However, it is known from field pressure data that the entire reservoir is flow-communicated. A total of 432 prior structural models are built by considering:

1) 3 different interpretations (Figs. 5.48a & 5.48b)

2) 3 different perturbations of the top horizons for each models from step 1, using a discontinuous perturbation field across the faults accounting for fault throw uncertainty: the uncertainty range is 200 m

3) 3 different perturbations of the top horizons for each models from step 2, using a continuous perturbation field: the uncertainty range is 100 m

4) 4 different perturbations of the bottom horizons for each models from step 3: the uncertainty range is 100 m

5) 5 different perturbations of the fault locations for each models from step 4: the uncertainty range is 150 m

As shown in Figure 5.48a, the first structural interpretation (Interpretation 1) includes a smaller number of faults than the "true" structure. The second interpretation (Interpretation 2) is exactly the same as the "true" reservoir (perfect geological scenario). The third interpretation (Interpretation 3) includes a larger number of faults than the "true" structure. The cross-sectional views of these structural models are shown in Figure 5.48b, together with permeability distribution (the selected cross-section is indicated by an arrow in Fig. 5.48a).

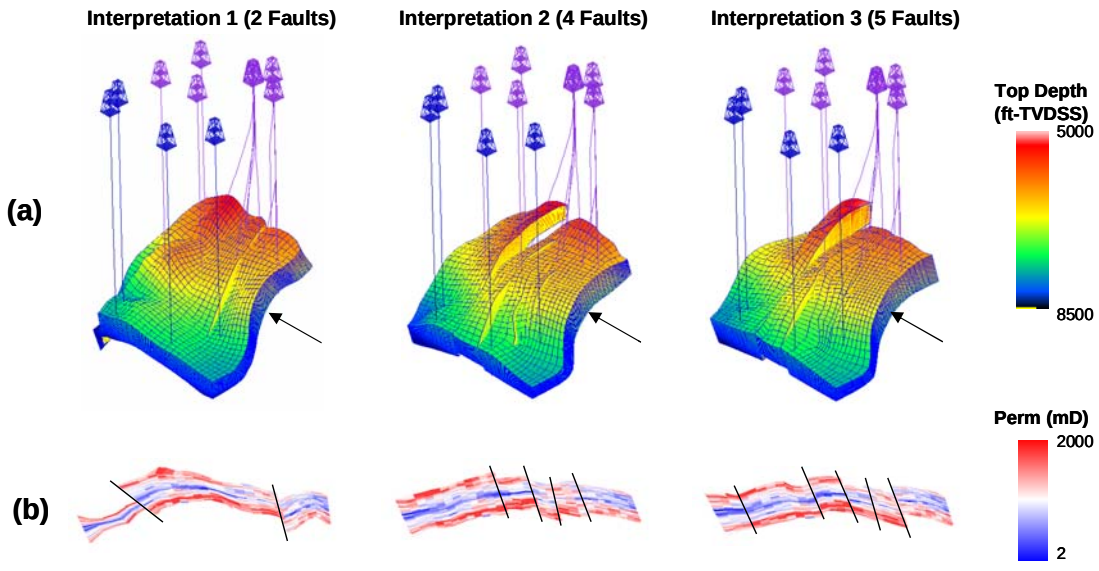

Figure 5.48: Structural models based on 3 different interpretations, (a) three-dimensional view, (b) Cross-sectional view, Case B

5.3.2.3 Case Setting

Using the structural dataset provided from the prior uncertainty modeling, stochastic search is performed using both the neighborhood algorithm (NA) and the tree search. The following 2 cases are considered.

Case B1: Perform history matching in the parameter space that consists of all structural models built in Section 3.2.2. This means that the structural models derived from the perfect geological scenario (Interpretation 2 in Figs. 5.48a & 5.48b), including the "true" reservoir model, are included in the parameter space.

Case B2: Perform history matching in the parameter space comprising only the structural models built from Interpretations 1&3. This means that the structural models derived from the perfect geological scenario are excluded from the parameter space. (A more realistic setting).

Bottom-hole shut-in pressure (BHSP) and water cut (W.C.) are simulated for 10 years by fixing oil production rate and water injection rate to the history, and matched to the synthetic historical production data. The petrophysical parameters are fixed to the "true" petrophysical model. In both cases, the stochastic searchs are carried out aiming at finding two structural models that reproduces the historical production performance.

5.3.2.4 Case B1

Figures 5.49, 5.51 depict the history matched structural models obtained from the neighborhood algorithm (NA) and the tree search optimizations. The history matching results are shown in Figures 5.50, 5.52, respectively, together with the simulated performance of initial runs. Figure 5.53 shows the behavior of the objective function during the optimization.

The number of flow simulations required for the history matching is tabulated in Table 5.4.

Table 5.4: Number of flow simulations required for history matching, Case B1

	# of flow simulations required	
	Total	per HM model
NA	46	23
Tree search	41	20.5

As depicted in Figures 5.50, 5.52, a history match is achieved with acceptable matching accuracy. All of the history matched structural models are those models derived from Interpretation 2 (perfect geological scenario), and exhibit a fairly similar structural geometry as the "true" reservoir structure (Figs. 5.49, 5.51).

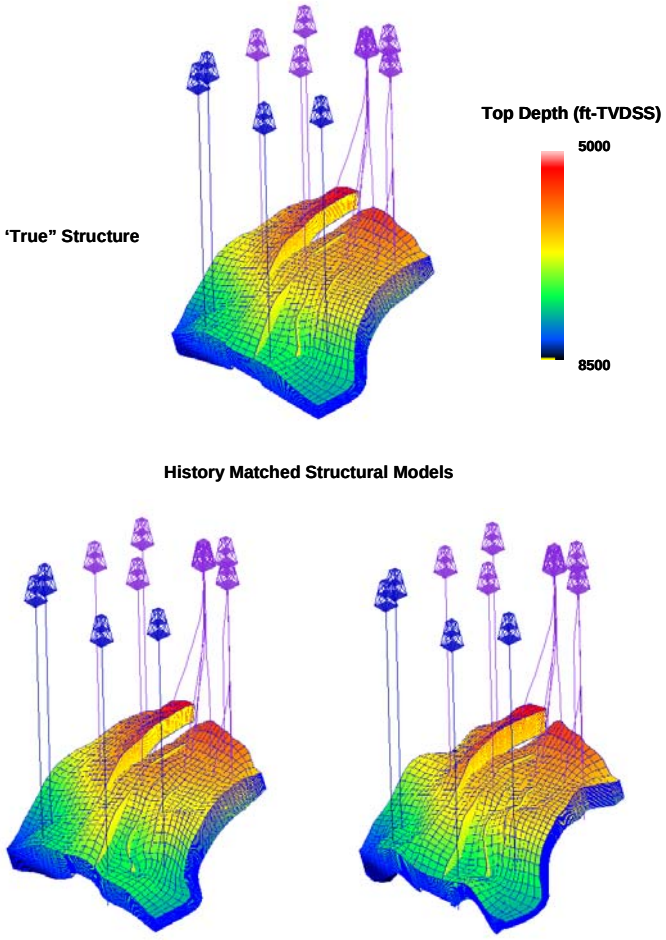

Figure 5.49: History matched structural models, NA, Case B1

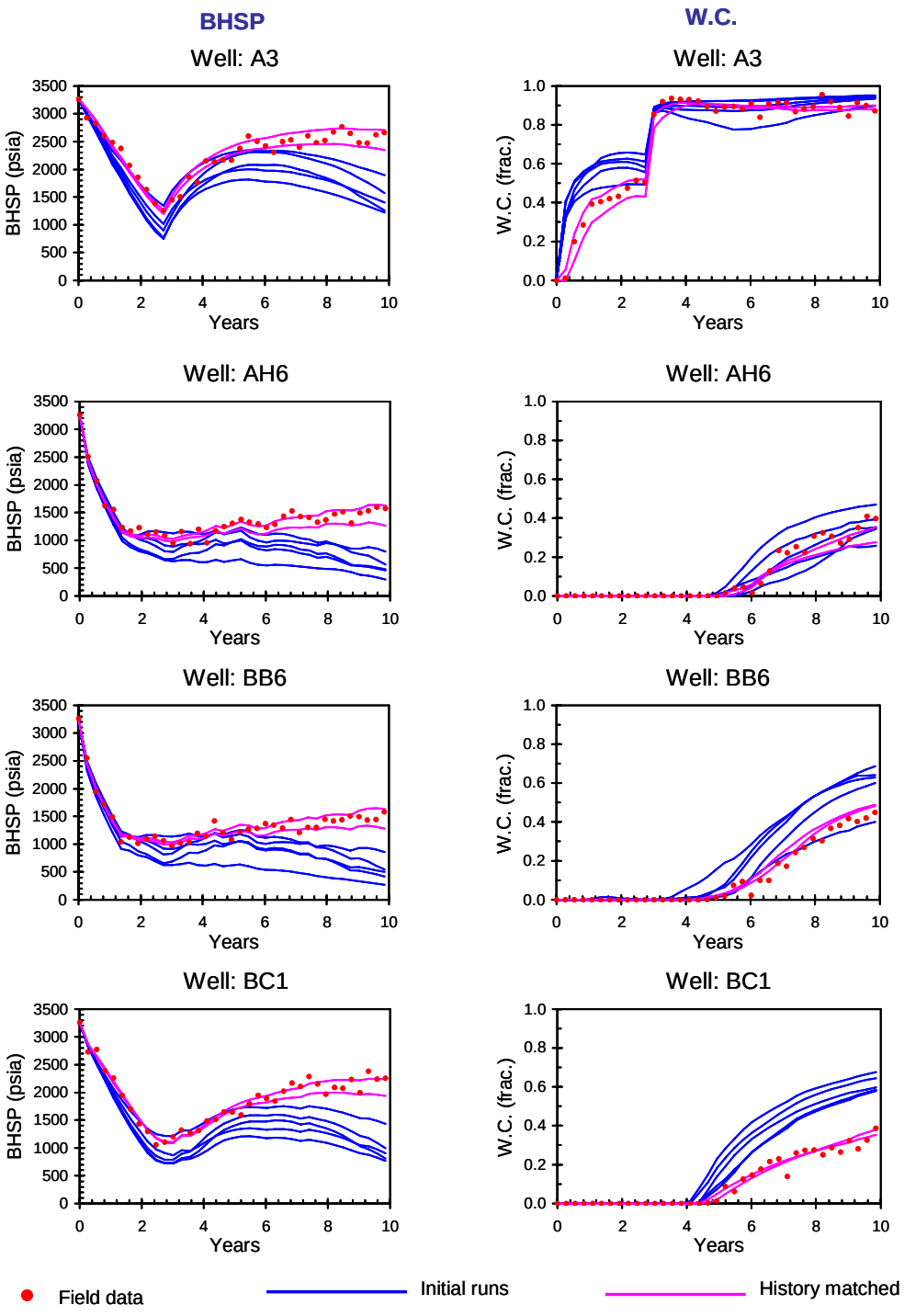

Figure 5.50: History matching result, NA, Case B1

(1/3)

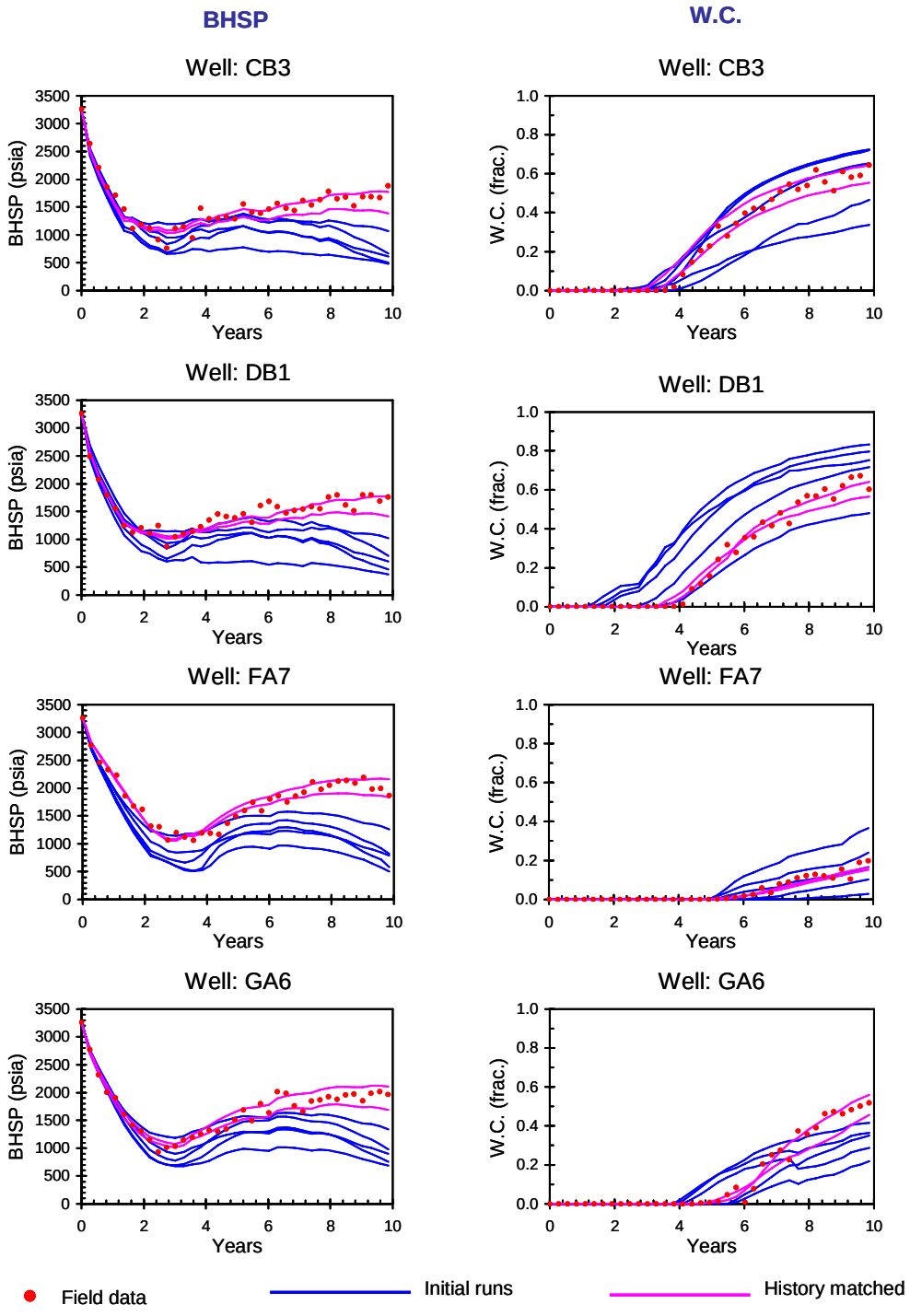

Figure 5.51: History matching result, NA, Case B1 (2/3)

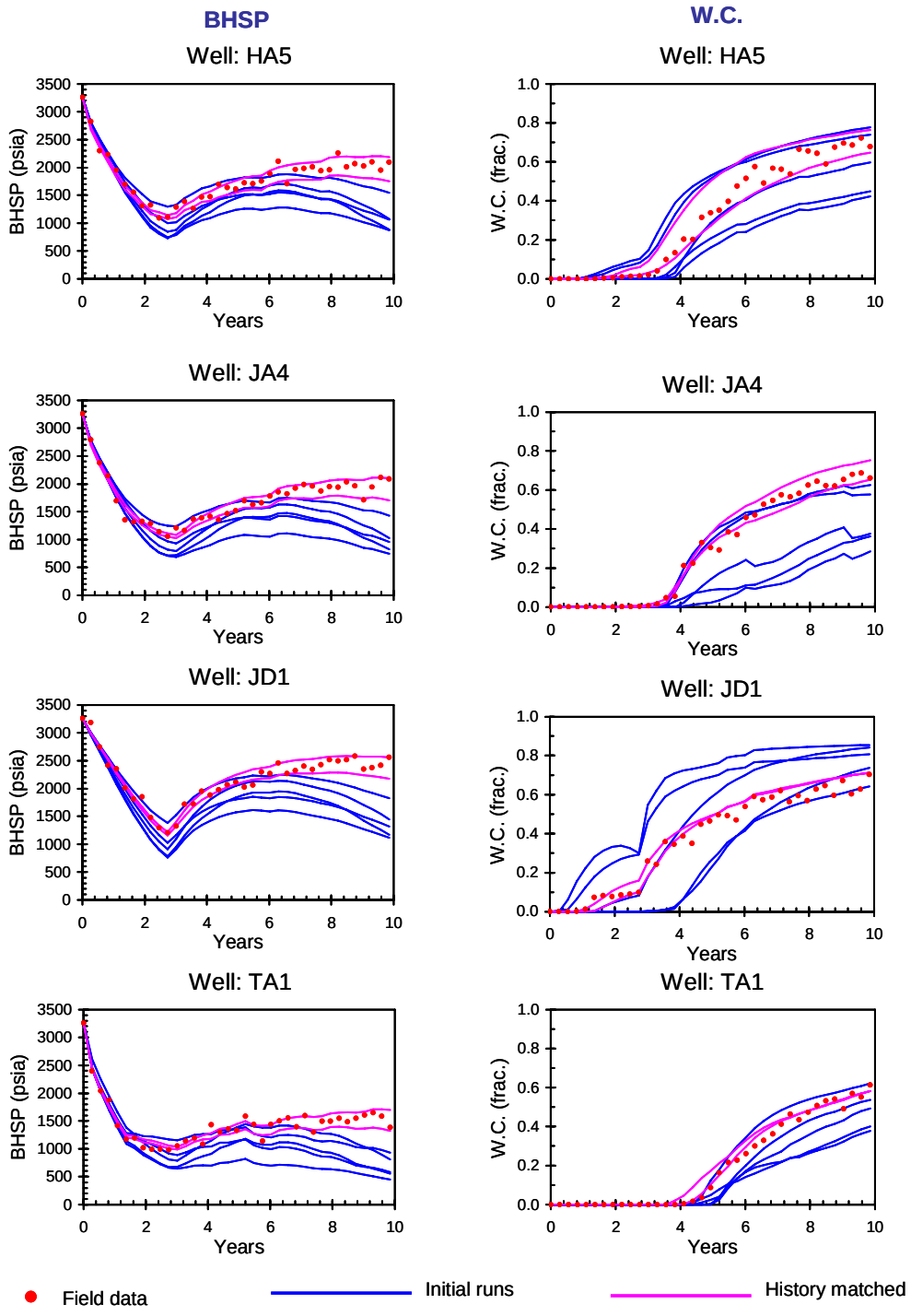

Figure 5.52: History matching result, NA, Case B1 (3/3)

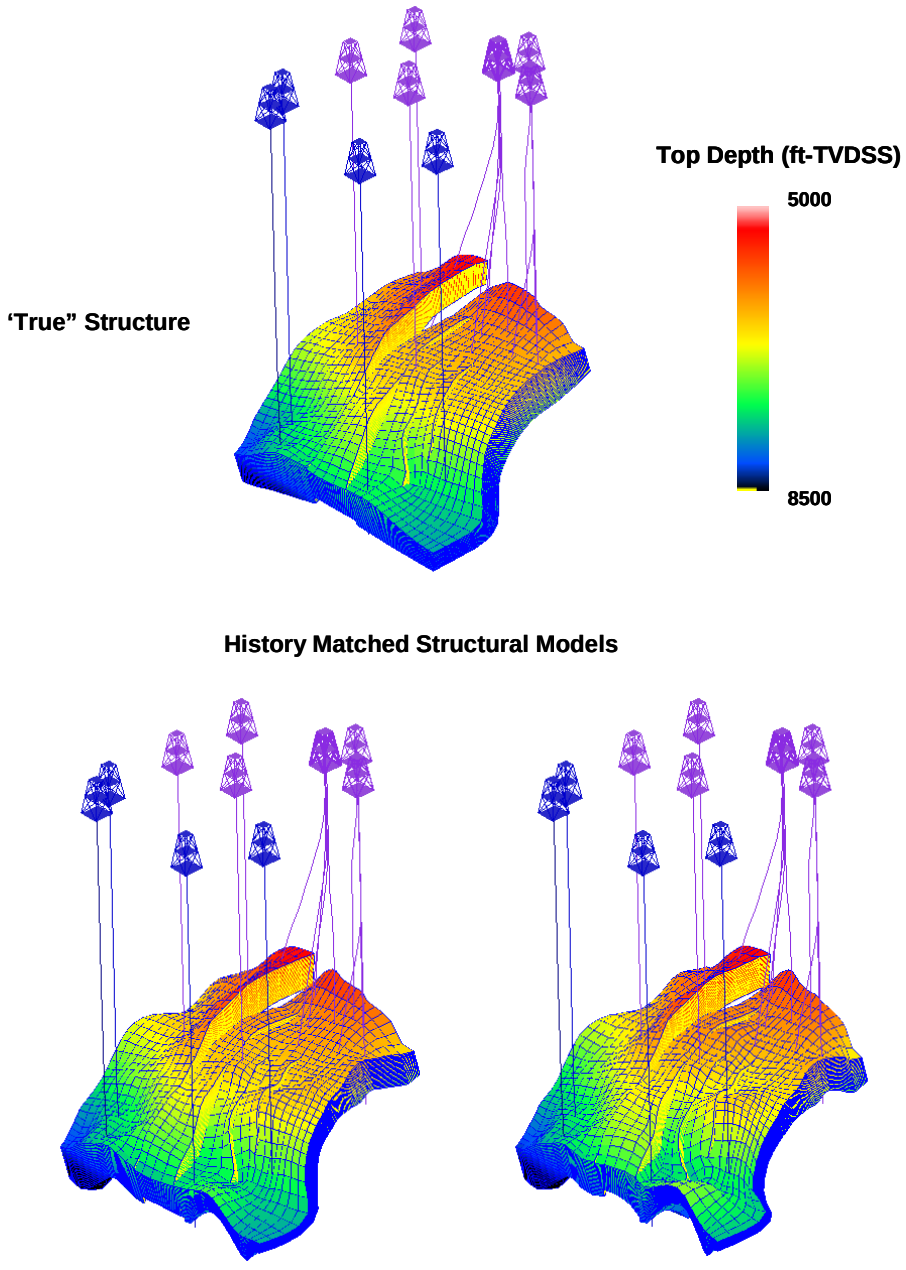

Figure 5.53: History matched structural models, Tree search, Case B1

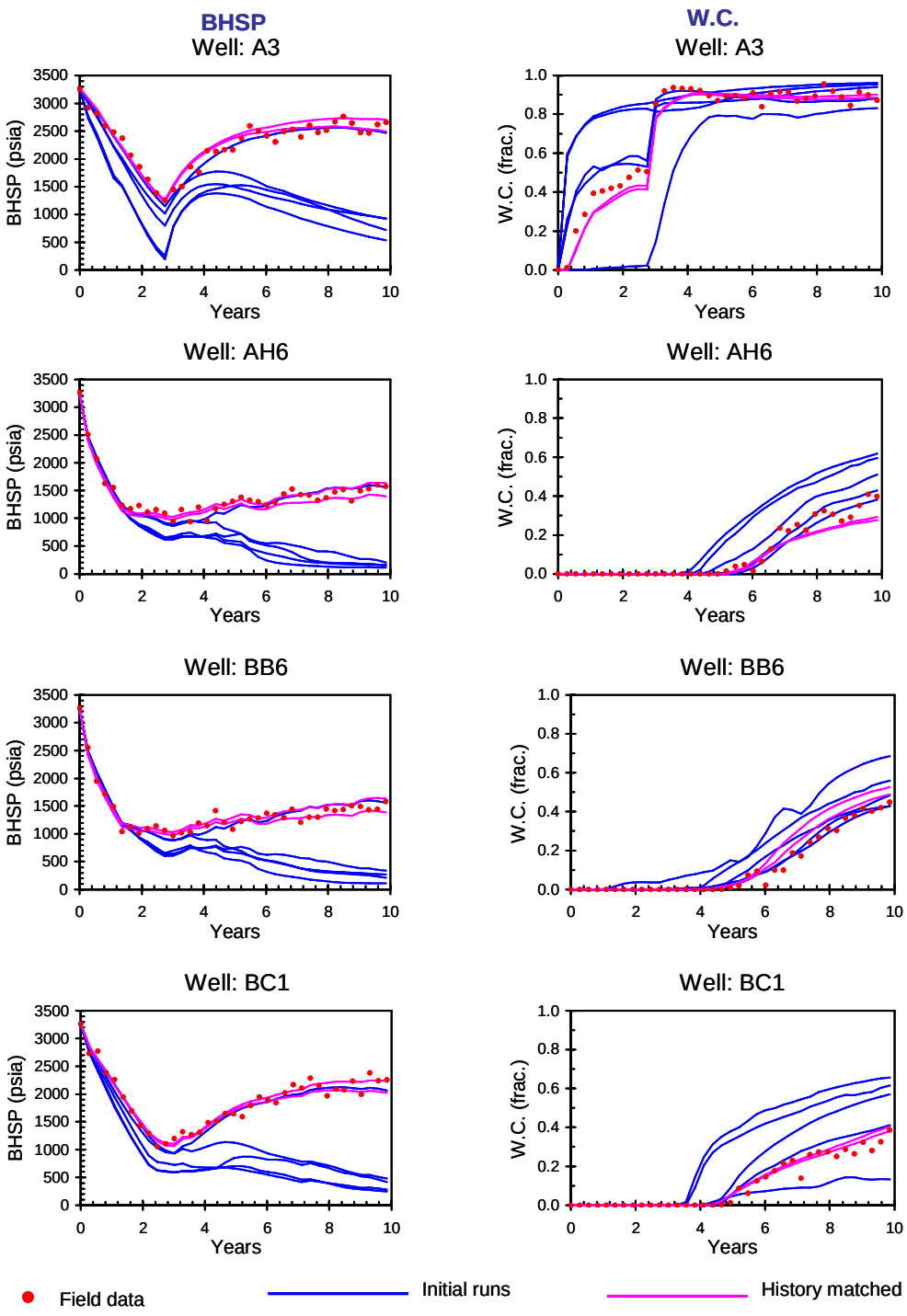

Figure 5.54: History matching result, Tree search, Case B1

(1/3)

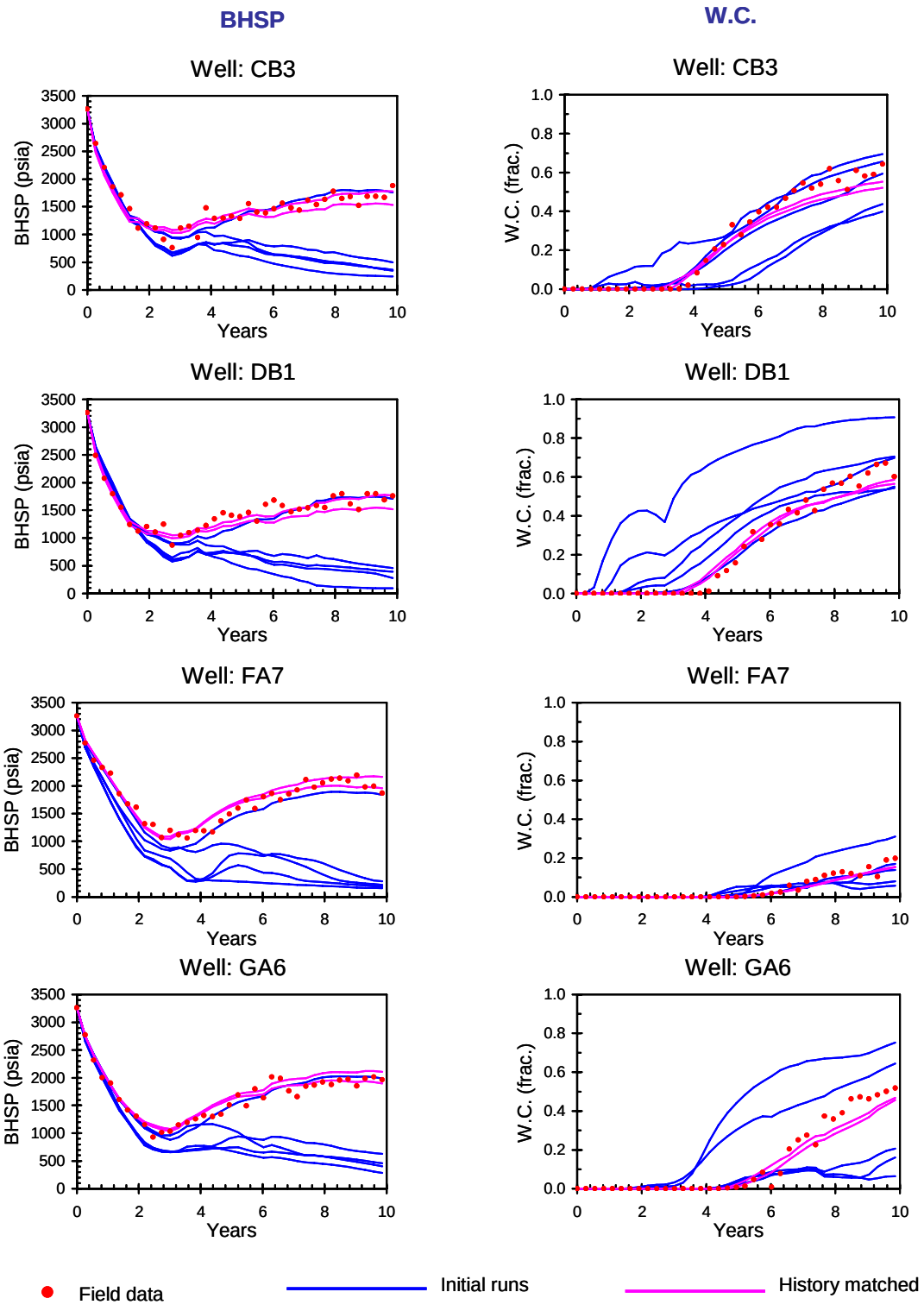

Figure 5.53: History matching result, Tree Search, Case B1 (2/3)

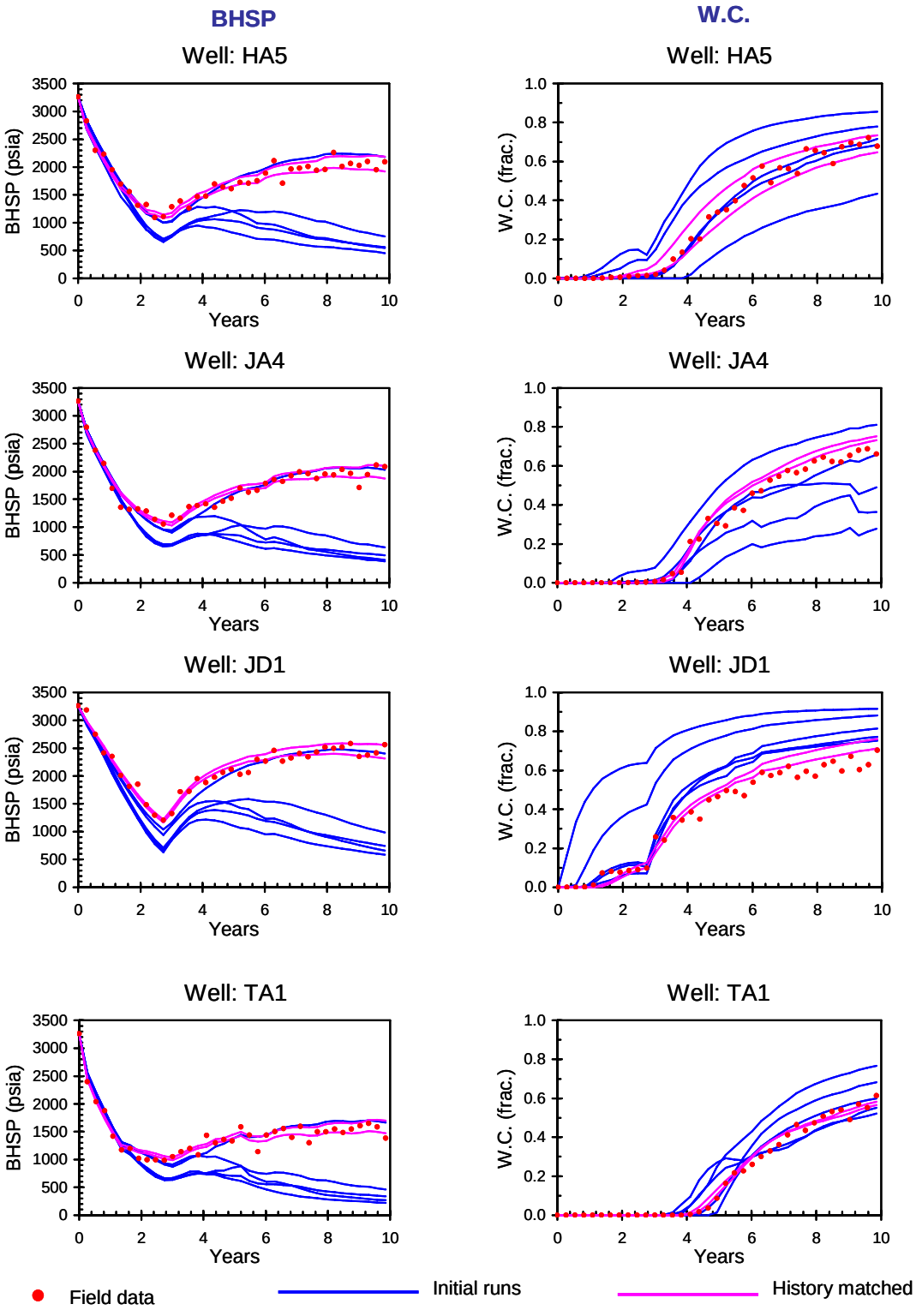

Figure 5.53: History matching result, Tree Search, Case B1 (3/3)

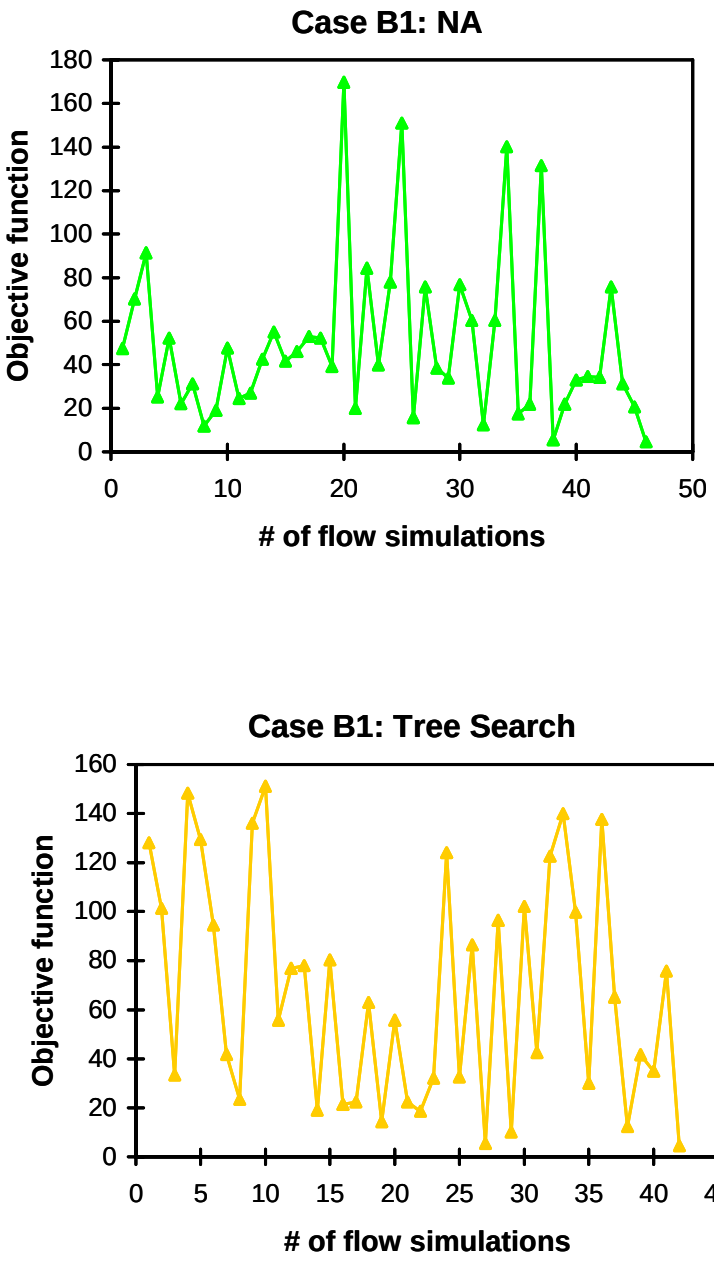

Figure 5.55: Optimization behavior, (a) NA, (b) Tree search, Case B1

5.3.2.5 Case B2

The history matching in this case is performed in the parameter space which does not include the perfect geological scenario, thus considered as a demonstration for a more realistic situation. The history matched structural models are compared to the truth in Figures 5.54, 5.56. The match to the production data is shown in Figures 5.55, 5.57, together with the simulated performance of initial runs. The behavior of the objective function during the optimization is illustrated in Figure 5.58.

The number of flow simulations required for the history matching is presented in Table 5.5.

Table 5.5: Number of flow simulations required for history matching, Case B2

	# of flow simulations required	
	Total	per HM model
NA	47	23.5
Tree search	76	38

The matching accuracy of the match to production data is somewhat less than in Case B1 (Figs. 5.55, 5.57). However, they are still within the acceptable range. As illustrated in Figures 5.54, 5.56, the structural models that achieved the best match are the models derived from Interpretation 3, i.e. the models with more faulting than the “true” geology. The efficiency of the optimization in this case (Fig. 5.58) did not change from that observed in Case B1 (Fig. 5.53), despite the smaller size of the prior uncertainty space.

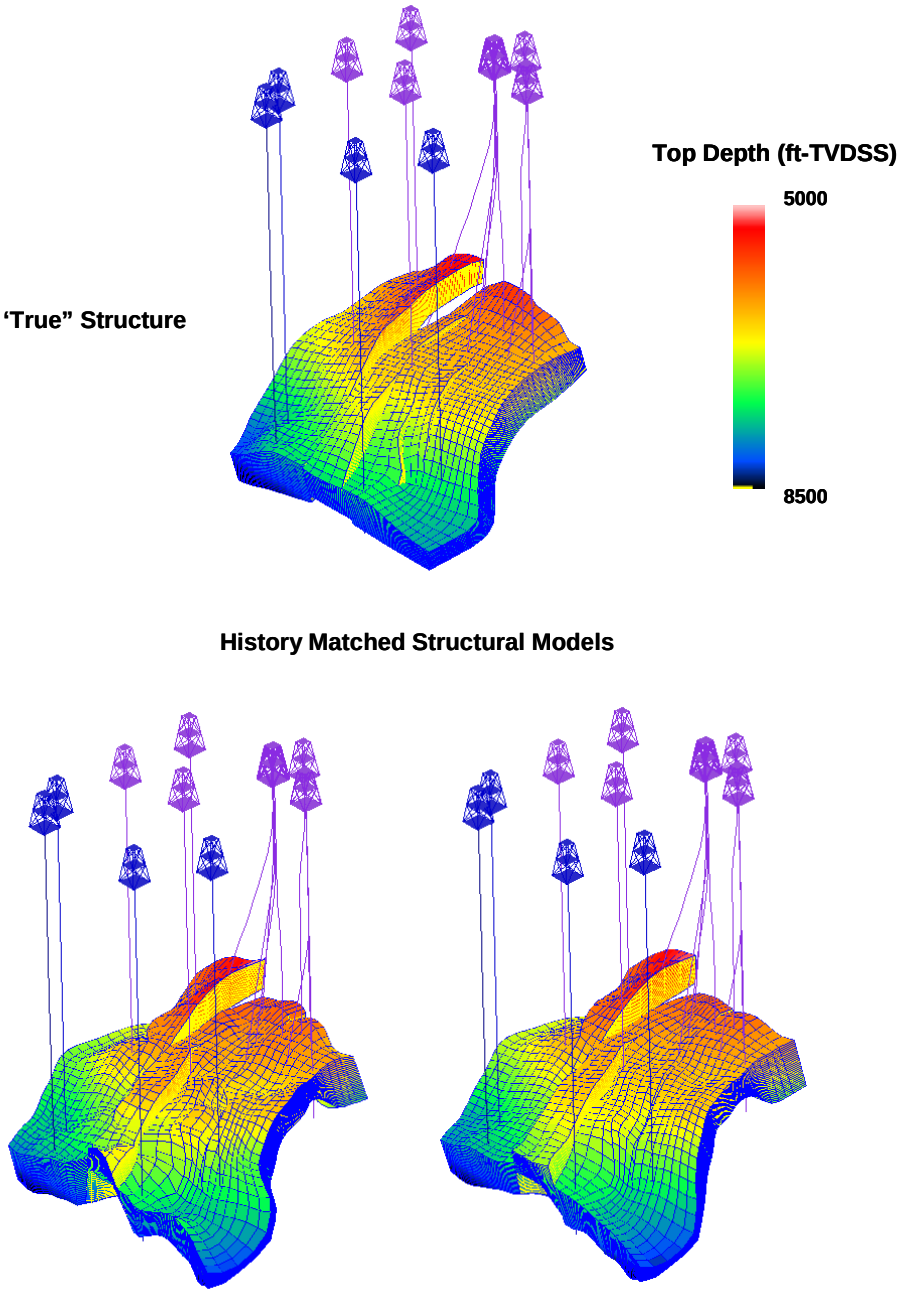

Figure 5.56: History matched structural models, NA, Case B2

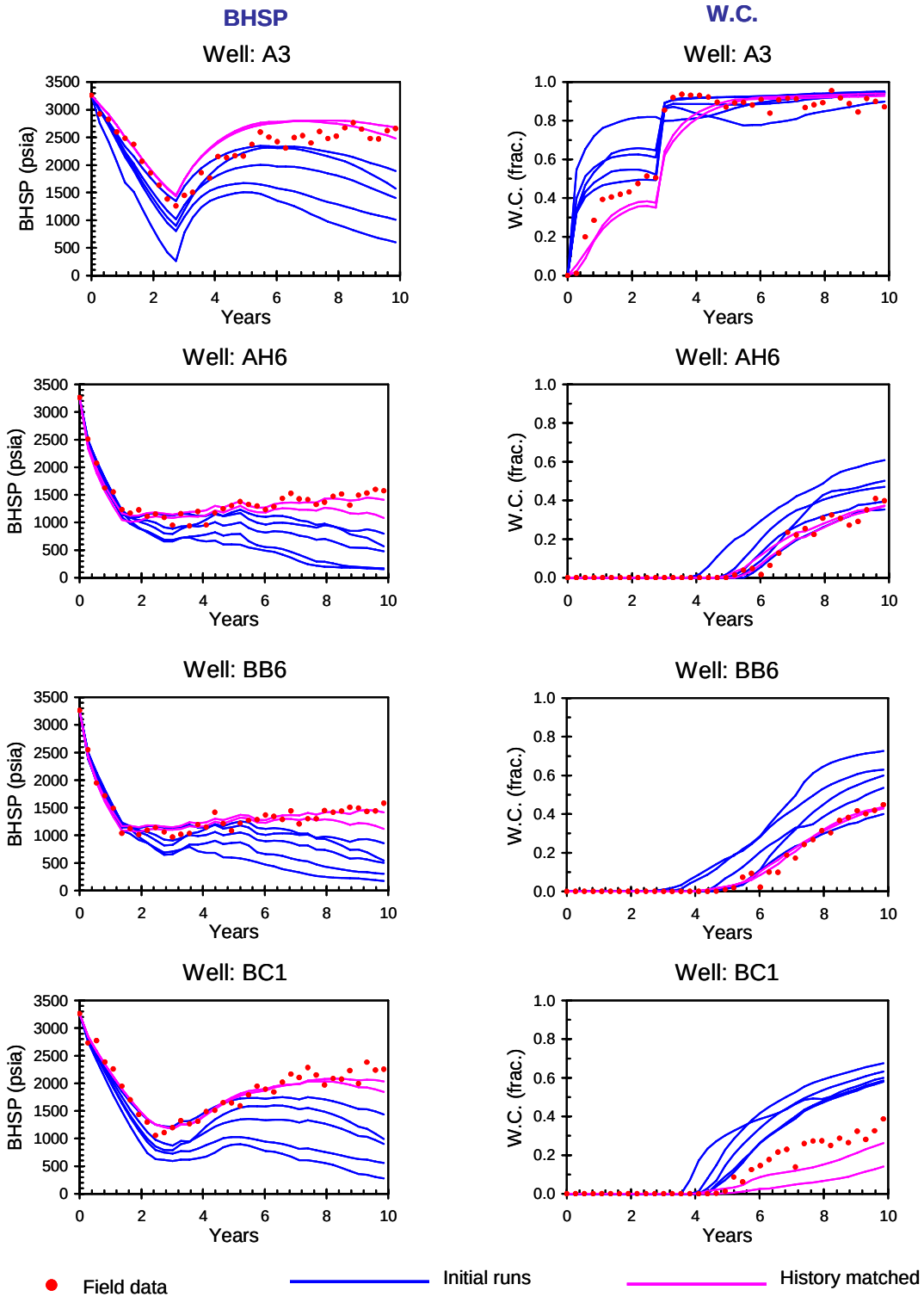

Figure 5.57: History matching result, NA, Case B2

(1/3)

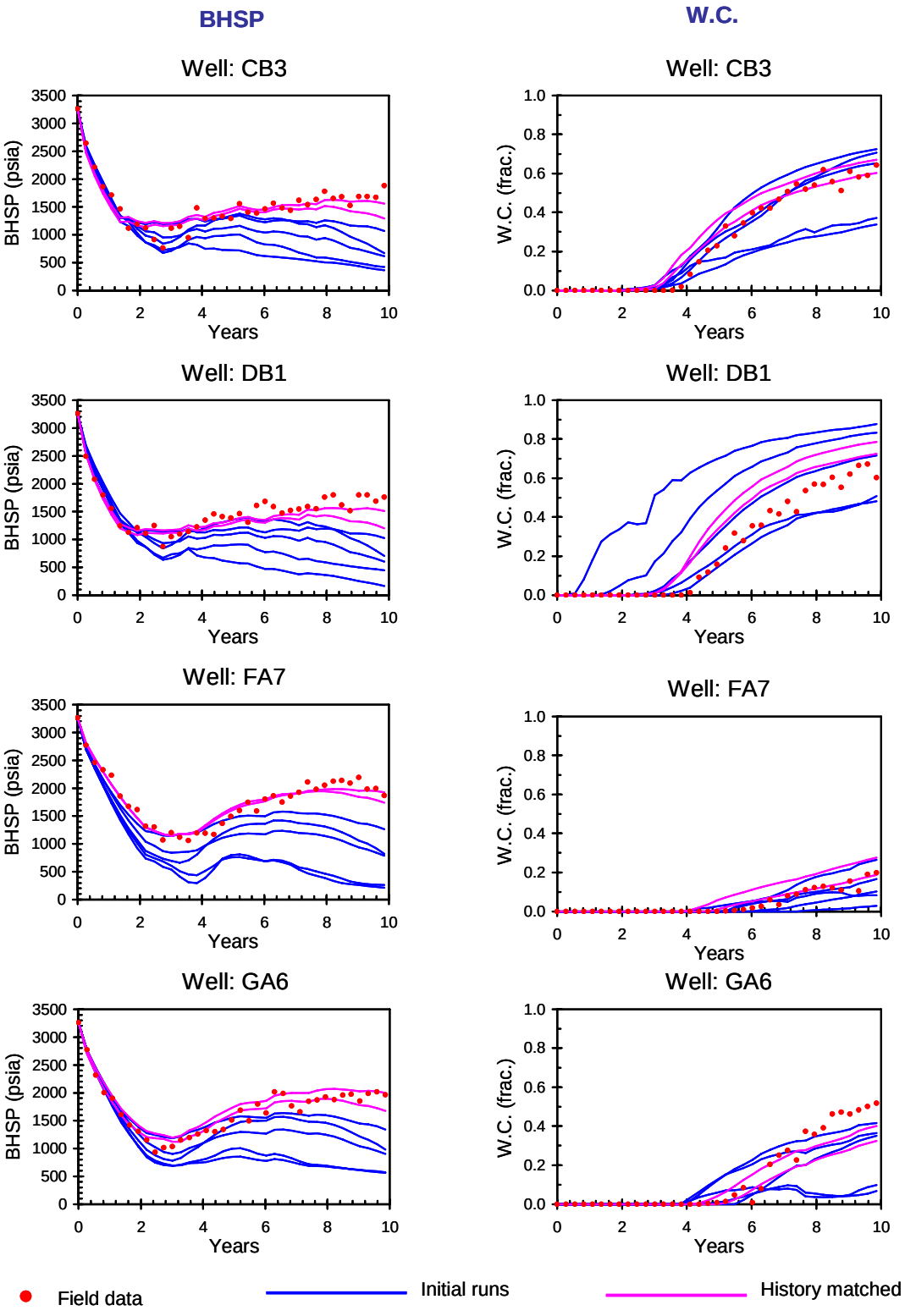

Figure 5.55: History matching result, NA, Case B2 (2/3)

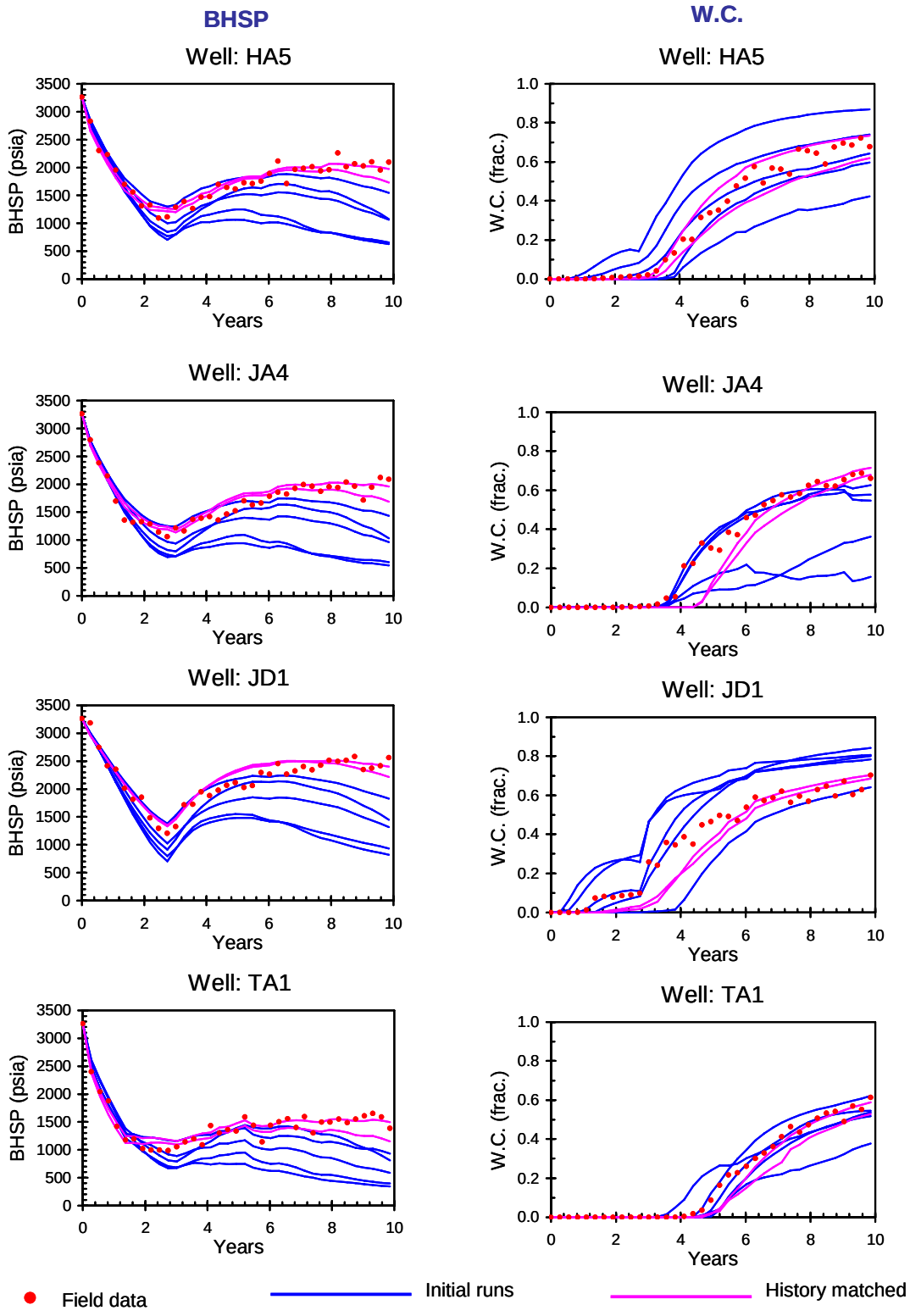

Figure 5.55: History matching result, NA, Case B2 (3/3)

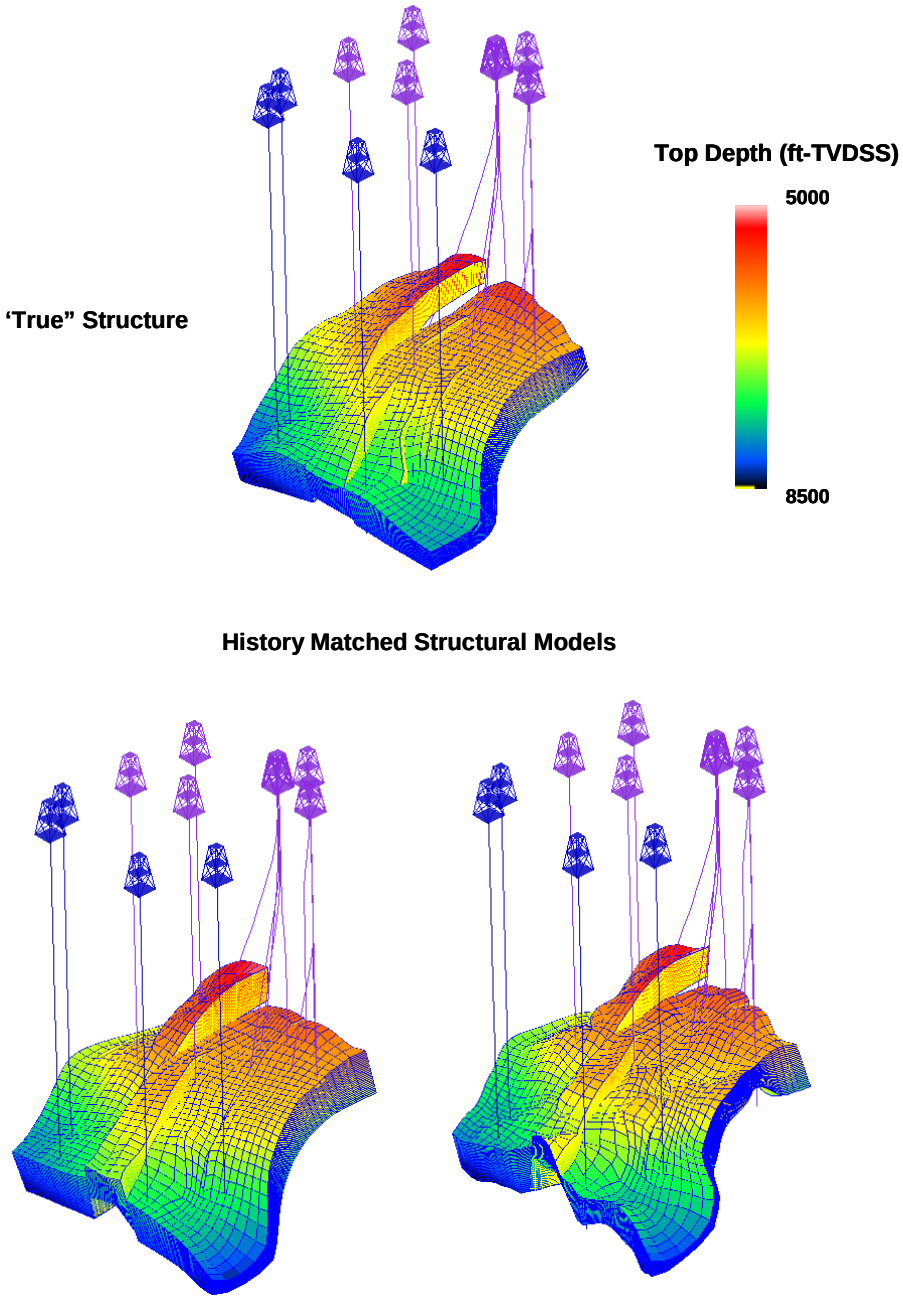

Figure 5.58: History matched structural models, Tree search, Case B2

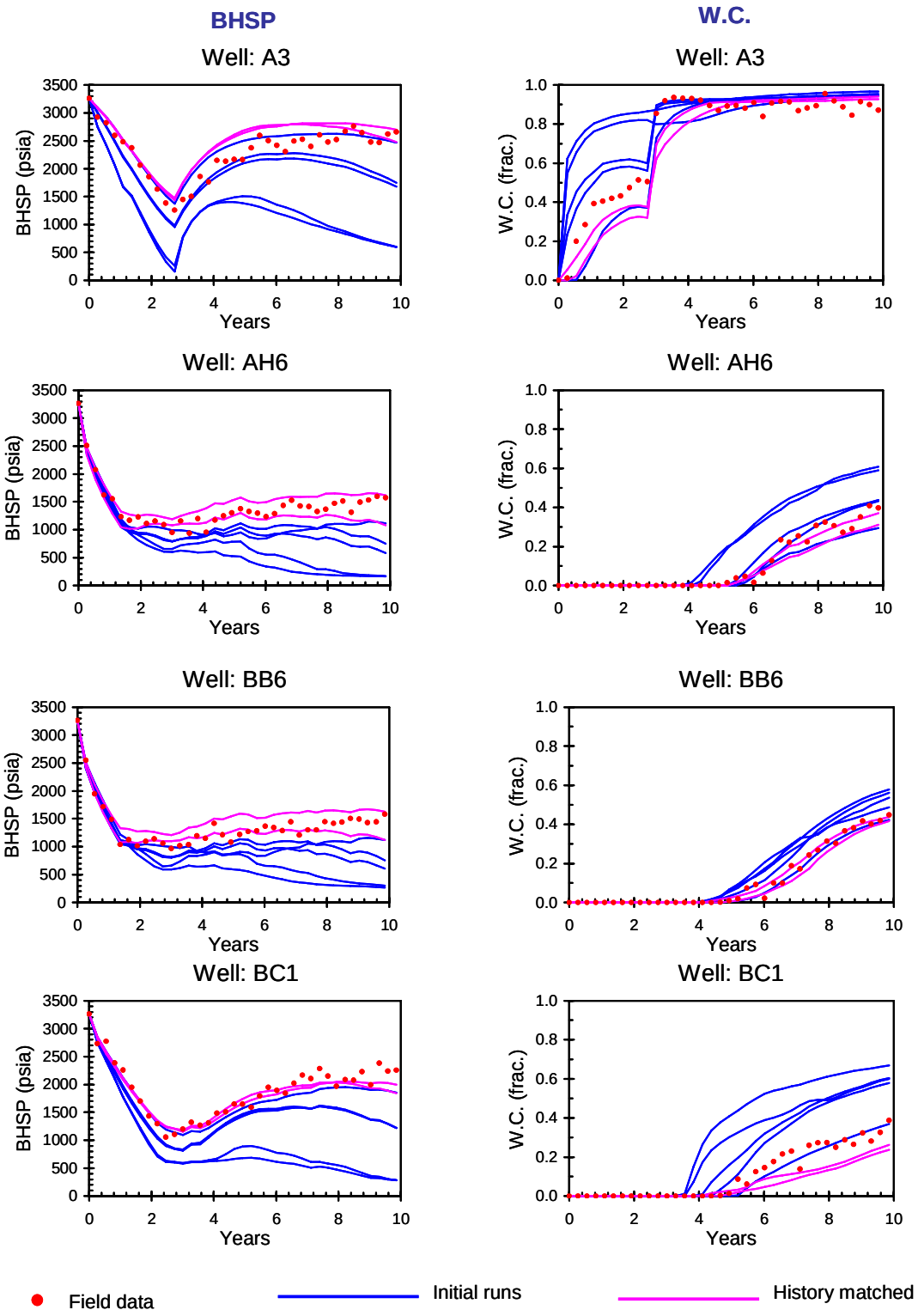

Figure 5.59: History matching result, Tree search, Case B2

(1/3)

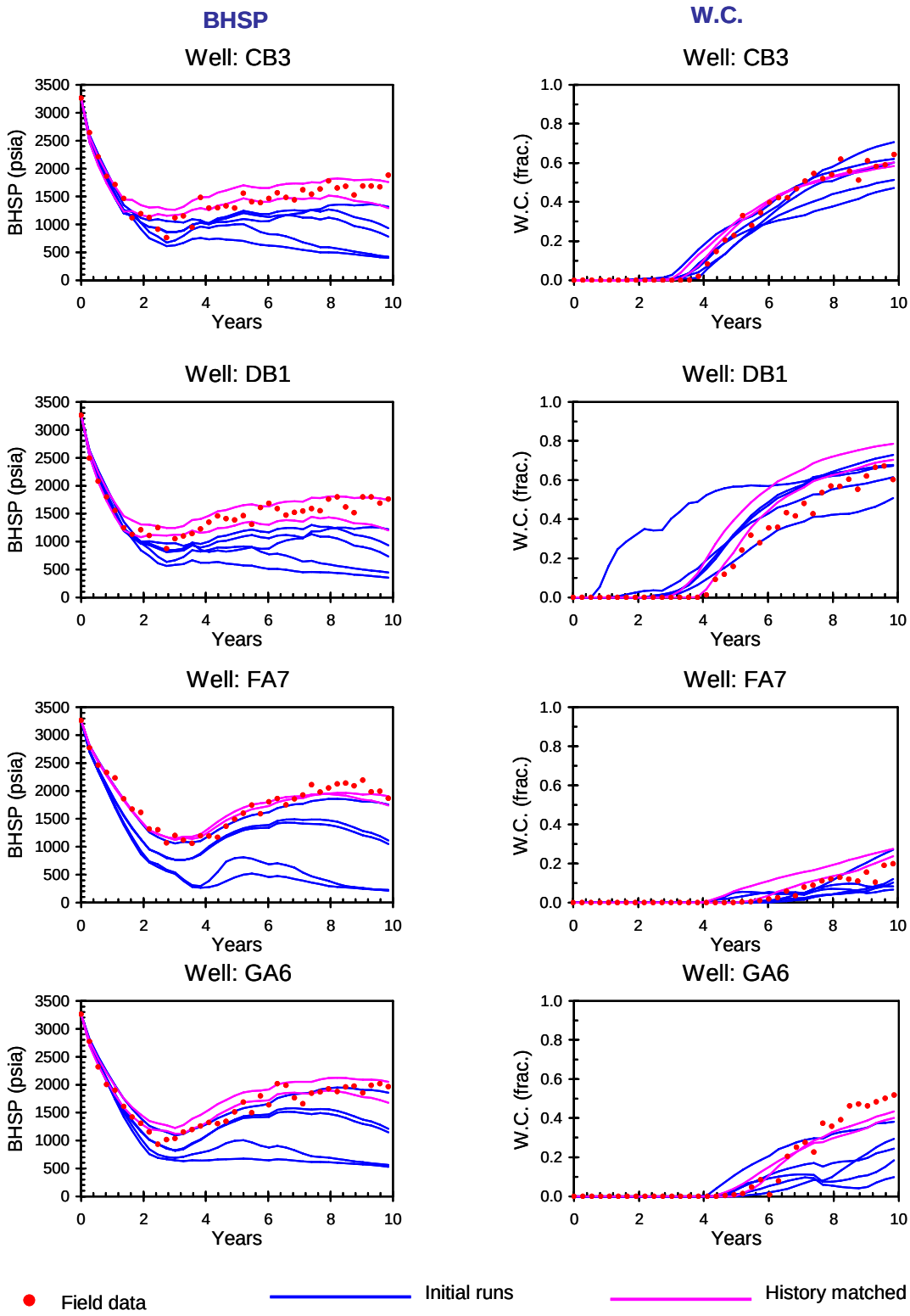

Figure 5.57: History matching result, Tree Search, Case B2 (2/3)

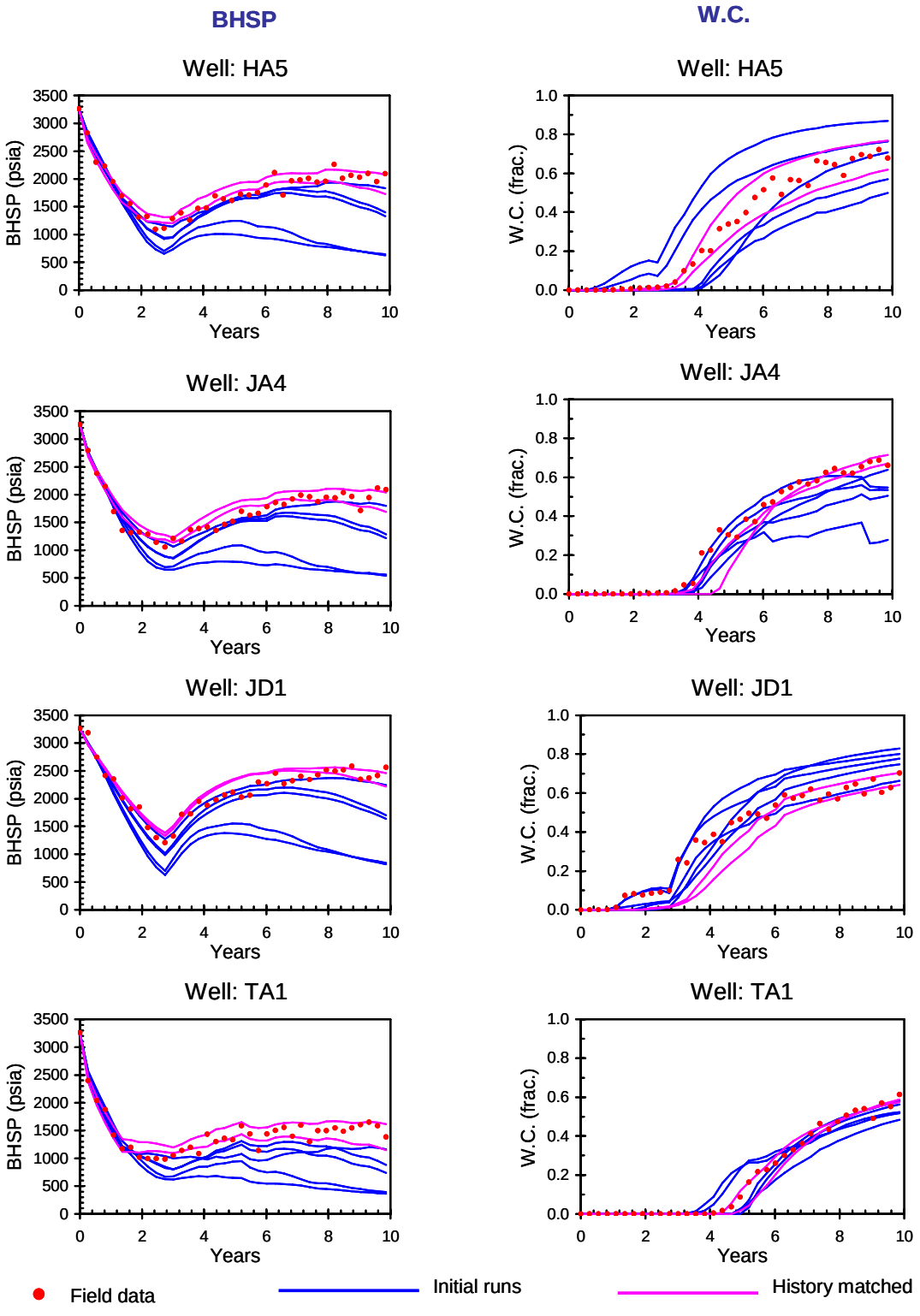

Figure 5.57: History matching result, Tree Search, Case B2 (3/3)

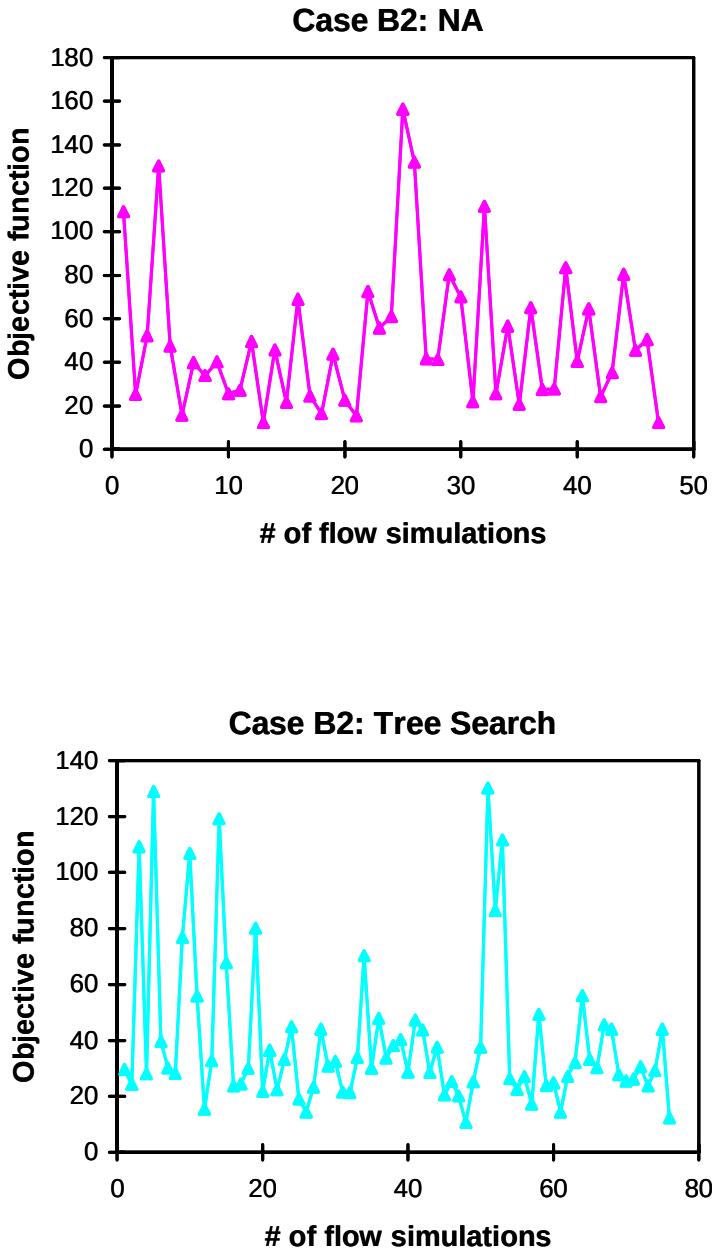

Figure 5.60: Optimization behavior, (a) NA, (b) Tree search, Case B2

5.3.2.6 Optimization Efficiency

The efficiency of optimization is investigated by performing 10 runs of stochastic search in the parameter space of Case B1, by changing the random number seed used for the stochastic search. Both the neighborhood algorithm (NA) and the tree search are run, aiming at finding a single history matched model. Figure 5.59 shows the number of flow simulations required for each run. As depicted in the figure, in Case B, the efficiency of the optimization is not robust compared to Case A even when using a stochastic search. The reason for this reduced robustness in terms of optimization efficiency is not the lack of a structure in the production response in the parameter space. As shown by the variogram of production data in this parameter space (Figure 5.60), which is generated after the history matching for an investigation, the production response exhibits clear structure. However, it is observed that the variance of production response in the parameter space is much smaller in Case B than in Case A (i.e. the sill of the variogram, before standardizing, is much lower), which means that the response surface of production data is relatively flat in this space. This is because, unlike Case A, all of the prior structural models are built without any completely sealing faults (known from the historical pressure). As a consequence, the dynamic change in simulated production between models with sealing faults and without sealing faults is lacking in Case B. Due to this flatness of the response surface, a stochastic search tends to be more random compared to Case A. This result indicates that the history matching method proposed in this dissertation is more effective and efficient when larger uncertainty (e.g. multiple geological scenarios very different from each other) is considered in a prior uncertainty model.

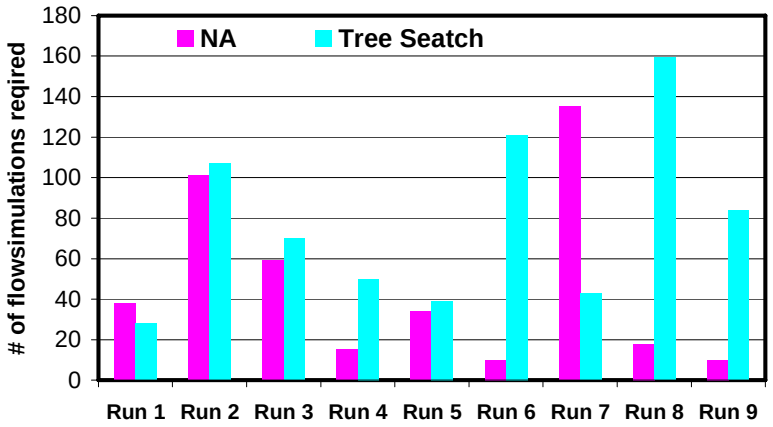

Figure 5.61: Optimization efficiency, NA and Tree search, Case B1

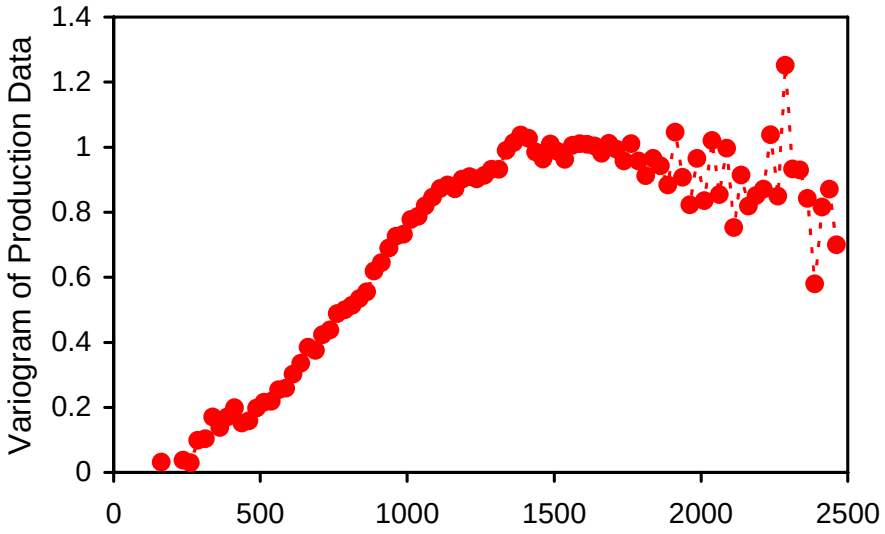

Figure 5.62: Variogram of production data, Case B1

Chapter 6

Conclusions and Future Work

The importance of structural uncertainty evaluation has been well recognized in both geological/geophysical domains and reservoir engineering domain. The quantative evaluation of structural uncertainty is already proposed in the area of geoscience and applied to the evaluation of hydrocarbon in-place uncertainty. However, this uncertainty modeling method has been restricted to an assessment of uncertainty related to geological/geophysical data and interpretation. In other words, this structural uncertainty modeling has rarely been extended to the dynamic data integration. As a result, structural uncertainty models build by geophysists/geologists are often neglected by reservoir engineers, although the engineers also realize the importance of structural uncertainty. Reservoir models for flow simulation are built by fixing a structural model to single deterministic reservoir geometry and then history matched by modifying other reservoir parameters such as permeability. Or at most, history matching is performed by perturbing reservoir geometry around a single deterministic structural interpretation.

This dissertation is motivated by the need to extend the structural uncertainty evaluation to dynamic data integration, and proposes a new method/workflow for structural uncertainty modeling which links a geophysical/geological approach to history matching. The proposed method/workflow is designed to account for multiple geological/geophysical alternatives provided as a prior model structural uncertainty. This is as opposed to defining a history matched model by perturbation around a single interpretation. Provided with the prior structural uncertainty model from geological/geophysical methods, the history matching serves as a way to screen out structural models/interpretations that can not explain past production behavior. By this way, the structural uncertainty can be reduced through the incorporation of the information from the production data.

A new workflow is proposed in Chapter 1. This workflow consists of 1) the generation of multiple structural interpretations accounting for seismic imaging uncertainty and interpretation uncertainty, 2) the prior structural uncertainty modeling by the stochastic perturbation of horizons and faults starting from the multiple interpretations, and 3) history matching by honoring the prior uncertainty model.

A geophysical methods to model seismic imaging uncertainty are reviewed in Chapter 2. The methodology focuses on uncertainty in seismic velocity, which is a key unknown parameter to seismic imaging. In this workflow, structural uncertainty is modeled as a set of multiple seismic images through multiple migrations of seismic data from alternative velocity models. The CPU cost for multiple migrations is still prohibitive for large-scale applications. However, the structural uncertainty modeling by assessing velocity uncertainty reviewed in Chapter 2 is one of the most promising methods to provide multiple structural interpretations for the proposed workflow.

In Chapter 3, a geostatistical method for semiautomatic seismic interpretation is proposed and applied to the multiple seismic images obtained by the method of Chapter 2. In this approach, the part of interpretation process is automated to reduce the modeling cost. The key idea in Chapter 3 is to retrieve the pattern-to-pattern correlation information from the database trained on a pair of 1) manual interpretation by an expert and 2) the seismic image used for the interpretation, and utilize it as a guidance for automatic seismic interpretation. It is shown that this approach is also effective to cases where the training seismic image and conditioning seismic image exhibit significant difference from each other. This effectiveness of the approach is achieved by introducing a dual-scale pattern recognition approach into the SIMPAT algorithm.

The methodology of Chapter 3 is designed following a traditional seismic interpretation approach; i.e., the interpretation on two-dimensional cross-sectional views sliced from a three-dimensional seismic image. However, the SIMPAT-aided semiautomatic seismic interpretation has the potential to be applied for full three-dimensional seismic interpretation. The principle of the techniques, namely pattern-to-pattern correlation and pattern recognition, is applicable to any dimension. Thus, in principle, it is possible to simulate proximity maps of fault surfaces and horizon surfaces in three-dimensional space, conditioning to three-dimensional volume of seismic amplitude. Once three-dimensional proximity maps are simulated and smoothed, the fault surfaces and horizon surfaces can be extracted from the proximity maps in the form of point sets, by sampling points at the proximity of fault/horizon locations indicated by the proximity maps. Recently, Frank (2006)

proposed a new method to reconstruct fault/horizon surfaces from point data (e.g. seismic interpretation result expressed as point sets). This methodology is proposed as a new semiautomatic three-dimensional geomodeling algorithm and applicable for modeling complex discontinuous surfaces such as faulted horizons. Frank (2006) showed that the method is robust for noisy and sparse point data. His method could be coupled with the SIMPAT algorithm to design a semiautomatic seismic interpretation in three-dimensional space. The expected challenge in this approach is the pattern reproduction accuracy of the SIMPAT simulation in three-dimensional space, since multiple-point geostatistical methods generally experience greater difficulty to reproduce three-dimensional training image patterns. The modeling accuracy of the SIMPAT algorithm to simulate proximity maps in three-dimensional space, conditioning to three-dimensional amplitude volume, is subject to further investigation.

In Chapter 4, a new method to parameterize geological architecture for solving an inverse problem is proposed. This methodology is a key technology to implement the workflow proposed in this dissertation that allows the posterior structural modeling through dynamic data integration. The central idea of this new parameterization is to replace Euclidian distance defined in Cartesian parameter space by a distance function (similarity measure) which is not restricted to the traditional vector-form representation. By eliminating the need to parameterize model realizations using a vector form, this new parameter space accommodates any type and variability of geological architecture, hence enables the inversion of discrete parameters such as outcomes from multiple geological scenarios. As a consequence, a greater flexibility in the prior model definition is achieved as opposed to the traditional parameterization techniques. Though the proposed parameter space is defined only by a distance metric, not by dimension/direction, it is shown through the synthetic application examples that an efficient stochastic search can be achieved solely relying on a distance metric. This distance metric can be tailored to the problem at hand. Given a proper choice of distance metric, the spatial structure of forward model response is achieved in the parameter space, allowing an effective stochastic search (not a random search).

In Chapter 5, the workflow of the proposed method for modeling reservoir structure, confronting several structural interpretations of geophysical/geological data with dynamic production data, is implemented through synthetic reservoir cases. This workflow relies on the structural uncertainty modeling techniques using geostatistical methods. It is shown that, by parameterizing this uncertainty model using the Hausdorff distance, an efficient history matching can be achieved by means of a stochastic search, honoring the modeled prior structural uncertainty. The workflow

enables to model complex reservoir structures by fully integrating geophysics, geology and reservoir engineering data. It also links the geophysical/geological approach for uncertainty modeling and automatic history matching. The methodology does not history match a reservoir structure by a mere perturbation from a single structural interpretation: it considers multiple alternatives of seismic processing/interpretation.

The synthetic reservoir cases of Chapter 5 treat other reservoir parameters, such as permeability and relative permeability, as “known” parameter, which is unrealistic in real reservoir cases. In real reservoir applications, a history matching may not be achieved by fixing such reservoir parameters to initial models especially when the number of producers is large. The proposed method for history matching of reservoir structure should be implemented as a first stage screening process of a hierarchical history matching workflow: i.e. we history match reservoir structure first by freezing other reservoir properties and eliminate those structural interpretations that can not explain historical production data. Then, by fixing structural geometry, we proceed to history match other reservoir properties which are of smaller scale. The aim of this first stage screening process is not to obtain a detailed history match of production data. Therefore, at this stage, it is a practical idea to use a coarse reservoir model grid and low resolution petrophysical properties models (without detailed geostatistical modeling) since the primary interest here is only in reducing the structural uncertainty through the incorporation of production data. Then, the CPU spent on flow simulation would be much less than a traditional flow simulation on a detailed petrophysical model. However, on the other hand, it is critical to construct a “rich” prior structural uncertainty model which covers a full range of structural uncertainty; otherwise, this first stage screening process may result in a “wrong” structural model. The synthetic reservoir study of Chapter 5 showed that the proposed history matching method is more efficient in terms of CPU cost when larger uncertainty range is considered as a prior uncertainty. Thus it is recommended not to restrict the prior uncertainty model to a single structural interpretation: multiple interpretations that cover rather extreme uncertainty range would work better in the proposed workflow.

Part of the question to be addressed will be: what type of production data should be used to constrain the structural framework? Such data should be selected focusing on production data that is most impacted by reservoir geometry. Good candidates, in addition to historical pressure data and water cut data, are interference test data, tracer test data, RFT data, TDT log etc. since these data provides information about flow communication between fault compartments or some information about juxtaposition of layers across faults. In reality, reservoir structure is not the only

parameter which affects flow communication between fault compartments. The magnitude of the fault seal due to shale gouge is another factor. Also, faults are only conductive when it is critically stressed (Zoback, 2001). The former can be modeled as a function of fault throw (Yielding et al., 1997; Manzocchi et al., 1999). With this technique, the magnitude of fault seal due to shale gouge is coupled with the fault geometry thus can be perturbed in history matching by the perturbation of structural geometry. The latter can be taken into account beforehand by evaluating the current stress status on fault surfaces based on the field stress information obtained by analyzing borehole failure while drilling (Zoback, 2001).

The most important contribution of this work is the proposal of a new model parameterization method by means of a distance function. In this dissertation, this parameterization method is motivated by the needs to 1) accommodate complex geological architecture (such as faulted horizons) in a parameter space for an inverse problem and 2) consider multiple geological/geophysical alternatives as a prior uncertainty. Also, the distance function is chosen to achieve a particular history matching goal, i.e. the inversion of reservoir structure from production data. However, the idea of the use of a distance function for model parameterization inspires further research directions. For example, Scheidt and Caers (2007) proposed a new method to select representative reservoir models from a large set of model realizations by parameterizing the model space using a distance function, in order to evaluate future production performance uncertainty. Park and Caers (2007) proposed a new distance function for solving an inverse problem which reduces the dimensionality of a parameter space, and also structures the parameter space such that the number of local minima is reduced. Also, the history matching workflow as a screening of reservoir structural model from production data can be extended to a screening of scenario (e.g. training image) as suggested by Park and Caers (2007).

APPENDIX A

Hausdorff Distance

The Hausdorff distance measures the spatial distance between the point set A and point set B. Let a_i and b_i be any point that belongs to the point sets A and B, respectively. The locations of points a_i and b_i are denoted as $\mathbf{u}_{ai}$ and $\mathbf{u}_{bi}$. Then, spatial distance between points a_i and b_i is defined as a vector norm $\|\mathbf{u}_{ai} - \mathbf{u}_{bi}\|$, i.e. Euclidean distance between the locations of points a_i and b_i. Using this definition, the spatial distance measured from a point a_i to the point set B, $d(a_i, B)$, is defined as:

$$d(a_i, B) = \min_{b_i \in B} \left\| \mathbf{u}^{a_i} - \mathbf{u}^{b_i} \right\| \qquad \text{(A1)}$$

Using Eq.A1, the distance measured from the set A to the set B is defined as:

$$d(A, B) = \max_{a_i \in A} d(a_i, B) \qquad \text{(A2)}$$

It should be noted that the distance measured from the set A to the set B, d(A, B), and the distance measured from the set B to the set A, d(B, A), can be different. The Hausdorff distance $d_H(A, B)$ is defined as:

$$d_H(A, B) = \max\{d(A, B), d(B, A)\} \qquad \text{(A3)}$$

The Hausdorff distance is applicable for any two-dimensional or three-dimensional object as long as it can be represented as a point set. Thus it covers various types of geological architecture. When applied to the channel system consisting of binary facies, the channel objects are represented as a set of points where each point corresponds to a foreground facies pixel. If the depositional system consists of more than 2 facies, the geological architecture can be expressed by a point set that consists of edge pixels extracted from a model realization. To measure the similarity of a geologic structure (such as faulted horizons), one extracts corner points of stratigraphic grid to represent a structure as a point set. Depicted in Figure A are some examples of the Hausdorff distance (d_H) computed between model realizations of channel system.

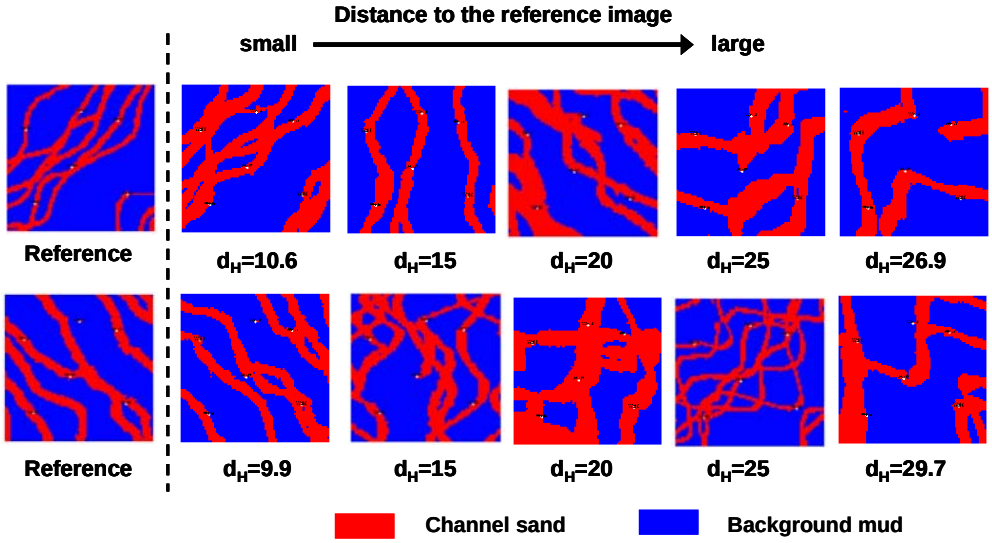

Figure A: Example of Hausdorff distance

Bibliography

Allen, J.R.L.: Studies in fluviatile sedimentation : an exploratory quantitative model for the architecture of avulsion-controlled alluvial suites. Sedimentary Geology, v. 21, p. 129-147 (1978)

Arpat, B. G.: Sequential simulation with patterns. unpbl. doctoral dissertation, Stanford University (2005)

Bridge, J.S., Leeder, M.R.: A simulation model of alluvial stratigraphy. Sedimentology, v. 26, no. 5, p. 617-644 (1979)

Boucher, A: The Formalism of Algorithm-Driven Random Function. SCRF Report. Stanford center of Reservoir Forecasting (2007)

Caers, J.: History matching under a training image-based geological model constraint. SPE Journal, SPE # 74716, v. 8, no. 3, p. 218-226 (2003)

Caers, J. and Hoffman, T.: The probability perturbation method - A new look at Bayesian inverse modeling. Math. Geol., v. 38, no. 1, p. 81-100 (2006)

Caers, J., Hoffman, T., Strebelle, S., and Wen, H.W.: Probabilistic integration of geologic scenarios, seismic, and production data—a West Africa turbidite reservoir case study. The Leading Edge, v. 25 (3), p. 240 – 244 (2006)

Caers, J., Strebelle, S. and Payrazyan, K.: Stochastic integration of seismic data and geologic scenarios: a West Africa submarine channel saga. The Leading Edge, v. 22 (3), p. 192-196 (2003)

Castro, S., Caers, J., Otterlei, C., Hoye, T., Andersen, T., Gomel, P.: A probabilistic integration of well log, geological information, 3D/4D seismic and production data: Application to the Oseberg Field. Proceedings of SPE Annual Technical Conference and Exhibition, San Antonio, SPE #103152 (2006)

Charles, T., Guéméné, J.M., Corre, B., Vincent, G., Dubrule O.: Experience with the quantification of subsurface uncertainties. Paper presented at SPE Asia Pacific Oil and Gas Conference and Exhibition, Jakarta, Indonesia, SPE 68703, 17-19 April 2001

Christie, M., Demyanov, V., Erbas, D.: Uncertainty qualification for porous media flows. Jour. Comp. Phys. 217 (1), 143-158 (2006)

Chu, L., Reynolds, A. C. and Oliver, D. S,: Reservoir description from static and well-test data using efficient gradient methods. Proceedings of SPE International Meeting on Petroleum Engineering, Beijing, SPE #29999 (1995)

Claerbout, J. and Fomel, S.: Image estimation by example: Geophysical soundings image construction: multidimensional autoregression. Lecture Note & Electronic publishing: http://sepwww.stanford.edu/sep/prof/index.html (2004)

Clapp, R. G.: Multiple realizations and data variance: Successes and failures. Stanford Exploration Project Report. 113 (2003)

Clapp, R. G.: Multiple realizations: Model variance and data uncertainty. Stanford Exploration Project Report. 108 (2001)

Clapp, R. G.: Velocity uncertainty: Non-linearity and the starting guess. Stanford Exploration Project Report. 117 (2004)

Corre, B., Thore, P., de Feraudy V., Vincent, G.: Integrated uncertainty assessment for project evaluation and risk analysis. Paper presented at SPE European Petroleum Conference, Paris, France, SPE 65205, 24-25 October 2000

Demyanov, V., Subbey, S. Christie, M.: Uncertainty assessment in PUNQ-S3: Neighbourhood algorithm framework for geostatistical modeling. In: Proceedings of the 9th European Conference on the Mathematics of Oil Recovery, Cannes, France, 31. Aug - 2. Sep 2004

Deutsch, C. V. and Wang L.: Hierarchical object-based stochastic modeling of fluvial reservoirs. Math. Geol., v. 28, no. 7, p. 857-880 (1996)

Dubuisson, M. P., Jain, A. K.: A modified Hausdorff distance for object matching. In: Proceedings of the 12th International Conference on Pattern Recognition, A, 566-568, Jerusalem, Israel, 9-13 October 1994

Earth Decision, GOCAD Earth Decision Suite 2.1 User Guide

Frank, T.: Advanced visualization and modeling of tetrahedral meshes. Doctoral dissertation, School of Geology, Nancy Université (2005)

Georgsen, F. and More, H.: Combining fiber processes and Gaussian random functions for modeling fluvial reservoirs. *in* Soares, A., ed., Geostatistics Troia '92: Kluwer Academic Publications, p. 425-439 (1993)

Grubb, H., Tura, A., Hanitzsch, C.: Estimating and interpreting uncertainty in migrated images and AVO attributes. Geophysics. 66, 1280-1216 (2001)

Guardiano, F. and Srivastava, R.M.: Multivariate geostatistics: beyond bivariate moments, *in* Soares, A., ed., Geostatistics Troia '92: Kluwer Academic Publications, v. 1, p. 133-144 (1993)

Hoffman, T.B., Strebelle, S. Wen, X-H and Caers, J.: Geologically consistent history matching of a deepwater turbidite reservoir. Proceedings of SPE Annual Technical Conference and Exhibition, Dallas, SPE #95557 (2005)

Holden, L., Hauge, R., Skare, O., Skorstad, A.: Modeling of fluvial reservoirs with object models. Math. Geol., v. 30, no. 5, p. 473-496 (1998)

Lecour M., Cognot R., Duvinage I., Thore P., Dulac J-C.: Modeling of stochastic faults and fault networks in a structural uncertainty study. Petroleum Geoscience. 7(supplement), 31-42 (2001)

Lee, T. Y. and Seinfeld, J. H.: Estimation of two-phase petroleum reservoir properties by regularization. Jour. Comp. Phys., v. 69, p. 397-419 (1987)

Li, R., Reynolds, A.C., Oliver, D.S.: History matching of three-phase flow production data. SPE Journal, SPE #87336, v. 8, no. 4, p. 328-340 (2003)

Mackey, S.C., Bridge, J.S.: Three-dimensional model of alluvial stratigraphy: Theory and application. Journal of Sedimentary Research, v. B65, no. 1, p. 7-31.

Maharja, A.: Assessing uncertainty on net-to-gross at the appraisal stage: application to a West Africa deep-water reservoir. SCRF report 16, Stanford University (2006)

Mavko, G, Mukerji, T, and Dvorkin, J.: The rock physics handbook. Cambridge (1998)

Moosegard, K. and Tarantola, A.: Monte Carlo sampling of solutions to inverse problems. J. Geophys. Res., B, v. 100, p. 12431-12447 (1995)

Oliver, D. S., He, N. and Reynolds, A. C.: Conditioning permeability fields to pressure data. *in* Leoben, M., Heinemann, Z. E., and Kriebernegg, M., ed., Proceedings of the 5th European Conference on the Mathematics of Oil Recovery, Leoben, p. 259-269 (1996)

Omre, H. and Tjelmeland, H.: Petroleum geostatistics. *in* Baafi, E.Y., and Schofield, N.A., ed., Proceedings of the 5th International Geostatistics Congress: Wollongong, Australia, v.1, p. 41-52 (1996)

Park, K. Caers, J.: History matching in low-dimensional connectivity-vector space. SCRF report 17, Stanford University (2007)

Rivenæs, J.C., Otterleti, C., Zachariassen, E., Dart, C., Sjoholm, J.: A 3D stochastic model integrating depth, fault and property uncertainty for planning robust wells, Njord Field, offshore Norway. Petroleum Geoscience. 11, 57-65 (2005)

Sambridge, M.: Geophysical inversion with a neighborhood algorithm - I: Searching a parameter space. Geophysical Journal International. 138 (2), 479-494 (1999)

Sambridge, M.: Geophysical inversion with a neighborhood algorithm - II: Appraising the ensemble. Geophysical Journal International. 138 (3), 727-746 (1999)

Samson, P., Dubrule, O., Euler, N.: Quantifying the impact of structural uncertainties on gross-rock volume estimates. Paper presented at European 3-D Reservoir Modelling Conference, Stavanger, Norway, SPE 35535, 16-17 April 1996

Scheidt, C. Caers, J.: A workflow for spatial uncertainty quantification using distances and kernels. SCRF report 17, Stanford University (2007)

Srivastava, R. M.: Reservoir characterization with probability field simulation. Paper presented at SPE Annual Technical Conference and Exhibition, Washington, D.C., SPE24753, 4-7 October 1992

Srivastava, M. : Iterative methods for spatial simulation. SCRF Report 5, Stanford Center for Reservoir Forecasting (1992)

Strebelle, S.: Conditional simulation of complex geological structures using multiple-point geostatistics. Math. Geol., v34, p1-22 (2002)

Suzuki, S., Caers, J.: History matching with an uncertain geological scenario. Paper presented at SPE Annual Technical Conference and Exhibition, San Antonio, Texas, USA, SPE 102154, 24-27 September 2006

Tarantola, A.: Inverse problem theory. Elsevier Science Publishers (1987)

Thore, P., Shtuka, A., Lecour, M, Ait-Ettajer, T., Cognot, R.: Structural uncertainties: Determination, management, and applications. Geophysics. 67, 840-852 (2002)

Tjelmeland H. and Besag J.: Markov random fields with higher order interactions. Scandinavian Journal of Statistics, v. 25, p. 415-433 (1998)

Tran, T.: Improving Variogram Reproduction on Dense Simulation Grids. Computers and Geosciences 20 (7), 1161-1168 (1994)

Viseur, S.: Stochastic boolean simulation of fluvial deposits: a new approach combining accuracy and efficiency. Proceedings of SPE Annual Technical Conference and Exhibition, Houston, SPE #56688 (1999)

Yamada, T., and Okano, Y.: A volcanic reservoir: facies distribution model accounting for pressure communication. Proceedings of SPE Asia Pacific Oil and Gas Conference and Exhibition, Jakarta, SPE #93159 (2005)

Zhang, L., Caumon, G.: Perturbation of fault network geometry on a stratigraphic grid. In: Proceedings of the 26th Gocad Meeting, Nancy School of Geology, Nancy, France, 6-9 June 2006

Zoback, M. D., Townend, J.: Implications of hydrostatic pore pressures and high crustal strength for the deformation of intraplate lithosphere. Tectonophysics (2001)